frontiers | Research Topics

Multiple field/scale rock mechanics in coordinated exploitation of coal and its associated resources

Edited by
Fangtian Wang, Lishuai Jiang, Svetlana Timofeeva,
Wai Li and Yun Zhang

Published in
Frontiers in Earth Science

ISSN 1664-8714
ISBN 978-2-8325-2606-4
DOI 10.3389/978-2-8325-2606-4

About Frontiers

Frontiers is more than just an open access publisher of scholarly articles: it is a pioneering approach to the world of academia, radically improving the way scholarly research is managed. The grand vision of Frontiers is a world where all people have an equal opportunity to seek, share and generate knowledge. Frontiers provides immediate and permanent online open access to all its publications, but this alone is not enough to realize our grand goals.

Frontiers journal series

The Frontiers journal series is a multi-tier and interdisciplinary set of open-access, online journals, promising a paradigm shift from the current review, selection and dissemination processes in academic publishing. All Frontiers journals are driven by researchers for researchers; therefore, they constitute a service to the scholarly community. At the same time, the *Frontiers journal series* operates on a revolutionary invention, the tiered publishing system, initially addressing specific communities of scholars, and gradually climbing up to broader public understanding, thus serving the interests of the lay society, too.

Dedication to quality

Each Frontiers article is a landmark of the highest quality, thanks to genuinely collaborative interactions between authors and review editors, who include some of the world's best academicians. Research must be certified by peers before entering a stream of knowledge that may eventually reach the public - and shape society; therefore, Frontiers only applies the most rigorous and unbiased reviews. Frontiers revolutionizes research publishing by freely delivering the most outstanding research, evaluated with no bias from both the academic and social point of view. By applying the most advanced information technologies, Frontiers is catapulting scholarly publishing into a new generation.

What are Frontiers Research Topics?

Frontiers Research Topics are very popular trademarks of the *Frontiers journals series*: they are collections of at least ten articles, all centered on a particular subject. With their unique mix of varied contributions from Original Research to Review Articles, Frontiers Research Topics unify the most influential researchers, the latest key findings and historical advances in a hot research area.

Find out more on how to host your own Frontiers Research Topic or contribute to one as an author by contacting the Frontiers editorial office: frontiersin.org/about/contact

Multiple field/scale rock mechanics in coordinated exploitation of coal and its associated resources

Topic editors

Fangtian Wang — China University of Mining and Technology, China
Lishuai Jiang — Shandong University of Science and Technology, China
Svetlana Timofeeva — National Research Irkutsk State Technical University, Russia
Wai Li — University of Western Australia, Australia
Yun Zhang — Xi'an University of Science and Technology, China

Citation

Wang, F., Jiang, L., Timofeeva, S., Li, W., Zhang, Y., eds. (2023). *Multiple field/scale rock mechanics in coordinated exploitation of coal and its associated resources*. Lausanne: Frontiers Media SA. doi: 10.3389/978-2-8325-2606-4

Table of contents

frontiers | Frontiers in Earth Science

TYPE Original Research
PUBLISHED 05 January 2023
DOI 10.3389/feart.2022.1027816

OPEN ACCESS

EDITED BY
Wai Li,
University of Western Australia, Australia

REVIEWED BY
Shi Xilin,
Institute of Rock and Soil Mechanics (CAS), China
Feng Du,
China University of Mining and Technology, China

*CORRESPONDENCE
Changfeng Wang,
wangcf@bupt.edu.cn

SPECIALTY SECTION
This article was submitted to Structural Geology and Tectonics, a section of the journal Frontiers in Earth Science

RECEIVED 25 August 2022
ACCEPTED 14 November 2022
PUBLISHED 05 January 2023

CITATION
Zheng Q, Wang C and Pang L (2023), Overburden and surface subsidence with slicing paste filling mining in thick coal seams.
Front. Earth Sci. 10:1027816.
doi: 10.3389/feart.2022.1027816

Overburden and surface subsidence with slicing paste filling mining in thick coal seams

Qiushuang Zheng[1], Changfeng Wang[1]* and Lifu Pang[2]

[1]School of Economics and Management, Beijing University of Posts and Telecommunications, Beijing, China, [2]College of Energy and Mining Engineering, Shandong University of Science and Technology, Qingdao, China

To overcome the difficulties of overburden failure and surface subsidence induced by the slicing mining of extra-thick coal seams, slicing filler paste is typically utilized. In this paper, a continuous curved beam mechanical model of paste filling mining was established by theoretical analysis against the background of the 3305 working face of Yangcheng Coal Mine, the main controlling factors of surface subsidence were analyzed using an orthogonal experiment method (OEM) and an analytic network process (ANP) coupled comprehensive assignment, and the vertical displacement distribution of the overlying rock under different filling intensity was simulated using numerical simulation software. The following main findings were obtained. First, the elastic modulus of the backfill is the primary regulating factor, as demonstrated by the results. Second, the greater the filling body's elastic modulus, the more efficiently it carries the overburden load and minimizes the maximum surface subsidence. Third, the distance from the open-cut mine likewise reflects the degree of surface subsidence, with the amount of subsidence increasing as the distance from the mine increases.

KEYWORDS

thick coal seams, paste filling mining, analytic network process, overburden deformation, surface subsidence

Introduction

In recent years, coal resources have continued to dominate China's energy structure, comprising more than 50% of the total share of all energy sources. However, the environmental issues caused by roof caving incidents and surface subsidence as a result of disturbances in coal mining remain severe. According to the relevant statistics (Wu and Li, 1995), it is typical in East China to mine coal under buildings, railways, and water bodies, which not only wastes resources but also compromises the integrity of the earth if the mining method is inappropriate. The backfill mining technique, which may prevent surface subsidence and maximize coal resources, is currently receiving widespread attention from domestic experts.

Numerous professionals and academics are now conducting research on roof overburden damage and surface subsidence, mostly through indoor experiments, theoretical analysis, numerical simulation, and field observations. Deng et al. (2015)

suggested a novel mining technique of upward slicing filling mining for the geological circumstances of extra-thick coal seams using indoor experiments, investigated and researched this filling effect using similar material modeling, and conducted engineering practice experiments. Yang et al. (2015) utilized similarity theory to create comparable physical models to simulate the mining operation of underground ore deposits and monitor displacement changes. Liu et al. (2017a) constructed the theory of continuous curving beams for backfill mining using a large number of engineering applications and theoretical analysis as a starting point, revealing the mechanism for backfill control on the roof. Gao et al. (2017) established a defect-coupled constitutive model based on the theory of damage mechanics and showed that the piecewise nonlinear model more accurately depicts the effect of complex backfill defects on the stress–strain curve. Using geological data from Xiaotun Mine and numerical modeling, Zhang et al. (2011) assessed the influence of the filling ratio on surface subsidence. The results indicated that when the filling ratio increases, the control impact on surface subsidence improves. Kostecki and Spearing (2015) utilized finite-difference software to model the rheological characteristics of coal pillars in backfill mining and studied the link between the mechanical properties of the backfill material and the coal pillars under backfill mining settings. Numerous researchers have undertaken studies on the techniques and methods of backfilling, as well as the materials used in conjunction with the site, to avoid and manage roof-caused surface subsidence problems. Zhao et al. (2019) established an enhanced analytical method for evaluating the safety of vertically exposed backfill faces and maintaining the stability of the exposed backfill face. Thirukumaran et al. (2016) stated that the influence of the filling body on the surrounding rock is dependent on the mechanism, which consists of local support, surface support, and overall support. Gong et al. (2017) and Guo et al. (2018) investigated the physical parameters of filling with coal gangue as aggregate and the rationale and applicability of coal gangue mixture as backfill material.

During thick coal seam paste filling mining, the filling body in the mined-out region may handle the majority of the overburden load, which is one of the characteristics that separates it from caving. There is currently no consensus regarding important theories and application solutions for the site's study status of the stress development law of the surrounding rock, overburdened rock, and surface movement deformation characteristics. The correlation between the strength of the filling material and the quantity of surface subsidence requires more investigation. To solve the problems of roof fall accidents and surface subsidence caused by thick coal seam mining, this paper analyzes the influencing factors of backfill, the effect of roof control, and predicts the amount of surface subsidence. Combining statistical principles and evaluation methods, the mining plan was finally chosen as using cement as the cementitious material, using tailing sand as the aggregate, mixed with fly ash and industrial slag as the filling material for backfill mining with the research background of the 3305 working face of Yangcheng Coal Mine.

Summary of the study area

Yangcheng Coal Mine is located in Jining City, Shandong Province, in the Liangshan coalfield in the southwestern block of the Luxi fault block and belongs to the North China sedimentary coalfield. Its stratigraphic distribution is Ordovician, Carboniferous, Permian, and Quaternary in order from the bottom to the top. There are two major coal-bearing strata in the study area, namely, the Upper Carboniferous Taiyuan Formation (C3t) and the Lower Permian Shanxi Formation (P1s). The 3# coal seams are the recoverable coal seams in the whole area, with the thickness ranging from 4 m to 9.5 m, and the average thickness being 7.5 m. The mine has an annual production capacity of 2.1 million t/a and a recoverable coal reserve of 133 million t in a near-horizontal seam. The 3305 working face is located on the west side of the third mining area, and the upper part is the 3303 working face goaf. The average coal seam thickness of the working face is 7.2 m, and the seam floor elevation is −870 m to −990 m. Due to the damage caused to the buildings and farmland of the nearby villages above the ground surface during the fully mechanized caving mining of the working face, the surface subsidence caused by mining was mitigated by using the paste filling mining method when extracting the coal seam of working face 3305; because the coal seam was thick, the whole coal seam could not be filled at one time, so the thick coal seam was extracted by using the slicing paste filling method. The working face layout and filling site are shown in Figure 1.

Mechanical modeling of roof overburden

Analysis of the mechanical model of continuous curved beams

During the mining operation, as the slurry is continuously filled into the goaf, the backfill material gradually solidifies and forms a stable support carrier, thereby limiting the sinking of the overlying rock layer, causing the rock layer to bend and sink, and preventing the irregular collapse of the roof (Shi et al., 2021). The pressure on the roof above the thick coal seam can be considered the uniform load (q_0), while the roof's rocking beam is considered the elastic foundation beam. In addition, we consider the

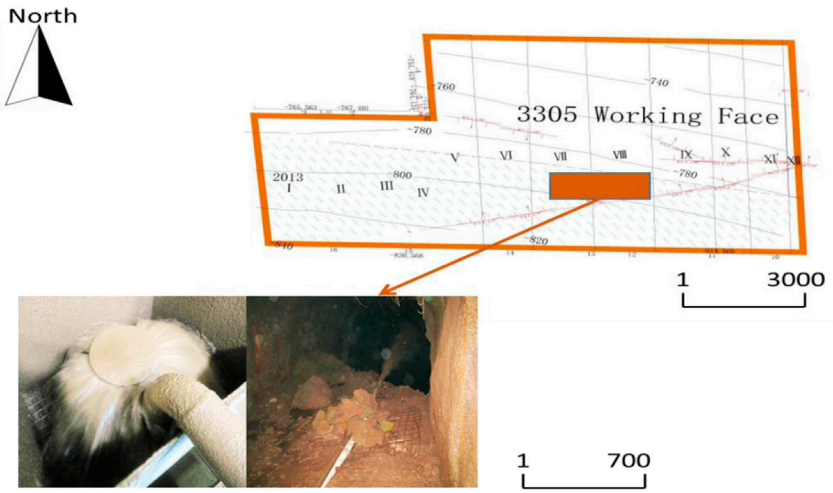

FIGURE 1
3305 mining area working face layout and mining area filling site.

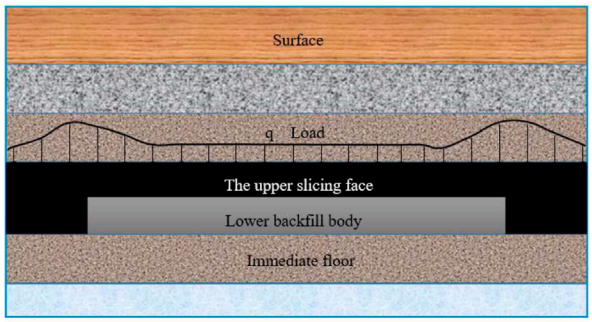

FIGURE 2
Mechanical model of slicing paste filling mining structure in thick coal seam.

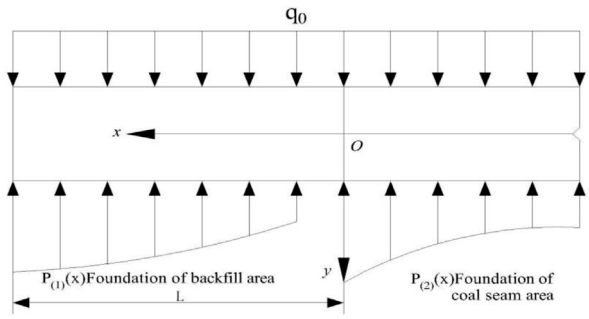

FIGURE 3
Mechanical force sketch of the roof of the filling mining.

subterranean ceiling, the filling body, and the coal seam floor to be the elastic base. Figure 2 (Wang et al., 2020) depicts a structural mechanical model of thick coal slicing paste filling mining based on the aforementioned assumptions.

Due to the supporting effect of the backfill body, the roof is more stable and less prone to fracture during the mining of thick coal seams with slicing paste filling. After mining damage, the roof is no longer supported on four sides and resembles a "simply supported beam" (Sandholtz et al., 2020). This structure's mechanical model matches that of the upper and lower slicing mining surface. To assist further qualitative calculations, the load q is approximated as a uniform load q_0, and a schematic diagram of the force is presented in Figure 3.

According to the Winkler foundation hypothesis, the pressure on any point on the foundation is positively correlated with the settlement at that point (Jena et al., 2020). Take the upper slicing face as an example, then,

$$\begin{cases} p_1(x) = k_1 w_1(x) & (0 \le x \le L) \\ p_2(x) = k_2 w_2(x) & (x \le 0), \end{cases} \tag{1}$$

where $p_1(x)$ is the support of the main roof by the foundation in the backfill area; $p_2(x)$ is the support of the main roof by the foundation in the coal seam area; $w_1(x)$ is the deflection of the main roof rock beam in the backfill area; $w_2(x)$ is the deflection of the main roof rock beam in the coal seam area; k_1, k_2 is the elastic foundation coefficient determined by the elastic modulus; L is the strike length of the backfill area; and q_0 is the uniform load.

When mining the thick coal seam with slicing and filling, for the main roof deflection differential equation:

$$\begin{cases} EI\dfrac{\mathrm{d}^4 w_1(x)}{dx^4} + k_1[w_1(x) - u_1] = q_0 & (0 \le x \le L) \\ EI\dfrac{\mathrm{d}^4 w_2(x)}{dx^4} + k_2 w_2(x) = q_0 & (x \le 0), \end{cases} \tag{2}$$

where E is the roof elastic modulus; I is the moment of inertia of the roof section; and u_1 is the final subsidence amount of the immediate roof contacting the backfill body.

Set $\beta_1 = \sqrt[4]{\frac{k_1}{4EI}}, \beta_2 = \sqrt[4]{\frac{k_2}{4EI}}$ and substitute the last formula:

$$\begin{cases} \dfrac{\mathrm{d}^4 w_1(x)}{dx^4} + 4\beta_1^4[w_1(x) - u_1] = \dfrac{q_0}{EI} & (0 \le x \le L) \\ \dfrac{\mathrm{d}^4 w_2(x)}{dx^4} + 4\beta_2^4 w_2(x) = \dfrac{q_0}{EI} & (x \le 0). \end{cases} \tag{3}$$

By solving the aforementioned equation we get

$$\begin{cases} w_1(x) = e^{-\beta_1 x}(A\cos\beta_1 x + B\sin\beta_1 x) + \dfrac{q_0}{k_1} + u_1 & (0 \le x \le L) \\ w_2(x) = e^{\beta_2 x}(C\cos\beta_2 x + D\sin\beta_2 x) + \dfrac{q_0}{k_2} & (x \le 0). \end{cases} \tag{4}$$

Since the mining method and the backfill body of the upper and the lower slicing face are the same, the amount of subsidence in the aforementioned Eq. 4 is the same. Combined with the boundary conditions, substituting x=0, $x = \pm\pi/2$ into Eq. 4, it can be determined that A, B, C, and D are as shown in Eq. 5:

$$\begin{cases} A = -\left(\dfrac{q_0}{k_1} + u_1\right) \\ B = \dfrac{\beta_1 - \beta_2}{\beta_1 + \beta_2}\left(\dfrac{q_0}{k_1} + u_1\right) \\ C = \dfrac{\beta_1^2}{\beta_2^2}\left(\dfrac{q_0}{k_1} + u_1\right) \\ D = \dfrac{\beta_2 - \beta_1}{\beta_1 + \beta_2}\left(\dfrac{q_0}{k_1} + u_1\right). \end{cases} \tag{5}$$

Finally, the deflection curve equations of the upper slicing face and coal seam area are obtained as follows:

$$\begin{cases} w_1(x) = e^{-\beta_1 x}\left(\dfrac{\beta_1 - \beta_2}{\beta_1 + \beta_2}\sin\beta_1 x - \cos\beta_1 x\right)\left(\dfrac{q_0}{k_1} + u_1\right) + \dfrac{q_0}{k_1} + u_1 & (0 \le x \le L) \\ w_2(x) = e^{\beta_2 x}\left(\dfrac{\beta_2 - \beta_1}{\beta_1 + \beta_2}\sin\beta_2 x + \cos\beta_2 x\right)\left(\dfrac{q_0}{k_1} + u_1\right)\dfrac{\beta_1^2}{\beta_2^2} + \dfrac{q_0}{k_2} & (x \le 0). \end{cases} \tag{6}$$

In the same way, the deflection curve equation of the lower slicing face and the coal seam area can be obtained as follows (Jena et al., 2020):

$$\begin{cases} w_3(x) = e^{-\beta_3 x}\left(\dfrac{\beta_3 - \beta_4}{\beta_3 + \beta_4}\sin\beta_3 x - \cos\beta_3 x\right)\left(\dfrac{q_0}{k_3} + u_1 + u_2\right) + \dfrac{q_0}{k_3} + u_1 + u_2 & (0 \le x \le L) \\ w_4(x) = e^{\beta_4 x}\left(\dfrac{\beta_4 - \beta_3}{\beta_3 + \beta_4}\sin\beta_4 x + \cos\beta_4 x\right)\left(\dfrac{q_0}{k_3} + u_1 + u_2\right)\dfrac{\beta_3^2}{\beta_4^2} + \dfrac{q_0}{k_4} & (x \le 0). \end{cases} \tag{7}$$

Main roof load and foundation coefficient

Main roof load

The main roof load during backfill mining can be regarded as the sum of the total pressure of the overlying strata, which is as follows:

$$q = \gamma_1 h_1 + \gamma_1 h_1 + \cdots + \gamma_m h_m. \tag{8}$$

Substituting the corresponding parameters of the overlying strata on the 3305 working face of Yangcheng Coal Mine 3# coal paste filling mining into the aforementioned formula, the main roof load q can be obtained as 22.5 MPa.

Foundation coefficient

Through the aforementioned analysis, it can be seen that the force and deformation of the roof are closely related to the foundation coefficient k (Chen and Park, 2020). When the coal seam is filled and mined, the elastic foundation is composed of the roof and the backfill body, which is regarded as an elastic body as a whole, and the constitutive relationship can be obtained as follows:

$$\sigma = E\varepsilon = E\frac{y}{h}, \tag{9}$$

that is, the total compression of the immediate roof and the backfill body is as follows:

$$\sigma_1 = E_1\frac{y_1}{h_1},\ \sigma_2 = E_2\frac{y_2}{h_2}, \tag{10}$$

where: E_1 is the immediate roof elastic modulus; E_2 is the backfill body elastic modulus (Liu et al., 2017b); y_1 is the immediate roof compression; y_2 is the backfill body compression; h_1 is the immediate roof height (Mangal, 2021); and h_2 is the backfill body height.

According to the Winkler foundation assumption:

$$\sigma = ky, \tag{11}$$

where σ is the overburden load; k is the foundation coefficient; and y is the total compression of the roof and backfill body.

The foundation coefficient of the 3# coal seam lower slicing filling mining is similar to that of the upper slicing filling mining. Combining Eqs. 9–11, there is the following relationship between the foundation coefficient of the $0 \le x \le L$ section and the foundation coefficient of the $x \le 0$ section in the upper and lower slicing backfill mining:

$$\begin{aligned} k_1 &= \frac{E_1 E_2}{E_2 h_1 + E_1 h_2} \\ k_2 &= \frac{E_1 E_3}{E_3 h_1 + E_1 h_3/2} \\ k_3 &= \frac{E_1 E_2}{E_2 h_1 + E_1 h_4} \\ k_4 &= \frac{E_1 E_3}{E_3 h_1 + E_1 h_3}, \end{aligned} \tag{12}$$

where k_1 is the foundation coefficient of upper slicing filling mining on 3# coal in the $0 \le x \le L$ interval; k_2 is the foundation coefficient of upper slicing filling mining on 3# coal in the $x \le 0$ interval; k_3 is the foundation coefficient of lower slicing filling mining on 3# coal in the $0 \le x \le L$ interval; k_4 is the foundation coefficient of lower slicing filling mining on 3# coal in $x \le 0$ interval; E_1 is the immediate roof elastic modulus; E_2 is the backfill body elastic modulus; E_3 is the coal seam elastic modulus; E_4 is the main roof elastic modulus; h_1 is the immediate roof height; h_2 is the height of the upper slicing backfill body; h_3 is the coal seam thickness; and h_4 is the backfill body height.

The relevant parameters of the upper face are as follows: E_1=6 GPa, h_1=4 m; E_2=0.5 GPa, h_2=3.24 m; E_3=3 GPa, h_3=7.2 m; E_4=21 GPa, and h_4=8 m (Ma et al., 2020). Substituting into the relevant parameters, we can obtain the foundation coefficient k_1=0.14 GN/m^3, k_2=0.54 GN/m^3.

The parameters of the immediate roof and the backfill body during the lower slicing mining are the same as those of the upper slicing mining. The overall height h_4 of the 3# coal backfill body is 6.48 m. Substituting the relevant parameters can obtain the foundation coefficient k_3=0.073 GN/m^3, k_4=0.33 GN/m^3.

Mechanical calculation of roof subsidence

Regarding the main roof subsidence characteristics of foundation in the filling area, from the aforementioned analysis, it can be seen that the main roof subsidence of the filling area of 3# coal upper and lower slicing paste filling mining is expressed as follows:

$$\begin{cases} \text{The upper: } w_1(x) = e^{-\beta_1 x}\left(\frac{\beta_1-\beta_2}{\beta_1+\beta_2}\sin\beta_1 x - \cos\beta_1 x\right)\left(\frac{q_0}{k_1}+u_1\right) + \frac{q_0}{k_1} + u_1 & (0 \le x \le l) \\ \text{The lower: } w_3(x) = e^{-\beta_3 x}\left(\frac{\beta_3-\beta_4}{\beta_3+\beta_4}\sin\beta_3 x - \cos\beta_3 x\right)\left(\frac{q_0}{k_3}+u_1+u_2\right) + \frac{q_0}{k_3} + u_1 + u_2 & (0 \le x \le l). \end{cases} \tag{13}$$

The buried depth of the 3# coal seam is 900 m. The upper and the lower slicing mining areas have the same roof subsidence during the slicing paste filling mining; both are 0.36 m. We find the foundation coefficient k_1=0.14 GN/m^3, k_2=0.57 GN/m^3 in the upper slicing filling mining, and the foundation coefficient k_3=0.073 GN/m^3, k_4=0.33 GN/m^3, with the main roof load q=22.5 MPa in the lower slicing filling mining. The mechanical parameters of each influencing factor are shown in Table 1. We then substitute the relevant parameters in Table 1 into Eq. 13 and analyze the main roof subsidence's characteristics of the upper and lower slicing mining filling areas (using MATLAB) and draw the fitting curve (using Origin) (Heinze et al., 2021). The schematic diagram of the influence curve of various factors on the main roof subsidence during upper slicing mining is shown in Figure 4, and the schematic diagram of the influence curve of various factors on the main roof subsidence during lower slicing mining is shown in Figure 5 (Deng et al., 2021).

In the upper and lower slicing mining, the influence of many sources on the principal roof subsidence has a clear, consistent tendency. As the distance from the coal wall (i.e., the distance of the open-off cut from the coal wall) grows, the backfill pressure first increases dramatically, peaks after a given distance, and then decreases gradually until it reaches the original rock stress (Yang et al., 2014). The following are the mechanical properties of the influencing factors' parameters:

1) The modulus of elasticity and the thickness of the main roof has a certain influence on the pressure of the backfill body during coal seam filling and mining, which is manifested as follows: as the elasticity modulus and the thickness of the main roof increase, the maximum value of the pressure on the backfill body is increasingly further from the wall. Compared with the main roof elastic modulus, the influence of the main roof thickness is relatively significant.
2) The buried depth of the coal seam has a more obvious impact on the pressure of the backfill. The further the buried depth of the coal seam is from the surface, the greater the pressure of the backfill and the higher its peak value.
3) During coal seam filling and mining, the amount of subsidence when the roof touches the backfill also has a significant influence on the pressure on it. The greater the subsidence value, the higher the peak pressure of the backfill body.
4) During coal seam filling and mining, regarding the backfill body, the larger the elastic modulus, the larger the peak pressure on it, and as the peak pressure point gradually approaches the wall, the smaller the range of pressure on the backfill body.
5) Regarding the elastic modulus of the coal, as the elastic modulus of the coal gradually increases, the peak pressure of the backfill gradually decreases, but the pressure on the backfill is less affected.

Comprehensive risk assessment and analysis of main roof subsidence based on the adopted method

The alternative ranges of the main control factors are selected by the foundation coefficients and hydrogeological data, and the ranking of the importance of the weights is determined by using the comprehensive assignment method coupled with the analytic network process (ANP) and orthogonal experiment method (OEM) (Mosaad and Basheer, 2020). With the assessment methods based on expert experience and documentary data, the advantages of subjective analysis and objective analysis can be combined to improve prediction accuracy and credibility.

TABLE 1 Mechanical property parameters of different influencing factors.

Main roof elastic modulus (GPa)	Main roof thickness (m)	Buried depth of the coal seam (m)	The subsidence of the roof contacting the backfill (m)	Backfill elastic modulus (GPa)	Coal elastic modulus (GPa)
15, 18, and 21	4, 6, and 8	700, 800, and 920	0.05, 0.20, and 0.36	0.1, 0.3, and 0.5	1, 2, and 3
24 and 27	10 and 12	1,000 and 1,100	0.50 and 0.65	0.7 and 0.9	4 and 5

TABLE 2 Cluster-weight matrix.

	B_1	B_2	B_3
B_1	0	0.25	0.111111
B_2	0.833333	0	0.888889
B_3	0.166667	0.75	0

TABLE 3 Unweighted supermatrix.

		B_1		B_2		B_3	
		C_{22}	C_{21}	C_{11}	C_{12}	C_{31}	C_{32}
B_1	C_{22}	0	0	0.33	0.17	0.33	0.30
	C_{21}	0	0	0.67	0.83	0.67	0.70
B_2	C_{11}	0.8	0.11	0	0	0.5	0.76
	C_{12}	0.2	0.89	0	0	0.5	0.24
B_3	C_{31}	0.875	0.875	0.5	0.33	0	0
	C_{32}	0.125	0.125	0.5	0.67	0	0

TABLE 4 Weighted matrix.

		B_1		B_2		B_3	
		C_{22}	C_{21}	C_{11}	C_{12}	C_{31}	C_{32}
B_1	C_{22}	0	0	0.08	0.04	0.04	0.03
	C_{21}	0	0	0.17	0.21	0.07	0.08
B_2	C_{11}	0.67	0.09	0	0	0.44	0.68
	C_{12}	0.17	0.74	0	0	0.44	0.21
B_3	C_{31}	0.15	0.15	0.38	0.25	0	0
	C_{32}	0.02	0.02	0.38	0.5	0	0

TABLE 5 Limit matrix.

		B_1		B_2		B_3	
		C_{22}	C_{21}	C_{11}	C_{12}	C_{31}	C_{32}
B_1	C_{22}	0.04	0.04	0.04	0.04	0.04	0.04
	C_{21}	0.11	0.11	0.11	0.11	0.11	0.11
B_2	C_{11}	0.25	0.25	0.25	0.25	0.25	0.25
	C_{12}	0.21	0.21	0.21	0.21	0.21	0.21
B_3	C_{31}	0.17	0.17	0.17	0.17	0.17	0.17
	C_{32}	0.20	0.20	0.20	0.20	0.20	0.20

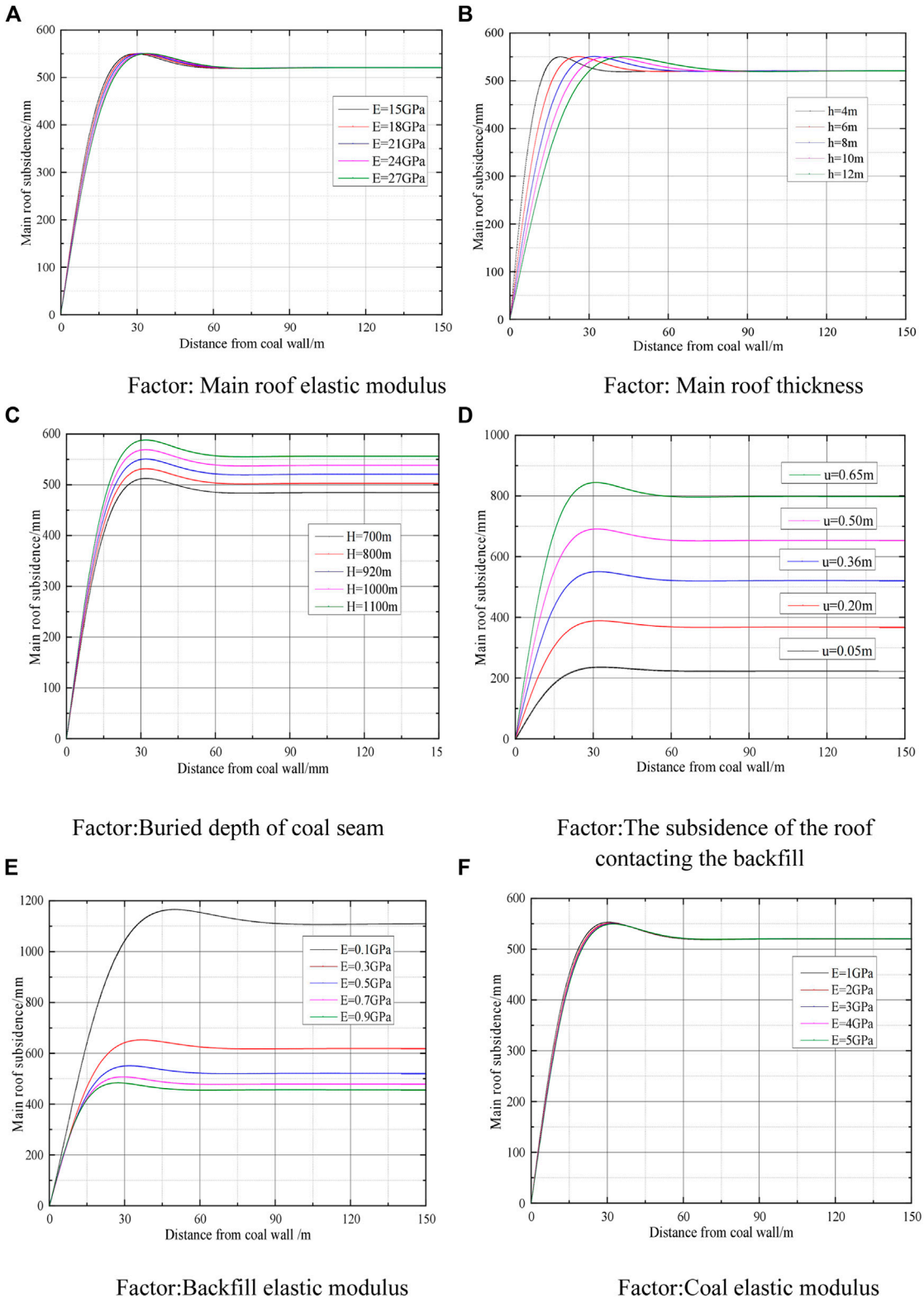

FIGURE 4
Schematic diagram of the influence of various factors on the main roof subsidence (upper slicing mining). **(A)** Factor: main roof elastic modulus. **(B)** Factor: main roof thickness. **(C)** Factor: buried depth of the coal seam. **(D)** Factor: the subsidence of the roof contacting the backfill. **(E)** Factor: backfill elastic modulus. **(F)** Factor: coal elastic modulus.

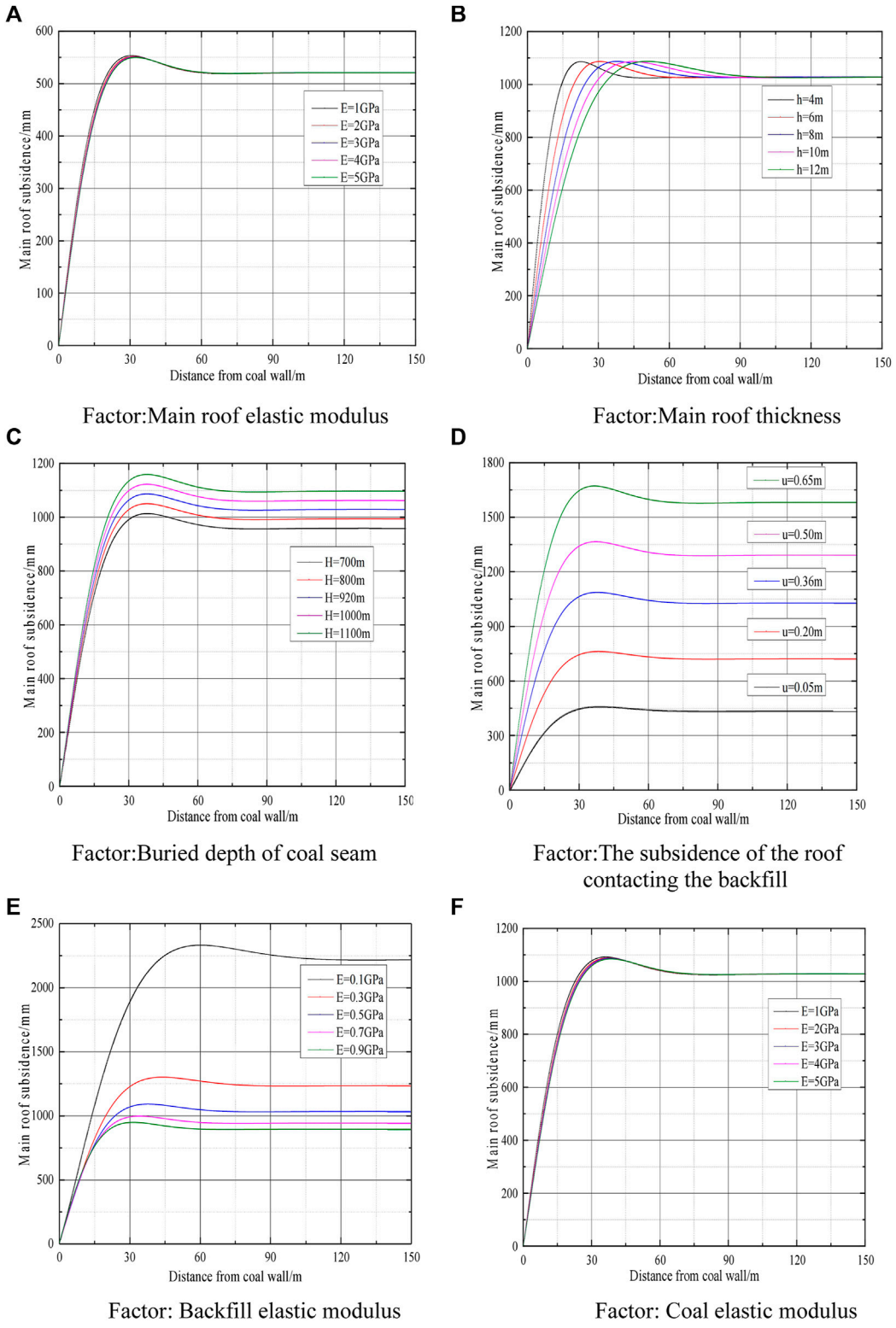

FIGURE 5
Schematic diagram of the influence of various factors on the main roof subsidence (lower slicing mining). **(A)** Factor: main roof elastic modulus. **(B)** Factor: main roof thickness. **(C)** Factor: buried depth of the coal seam. **(D)** Factor: the subsidence of the roof contacting the backfill. **(E)** Factor: backfill elastic modulus. **(F)** Factor: coal elastic modulus.

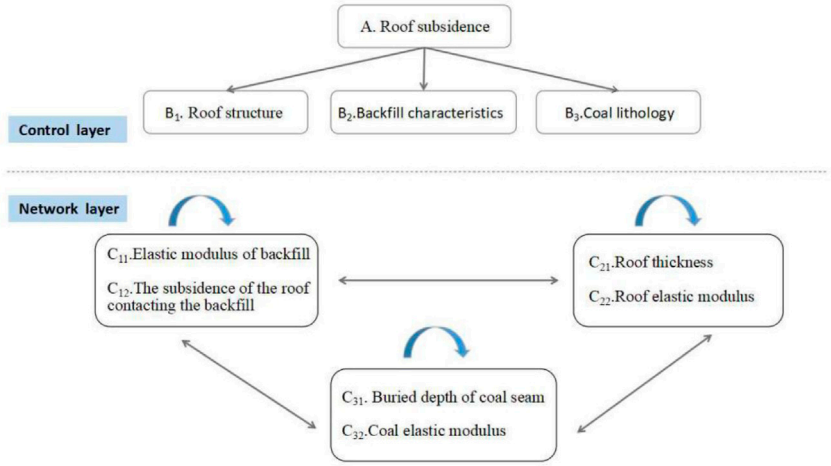

FIGURE 6
Three-cluster ANP network model.

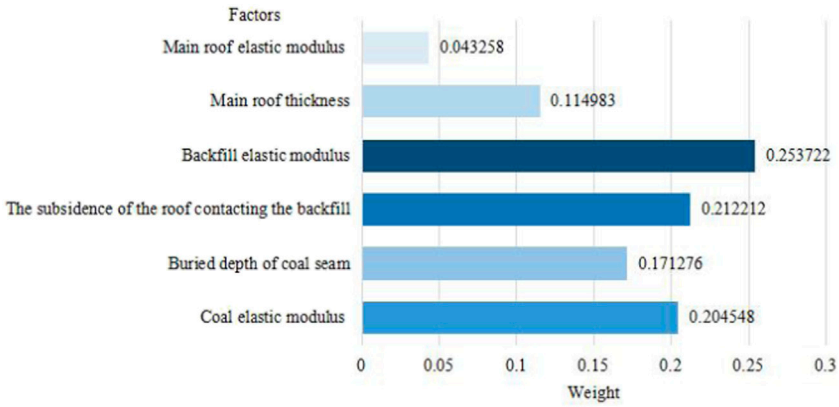

FIGURE 7
Distribution diagram of the weights for the main roof subsidence factors.

Analytic network process (ANP)

An overview of the analytic network process (ANP)

Thomas L. Saaty enhanced the analytic network technique based on the analytic hierarchy process (AHP) (Huang et al., 2020), which is an evaluation approach that combines qualitative and quantitative analysis. ANP can take into account the internal connections between nodes of various factor groups in a more thorough way than the classic AHP, which merely stresses the flaws of reciprocal impact across criteria levels (Kundu et al., 2021).

The weights are calculated as follows:

1) Construction of the judgment matrix. The control layer of the ANP has criterion elements B_1, B_2, B_3..., and the network layer under the control layer has element groups B_{i1}, B_{i2}, B_{i3}..., where i=1,2,...,n (Mirarabrazi and Navrodi, 2020). Take the control layer elements as the criteria and the network layer elements as the secondary criteria. The elements in the element group are compared according to their influence on B_{ij}, and the construction judgment matrix is obtained:

$$W_{ij} = \begin{bmatrix} w_{(i1)}^{(j1)} & w_{(i1)}^{(j2)} & \cdots & w_{(i1)}^{(jn_j)} \\ w_{(i2)}^{(j1)} & w_{(i2)}^{(j2)} & \cdots & w_{(i2)}^{(jn_j)} \\ \cdots & \cdots & \cdots & \cdots \\ w_{(in_i)}^{(j1)} & w_{(in_i)}^{(j2)} & \cdots & w_{(in_i)}^{(jn_j)} \end{bmatrix}.$$

10.3389/feart.2022.1027816

TABLE 6 Orthogonal experiment table of various influencing factors.

Number	Main roof elastic modulus (GPa)	Main roof thickness (m)	Buried depth of the coal seam (m)	The subsidence of the roof contacting the backfill (m)	Backfill elastic modulus (GPa)	Coal elastic modulus (GPa)	Maximum subsidence of main roof (mm)
1	1 (15)	1 (4)	1 (700)	1 (0.05)	1 (0.1)	1 (1)	1,350
2	1 (15)	2 (6)	2 (800)	2 (0.20)	2 (0.3)	2 (2)	865
3	1 (15)	3 (8)	3 (900)	3 (0.35)	3 (0.5)	3 (3)	1,028
4	1 (15)	4 (10)	4 (1,000)	4 (0.50)	4 (0.7)	4 (4)	1,238
5	1 (15)	5 (12)	5 (1,100)	5 (0.65)	5 (0.9)	5 (5)	1,499
6	2 (18)	1 (4)	2 (800)	3 (0.35)	4 (0.7)	5 (5)	878
7	2 (18)	2 (6)	3 (900)	4 (0.50)	5 (0.9)	1 (1)	1,171
8	2 (18)	3 (8)	4 (1,000)	5 (0.65)	1 (0.1)	2 (2)	2,771
9	2 (18)	4 (10)	5 (1,100)	1 (0.05)	2 (0.3)	3 (3)	770
10	2 (18)	5 (12)	1 (700)	2 (0.20)	3 (0.5)	4 (4)	849
11	3 (21)	1 (4)	3 (900)	5 (0.65)	2 (0.3)	4 (4)	1,759
12	3 (21)	2 (6)	4 (1,000)	1 (0.05)	3 (0.5)	5 (5)	473
13	3 (21)	3 (8)	5 (1,100)	2 (0.20)	4 (0.7)	1 (1)	686
14	3 (21)	4 (10)	1 (700)	3 (0.35)	5 (0.9)	2 (2)	859
15	3 (21)	5 (12)	2 (800)	4 (0.50)	1 (0.1)	3 (3)	2,249
16	4 (24)	1 (4)	4 (1,000)	2 (0.20)	5 (0.9)	3 (3)	605
17	4 (24)	2 (6)	5 (1,100)	3 (0.35)	1 (0.1)	4 (4)	2,553
18	4 (24)	3 (8)	1 (700)	4 (0.50)	2 (0.3)	5 (5)	1,373
19	4 (24)	4 (10)	2 (800)	5 (0.65)	3 (0.5)	1 (1)	1,550
20	4 (24)	5 (12)	3 (900)	1 (0.05)	4 (0.7)	2 (2)	345
21	5 (27)	1 (4)	5 (1,100)	4 (0.50)	3 (0.5)	2 (2)	1,357
22	5 (27)	2 (6)	1 (700)	5 (0.65)	4 (0.7)	3 (3)	1,459
23	5 (27)	3 (8)	2 (800)	1 (0.05)	5 (0.9)	4 (4)	271
24	5 (27)	4 (10)	3 (900)	2 (0.20)	1 (0.1)	5 (5)	1,897
25	5 (27)	5 (12)	4 (1,000)	3 (0.35)	2 (0.3)	1 (1)	1,273

TABLE 7 Orthogonal experiment table of various influencing factors.

	Comprehensive average	Factor					
		Main roof elastic modulus	Main roof thickness	Buried depth of the coal seam	The subsidence of the roof contacting the backfill	Backfill elastic modulus	Coal elastic modulus
Assessment index	*k1*	1,072	1,066	1,054	518	2,040	1,082
	k2	1,288	1,304	1,163	980	1,208	1,463
	k3	1,205	1,226	1,240	1,318	1,051	1,076
	k4	1,285	1,263	1,272	1,478	921	1,334
	k5	1,251	1,243	1,373	1,808	881	1,224
	R	92	114	210	1,165	1,283	387
Importance ranking	6	5	4	2	1	3	

That the italic values indicate the values of K1, K2, K3, K4, and K5 are the sum of the test index values at the first, second, third, fourth, and fifth levels for each corresponding factor respectively. R stands for Range.

TABLE 8 Geomechanical parameters of coal and rock formations.

Rock strata type	Elastic modulus	Poisson's ratio	Cohesion	Angle of internal friction	Tensile strength	Density
	G (GPa)	*μ*	*c* (MPa)	*φ* (°)	*Rm* (MPa)	*ρ* (g/cm^3)
Medium sandstone	10	0.27	6.2	36	2.8	2.24
Mudstone	8	0.29	2.6	33	1.3	2.22
Fine sandstone	12	0.27	4.0	34	2.0	2.59
Siltstone	10	0.27	3.0	33	1.0	2.48
Mudstone	5	0.29	2.5	32	1.2	2.17
Siltstone	7	0.28	2.8	33	2.4	2.12
Fine sandstone	10	0.27	3.8	33	2.8	2.45
Mudstone	4	0.29	1.8	32	1.6	2.31
Fine sandstone	7	0.27	4.2	33	2.0	2.10
Siltstone	6	0.28	2.6	34	2.4	2.20
3# coal seam	7	0.29	1.6	32	0.8	1.35
Siltstone	6	0.29	2.0	33	2.2	2.20
Fine sandstone	8	0.28	3.2	34	2.5	2.03
Siltstone	7	0.28	2.6	33	1.8	2.63
Mudstone	5	0.28	1.8	33	1.6	2.09
Three kinds of ash	9	0.27	6.0	34	2.4	2.53
Mudstone	4	0.29	3.0	34	1.6	2.50
Fine sandstone	8	0.26	6.0	35	2.0	2.03
Mudstone	5	0.28	3.2	34	1.6	2.50
Fault fracture zone	2	0.35	0.6	15	0.2	1.90

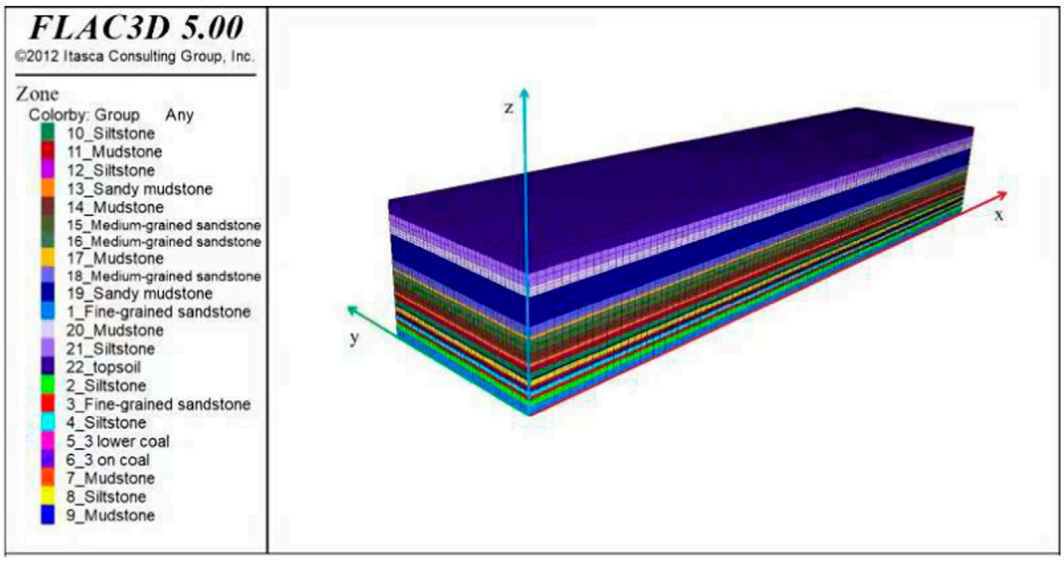

FIGURE 8
Numerical calculation model.

A

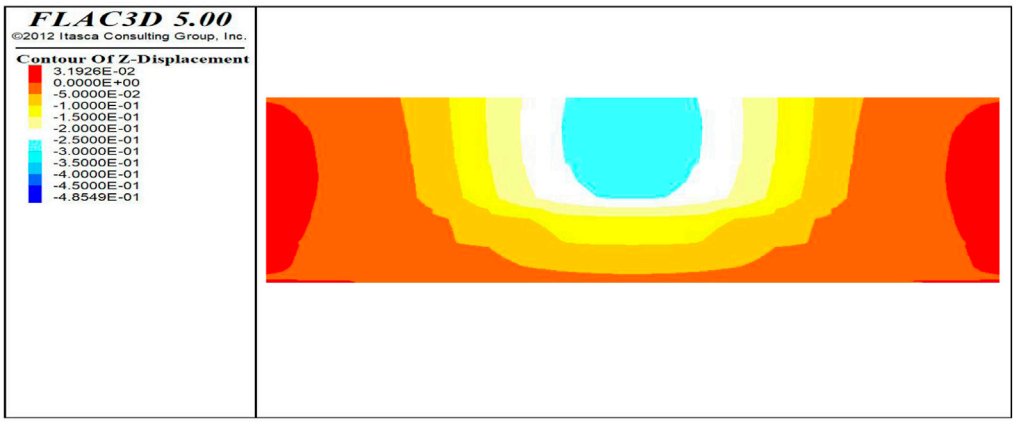

Cloud image of vertical displacement distribution of 1.0GPa 3#coal overlying strata

B

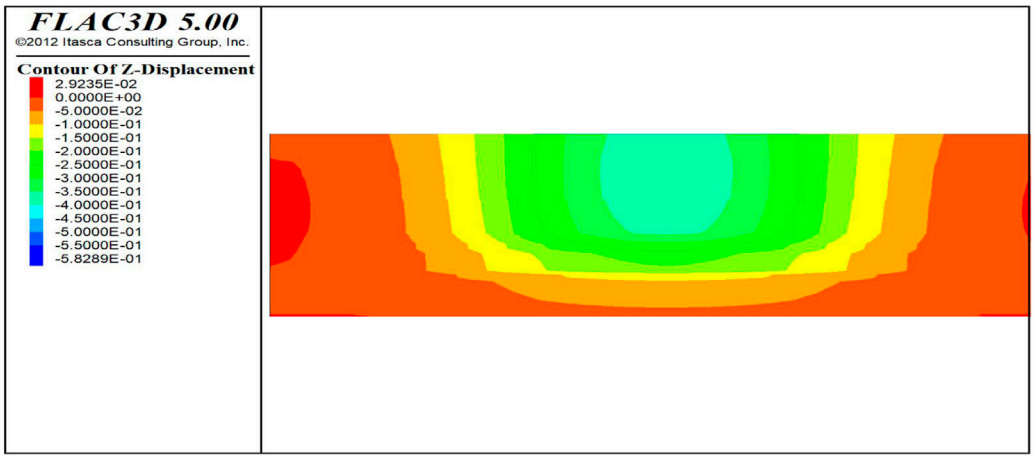

Cloud image of vertical displacement distribution of 0.5GPa 3#coal overlying strata

C

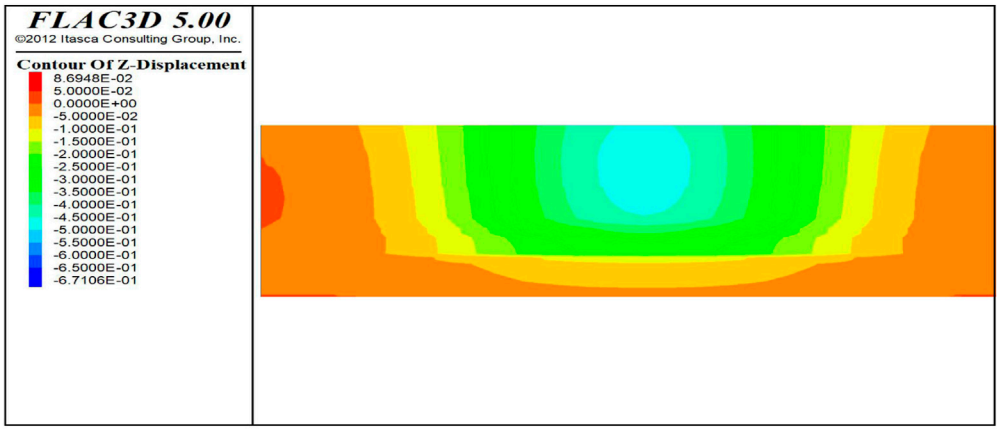

Cloud image of vertical displacement distribution of 0.3GPa 3#coal overlying strata

FIGURE 9
Vertical displacement distribution of overlying strata under different backfill strengths. **(A)** Cloud image of vertical displacement distribution of 1.0 GPa 3# coal overlying strata. **(B)** Cloud image of vertical displacement distribution of 0.5 GPa 3# coal overlying strata. **(C)** Cloud image of vertical displacement distribution of 0.3 GPa 3# coal overlying strata.

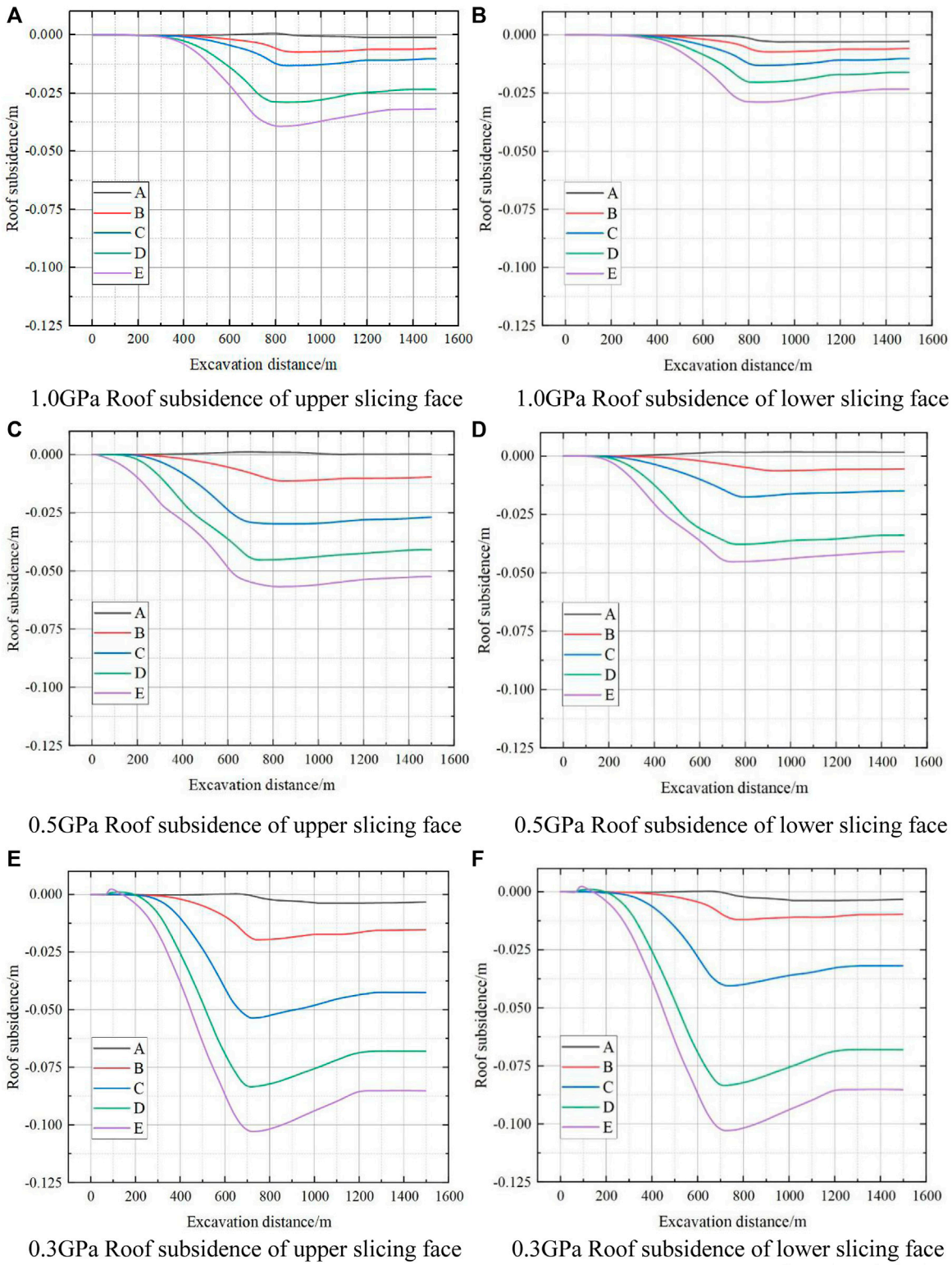

FIGURE 10
Diagram of the overburden movement process during slicing mining. **(A)** 1.0 GPa roof subsidence of the upper slicing face. **(B)** 1.0 GPa roof subsidence of the lower slicing face. **(C)** 0.5 GPa roof subsidence of the upper slicing face. **(D)** 0.5 GPa roof subsidence of the lower slicing face. **(E)** 0.3 GPa roof subsidence of the upper slicing face. **(F)** 0.3 GPa roof subsidence of the lower slicing face.

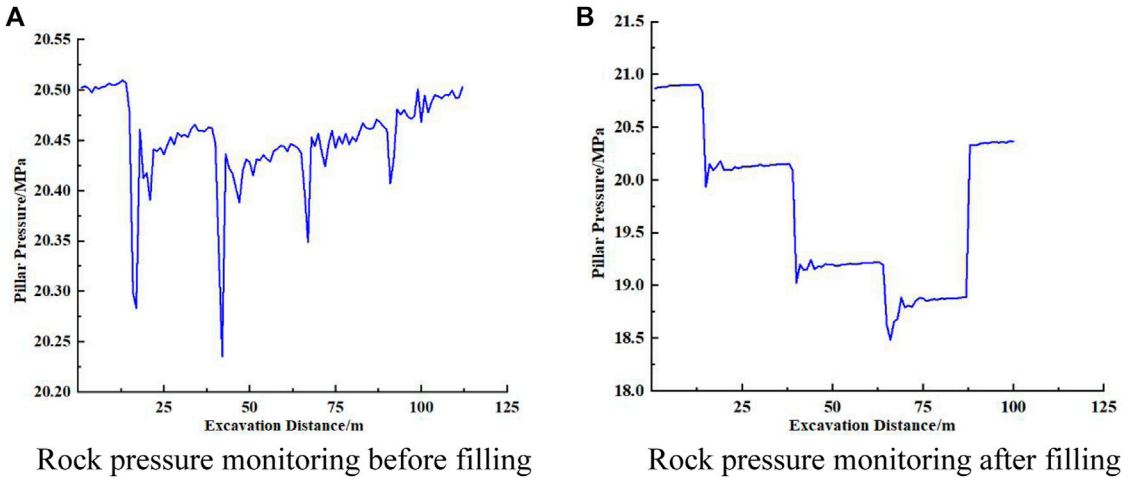

FIGURE 11
Rock pressure monitoring on the 3305 working face. **(A)** Rock pressure monitoring before filling. **(B)** Rock pressure monitoring after filling.

2) The ANP super cluster-weighted matrix and limit matrix (Camara et al., 2020). Combining the ranking vectors of the degree of mutual influence of the elements of the network layer, the supermatrix under the control element is obtained:

$$W = \begin{bmatrix} w_{11} & w_{12} & \cdots & w_{1n} \\ w_{21} & w_{22} & \cdots & w_{2n} \\ \cdots & \cdots & \cdots & \cdots \\ w_{n1} & w_{n2} & \cdots & w_{nn} \end{bmatrix}.$$

Each element of the aforementioned matrix is a non-negative matrix, and the columns of each supermatrix's submatrices are normalized, but the entire matrix's columns are not. The relevance of each element group is compared using the control level B as the criterion and the arbitrary element group B_i as the sub-criterion to generate the characteristic matrix:

$$P = \begin{bmatrix} p_{11} & p_{12} & \cdots & p_{1n} \\ p_{21} & p_{22} & \cdots & p_{2n} \\ \cdots & \cdots & \cdots & \cdots \\ p_{n1} & p_{n2} & \cdots & p_{nn} \end{bmatrix}.$$

Use the formula $\bar{W} = W \cdot P$ to obtain the weighted supermatrix and use the formula $W^{\infty} = \lim_{n \to \infty} \bar{W}^n$ to obtain the limit matrix so as to obtain the importance ranking of each index.

Weight calculation by the analytic network process (ANP) model

According to the analysis of the mechanical model, we obtain six factors that affect the main roof subsidence: main roof elastic modulus; main roof thickness; buried depth of the coal seam; coal elastic modulus; backfill elastic modulus; and the subsidence of the roof contacting the backfill. Based on the attributes of the factors, they can be classified into three categorizations: roof structure; backfill characteristics; and coal lithology. A three-cluster ANP network model was developed as shown in Figure 6.

Using group decision-making expert scoring, using 1–9 scales as the measurement criteria, and using (0,1) as the scoring range for the importance of the criteria or elements at the same level, pairwise comparison scores are obtained. The supermatrix composed of the judgment matrix is shown in Table 2, Table 3, Table 4, and Table 5.

The maximum eigenroots and the corresponding eigenvectors are calculated according to the limit matrix, and then the eigenvectors are normalized to obtain the final weight of the roof subsidence amount evaluation index, as shown in Figure 7.

It can be seen from Figure 7 that the backfill elastic modulus and the subsidence of the roof contacting the backfill are the main controlling factors. They play a decisive role in the failure state of the overlying rock during sliced filling mining.

Verification experiment

Overview of the orthogonal experiment method (OEM)

Orthogonal experimental design and analysis methods are scientific calculation methods based on mathematical statistics, probability theory, and practical experience, using standardized orthogonal table design schemes and analyzing the results of precision and sensitivity. In the analysis of actual problems, the use of orthogonal tables to optimize the test plan can reduce the number of experiments while ensuring a certain level of accuracy, efficiently handling multi-factor optimization problems, and finding the main factors that have a significant impact on the test indicators among many factors.

The design process of the OEM (Xuan and Leung, 2011) is as follows: 1) determine the experimental factors and the number of levels; 2) select the applicable orthogonal table; 3) list the experimental plan and the experimental results; 4) perform range analysis and variance analysis on the experimental results; and 5) determine the optimal or better combination of factor levels.

Background of the orthogonal experiment method (OEM)

Weight calculation by the orthogonal experiment method (OEM)

Regarding at the six factors that affect the main roof subsidence in the 3305 coal face of Yangcheng Coal Mine, the primary and secondary degrees of each influencing factor are clarified by the OEM, and the orthogonal test table is designed as an example at 150 m behind the 3305 filling face of the lower slicing face. The main roof elastic modulus is selected as 15 GPa, 18 GPa, 21 GPa, 24 GPa, and 27 GPa; the main roof thickness is selected as 4 m, 6 m, 8 m, 10 m, and 12 m; the buried depth of the coal seam is selected as 700 m, 800 m, 900 m, 1000 m, and 1100 m; the subsidence of the roof contacting the backfill is selected as 0.05 m, 0.20 m, 0.35 m, 0.50 m, and 0.65 m; the backfill elastic modulus is selected as 0.1 GPa, 0.3 GPa, 0.5 GPa, 0.7 GPa, and 0.9 GPa; and the coal elastic modulus is selected as 1 GPa, 2 GPa, 3 GPa, 4 GPa, and 5 GPa. The orthogonal test table with six factors and five levels is established as shown in Table 6.

We use the data in Table 6 to obtain the k_i value and the range value R of each factor through orthogonal calculation, and the results are shown in Table 7.

The importance ranking was performed by finding the comprehensive average of the five levels (k_1, k_2, k_3, k_4, and k_5) of the six main control factors and conducting the range analysis to find the range value R corresponding to each factor. The order of importance positively reflects the importance of the factors, i.e., the first one is the most important and has the greatest weight, and so on. As can be seen from Table 7, the first two are the backfill elastic modulus and the subsidence of the roof contacting the backfill.

Determine the main control factors

The weight of contribution to the aim, as determined by the ANP expert scoring panel, is as follows: backfill elastic modulus > roof subsidence contacting the backfill > coal elastic modulus > buried depth of the coal seam > main roof thickness > main roof elastic modulus. The results were confirmed by the construction of orthogonal experiments based on objective data, and the ranking of the relevance of the main control factors derived by analysis of variance was compatible with the empirical analysis-based ANP group decision scoring approach. It can be determined that the elastic modulus of the backfill body is the main control factor for the subsidence of the backfill mining, and simulations were conducted for various orders of the backfill elastic modulus. In addition, the filling material that can reach the ideal modulus was chosen to handle the surface subsidence and destruction problem.

Numerical simulation of movement and deformation of overlying strata in the slicing paste filling mining of thick coal seams

Geomechanical parameters of the model

The numerical calculation model is established based on the engineering background of the geological mining conditions of the 3305 filling face of Yangcheng Coal Mine (Miranda et al., 2011). The simulated coal seam thickness is 7.2 m, the coal seam advancement distance is 750 m, and the working face width is 120 m. Due to the deep location of the coal seam, only the positions between 120 m above and below the coal seam (distance from the z-direction 240 m) are simulated, and the overburden gravity of 21.25 MPa is applied on the top. Considering the boundary effect factor, the simulated size is determined to be 1,500 m*350 m*463 m. The working face adopts the operation of aligning itself with the inclination, mining toward the direction, and filling while mining. The advancing amount is 1,000 m with 250-m coal pillars reserved at both ends, and 50-m protection coal pillars are reserved at both ends of the inclination. The simulation excavation is set with 20 excavation steps, where each step is 50 m, and a total of 109,224 grids are generated by the finite difference method of FLAC3D. From the 60 observation points, we selected five representative points (A, B, C, D, and E) with different orientations as sample data collection points. Taking the orientation of the model as the X axis, the inclination as the Y axis, and the height as the Z axis, an XOY space rectangular coordinate system is established. The coordinates of A, B, C, D, and E are as follows: A (300; 100;400); B (500;150;360); C (700;200;320); D (900;280;280); and E (1,100;300;240).The geomechanical parameters of coal and rock are shown in Table 8, and the numerical model is shown in Figure 8.

Overlying strata and surface deformation characteristics of thick coal seam slicing paste filling mining under different backfill strengths

Paste filling materials can be calculated by the Salamon formula double-yield plasticity model (Du et al., 2020; Wang and Du, 2020; Yang et al., 2020). From the conclusion of the previous section, it can be seen that the strength of the backfill is a key factor affecting the

filling effect of the paste (Liu et al., 2017c). In order to verify the effect of backfill strength on overburden and surface control, numerical simulation was conducted to analyze the overburden and surface subsidence by comparing three cases of 0.3 GPa, 0.5 GPa, and 1.0 GPa backfill strength at a 95% fill rate.

We compared three different backfill strengths of 0.3 GPa, 0.5 GPa, and 1.0 GPa. We took the vertical displacement distribution of overburden strata after all the advancing of the 3# coal 3305 working face as an example for comparison, as shown in Figure 9, and the surface subsidence comparison graph is shown in Figure 10.

Five points with different orientations (A, B, C, D, and E) were selected from the 60 observation points in FLAC3D numerical simulation to observe the amount of roof subsidence corresponding to the filling of the slicing mining with different elastic moduli of 0.3 GPa, 0.5 GPa, and 1.0 GPa at a 95% filling rate. With the advancement of the 3305 working face, the overlying rock layer gradually sinks on the original foundation, and the amount of subsidence increases with the advancement of mining. The upper slicing face reaches its peak at an excavation step distance of about 800 m, and the lower slicing face reaches its peak at an excavation step distance of about 1,500 m; until the direction of mining is infinite, the amount of subsidence tends to be stable. We observed the change of the effect of surface subsidence and overburden damage at five points (A, B, C, D, and E) using backfill with different elastic moduli. The subsidence of the roof with mining damage was ranked 0.3 GPa>0.5 GPa>1.0 GPa. In the maximum settlement curves of the upper and lower strata, 1.0 GPa<0.5 GPa<0.3 GPa, and the peak of the main roof subsidence of the upper slicing face is greater than that of the lower slicing face.

Analysis of mine pressure monitoring data

According to the mine monitoring pressure data before and after backfill mining at the 3305 working face, a comparative analysis was conducted. With the advancement of mining, the pressure on the protective coal pillars showed different changes, and the mine monitoring pressure graphs before and after filling were obtained as shown in Figure 11.

From Figure 11A, it can be seen that in the unfilled area, the mine pressure is obvious and the pillar is under greater force. During the mining process, the mine pressure started to decrease at 10 m of excavation because the coal body was extracted one after another. When the excavation reaches 40 m, the periodic incoming pressure appears, and comparing this part of mine pressure with the previous numerical simulation, it can be found that it basically matches. According to Figure 11B, it can be seen that, after filling, the mine incoming pressure shows a large and stable decrease, and the increase tends to be stable in the later period. The peak and average values of the pillar pressure are significantly reduced, which reduces the risk of rock impact and roof collapse and deformation. Therefore, it can be concluded that slicing paste filling mining with cement, tailing sand, fly ash, and industrial slag as the filling materials for thick coal seams can effectively support the roof and reduce the amount of subsidence.

Conclusion

1) The mechanical model of the roof elastic foundation beam model was constructed using mechanical knowledge, and the deflection curve equations in the filling area and coal body area were established. Through the force analysis of the roof, the range of factors that affect the amount of roof sinking was obtained. The relationship curves between the roof elastic modulus, the roof thickness, the buried depth of the coal seam, the elastic modulus of backfill, the coal elastic modulus, and the subsidence were drawn.
2) From the expression of the main roof subsidence in the filling area of 3# coal upper and lower slicing paste filling mining and the geological data of the 3305 working face of Yangcheng Coal Mine, six influencing factors affecting the amount of main roof subsidence were inductively analyzed, and the weights were derived using the subjective group decision method of the ANP and verified by the OEM based on objective data, and the importance ranking coinciding with the weight ranking was derived. The results show that the backfill elastic modulus is the main controlling factor.
3) FLAC3D was used to model backfill elastic moduli of 0.3 GPa, 0.5 GPa, and 1 GPa during excavation while maintaining a constant filling rate. The simulation revealed the effect of the filling body's elastic modulus on the overburden and surface sinking. The results demonstrate that increases the elastic modulus of the backfill reduces the degree of overburden damage and the quantity of surface subsidence, indicating that increasing the elastic modulus of the filling body can effectively enhance the effect while maintaining the filling rate.

Data availability statement

The datasets presented in this study can be found in online repositories. The names of the repository/repositories and accession number(s) can be found in the article/Supplementary material.

Author contributions

All authors listed have made a substantial, direct, and

intellectual contribution to the work and approved it for publication. QZ was responsible for writing the paper, deriving the model, and translating and embellishing it. CW directed the structure of the thesis. LP was responsible for the literature proofreading.

Funding

This research was funded by the National Emergency Management System Construction Project (grant 20VYJ061) and the Construction and Empirical Research on Early Warning Index System of Major Engineering Safety Risks Based on Optimal Control Theory, National Natural Science Foundation of China (grant 71271031).

Conflict of interest

The authors declare that the research was conducted in the absence of any commercial or financial relationships that could be construed as a potential conflict of interest.

Publisher's note

All claims expressed in this article are solely those of the authors and do not necessarily represent those of their affiliated organizations, or those of the publisher, the editors, and the reviewers. Any product that may be evaluated in this article, or claim that may be made by its manufacturer, is not guaranteed or endorsed by the publisher.

References

Camara, M., Jamil, N. R., Abdullah, A. F. B., Hashim, R. b., and Aliyu, A. G. (2020). Economic and efficiency based optimisation of water quality monitoring network for land use impact assessment. *Sci. Total Environ.* 737, 139800. doi:10.1016/j.scitotenv.2020.139800

Chen, Y., and Park, Y. H. (2020). A Helmholtz resonator on elastic foundation for measurement of the elastic coefficient of human skin. *J. Mech. Behav. Biomed. Mat.* 101, 103417. doi:10.1016/j.jmbbm.2019.103417

Deng, X. J., Liu, H., Feng, J., Li, Y., de Wit, B., and Yang, Y. (2021). A continuous Conversion Technology from Top coal caving into multi-slice mining for thick Bifurcated coal seams. *Geotech. Geol. Eng. (Dordr).* 39, 5983–5992. doi:10.1007/s10706-021-01898-6

Deng, X. J., Zhang, J. X., Huang, P., Zhang, Q., and Hao, X. J. (2015). Analysis of roof movement characteristics in upward slicing and filling mining in ultra-thick coal seams. *J. Chin. Coal. Soc.* 40, 994–1000.

Du, F., Wang, K., Zhang, X., Xin, C., Shu, L., and Wang, G. (2020). Experimental study of coal–gas outburst: Insights from coal–rock structure, gas pressure and adsorptivity. *Nat. Resour. Res.* 29, 2481–2493. doi:10.1007/s11053-020-09621-7

Gao, R., Zhou, K., and Yang, C. (2017). Damage mechanism of composite cemented backfill based on complex defects influence. *Materwiss. Werksttech.* 48, 893–904. doi:10.1002/mawe.201600722

Gong, P., Ma, Z., Zhang, R. C., Ni, X. Y., Liu, F., and Huang, Z. (2017). Surrounding rock deformation mechanism and control Technology for Gob-side entry Retaining with fully mechanized gangue backfilling mining: A case study. *Shock Vib.* 3, 1–15. doi:10.1155/2017/6085941

Guo, P., Meng, Z. G., Ning, X. Y., and Zhang, R. R. (2018). An experimental investigation on the mechanical properties of gangue Concrete as a Roadside support body material for backfilling Gob-side entry Retaining. *Adv. Mater. Sci. Eng.* 17, 1–11. doi:10.1155/2018/1326053

Heinze, T., Frank, S., and Wohnlich, S. (2021). FSAT - A fracture surface analysis toolbox in MATLAB to compare 2D and 3D surface measures. *Comput. Geotech.* 132, 103997. doi:10.1016/j.compgeo.2020.103997

Huang, Z., Le, T., Gao, Y., Yao, X., Wang, H., Zhao, W., et al. (2020). Safety assessment of Emergency Training for industrial accident Scenarios based on analytic Hierarchy process and Gray-Fuzzy comprehensive assessment. *IEEE Access* 8, 144767–144777. doi:10.1109/access.2020.3013671

Jena, S. K., Chakraverty, M., and Ma, L. (2020). Vibration and buckling characteristics of nonlocal beam placed in a magnetic field embedded in Winkler–Pasternak elastic foundation using a new refined beam theory: An analytical approach. *Eur. Phys. J. Plus* 135, 164–218. doi:10.1140/epjp/s13360-020-00176-3

Kostecki, T., and Spearing, A. (2015). Influence of backfill on coal pillar strength and floor bearing capacity in weak floor conditions in the Illinois Basin. *Int. J. Rock Mech. Min. Sci. (1997).* 76, 55–67. doi:10.1016/j.ijrmms.2014.11.011

Kundu, A., Dutta, D., Patel, N. R., Denis, D. M., and Chattoraj, K. K. (2021). Evaluation of Socio-Economic Drought risk over Bundelkhand region of India using analytic Hierarchy process (AHP) and Geo-Spatial techniques. *J. Indian Soc. Remote Sens.* 49, 1365–1377. doi:10.1007/s12524-021-01306-9

Liu, E. Y., Zhang, Q. l., Feng, Y., and Zhao, J. w. (2017). Experimental study of static and dynamic mechanical properties of double-deck backfill body. *Environ. Earth Sci.* 76, 689–6897. doi:10.1007/s12665-017-7011-0

Liu, J. G., Zhao, J. W., and Yang, H. Z. (2017). Research on the time and space characteristics of elastic foundation beam in filling mining. *Coal Sci. Technol.* 45, 41–47.

Liu, J., Sui, W., and Zhao, Q. (2017). Environmentally sustainable mining: A case study of intermittent cut-and-fill mining under sand aquifers. *Environ. Earth Sci.* 76, 562. doi:10.1007/s12665-017-6892-2

Ma, Q., Tan, Y., Liu, X., Gu, Q., and Li, X. (2020). Effect of coal thicknesses on energy evolution characteristics of roof rock-coal-floor rock sandwich composite structure and its damage constitutive model. *Compos. Part B Eng.* 198, 108086. doi:10.1016/j.compositesb.2020.108086

Mangal, A. (2021). A study of stability investigation of immediate roof for extraction of thick coal seam in India. *J. Ins. Eng. (India) Ser. D.*, 102, 203–221.

Miranda, T., Dias, D., Eclaircy-Caudron, S., Gomes Correia, A., and Costa, L. (2011). Back analysis of geomechanical parameters by optimisation of a 3D model of an underground structure. *Tunn. Undergr. Space Technol.* 26, 659–673. doi:10.1016/j.tust.2011.05.010

Mirarabrazi, J., and Navrodi, I. H. (2020). Identifying optimal location of ecotourism sites by analytic network process and genetic algorithm (GA): (Kheyroud forest). *IJEST* 17, 2583–2592.

Mosaad, S., and Basheer, A. A. (2020). Utilizing the Geophysical and hydrogeological data for the assessment of the Groundwater Occurrences in Gallaba plain, western Desert, Egypt. *Pure Appl. Geophys.* 177, 3361–3382. doi:10.1007/s00024-019-02414-x

Sandholtz, S. H., Kannan, D., Beltran, B. G., and Spakowitz, A. J. (2020). Chromosome structural mechanics Dictates the local Spreading of Epigenetic Marks. *Biophys. J.* 119, 1630–1639. doi:10.1016/j.bpj.2020.08.039

Shi, X., Zhou, H., Sun, X., Cao, Z., and Zhao, Q. (2021). Floor damage mechanism with cemented paste backfill mining method. *Arab. J. Geosci.* 14 (2021), 80–89. doi:10.1007/s12517-020-06368-6

Thirukumaran, S., Indraratna, B., Brown, & E. T., and Kaiser, P. K. (2016). Stability of a rock block in a Tunnel roof under constant normal Stiffness conditions. *Rock Mech. Rock Eng.* 49, 1587–1593. doi:10.1007/s00603-015-0770-6

Wang, H., Wang, E., Li, Z., Shen, R., Li, B., Zhang, Q., et al. (2020). Study and application of dynamic inversion model of coal seam gas pressure with drilling. *Fuel* 280, 118653. doi:10.1016/j.fuel.2020.118653

Wang, K., and Du, F. (2020). Coal-gas compound dynamic disasters in China: A review. *Process Saf. Environ. Prot.* 133, 1–17. doi:10.1016/j.psep.2019.10.006

Wu, K., and Li, B. (1995). Energy development in China: National policies and regional strategies. *Energy Policy* 23, 167–178. doi:10.1016/0301-4215(95)91420-h

Xuan, W., and Leung, D. (2011). Optimization of biodiesel production from camelina oil using orthogonal experiment. *Appl. Energy* 88, 3615–3624. doi:10.1016/j.apenergy.2011.04.041

Yang, R. S., Zhu, Y., Li, Y., Li, W., and Lin, H. (2020). Coal pillar size design and surrounding rock control techniques in deep longwall entry. *Arab. J. Geosci.* 13, 453. doi:10.1007/s12517-020-05454-z

Yang, W., Lin, B. Q., and Xu, J. T. (2014). Gas outburst affected by original rock stress direction. *Nat. Hazards (Dordr).* 72, 1063–1074. doi:10.1007/s11069-014-1049-z

Yang, Z. Q., Zhai, S. H., Gao, Q., and Li, M. H. (2015). Stability analysis of large-scale stope using stage subsequent filling mining method in Sijiaying Iron Mine. *J. Rock Mech. Geotech. Eng.* 7, 87–94. doi:10.1016/j.jrmge.2014.11.003

Zhang, Q. L., Zhou, H. Q., and Bo, J. B. (2011). Research and Practice on stability of overlying strata in paste filling mining. *J. Min. Saf. Eng.* 28, 279–282.

Zhao, X., Fourie, A., and Qi, C. C. (2019). An analytical solution for evaluating the safety of an exposed face in a paste backfill stope incorporating the arching phenomenon. *Int. J. Min. Metall. Mat.* 26, 1206–1216. doi:10.1007/s12613-019-1885-7

frontiers | Frontiers in Earth Science

TYPE Original Research
PUBLISHED 09 January 2023
DOI 10.3389/feart.2022.1031604

OPEN ACCESS

EDITED BY
Yun Zhang,
Xi'an University of Science and Technology, China

REVIEWED BY
Feiyong Wang,
China University of Geosciences, China
Xiaopeng Su,
Chongqing Jiaotong University, China

*CORRESPONDENCE
Yanzhong Li,
liyanzhong415@163.com

SPECIALTY SECTION
This article was submitted to Structural Geology and Tectonics, a section of the journal Frontiers in Earth Science

RECEIVED 30 August 2022
ACCEPTED 28 September 2022
PUBLISHED 09 January 2023

CITATION
Yang Y, Li Y, Yuan K, Lu Z and Li G (2023), Experimental study on creep failure characteristics of coal mass under multistage stress and construction of prediction model.
Front. Earth Sci. 10:1031604.
doi: 10.3389/feart.2022.1031604

Experimental study on creep failure characteristics of coal mass under multistage stress and construction of prediction model

Yiran Yang[1,2], Yanzhong Li[3]*, Kekuo Yuan[1], Zidong Lu[4] and Gang Li[1]

[1]Shaanxi Key Laboratory of Safety and Durability of Concrete Structures, School of Civil Engineering, Xijing University, Xi'an, Shaanxi, China, [2]School of Energy and Resource, Xi'an University of Science and Technology, Xi'an, Shaanxi, China, [3]State Key Laboratory of Mining Response and Disaster Prevention and Control in Deep Coal Mines, College of Mechanical Engineering, Anhui University of Science and Technology, Huainan, Anhui, China, [4]Yunnan Vocational Institute of Energy Technology, Qujing, Yunnan, China

The creep and failure mode of stratified coal is complex and challenging to predict. This is highly attributed to the internal stratified structure generated during coal forming. In this study, the inner stratified structure of coal during creep failure was explored. The evolution relationship between the key creep parameters and the inner stratified structure was evaluated through creep tests. The creep failure characteristics of coal under complex stress were determined. A neural network model was established to predict the creep failure modes, and the output results were subjected to smoothing and tracking to reduce the error. The results showed distinct creep characteristics of coal with various types of stratified structure. Key parameters such as creep variable, steady creep state and creep rate exhibited a nonlinear relationship with stress. The dual control neural network model constructed in the study showed high accuracy and stability. This model can be used as a guidance and reference for the study of creep failure mechanism and elucidation of creep behavior prediction of stratified coal.

KEYWORDS

experimental study, creep model, stratified structure, BP neural network, prediction model

Introduction

Creep damage and coal failure significantly affects safe mining (Hoek and Brown, 1997). Creep failure of the coal body is more common when the mining depth increases. The disaster management methods previously used do not alleviate new disasters due to the complexity and variability of the coal creep mechanism. This results in the significant increase in disaster risk and low efficiency of disaster relief strategies, ultimately threatening safe mining of coal resources. Therefore, it is imperative to explore the coal creep formation process to lay a basis for safety coal mining.

Experimental studies are currently the main approaches used to study the creep characteristics of coal. Advances in experimental procedures in the recent past has promoted the development of experimental coal creep research. Previous researchers modified experimental equipment according to their needs and upgraded the original single experimental equipment to multi-functional intelligent control devices, which enhanced the process of coal creep research.

A study was previously conducted to explore the creep behavior and characteristics of saturated rock under high stress and *in situ* stress under the mode of uniaxial single-stage loading and graded incremental cyclic loading (Liu et al., 2013). The findings provided a basis for control of coal deformation and alleviated deep saturated rock mass risks. Dubey and Gairola (2005) evaluated the effect of internal structural anisotropy of rock salt on the creep behavior through experimental methods. The findings indicated that structural anisotropy significantly modulated the instantaneous strain, transient strain, steady strain and enhanced strain development in rock salt. The effect of structural anisotropy on rock salt deformation is negatively correlated with stress. Pellet and Fabre (2007) conducted static, quasi-static, and cyclic creep experiments on sedimentary rocks. The results showed that clay particles significantly affected the creep behavior, and the particle creep markedly affected the overall creep behavior. Rahimi and Hosseini (2014) conducted triaxial creep tests using thick-walled hollow columnar salt rock specimens, and explored the effects of confining pressure, deviating stress and strain rate on salt rock creep behavior. The results indicated that strain rate increased with increase in deviating stress and confining pressure, and the lateral pressure had higher effect on tangential strain rate changes compared with deviating stress. Grgic and Amitrano (2009) conducted by uniaxial creep experiment to explore the effect of water saturation on rock creep. Analysis of strain and acoustic emission monitoring data showed that micro-fracture plays an essential role in the creep process.

Nadimi et al. (2011) conducted a triaxial creep test using rock samples to evaluate the aging characteristics of rock mass, and estimated the dynamic constitutive creep model parameters of rock mass using creep test and experimental data. The test results were consistent with the experimental data. These findings thus provide a theoretical basis for the support design of underground engineering. Herrmann et al. (2020) explored the creep behavior of shale by conducting a creep experiment under high confining pressure and varying temperature. The creep strain was enhanced under high temperature, axial differential pressure stress and low confining pressure. The initial creep strain was associated with the mechanical properties determined by short-term constant strain rate experiment. Bhat and Bhandary (2013) improved the torsional ring shear device, determined the change in displacement over time and under constant creep stress, explored the residual state creep behavior of typical cohesive soil. A residual state creep failure prediction curve was generated for determination of the failure time and prediction of displacement of the creep landslide. Bagheri et al. (2015) conducted triaxial creep experiments under different

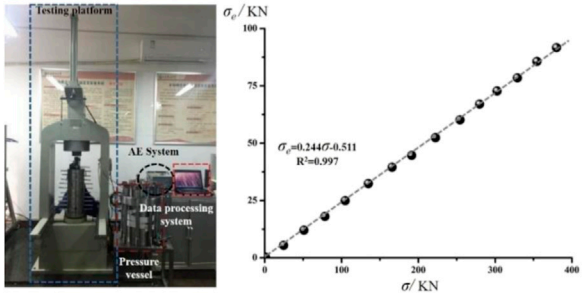

FIGURE 1
THMC multi-field coupled rheological test system.

TABLE 1 Sample grouping list.

Number	Structural features	Angle	Quantity
USN	None	None	4
USH	Horizontal stratified structure	5.0°	8
USO	Oblique stratified structure	45.0°	8
USV	Vertical stratified structure	87.0°	8

shear stresses and strain rates using clay samples, evaluated the volumetric strain rates, and explored the relationship between initial volumetric strain and time. The volumetric strain–time and volumetric strain rate–time responses were found to be in good agreement with the literature, the observed time- and stress-level-dependency of the were found to be in contradiction with the general assumption as a material constant.

Fabre and Pellet (2006) carried out creep experiments on argillite under multiple stresses. The findings indicated that the overall mechanical properties of the argillite rapidly deteriorated when the cracks of argillite were unstable, and the creep process of clay particles caused viscoplastic strain of the argillite. Brantut et al. (2012) constructed a micromechanical model for simulation of brittle creep of rock under triaxial stress. Davis et al. (2008) conducted triaxial compression experiments on dolomite under varying temperature conditions. The results revealed the differences in creep mechanisms between coarse-grained dolomite and fine-grained dolomite with different grain sizes.

Several scholars have widely explored the mechanical properties of coal with significant findings. Cao et al. (2016) established a nonlinear damage creep constitutive model of soft rock under high stress based on the nonlinear damage creep characteristics and damage variables of rock to explore the creep deformation of soft rock. Tomanovic (2006) conducted experiments on the creep of soft rock at room temperature, and established a rheological model of soft rock. The rheological model was used to evaluate the creep process after loading, full unloading or partial

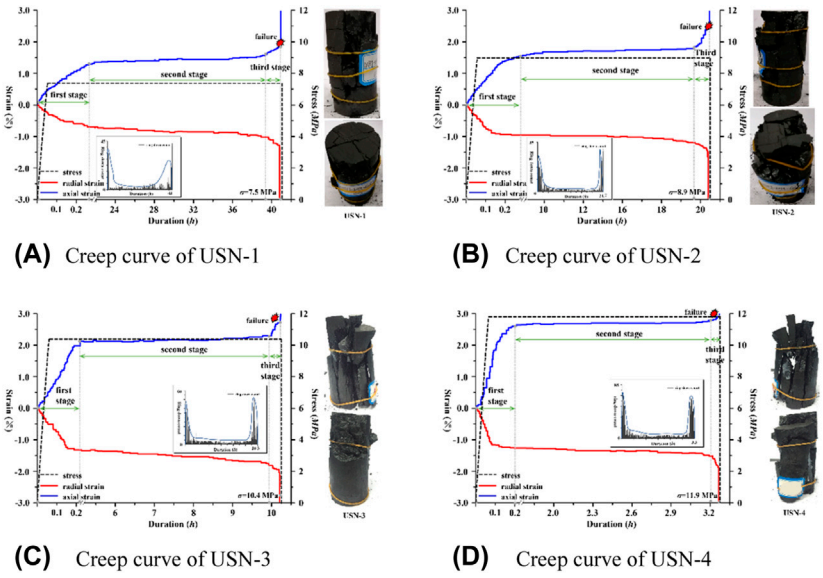

FIGURE 2
Laboratory findings of USN group samples.

unloading. It is imperative to explore the creep process of tunnel surrounding rock. Fahimifar et al. (2015) modified a viscoplastic model originally established under high stress during the extrusion state. The numerical finite-difference method was used to solve the equation of the model by approximating derivatives with finite differences. The model was applied to a series of indoor creep experiments and it exhibited high accuracy.

Nazary Moghadam et al. (2013) established creep process numerical models to determine dilatancy, short-term failure and long-term failure of salt rock samples during transient and steady creep processes in underground cavern. The validity and applicability of the proposed model were evaluated by finite element analysis. Firme et al. (2018) optimized the DM creep model using different methods and the optimized model effectively expressed the transient creep process. Hajiabadi and Nick (2020) established a rate-dependent constitutive model for accurately predicting the change in axial yield stress as a power function of applied axial strain rate. The model reproduced the rate-dependent behavior of porous rock under various loading conditions. Sterpi and Gioda (2009) evaluated the effect of viscoelasticity (primary) and viscoplastic (secondary) on the rheological model, performed finite element analysis on the strain of deep circular tunnel, and determined the effect of creep on tunnel shrinkage the finite element results show that the contribution of tertiary creep is crucial in the prediction of the short-term closure of the tunnel. This could have a notable negative effect in case of TBM driven tunnels. Pellet et al. (2005) established a rock constitutive model that considered the viscoplastic behavior and damage evolution over time. The model was used to simulate the creep delay instability of the third stage, which represented simulation of the evolution of the damage zone during underground cavern excavation. Nedjar and Le Roy (2013) constructed a local damage model based on the concept of yield surface and verified its applicability through numerical simulation. Heusermann et al. (2003) constructed a constitutive model for exploring the nonlinear creep behavior of rock salts and verified its stability and validity. Olivella and Gens (2002) established a creep constitutive model based on transfer creep and dislocation creep, which accurately predicted the creep strain rate of rock.

Coal is characterized by several micro-cracks, voids and defects, which cause nonlinear mechanical behavior. Currently, the rheological behavior model is commonly used idealized analysis model in studying coal creep behavior. The mechanical properties of coal have high variability. Therefore, study of the mechanical properties of coal using an idealized model is challenging.

Several constitutive models have been established to explore the creep behavior characteristics of coal under different stress. Constitutive models have been used to obtain the deformation features of underground space such as tunnel or chamber surface (Zhifa et al., 2001; Kontogianni et al., 2006; Fahimifar et al., 2010). Different properties and the behavior characteristics of the same material under different mechanical parameters have been elucidated. Previous findings indicate that the classical viscoelastic model has limitations. Several rheological models have been proposed in different studies to simulate the creep damage-failure mechanical behavior of coal (Guan et al., 2007). Previous experimental results exhibited an unrecoverable creep of rock even under minimal stress. Therefore, scholars assumed that the first, second and third stages of creep curve were

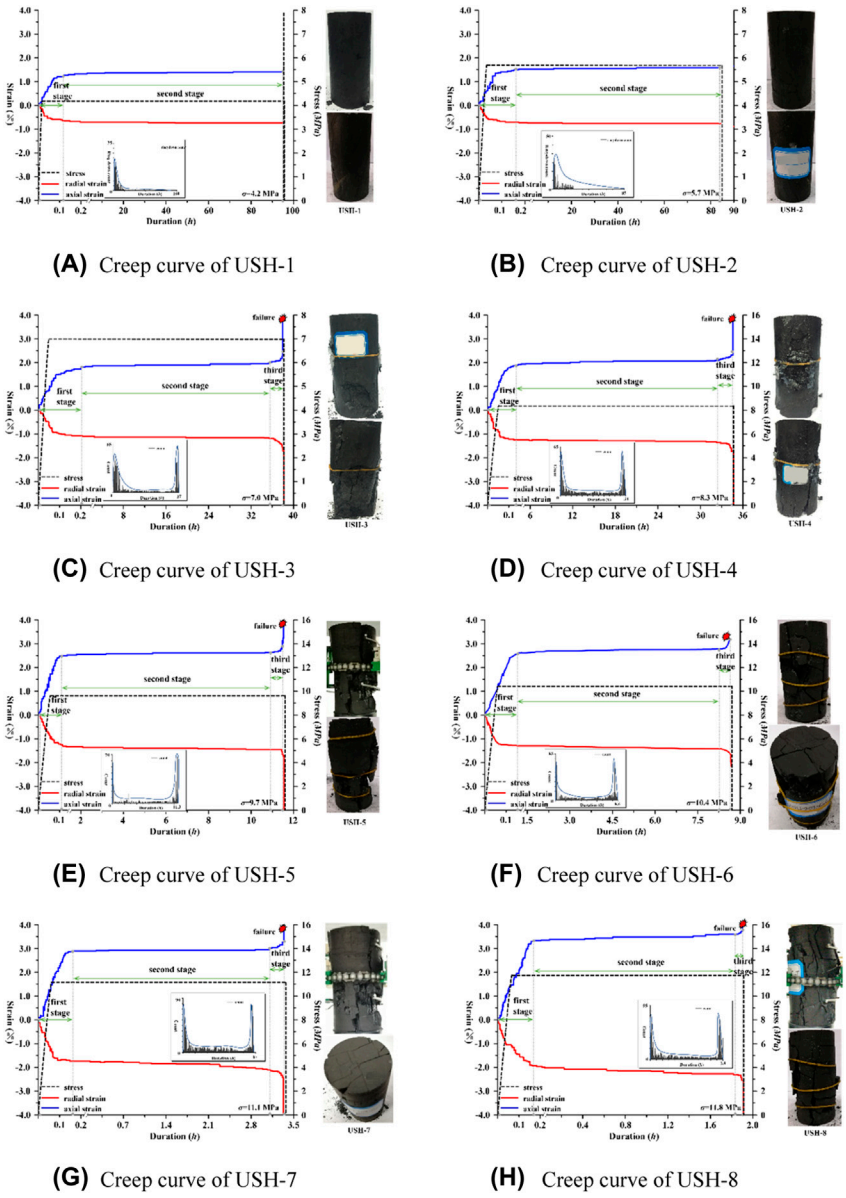

FIGURE 3
Laboratory findings of USH group samples.

completely irreversible deformation stages. A model with different characteristics compared with the viscoelastic model was constructed based on this assumption to evaluate the long-term stability of surrounding rock after underground chamber excavation (Parsapour and Fahimifar, 2016). (Li and Xia, 2000) studied the influence of strain history on rock specimen deformation during multi-level loading and unloading cyclic uniaxial compression creep tests. Results show that the creep of rock usually undergoes the three stages of deceleration, steady, and accelerated for a given constant stress, whether each stage is evident and the duration of every stage depends on the behavior of the rock material observed and the load level applied.

Construction of creep model requires accurately describing the creep and failure characteristics of rock under varying stress. The coal creep prediction model based on artificial neural network is currently used to determine the creep characteristics of coal. Neural network has be used in previous studies to explore coal creep characteristics and good results have been obtained. However, the results from previous studies are not consistent.

In this study, the failure characteristics of coal under complex stress were studied based on the underground stress path. In addition, artificial neural network was utilized to explore the creep-damage-failure characteristics of coal, and for simulation of the creep characteristics and

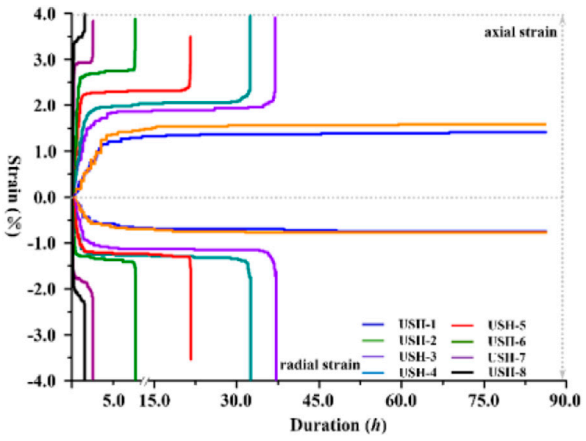

FIGURE 4
Strain-time curve of USH group samples.

instability mechanism of coal. A BP neural network model was established and optimized using creep test data, then, the Lyapunov function was used to verify the stability of the model.

Materials and methods

The creep test under uniaxial static load used in this study adopts the method for measurement of rock creep characteristics recommended by ISRM (2014). Saturated sodium nitrate solution infiltration was used during the test to maintain a stable relative humidity. The relative humidity was maintained at 40% at 20°C. The range of relative humidity and temperature was maintained at ±5.0% and ±1.0°C, respectively.

The rock THMC rheological test method was used in this study. A calibration curve was generated to evaluate the relationship between the effective stress of the equipment and the applied stress, which was expressed as (y=0.244x-0.511) (Figure 1). Other equipment used in the study included strain gauge, digital Micro II-Express multi-channel acoustic emission device, and high-speed digital camera. Strain gauge and DD1 cantilever strain sensor were used to determine the axial and radial strain to obtain various signal forms generated by the sample under stress.

The test samples were assigned to four groups according to the differences in the internal structure (Table 1). In the current study, 30%, 40%, 50%, 60%, 70%, 75%, 80% and 85% compressive stresses of the uniaxial compressive strength were applied to simulate the effect of comprehensive *in situ* stress caused by overburden geological body and tectonic stress. The unstructured samples were subjected to compressive stress equivalent to 50%, 60%, 70%, 80% of the respective uniaxial compressive strength. The stress control method was used for sample loading, and the loading rate was 0.01 kN/s. Experimental parameters were determined at the initial stages of the creep test at intervals of 1.0 min, 5.0 min, and 10.0 min, and then the interval was extended to 0.5–1.0 h at the course of the experiment. At the end of the experiment, the interval of recording the parameters were changed to 10.0 min, 5.0 min and 1.0 min when the samples approached the failure mode.

Results and Discussion

Experimental analysis of coal specimen without stratified structure

Static creep tests for rock specimens without stratified structures were performed at stress levels comparable to the average σ_{AID} of CI threshold σ_{CI} and CD threshold σ_{CD}. The constant stress was applied in this test and maintained by controlling the axial load. Increase in strain (axial and transverse) was monitored as the sample progressed to the failure mode.

The strain-time evolution and failure characteristics of USN-1 under a loading stress of 50% UCS are presented in Figure 2A. The results showed that the specimen underwent three typical creep stages. The creep experiment lasted for about 43.1 h. In the initial stage, cracks developed and evolved inside the specimen when the force was applied to the specimen. The acoustic emission signal gradually increased and reached the initial peak value. The creep then progressed to the second creep stage. The AE signal weakened gradually, however, the AE signal did not progress to the silent stage and was stable and active during the entire experiment. The cracks significantly changed as the experiment progressed to the third creep stage. The second peak value of AE signals was caused by emergence of new cracks and the development of original cracks, and the specimen was markedly deformed and fractured. The entire specimen was ultimately destroyed. Fracture development and evolution of the sample during the experiment exhibited random characteristics, and the final failure mode was not predictable.

The strain-time evolution and failure characteristics of USN-2 under a stress load of 60% UCS are shown in Figure 2B. The creep stage duration of USN-2 was shorter compared with USN-1, and the behavior of the three typical creep stages was predictable. The number of acoustic emission signals of USN-2 was higher. The number of signals significantly increased when the creep progressed to the second peak. This finding indicates that more energy was stored in the failure mode of the sample under relatively high stress state. The energy was released immediately after destruction of the sample resulting in evident failure characteristics. The specimen exhibited irregular failure development path. The blocks in some positions were completely detached from the sample and exhibited fragmentation phenomenon.

The failure characteristics of USN-3 under a stress load of 70% UCS are shown in Figure 2C. The duration of the overall creep stage was about 11.7 h, and the maximum axial creep before failure was 2.1%. The acoustic emission signal was restored to the normal state when the sample progressed to

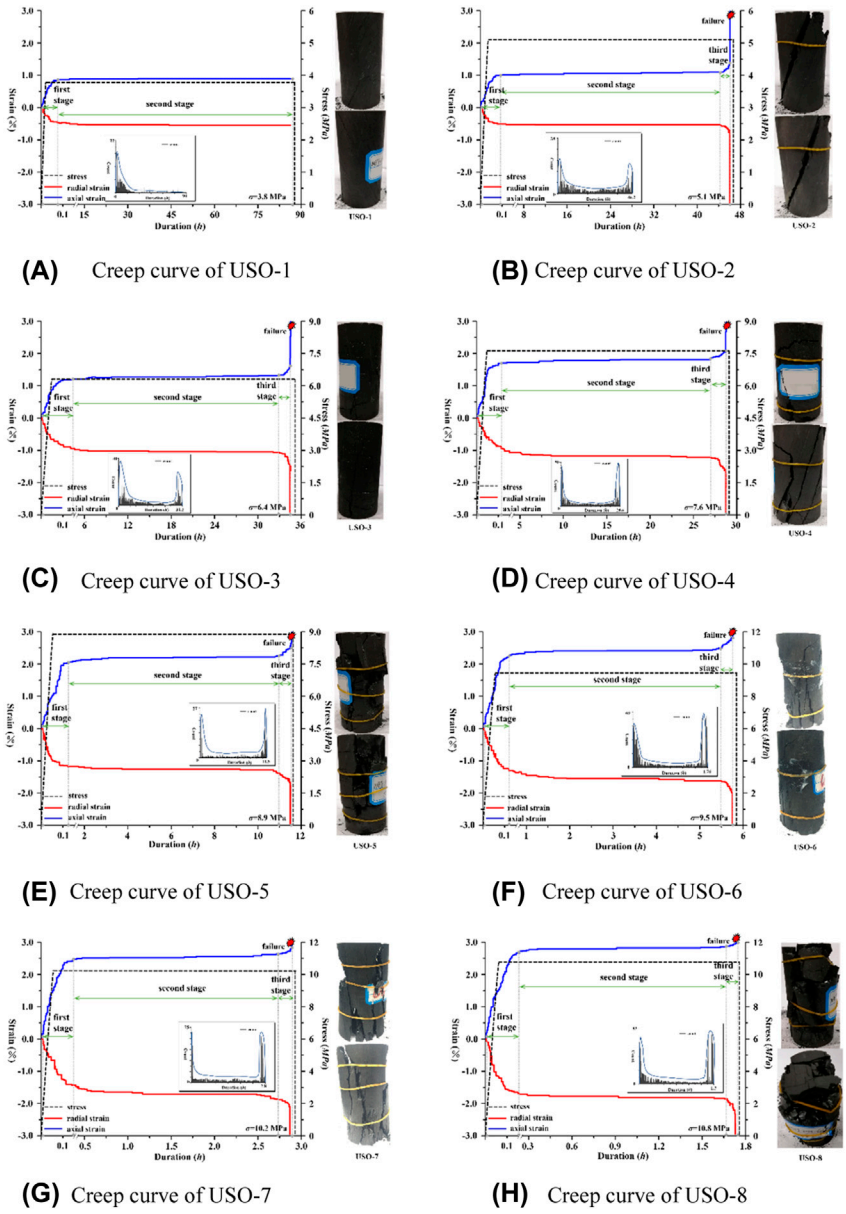

FIGURE 5
Laboratory findings of USO group samples.

the second creep stage, and the sample exhibited a relatively strong signal. Medium and large cracks were observed on the surface of the sample at a creep time of 8.3 h. In addition, acoustic emission signals increased at this point, and the sample progressed to the stable creep state and the third creep stage. The sample exhibited completely detached and scattered blocks, accompanied by significant slagging phenomenon. The crack development path was irregular, which was attributed to the occurrence of impurities and the sample mechanical properties.

The USN-4 creep stage was 3.3 h long (Figure 2C). The maximum axial deformation of specimen before failure was 2.7%. The intensity and quantity of AE signals enhanced the phenomenon of energy concentration and significant energy release was observed. The overall failure of the sample ultimately occurred under the synergistic action of transverse and longitudinal cracks. The USN-4 exhibited a crumpled bulk structure and had essentially no bearing capacity. The longitudinal cracks played a dominant role in the failure process, whereas the transverse cracks mainly accelerated the failure process and caused loss in residual strength. Loss in residual strength markedly affected the overall failure of the sample.

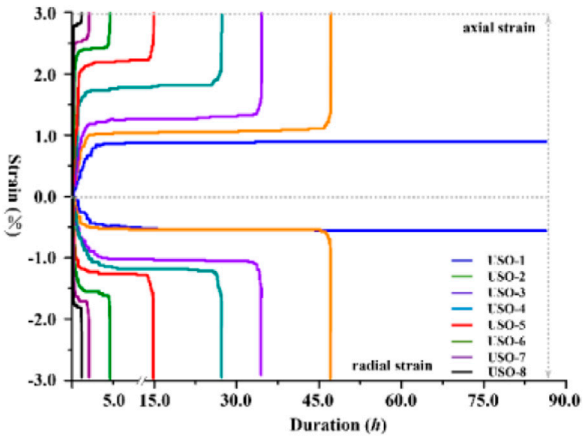

FIGURE 6
Strain-time curve of USO group samples.

The fracture development and evolution of the sample exhibited evident random characteristics since the samples had random structures, and the final failure mode was unpredictable.

Experimental analysis of stratified coal samples

Compressive stresses equivalent to 30%, 40%, 50%, 60%, 70%, 75%, 80%, and 85% of the UCS were applied in analysis of stratified coal samples. The relationships between the stress and strain of USH, USO and USV samples are shown in Figures 3.

The evolution of stress and strain of USH-1 and USH-2 under static loading are presented in Figures 3A,B. The axial strain and radial strain of the sample primarily occurred in the first creep stage. The strain slightly increased when the samples progressed to the second stage. The axial strain and radial strain exhibited a static state at 71.5 h, and the samples progressed to the stress equilibrium stage. Acoustic emission monitoring indicated that the samples had abundant acoustic emission signals in the initial stage of loading. The acoustic emission signals were gentle with a continuous downward trend as the sample progressed to the second stage. The samples then progressed to the stress equilibrium stage, and the acoustic emission signals gradually decreased to a value less than the threshold value. Notably, the specimen remained intact.

The creep curves of USH-3 and USH-8 are presented in Figures 3C–H. The results showed that all samples ultimately exhibited the failure mode, and had distinct failure parameters. The creep durations of USH-3 and USH-4 samples were 38.1 h and 34.3 h, respectively. The axial strains of the two samples were approximately 2.0% at the second creep stage. The final failure modes of the two samples were similar. The two samples were characterized by failure of small wedge-shaped blocks and vertical multi-crack breakdown of stratified structure. The general failure mode was a top-bottom penetrating failure. The shear development of transverse structure was not significant, thus there was no the phenomenon of large coal body detaching from the main body. The creep test durations of USH-5 to USH-8 samples were 9.5 h, 8.6 h, 3.3 h and 1.9 h, respectively. The failure of each sample occurred within a relatively short time (Figure 4). Energy accumulated in the sample during the creep process due to the large load. Therefore, energy was rapidly released in the failure stage, resulting in fragmentation or complete transfixion failure mode of all the samples at varying degrees. The damaged samples were scattered, and the residual strength was approximately zero. Development of cracks in the samples did not exhibit clear directivity. The statistics showed that the number of transverse and longitudinal fractures which significantly influenced the strength of the sample was relatively equal. This finding indicates that the structural characteristics of the coal samples did not exhibit distinct effect on the creep deformation and failure characteristics under relatively high stress.

USO-1 exhibited a state of stress equilibrium, and the sample did not undergo damage at final stage (Figure 5A).

The creep curves of USO-2, USO-3 and USO-4 are presented in Figures 5B–D, respectively. The final failure mode was observed in all samples, but the failure time and morphology were significantly different. The experimental duration of USO-2 under an axial stress of 5.1 MPa was 45.9 h. The axial strain and radial strain at the second creep stage were 1.06% and 0.57%, respectively. The sample failure mode was characterized by top-bottom shear failure along the stratified structural plane, as well as fragmentation and shedding of small wedge-shaped blocks at the top. The stratified structural plane played a key control and induction role during the failure process of the sample. The results showed that it was a typical structure-dominated sample. The constant load of USO-3 was 6.4 MPa, the creep duration was about 34.6 h, and the axial strain and radial strain were approximately 1.18% and 0.95%, respectively, at the second creep stage. The sample failure mode was mainly characterized by a stratified structure, with the failure plane relatively along the stratified structure plane. The laminar failure phenomenon occurred locally, with a small range and relatively weak bedding plane. The stress load for USO-4 was 7.6 MPa and the creep duration was 28.8 h. The axial strain significantly increased by 1.67% and the radial strain increased to 1.04%. The sample failure mode was mainly characterized by stratified structures. Medium and large block cracks and detached blocks were generated on one side of the failure plane. The acoustic emission exhibited peak signals at both ends and weak signals at the middle, which was attributed to the internal structure of the sample.

Creep curves of USO-5—USO-8 samples are shown in Figures 5E–H, respectively. The creep duration of the USO-5 sample under 8.9 MPa stress was 11.4 h, and the axial strain and radial strain were 2.11% and 1.28%, respectively. The failure mode of the sample was characterized by co-dominant failure mode with stratified structure and random fracture. Most of the failure planes were distributed along the direction of the stratified

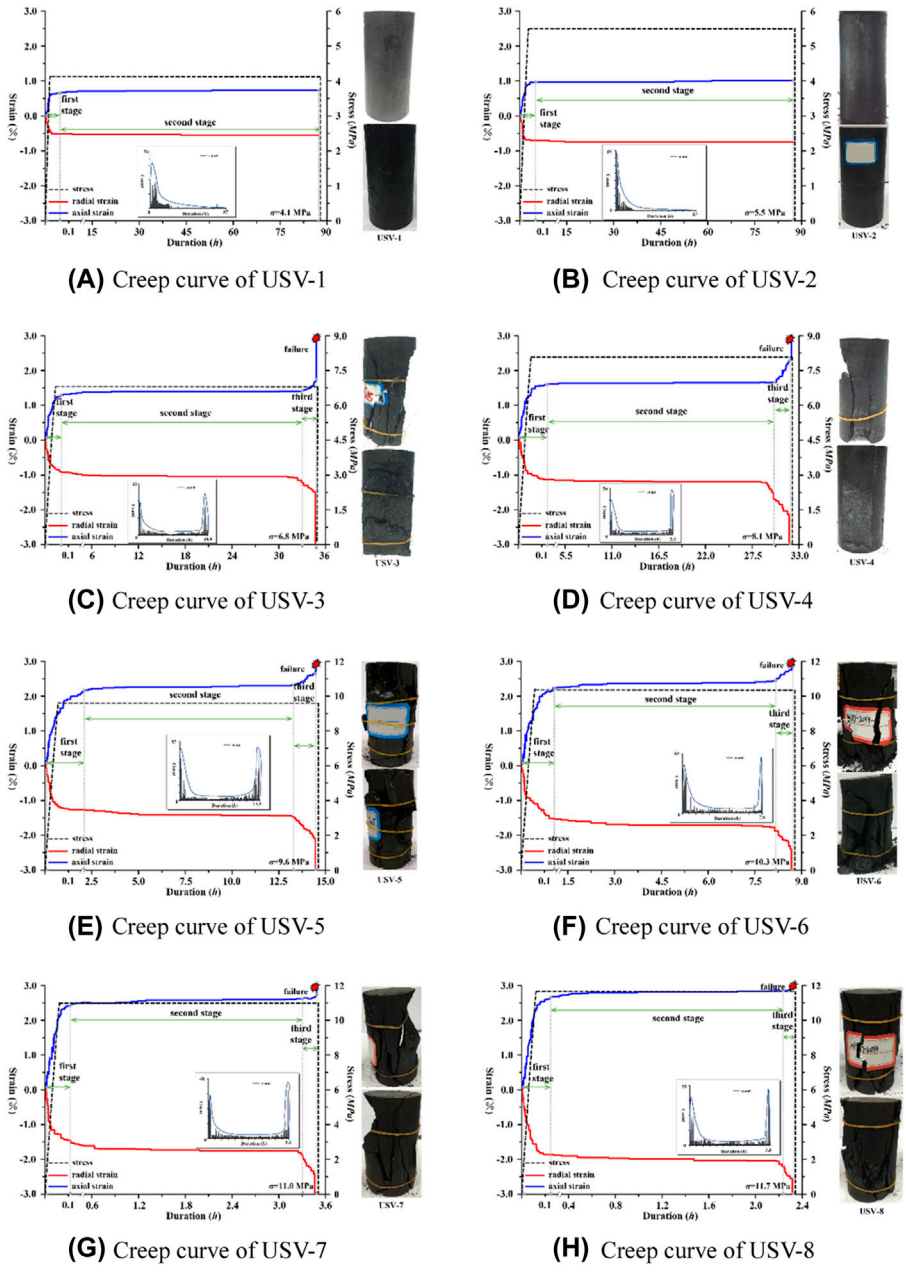

FIGURE 7
Laboratory findings of USV group samples.

structure, and some dominant fractures were caused by the random occurrence of the primary fracture after development for a long time. The final failure mode of the sample exhibited a cataclastic structure. Increase in axial and radial strain of USO-6 coal sample was smaller compared with that of USO-5, but the failure mode of USO-6 coal sample significantly changed. USO-6 coal sample exhibited a large block splitting failure mode dominated by stratified structure. Shear failure along the stratified structure and large block splitting failure were observed near the free surface, and the superposition of the two failures caused the overall strength to decline. USO-7 and USO-8 exhibited similar strain evolution and failure modes. In the second creep stage, the axial and radial strains of USO-7 and USO-8 were approximately 2.55% and 1.68%, respectively. Acoustic emission monitoring showed that the two samples had similar acoustic emission energy characteristics, with peak

signals at the sides and low signals at the middle. The failure mode of USO-7 was characterized by a stratified structure dominated failure, accompanied by local block structure exfoliation. The creep duration of USO-8 was 1.77 h, and the sample exhibited random cracks. The sample showed a fragmentation state after the failure, and the dominant failure structure was not distinct. This observation was mainly because the sample was in an energy-absorbing state in the early stage, and energy was released when the sample was destroyed at the final stage. This caused complete breakdown damage to the internal structure of the sample, resulting in overall fragmentation failure of the sample (Figure 6).

The creep curves of USV-1 and USV-2 samples under 30% UCS and 40% UCS loads are shown in Figures 7A,B. The two samples progressed to the stress equilibrium stage at approximately 50–60 h loading time, and no damage was observed in the two samples.

The creep curves of USV-3 and USV-4 samples under 50% UCS and 60% UCS loads are presented in Figures 7C,D. The two samples underwent the three typical creep stages. The samples showed partial splitting and failure characterized by stratified structure. The local splitting phenomenon was observed near the free surface causing splitting failure locally. The USV-2 sample exhibited three medium and large cracks, which did not penetrate into the sample. USV-3 samples had two large cracks. One of the cracks traversed the upper and lower surfaces of the sample. This crack was the main cause of failure in the USV-3 sample. The other fracture developed along the stratified structure and did not penetrate into the sample. Therefore, it played a secondary role in the failure process.

The creep curves of USV-5—USV-8 samples at 70%–85% UCS load are shown in Figures 7E–H. The failure process in of USV-5—USV-8 samples is presented in Figure 8. The failure modes of these samples were not limited to the failure type dominated by the stratified structure. The failure type of most of the samples exhibited mixed failure modes. Acoustic emission monitoring showed that the evolution pattern was characterized by high peaks at both ends and low peaks at the middle, which corresponded to the general evolution mode of fracture development at the early stage, energy accumulation during the middle stage and energy release in the late stage.

The results showed that the strain of the USV sample was the highest, followed by that of USO samples, whereas the strain of the USH was the lowest. The strain of the samples increased with increase in creep stress (Figure 9). The strain can be expressed as a logarithmic function as shown below:

$$\varepsilon_{in}^{H} = 1.2859\, ln\, \sigma - 4.1467 \quad (1)$$

$$\varepsilon_{in}^{O} = 1.272\, ln\, \sigma - 3.9528 \quad (2)$$

$$\varepsilon_{in}^{V} = 1.5239\, ln\, \sigma - 4.6923 \quad (3)$$

where, ε_{in} represents the creep strain and σ denotes the creep stress.

The duration of the steady-state creep stage decreased with increase in creep stress as the load was increased (Figure 10). The duration of the steady-state creep stage can be expressed as a logarithmic function: $t_s = aln\sigma + b$.

$$t_s^{H} = -71.31\, ln\, \sigma + 317.78 \quad (4)$$

$$t_s^{O} = -62.08\, ln\, \sigma + 275.65 \quad (5)$$

$$t_s^{V} = -68.97\, ln\, \sigma + 307.7 \quad (6)$$

Where, t_s represents the duration of the steady-state creep stage and σ indicates the constant load.

The steady-state creep duration decreased with increase in stress load. This finding indicates that the effect of structural anisotropy on the steady-state creep duration decreased with increase in the stress load. The steady creep stage only lasted for a short time after application of 70% UCS stress load, and the accelerated creep stage significantly modulated deformation of the stratified structure samples.

Statistical data analysis showed that the creep rates of all the samples were not significantly different under a 60% UCS load. The creep rates of the samples significantly changed when the load was more than 60% of UCS. The creep rate of the USV sample was the lowest among the three kinds of samples, whereas the creep rates of USH and USO samples exhibited a significant fluctuation. Increase in stress load caused an increase in the incremental creep rate (Figure 11). The relationship between the creep rate and the load can be expressed as an exponential function with base e as shown below:

$$v_s^{H} = 0.0858e^{0.0859\sigma} \quad (7)$$

$$v_s^{O} = 0.0893e^{0.0871\sigma} \quad (8)$$

$$v_s^{V} = 0.0311e^{0.0968\sigma} \quad (9)$$

where, Vs. denotes the creep rate and σ represents the creep stress.

BP neural network model for creep prediction under smooth control

Advances in artificial intelligence (AI) has significantly revolutionized geotechnical engineering research. Artificial neural network (ANN) has been widely applied in this field. Application of neural network model is effective in solving multi-parameter problems whereby the process and results are not fully elucidated. BP neural network is an artificial neural networks method widely used for construction of neural network models. BP network comprises an input layer, hidden layer and output layer, and all layers are completely connected. The binding strength (weight) between the layers is adjusted in cases whereby the actual output on the output layer is inconsistent

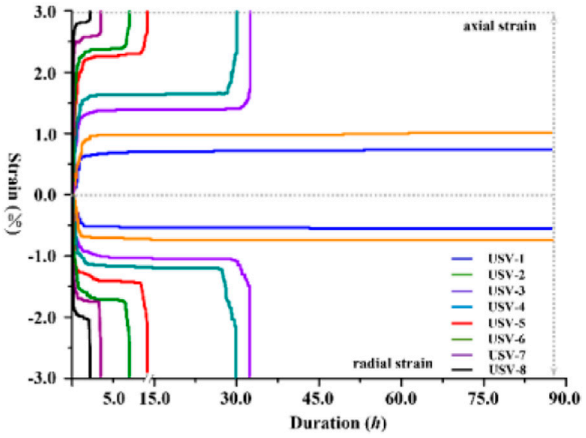

FIGURE 8
Strain-time curve of USV group samples.

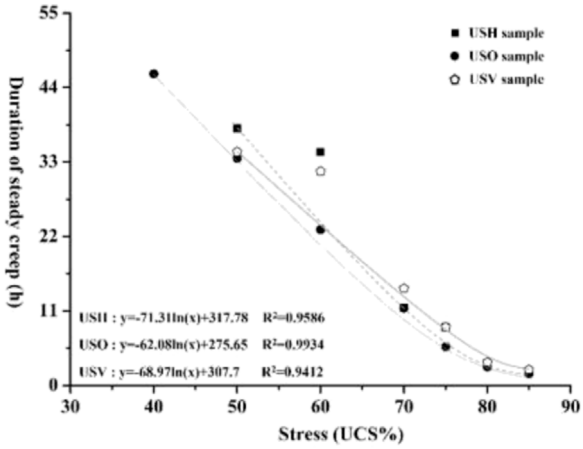

FIGURE 10
Duration-constant stress curve during load increasing stage.

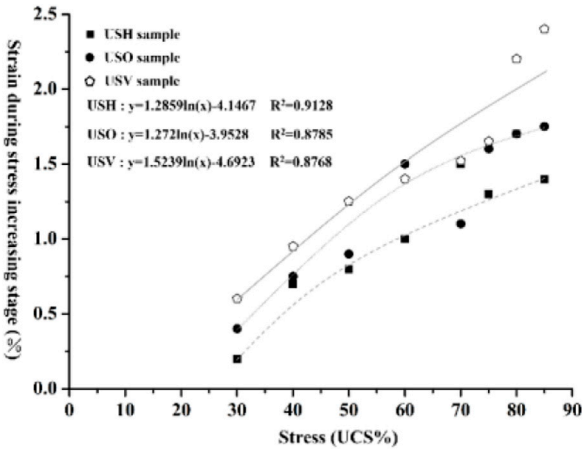

FIGURE 9
Strain-constant stress curve of coal samples.

with the given output until the given input-output relationship is finally satisfied. The learning process of BP network can be grouped in four stages: pattern propagation → error propagation → memory training → learning convergence. The steps of the algorithm are explained below.

(1) The connection weights and node thresholds of nodes at each layer are initialized with random numbers between [−1, +1].
(2) Assume the input xi and the expected output yi.
(3) Figure up the input of each layer node.

$$N_j = \sum_i \omega_{ij} x_i + \theta_j \tag{10}$$

The output

$$y_i = f(N_j) \tag{11}$$

Where, ω_{ij} is the connection weight between input node i and output node ij, θ_j is the node threshold, f is the Sigmoid function, $f(x) = (1 + e^{-x})^{-1}$.

(4) Define the cumulative error function.

$$E = \sum_k E_k = \sum_k \sum_j \frac{1}{2}\left(y_j - \hat{y}_j\right)^2 \tag{12}$$

Where, K is the sequence of input and output mode pairs.

(5) The revised weight

$$\omega_{ij}(t+1) = \omega_{ij}(t) + \vartheta \Delta\omega_{ij}(t) \tag{13}$$

Where, t is the training times, η is the learning rate, $\Delta\omega_{ij}(t) = \sum_k \delta_j y_i$

Output layer

$$\delta_j = y_i(1 - y_i)\left(\hat{y}_j - y_i\right) \tag{14}$$

Hidden layer

$$\delta_j = y_i(1 - y_i)\sum_k \omega_{ik}\delta_k \tag{15}$$

BP algorithm is prone to fall into local minimum and slow convergence in iterative calculation. In this study, additional momentum method and adaptive learning rate improved BP algorithm were used to overcome the above two problems. The additional momentum method is based on the inverse propagation method in each weight change to add a value proportional to the previous weight change (momentum

term), and according to the inverse propagation method to produce a new weight change. The weight adjustment formula with additional momentum factor can be expressed as

$$\Delta\omega_{ij}(t+1) = (1-m_c)\vartheta\delta_i P_j + m_c\Delta\omega_{ij}(t) \tag{16}$$

$$\Delta b_j(t+1) = (1-m_c)\vartheta\delta_i + m_c\Delta b_j(t) \tag{17}$$

Where, $\Delta\omega_{ij}$ is the weight change, Δb_j is the threshold change, δ_i is the error term, P_j is the input variable, η is the learning rate, t is the training times, m_C is the momentum factor.

The output error of BP neural network can be reduced by tracking control method, which is as follows:

Neural network system output is

$$x(k+1) = f(x(k)) + u(k) \tag{18}$$

The system input $u(k)$ has input saturation limitation

$$u(k) = \begin{cases} \bar{v} & |v(k)| > \bar{v} \\ v(k) & |v(k)| \le \bar{v} \end{cases} \tag{19}$$

To avoid the controller's non-smoothness, define the following functions

$$g(v(k)) = \bar{v} \times \tanh\left(\frac{v(k)}{\bar{v}}\right) \tag{20}$$

The $u(k)$ can be got

$$u(k) = g(v(k)) + d(v(k)) \tag{21}$$

Where, $|d(v(k))| = |u(k) - g(v(k))| \le \bar{v}(1-\tanh(1)) = \bar{d}$.

To track *y(k)* with *x(k)*, we set up the controller here. Define the tracking error $z(k) = x(k) - y(k)$, we can get,

$$\begin{aligned} z(k+1) &= f(x(k)) + u(k) - y(k) \\ &= f(x(k)) + g(v(k)) + d(v(k)) - y(k) \\ &= f(x(k)) + g_v v(k) + d(v(k)) - y(k) \end{aligned} \tag{22}$$

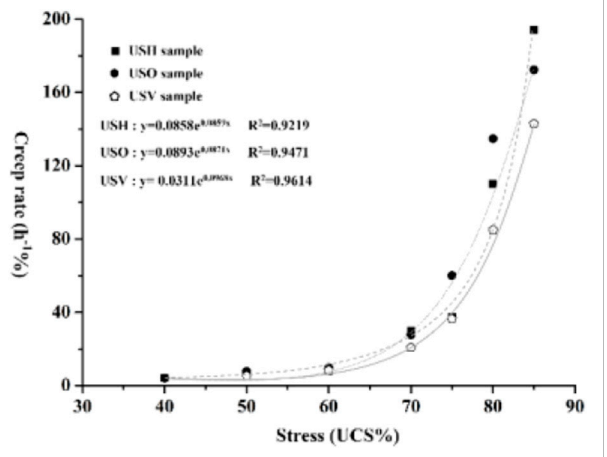

FIGURE 11
Curve of creep rate-constant stress.

Where, $g_v = \partial g(v(k))/\partial v(k)|_{v(k)=v_a}$, $v_a = av(k) + (1-a)v_a(k)$

Since the system function $f(x(k))$ and g_v are unknown, neural network is used for approximation.

$$h(x(k), y(k)) = \frac{y(k) - f(x(k))}{g_v} = W^T S(x(k)) + \varepsilon(k) \tag{23}$$

Substitute (23) into (22), we can get

$$\begin{aligned} z(k+1) &= f(x(k)) + g_v v(k) + d(v(k)) - y(k) \\ &= g_v v(k) - g_v\frac{f(x(k)) - y(k)}{g_v} + d(v(k)) \\ &= g_v\left(v(k) - W^T S(x(k)) - \varepsilon(k)\right) + d(v(k)) \\ &= g_v\left(v(k) - W^T S(x(k))\right) + d_1(k) \end{aligned} \tag{24}$$

Where, $d_1(k) = d(v(k)) - g_v\varepsilon(k) \le \bar{d}_1$

The expression of the constructed controller is

$$v(k) = \hat{W}^T(k)S(k) \tag{25}$$

Substitute (25) into (24), we can get

$$\begin{aligned} z(k+1) &= g_v\left(\hat{W}^T(k)S(k) - W^T S(x(k))\right) + d_1(k) \\ &= g_v\left(\tilde{W}^T(k)S(k)\right) + d_1(k) \end{aligned} \tag{26}$$

The renewal rate of the constructed neural network is

$$\hat{W}(k+1) = \hat{W}(k) - \sigma S(k) z(k+1) \tag{27}$$

Therefore, the error system can be expressed as

$$\begin{aligned} z(k+1) &= g_v\left(\tilde{W}^T(k)S(k)\right) + d_1(k) \\ \tilde{W}(k+1) &= \tilde{W}(k) - \sigma S(k) z(k+1) \end{aligned} \tag{28}$$

The following part is the stability analysis.

Construct Lyapunov function for stability analysis, and its function expression is

$$V(k) = z^2(k) + \frac{1}{\sigma}\tilde{W}^T(k)\tilde{W}(k) \tag{29}$$

Its difference can be expressed as

$$\begin{aligned} \Delta V(k) &= z^2(k+1) - z^2(k) + \frac{1}{\sigma}\tilde{W}^T(k+1)\tilde{W}(k+1) \\ &\quad - \frac{1}{\sigma}\tilde{W}^T(k)\tilde{W}(k) \end{aligned} \tag{30}$$

Insert (28) into (30), we can get

$$\begin{aligned} \Delta V(k) &= z^2(k+1) - z^2(k) + \frac{1}{\sigma}\tilde{W}^T(k+1)\tilde{W}(k+1) - \frac{1}{\sigma}\tilde{W}^T(k)\tilde{W}(k) \\ &= z^2(k+1) - z^2(k) - 2\tilde{W}^T(k)S(k)z(k+1) + \sigma\|S(k)\|^2 z^2(k+1) \end{aligned} \tag{31}$$

The Eq. 28 can be converted into

$$z^2(k+1) = g_v\tilde{W}^T(k)S(k)z(k+1) + d_1(k)z(k+1) \tag{32}$$

The Eq. 32 can be rewritten as

$$-\tilde{W}^T(k)S(k)z(k+1) = -\frac{z^2(k+1)}{g_v} - \frac{d_1(k)}{g_v} \quad (33)$$

Due to $g_v \leq 1$, then, the following can be obtained,

$$-\tilde{W}^T(k)S(k)z(k+1) \leq z^2(k+1) - \bar{d}_1^2 \quad (34)$$

Substitute (34) into (31), we can get,

$$\Delta V(k) \leq -z^2(k+1) - z^2(k) + \bar{d}_1^2 + \sigma\|S(k)\|^2 z^2(k+1) \quad (35)$$

Eq. 36 can be obtained by transforming (35),

$$\Delta V(k) \leq -\left(1-\sigma s^2\right)z^2(k+1) - z^2(k) + \bar{d}_1^2 \quad (36)$$

Construct a design parameter σ whose range is $1-\sigma s^2 > 0$, and the following can be obtained,

$$\Delta V(k) \leq -z^2(k) + \bar{d}_1^2 \quad (37)$$

According to Lyapunov theorem, the tracking error of the system is small enough to meet the accuracy requirement.

The BP neural network has robust nonlinear mapping ability and flexible network structure compared with other neural networks. In this study, the output data from the BP neural network was compared with the creep test results to verify the accuracy and stability of the BP neural network. Analysis of the rock strain data from the BP neural network and creep test showed that the mean values were 0.611 and 0.627, and the median values were 0.703 and 0.715, respectively. The K-fold was used to classify the dataset into the training dataset and the testing dataset. The testing dataset was used for evaluation of the model. A portion of the training data was set aside as the validation dataset to evaluate the training effectiveness of the model to solve the overfitting problem. The validation dataset obtained from the training dataset was used to validate the model.

The average relative errors of the data from BP neural network and the viscoelastic–viscoplastic model were 0.51 and 0.57%, respectively, relative to the creep test data, which shows a high degree of consistency. This finding further showed that the BP neural network had high accuracy and stability and indicates that the viscoelastic–viscoplastic model was scientifically viable and accurate.

Conclusion

The following conclusion were drawn from the present study:

(1) The crack paths of the USN coal samples were random causing significant irregularity of the failure characteristics. The failure modes of the USH coal samples were mainly characterized by oblique shear failure mode with a stratified structure and failure that traversed from the top to bottom surfaces. The angle between the failure surface and the horizontal plane was greater than 60°. The failure modes of the USO coal samples were mainly shear failure type and a stratified structure dominated the block splitting failure. The failure modes of coal samples in the USV group were not limited to failure mode dominated by the stratified structure. These samples mainly exhibited mixed failure mode.

(2) A positive correlation was observed between strain and creep stress during stress loading, which can be expressed as a logarithmic function. In addition, the steady-state creep time and creep stress can be expressed as a logarithmic function. The relationship between the creep rate and creep stress before failure can also be expressed as an exponential function.

(3) A BP neural network model was established and optimized using the creep test data. The Lyapunov function was constructed to validate the stability and accuracy of the model.

Data availability statement

The original contributions presented in the study are included in the article/supplementary material, further inquiries can be directed to the corresponding author.

Author contributions

YY: project administration, supervision. YL, writing-reviewing and editing. KY and GL: software, validation. ZL: visualization, investigation.

Funding

This research was funded by the General Project of Shaanxi Provincial Department of Science and Technology, grant number 2022JQ-463, the General Project of Shaanxi Provincial Department of Education, grant number 21JK0952, the High-level Talents Special Fund of Xijing University, grant number XJ21B12.

Conflict of interest

The handling editor YZ declared a shared affiliation with the author YY at the time of review.

The authors declare that the research was conducted in the absence of any commercial or financial relationships that could be construed as a potential conflict of interest.

Publisher's note

References

Bagheri, M., Rezania, M., and Mousavi Nezhad, M. (2015). An Experimental study of the initial volumetric strain rate effect on the creep behaviour of reconstituted clays. *IOP Conf. Ser. Earth Environ. Sci.* 26, 012034. doi:10.1088/1755-1315/26/1/012034

Bhat, D. R., Bhandary, N., and Yatabe, R. (2013). Residual-state creep behavior of typical clayey soils. *Nat. Hazards (Dordr).* 69, 2161–2178. doi:10.1007/s11069-013-0799-3

Brantut, N., Baud, P., Heap, M. J., and Meredith, P. (2012). Micromechanics of brittle creep in rocks. *J. Geophys. Res.* 117, 8412. doi:10.1029/2012JB009299

Cao, P., Youdao, W., Wang, Y., Haiping, Y., and Yuan, B. (2016). Study on nonlinear damage creep constitutive model for high-stress soft rock. *Environ. Earth Sci.* 75, 900. doi:10.1007/s12665-016-5699-x

Davis, N. E., Kronenberg, A. K., and Newman, J. (2008). Plasticity and diffusion creep of dolomite. *Tectonophysics* 456, 127–146. doi:10.1016/j.tecto.2008.02.002

Dubey, R., and Gairola, V. (2005). Influence of stress rate on rheology – an experimental study on rocksalt of simla himalaya, India. *Geotech. Geol. Eng. (Dordr).* 23, 757–772. doi:10.1007/s10706-003-2596-3

Fabre, G., and Pellet, F. (2006). Creep and time dependent damage in argillaceous rocks. *Int. J. Rock Mech. Min. Sci.* 43, 950–960. doi:10.1016/j.ijrmms.2006.02.004

Fahimifar, A., Karami, M., and Fahimifar, A. (2015). Modifications to an elasto-visco-plastic constitutive model for prediction of creep deformation of rock samples. *Soils Found.* 55, 1364–1371. doi:10.1016/j.sandf.2015.10.003

Fahimifar, A., Tehrani, F., Hedayat, A., and Vakilzadeh, A. (2010). Analytical solution for the excavation of circular tunnels in a visco-elastic Burger's material under hydrostatic stress field. *Tunn. Undergr. Space Technol.* 25, 297–304. doi:10.1016/j.tust.2010.01.002

Firme, P., Brandao, N., Roehl, D., and Romanel, C. (2018). Enhanced double-mechanism creep laws for salt rocks. *Acta Geotech.* 13, 1329–1340. doi:10.1007/s11440-018-0689-7

Grgic, D., and Amitrano, D. (2009). Creep of a porous rock and associated acoustic emission under different hydrous conditions. *J. Geophys. Res.* 114, B10201. doi:10.1029/2006JB004881

Guan, Z., Jiang, Y., Tanabashi, Y., and Huang, H. (2007). A new rheological model and its application in mountain tunnelling. *Tunn. Undergr. Space Technol.* 23, 292–299. doi:10.1016/j.tust.2007.06.003

Hajiabadi, M., and Nick, H. (2020). A modified strain rate dependent constitutive model for chalk and porous rock. *Int. J. Rock Mech. Min. Sci.* 134, 104406. doi:10.1016/j.ijrmms.2020.104406

Herrmann, J., Rybacki, E., Sone, H., and Dresen, G. (2020). Deformation experiments on bowland and posidonia shale—Part II: Creep behavior at *in situ* pc–T conditions. *Rock Mech. Rock Eng.* 53, 755–779. doi:10.1007/s00603-019-01941-2

Heusermann, S., Rolfs, O., and Schmidt, U. (2003). Nonlinear finite-element analysis of solution mined storage caverns in rock salt using the LUBBY2 constitutive model. *Comput. Struct.* 81, 629–638. doi:10.1016/S0045-7949(02)00415-7

Hoek, E., and Brown, E. (1997). Practical estimates of rock mass strength. *Int. J. Rock Mech. Min. Sci.* 34, 1165–1186. doi:10.1016/S1365-1609(97)80069-X

Kontogianni, V., Psimoulis, P., and Stiros, S. (2006). What is the contribution of time-dependent deformation in tunnel convergence? *Eng. Geol.* 82, 264–267. doi:10.1016/j.enggeo.2005.11.001

Li, Y., and Xia, C. (2000). Time-dependent tests on intact rocks in uniaxial compression. *Int. J. Rock Mech. Min. Sci.* 37, 467–475. doi:10.1016/S1365-1609(99)00073-8

Liu, L., Wang, G.-m., Chen, J.-h., and Yang, S. (2013). Creep experiment and rheological model of deep saturated rock. *Trans. Nonferrous Metals Soc. China* 23, 478–483. doi:10.1016/S1003-6326(13)62488-7

Nadimi, S., Shahriar, K., Sharifzadeh, M., and Moarefvand, P. (2011). Triaxial creep tests and back analysis of time-dependent behavior of Siah Bisheh cavern by 3-Dimensional Distinct Element Method. *Tunn. Undergr. Space Technol.* 26, 155–162. doi:10.1016/j.tust.2010.09.002

Nazary Moghadam, S., Mirzabozorg, H., and Noorzad, A. (2013). Modeling time-dependent behavior of gas caverns in rock salt considering creep, dilatancy and failure. *Tunn. Undergr. Space Technol.* 33, 171–185. doi:10.1016/j.tust.2012.10.001

Nedjar, B., and Le Roy, R. (2013). An approach to the modeling of viscoelastic damage. Application to the long-term creep of gypsum rock materials. *Int. J. Numer. Anal. Methods Geomech.* 37, 1066–1078. doi:10.1002/nag.1138

Olivella, S., and Gens, A. (2002). A constitutive model for crushed salt. *Int. J. Numer. Anal. Methods Geomech.* 26, 719–746. doi:10.1002/nag.220

Parsapour, D., and Fahimifar, A. (2016). Semi-analytical solution for time-dependent deformations in swelling rocks around circular tunnels. *Geosci. J.* 20, 517–528. doi:10.1007/s12303-015-0050-1

Pellet, F., and Fabre, G. (2007). Damage evaluation with P-wave velocity measurements during uniaxial compression tests on argillaceous rocks. *Int. J. Geomech.* 7, 431–436. doi:10.1061/(asce)1532-3641(2007)7:6(431)

Pellet, F., Hajdu, A., Deleruyelle, F., and Besnus, F. (2005). A viscoplastic model including anisotropic damage for the time dependent behaviour of rock. *Int. J. Numer. Anal. Methods Geomech.* 29, 941–970. doi:10.1002/nag.450

Rahimi, S., and Hosseini, M. (2014). Laboratory studies of creep behavior on thick-walled hollow cylindrical salt rock specimens. *Arab. J. Geosci.* 8, 5949–5957. doi:10.1007/s12517-014-1622-5

Sterpi, D., and Gioda, G. (2009). ViscoPlastic behaviour around advancing tunnels in squeezing rock. *Rock Mech. Rock Eng.* 42, 319–339. doi:10.1007/s00603-007-0137-8

Tomanovic, Z. (2006). Rheological model of soft rock creep based on the tests on marl. *Mech. Time. Depend. Mat.* 10, 135–154. doi:10.1007/s11043-006-9005-2

Zhifa, Y., Zhiyin, W., Luqing, Z., Ruiguang, Z., and Nianxing, X. (2001). Back-analysis of viscoelastic displacements in a soft rock road tunnel. *Int. J. Rock Mech. Min. Sci.* 38, 331–341. doi:10.1016/S1365-1609(00)00081-2

frontiers | Frontiers in Earth Science

TYPE Original Research
PUBLISHED 09 January 2023
DOI 10.3389/feart.2022.1021436

OPEN ACCESS

EDITED BY
Lishuai Jiang,
Shandong University of Science and Technology, China

REVIEWED BY
Shun Liang,
China University of Mining and Technology, China
Li Jianghua,
China Coal Research Institute, China

*CORRESPONDENCE
Cheng Peng,
cphappy@163.com

SPECIALTY SECTION
This article was submitted to Structural Geology and Tectonics, a section of the journal Frontiers in Earth Science

RECEIVED 17 August 2022
ACCEPTED 21 September 2022
PUBLISHED 09 January 2023

CITATION
Peng C (2023), Research on the breaking mechanism of bolts and cables in the gateway driven along a small coal pillar in the Datong mining area and the corresponding control technology. *Front. Earth Sci.* 10:1021436. doi: 10.3389/feart.2022.1021436

Research on the breaking mechanism of bolts and cables in the gateway driven along a small coal pillar in the Datong mining area and the corresponding control technology

Cheng Peng[1,2,3]*

[1]School of Energy and Mining Engineering, China University of Mining and Technology Beijing, Beijing, China, [2]Tiandi Science and Technology Co, Ltd, Beijing, China, [3]Coal Mining Research Institute, China Coal Technology & Engineering Group, Beijing, China

The gateway of the thick coal seam working face in the Datong mining area was excavated along a small coal pillar, resulting in serious bolt (cable) breaking failure, strong surrounding rock deformation, serious ground pressure appearance, and difficulties surrounding rock control. So, the bolt (cable) breaking characteristics and corresponding causes of the 5106 return air gateway with a small coal pillar in Dongzhouyao coal mine (a mine in the Datong mining area) were analyzed through an on-site investigation, surrounding rock geotechnical parameters test, theoretical analysis, laboratory experiment, on-site engineering test, and other research means. The study carried out laboratory testing and analysis on the stress distribution characteristics and laws of the bolts, put forward the bolt (cable) breaking mechanism and prevention countermeasures, and completed the field industrial test of the surrounding rock pressure relief and support joint control technology in the gateway. The on-site tracking and data showed that the breaking conditions of the bolts (cables) were significantly reduced by improving the initial force of the bolts (cables), optimizing the supporting materials and components, canceling the pressure ring, and implementing the hydraulic fracturing top cutting and pressure relief + high prestressed full cable support technology. The displacement of the top and bottom plates was reduced by 51%, the displacement of the two sides was reduced by 46%, and the influence distance of the working face advance stress was reduced from 85 m to 30 m. The successful implementation of the study results in the small pillar gateway of the Dongzhouyao coal mine provided a reference for the promotion and application of similar gateway conditions in the Datong mining area.

KEYWORDS

Datong mining area, thick coal seams, gob side gateway, support failure, top cutting and pressure relief, ground pressure monitoring

1 Introduction

For China, coal has always been the main energy supply, accounting for more than half of the total energy. However, with the increase in mining intensity and depth year by year, the deep mining of underground coal mines has brought many problems (Kang et al., 2021a; Kang et al., 2021b), such as high stress (Xie et al., 2017; Xie et al., 2018), strong dynamic pressure (Li et al., 2022), rock burst (Zhang et al., 2019; Zhang et al., 2020), coal and gas outburst (Liu et al., 2020), roof fall (Lu et al., 2013; Lu et al., 2015), and high temperature (Ranjith et al., 2017). Among these disasters, the problems caused by the strong dynamic pressure and rock burst are more serious (Kang et al., 2019; Gao et al., 2021). Deep mining has also caused the length of affected roadways to increase year by year (Zhang et al., 2021), and the proportion of complex and difficult supporting roadways is increasing (Yang et al., 2018), especially the dynamic pressure gateways with small coal pillars. The deformation of roadways is generally strong, resulting in a larger range of plastic zones (Guo et al., 2019; Ma et al., 2019) and more diversified forms (Shan et al., 2021; Ren et al., 2022). Due to the larger scope of mining (Zhao, 2014), violent movement of overlying strata (Wang et al., 2017), and the generation of void fraction (Wang et al., 2016; Wang and Li, 2017), some bolts and cables are broken, causing serious damage, which makes it difficult to maintain the gateway and poses a higher challenge to safety production (Xie et al., 2019). In deep mining, if thick coal seam mining is simultaneously encountered, it will cause more severe ground bolts supporting (Wu et al., 2019) and cables supporting (Shichang et al., 2021), which is mainly due to the increase in mining intensity and mined out area. Therefore, the deep thick coal seam has a greater impact on safe tunneling and maintenance of the gateway.

In solving the problem of gateway support caused by strong dynamic pressure, scholars have adopted the method of leaving small coal pillars, which makes the gateway arranged before the lateral peak pressure, and reduces the impact of dynamic pressure on the chute. There are usually two methods to retain small coal pillars. One is to retain the gateway of the previous working face as the gateway of the next working face (Wang et al., 2020) and the other is to excavate a new gateway at a small distance on the side of the last gateway after the mining of the previous working face (Jia and Hu, 2020). These two methods can achieve the purpose of mining only by retaining small coal pillars, which are relatively mature for working faces with relatively low mining height, but they are not very mature for thick coal seams (Zhu et al., 2019). These measures have solved the problem of pressure to some extent, but they have not been further studied from the perspective of gateway support.

Dynamic pressure and high-intensity mining have a severe impact on support technology and production safety (Kang et al., 2018; Kang et al., 2020); however, it may be more affected by the support effect of the serving gateway (Lian et al., 2021). For complex and difficult supporting gateways, on the one hand, the method of reducing the influence of dynamic pressure on the working face can be adopted (Mondal and Roy, 2019). On the other hand, most coal mines generally adopt the method of reducing the row spacing between bolts and cables (Nierobisz, 2017), improving the structure (Kang et al., 2016), and capacity (Gao et al., 2014) of bolts, or add an auxiliary shed to strengthen the support. Although the bolts and cables density is very high, the support effect is still not ideal in many cases, and the deformation is still large. Some gateways need to be lifted and bottomed during the tunneling period. According to statistics, the total amount of gateway bottoming works from the excavation to the installation of the working face has reached 2–3 m. Under such conditions, the traditional gateway support method is not effective, and cannot fundamentally solve this kind of gateway support problem.

At present, the coal mine mainly adopted two treatment methods for the first caving of the working face and control of rock burst: blasting and water injection softening (Yongzheng, 2018). Domestic and foreign experts and scholars mainly focused on hydraulic fracturing pressure relief mechanism (Yuanjie et al., 2022), hydraulic fracturing fracture simulation (Gao, 2021), expansion law research (Zhao et al., 2021), and fracturing monitoring technology (Ziyi et al., 2022). Wu and Kang, (2017) pointed out that the directional hydraulic fracturing technology could eliminate the overhang effect of a hard roof and improve the surrounding rock stress environment of the second retaining gateway. Feng and Kang, (2013) analyzed the direction and conditions of crack propagation under the action of *in-situ* stress. Feng, (2013) established a set of physical simulation and characterization methods for shale hydraulic fracturing. Guo et al, (2014) studied the fracturing expansion law under triaxial conditions and discussed the formation mechanism of a fracture network. Hou et al, (2016) described a method of monitoring hydraulic fracturing fractures using seismic technology. In recent years, directional hydraulic fracturing technology had been developed rapidly. Compared with blasting technology, hydraulic fracturing had some prominent safety and cost advantages. At present, it has been popularized and applied on a large scale in coal mines, mainly focus on the first caving of the working face and the prevention and control of rock bursts (Jiang et al., 2017a; Jiang et al., 2017b). There were few relevant research results on the strength and scope of fracturing roof control technology, pressure relief technology, and anchor cable support technology (Chen et al., 2022a; Chen et al., 2022b), especially on solving the influence of concentrated stress in advance of working face and dynamic pressure gateway in the extra thick coal seam.

Based on the abovementioned background, this study carries out hydraulic fracturing roof cutting, pressure relief, and roof control tests for the typical hard roof in the Datong mining area. The pressure relief effect of gateways with different fracturing parameters is studied, the pressure in the process of hydraulic

FIGURE 1
Deformation of strong dynamic pressure roadway in the Datong mining area.

fracturing and the water output of boreholes are analyzed, and the variation laws of gateway deformation and support pressure are monitored. The obtained results provide a reference for hydraulic fracturing and roof cutting pressure relief of gateways with dynamic pressure in similar extra-thick coal seams.

2 Breaking shape and characteristics of bolts (cables)

In recent years, the geological conditions gradually extend from simple Jurassic to complex Carboniferous with the expansion of mining scale and production capacity of the Datong mining area. The mining intensity and depth of coal seams have increased year by year, resulting in the gradual deterioration of the geological conditions of the gateway surrounding rock. The proportion of complex and difficult supporting gateways has increased year by year, especially for the dynamic pressure gateways with small coal pillars. The gateway deformation is strong, and the breaking of bolts and cables is serious, as shown in Figure 1. Dongzhouyao coal mine (a coal mine in the Datong mining area) began to use snake-shaped bolts and bird's nest cables in 5103 and 5203 gateways, and then popularized and applied them in the tunneling of the whole mine. In the process of popularization and application of the Dongzhouyao coal mine, the bolts and cables were broken and invalid in the gob side gateway along a small coal pillar or someplace nearby an abnormal geological structure, which seriously affected the safety of the supporting system. In view of the above situation, a large number of underground bolts and cables with broken ends and fractures were collected, the breaking characteristics and morphology of bolts and cables were studied, the breaking characteristics and laws of bolts and cables were analyzed, and the prevention and control measures of bolt and cable were put forward.

2.1 Breaking state and characteristics of bolts

The broken forms of underground bolts were collected and analyzed, as shown in Figure 2. The fracture positions of bolts were mainly concentrated in the range of 0.5–1.5 m above the orifice, and the forms of fractures were mainly tensile, with obvious necking phenomena like ① and ② in Figure 2, while some were shear fractures without obvious necking phenomenon like ③ in Figure 2.

2.2 Breaking state and characteristics of cables

The broken forms of underground cables were also collected and analyzed, as shown in Figure 3. The facts showed that the cable fractures were mainly bending form, and the fracture locations were mostly concentrated near the orifice location. In addition, the compression rings were deformed, and the damaged ports were neat without necking.

3 Test and analysis of surrounding rock conditions of the roof

In order to analyze the reasons for the breaking, the underground borehole structure peeping and the surrounding rock *in-situ* strength measuring device are used to test the structure and *in-situ* strength in the area where a large number of underground bolts and cables are broken. Analyze the surrounding rock structure, strength data, and characteristics to master the geological conditions of the underground surrounding rock, and then put forward corresponding measures and prevention countermeasures.

The thickness of 3–5 coal seams in the Datong area is mostly large, and the gateway is generally driven along the coal seam floor, so most of the roofs are the coal seams. Due to the complex geological

FIGURE 2
Breaking form of bolts.

FIGURE 3
Breaking form of cables.

conditions of the Dongzhouyao coal mine, it is greatly affected by the geological structure, especially in the local area invaded by lamprophyre, which results in great fluctuations in the strength of the gateway roof. The underground surrounding rock structure and strength test results of the Dongzhouyao coal mine are shown in Figure 4. Because lamprophyre is an igneous rock, the underground test strengths are very high, generally reaching 90–100 MPa. While the strengths of 3–5# coal are reduced from 10 to 25 MPa to 5–10 MPa due to the influence of lamprophyre, which leads to the result that the strengths of surrounding rock in the shallow part of the gateway roof fluctuate greatly. At the same time, the horizontal joints of the roof are developed, and the roofs are prone to the horizontal dislocation between lamprophyre and coal joint fissures, which is one of the important reasons for the serious shear failures of bolts and cables.

4 Analysis of stress and deformation characteristics of the bolt under compound stress

Due to the installation angle of the underground bolt and the actual conditions of the gateway surrounding rock, the bolt may inevitably have a certain installation angle with the surface of the gateway surrounding rock, resulting in the complex stress state of the bolt tail, and from the pure tensile stress state to the tension torsion bending stress state. At the same time, there is a tension bending torsion shear composite stress state due to the influence of geological structure and horizontal displacement of surrounding rock, which results in extremely complex stress, uneven load, breaking, and failure of support bodies and support members. There is usually a non-conforming surface between the steel strip and the rock layer interface, resulting in the load mostly concentrated at point K and the formation of uneven stress, as shown in Figure 5A. Affected by the uneven force, the bolt will rotate laterally, forming a new stress point B and breaking, as shown in Figure 5B.

In this study, ABAQUS numerical simulation software is used to establish different simulation schemes, the stress and deformation characteristics of the bolt body and threaded section under the action of single and composite stresses of tension, torsion, bending, and shear are analyzed.

4.1 Numerical simulation model

The ABAQUS software is used for simulation calculation, and the model is shown in Figure 6. The total length of the bolt model is 305 mm, the length of the ribbed bolt body is 205 mm,

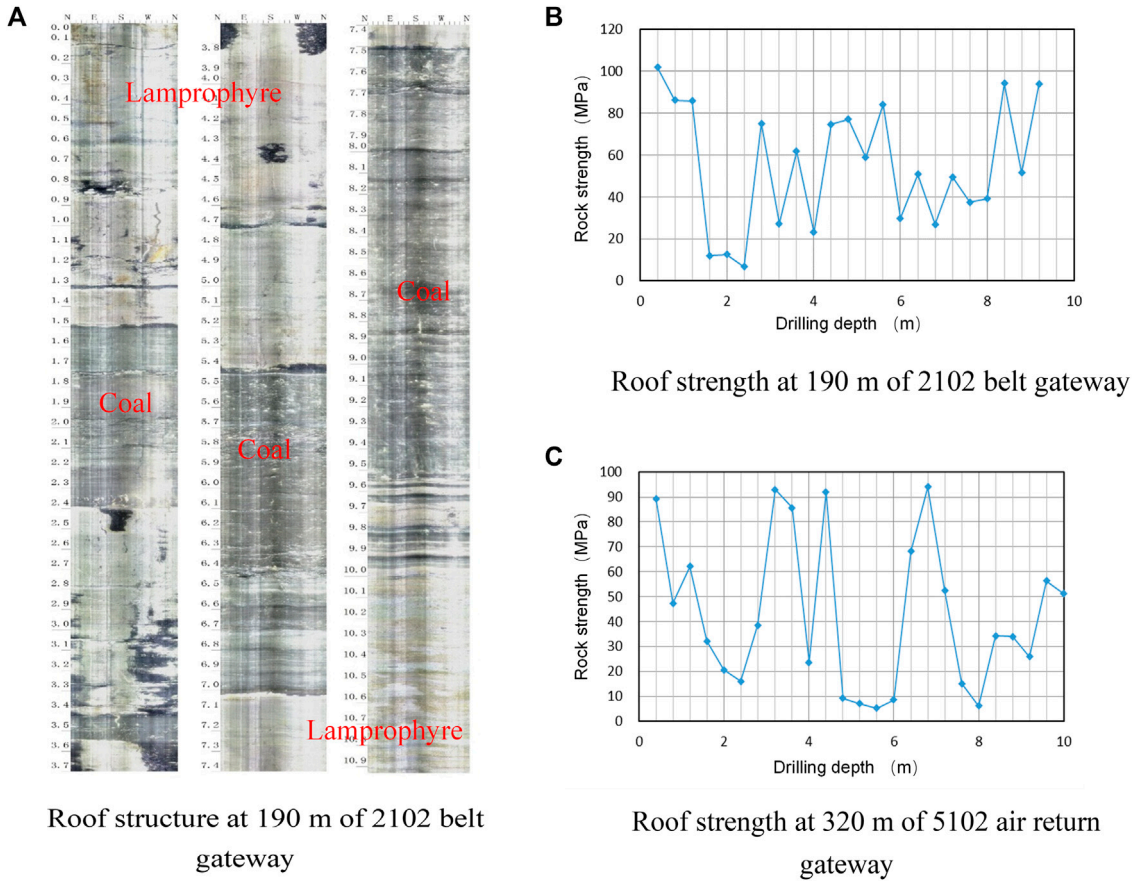

FIGURE 4
Structure and strength test of underground surrounding rock in Dongzhouyao coal mine. Roof structure at 190 m of 2102 belt gateway. Roof strength at 190 m of 2102 belt gateway. Roof strength at 320 m of 5102 air return gateway.

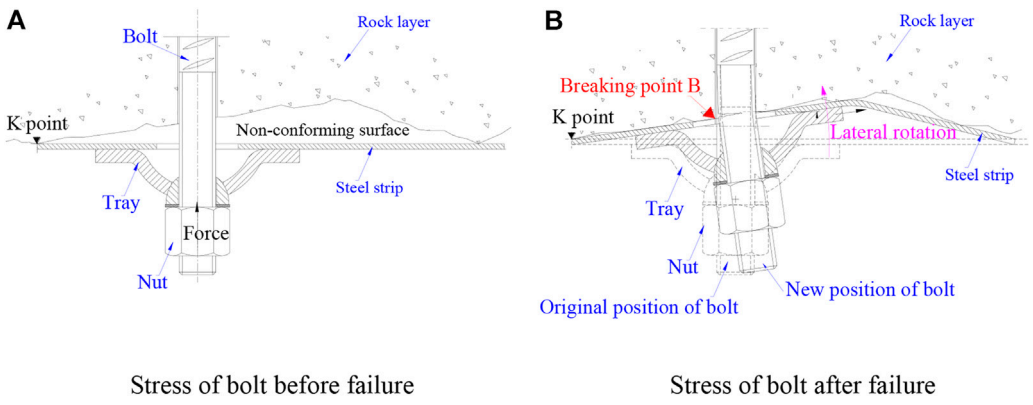

FIGURE 5
Force analysis of breaking bolts. **(A)** Stress of bolt before failure. **(B)** Stress of bolt after failure.

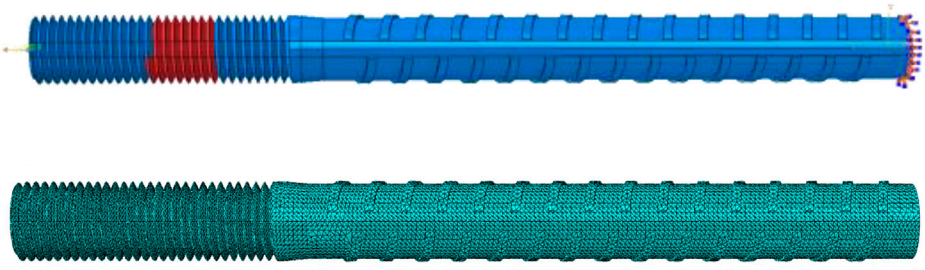

FIGURE 6
Model and mesh generation.

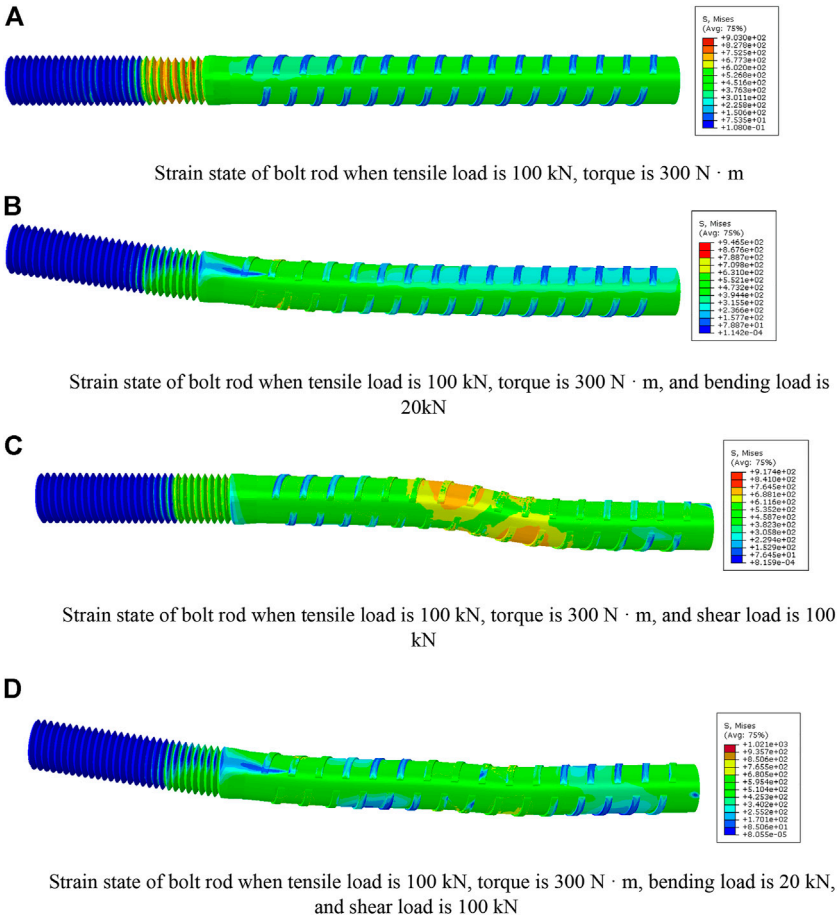

FIGURE 7
Stress-strain state of the bolt under composite stress state. **(A)** Strain state of bolt rod when a tensile load is 100 kN, torque is 300 N m. **(B)** Strain state of bolt rod when a tensile load is 100 kN, torque is 300 N m, and bending load is 20 kN. **(C)** Strain state of bolt rod when a tensile load is 100 kN, torque is 300 N m, and shear load is 100 kN. **(D)** Strain state of bolt rod when tensile load is 100 kN, torque is 300 N m, bending load is 20 kN, and shear load is 100 kN.

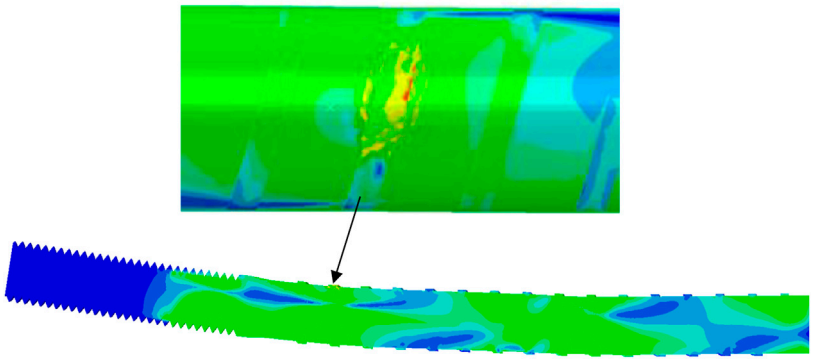

FIGURE 8
Stress concentration of bolt under composite stress state.

the horizontal rib is left-handed, the top width of the rib is 3 mm, the height of the rib is 0.8 mm, the spacing of the horizontal ribs is 11 mm, the horizontal ribs on both sides are asymmetric, and the diameter of the rod body is 22 mm. Thread parameters: thread M 24, pitch 3 mm, the actual total length of thread 93 mm, thread section plus transition section 100 mm in total.

4.2 Numerical simulation schemes

The specific numerical simulation schemes are as follows:

1) Tension: different tensile loads 30 kN, 100 kN, 160 kN, and 210 kN
2) Tension + torsion: initially apply 100 N m, 300 N m, and 500 N m, and then increase the axial load to 210 kN
3) Tension + torsion + bending: on the basis of (2), apply different levels of bending loads 20 kN, 50 kN, and 80 Kn, respectively
4) Tension + torsion + bending + shear: on the basis of (3), apply different levels of shear loads 1 kN/mm, 2.5 kN/mm, 5 kN/mm at a certain position in the middle of the rod (in the middle of the non-threaded section), simulating the shear force caused by rock dislocation

4.3 Numerical simulation analysis

Through the simulation and analysis of the actual working conditions in the process of underground bolt support, it is found that the underground bolt has the effects of tension, bending, torsion, shear, and other loads in the process of use, and is in a composite stress state, especially for the threaded section from the bolt installation orifice to the bolt tail. The stress of the rod is extremely complex, with high stress and a large variation gradient, as shown in Figure 7. Under the action of bending load and shear load, the stress concentration effect is significant (Figure 8). The load borne by the bolt obviously exceeds the strong performance of the bolt itself, resulting in the breakage and failure of the support body and support components. Therefore, it can be seen that it is very important to match the mechanical properties of underground bolts with the mechanics of supporting components, which can optimize the stress state of bolts and reduce the impact of harmful loads on the bearing performance of bolts.

5 Cause analysis and prevention countermeasures of broken bolts and cables

5.1 Cause analysis of broken bolts and cables

Through the analysis of the breaking shape and characteristics of the bolts and cables, the test results of the geological conditions of the surrounding rock of the underground gateway, and the theoretical analysis and numerical calculation results, it is considered that the followings are the main reasons for the breaking failure of the bolts and cables in Dongzhouyao coal mine:

1) Geological conditions: the geological factors of the Dongzhouyao coal mine are complex, the geological conditions change greatly affected by lamprophyre intrusion, resulting in great changes in the lithology and strength of lamprophyre and coal body in the roof, which leads to horizontal dislocation deformation of the roof, and shear fracture under horizontal shear load.
2) Gateway stress environment: the surrounding rock stress environment of the gateway along a small coal pillar in the Dongzhouyao coal mine is poor. The gateway is strongly affected by the dynamic pressure of the working face, and the strength requirements of the bolts and cables are high, which

are required to have high bearing capacity and elongation. Ordinary 1×7–17.8 mm cable and 20 mm - 335# bolt are difficult to resist the impact of small coal pillar dynamic pressure.

3) Gateway support parameters: through the investigation and sampling inspection of the initial preload of the underground bolts and cables, it is found that the initial prestress of the bolts and cables are low. The control abilities of the roof are poor, which are prone to harmful deformation such as delamination and expansion, and the bolts are prone to tensile failure, resulting in shrinkage fracture failure.
4) Gateway support materials: through the mechanical properties and matching analysis of the original support materials, it is found that the matching between the original support cable and the corresponding tray is poor. There is no self-aligning ball pad, and the stress state at the hole of the cable cannot be adjusted. The pressure ring is easy to deform, and the poor stress state at the hole of the rod and cable is formed when bearing the bending load, and furthermore causes shear failure.

5.2 Prevention countermeasures of broken bolts and cables

Based on the analysis of the abovementioned reasons for the breaking of bolts and cables, the following prevention countermeasures are put forward:

1) Gateway pressure relief: blasting, hydraulic fracturing, and other means are used to relieve the pressure of the gateway, change the structure and thickness of the surrounding rock of the goaf roof, reduce the stress of the surrounding rock, improve the stress environment, and thus reduce the deformation degree.
2) Increase the initial preload of the bolts and cables: the pre-tightening torque of the bolt rod is increased from 200 N m to 400 N m, and the initial pretension of the cable is increased from 100 kN to 300 kN. Improve the control of the support on the surrounding rock of the roof, fully improve the mechanical properties of the surrounding rock of the support and enhance the bearing capacity.
3) Improve the strengths, mechanical properties, and toughness of support materials: the diameter of the bolts rod is adjusted from 20 mm to 22 mm, and the specification of the cable is changed from 1×7–17.8 mm to 1×19–21.8 mm.
4) The structure of the bolt and cable supporting plate is systematically optimized. The pressure ring is canceled, and the self-aligning ball pad is adopted to improve the stress state. Enhance the bearing capacity of the bolt and cable supporting plate, and optimize the mutual matching of supporting materials and components.

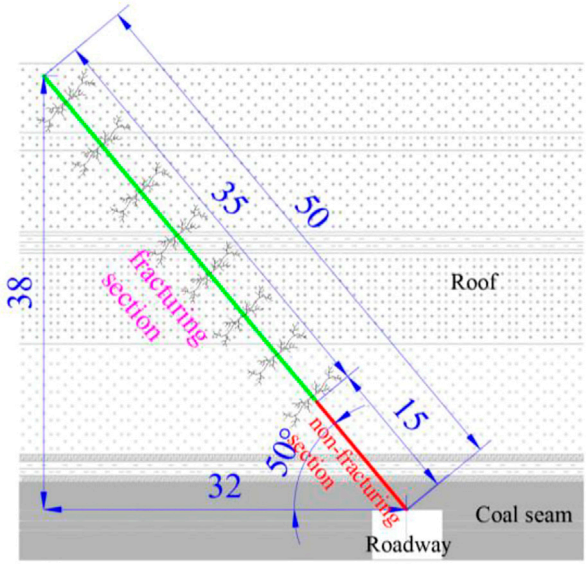

FIGURE 9
Schematic diagram of hydraulic fracturing.

6 Field test

6.1 Project overview

Dongzhouyao coal mine is located in Zuoyun County, Datong City, Shanxi Province, with a design production capacity of 10 million tons per year. Working face 8106 is located in panel 1 of 5 layer of Carboniferous Taiyuan formation. The main mining area is mountain five coal. The average thickness of the coal seam is 6.9 m, the dip angle of the coal seam is 5°, and the burial depth is 470–540 m. The northwest side of 8106 working face is the mined 8102 working face (which has been mined for 4–5 years), the coal pillar size between 5106 air return gateway and the goaf of 8102 working face is 6 m. Due to the large thickness of the coal seam and the small size of the coal pillar, the 5106 air return gateway may be affected by the double mining of the 8102 and 8106 working face during the service period. The stressed environment is complex, the peak stress of the coal pillar is high, and the gateway deformation or damage is serious, which poses a great challenge to mine safety production.

6.2 Hydraulic fracturing and pressure relief technology of gateway

The hydraulic fracturing pressure relief test length of 5106 return air gateway is 300 m, the number of pressure

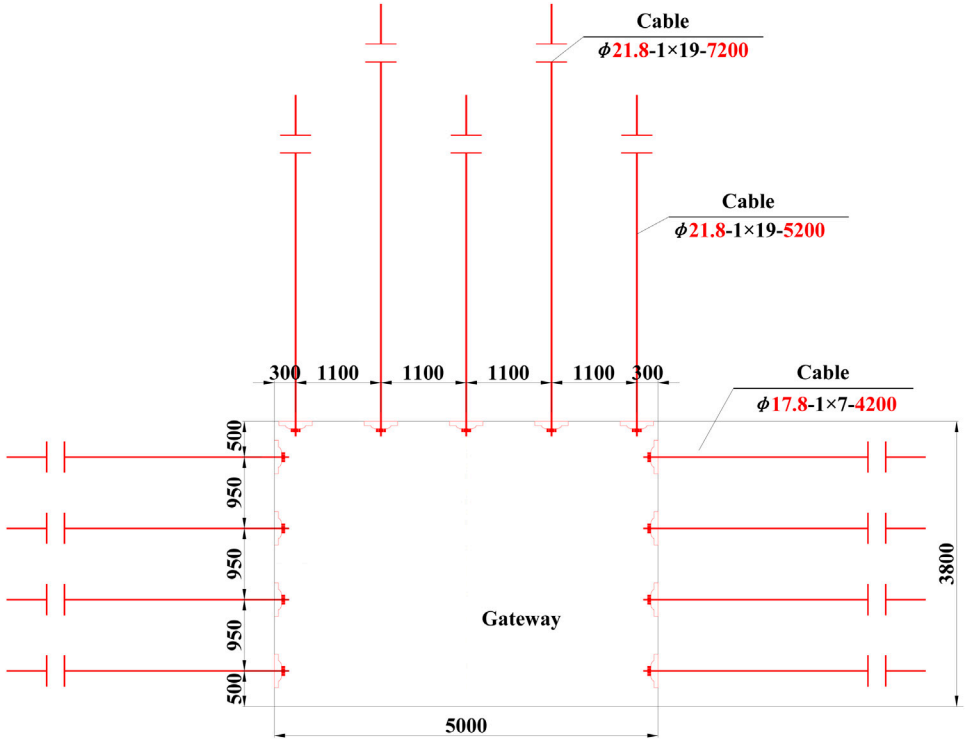

FIGURE 10
Schematic diagram of high prestressed full cable strong support technology (unit: mm).

relief holes is 31, and the depth and diameter of the hole are 50 m (including 35 m in the fracturing section and 15 m in the non-fracturing section) and 60 mm, respectively. The hole spacing is 8–10 m and the elevation of the hole is 50°, see Figure 9 for details. Considering that the hard roof rock formation in the deep part of the working face forms a fracture line at the edge of the coal pillar, the included angle range between the horizontal direction of the borehole and the strike of the gateway is designed to be between 5°–10°. The mining high-pressure pump with a large flow is used for water injection. The drilling fracturing range is 15–50 m, and the fracturing is carried out every 2–3 m, with a water injection volume of 2.4 m^3 each time.

6.3 High-prestressed full cable support technology

After a comprehensive analysis, it is determined to adopt high-prestressed full cable strong support technology. Five cables, with a diameter of 21.8 mm, length of 5.2 m, and 1 × 19 high-strength prestressed steel strands, are used in the gateway roof, as shown in Figure 10. The ultimate bearing capacity is 582 kN, the elongation is 5%, the preload is 300 kN, and the spacing between rows is 1.1 m × 0.9 m. The top plate cable adopts a W-shaped steel guard plate and a special-shaped cable support plate to protect the top. At the same time, two single cables with a diameter of 21.8 mm and a length of 7.2 m are constructed for every two rows of steel belts. The upper adopts four cables, with a diameter of 17.8 mm and 1 × 7 strands of prestressed steel strands, and the row spacing is 0.9 m × 0.95 m, the preload is 200 kN.

6.4 Gateway support effect and the analysis

The field test shows that hydraulic fracturing and pressure relief drilling in the deep part of the roof of the small coal pillar gateway can change the basic roof structure and strength and reduce the influence of the advanced abutment pressure during mining. At the same time, the strength and matching of support materials are optimized combined with the gateway high prestressed full cable support technology, and the effective anchoring of the shallow surrounding rock of the gateway is realized. The support breaking situation is effectively alleviated and improved, and there is no large-scale breaking failure. The ground pressure monitoring data shows that

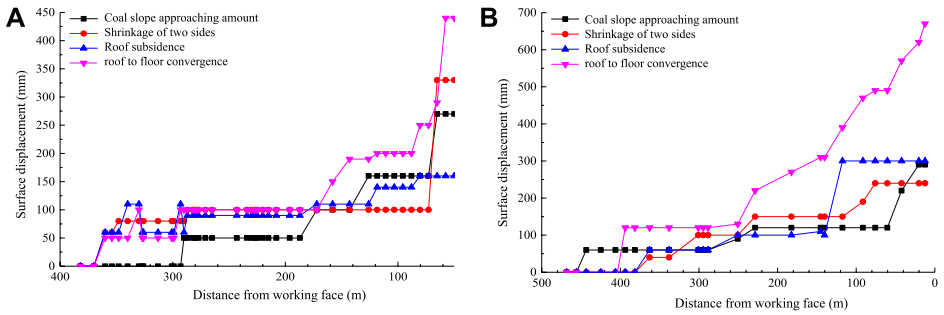

FIGURE 11
Deformation monitoring curve of underground gateway after hydraulic fracturing and pressure relief + high prestressed full cable support" technology. **(A)** "Hydraulic fracturing and pressure relief + high prestressed full cable support" technology. **(B)** " High prestressed full cable support" technology.

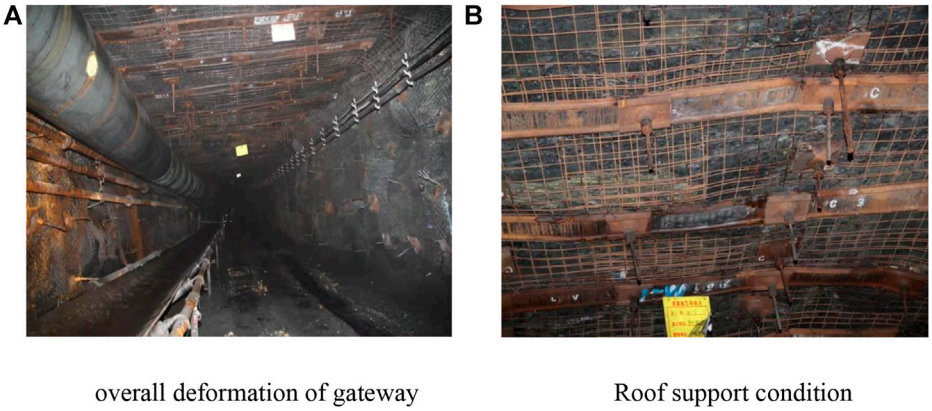

FIGURE 12
Underground gateway condition after "hydraulic fracturing and pressure relief + high prestressed full cable support" technology. **(A)** Overall deformation of the gateway. **(B)** Roof support condition.

the combined control technology of hydraulic fracturing and pressure relief + high prestressed full cable support has a very significant effect on the surrounding rock control of a small coal pillar dynamic pressure gateway. The overall deformation of the gateway has been significantly reduced, of which the maximum displacement of the two sides is 330 mm, and the maximum displacement of the roof and floor is 440 m, as shown in Figure 11. Compared with other gateways with similar conditions in the mine, the roof and floor displacements are reduced by 51% after the application of the "support unloading coupling" joint control technology. The displacements of two sides are reduced by 46%, and the influence distance of the advance stress of the working face is reduced from 85 m to within 30 m, the final deformation of the gateway is shown in Figure 12.

7 Conclusion

1) This study makes a comprehensive analysis of the breaking shape of the bolts and cables in the Dongzhouyao coal mine, gets the stress characteristics of underground bolts (cables), and measurement of the geomechanical parameters of the gateway surrounding rock. It is considered that the changes in the geological conditions of gateway surrounding rock, stress environment, unreasonable support parameters, and mismatching of support materials are the important reasons for the failure of dynamic pressure gateway along small coal pillar.
2) In view of the difficult problem of surrounding rock control of dynamic pressure gateway along small coal pillar, the measures

including the hydraulic fracturing technology, pressure relief technology, optimizing strength and matching of support materials, and improving the initial support prestress are proposed, which effectively solves the fracture failure and support of dynamic pressure gateway along small coal pillar.

3) Compared with other similar dynamic pressure gateways along small coal pillars in the mine, the combined control technology of "hydraulic fracturing and pressure relief + high prestressed full cable support" is adopted. Results show that the roof and floor displacement of the gateway is reduced by 51%, the displacement of the two sides is reduced by 46%, and the influence distance of the advance stress of the working face is reduced from 85 m to 30 m.

Data availability statement

The original contributions presented in the study are included in the article/Supplementary Material; further inquiries can be directed to the corresponding author.

Author contributions

The author completed all the contents by himself.

Funding

The author gratefully acknowledges the financial support by the Natural Science Foundation of China (Grant no. 52004126) and the special project of science and technology innovation and entrepreneurship fund of Tiandi Science and Technology Co., Ltd. (Grant no. 2022-2-TD-MS013).

Conflict of interest

Author CP was employed by Tiandi Science and Technology Co., Ltd.

Publisher's note

All claims expressed in this article are solely those of the authors and do not necessarily represent those of their affiliated organizations, or those of the publisher, the editors, and the reviewers. Any product that may be evaluated in this article, or claim that may be made by its manufacturer, is not guaranteed or endorsed by the publisher.

References

Chen, J., Liu, P., Liu, L., Zeng, B., Zhao, H., Zhang, C., et al. (2022). Anchorage performance of a modified cable anchor subjected to different joint opening conditions. *Constr. Build. Mater.* 27 (03), 607–614. doi:10.1016/j.conbuildmat.2022.127558

Chen, J., Zeng, B., Liu, L., Tao, K., Zhao, H., Zhang, C., et al. (2022). Investigating the anchorage performance of full-grouted anchor bolts with a modified numerical simulation method. *Eng. Fail. Anal.* 106640. doi:10.1016/j.engfailanal.2022.106640

Feng, Y., and Kang, H. (2013). The initiation of I-II mixed mode crack subjected to hydraulic pressure in brittle rock under compression. *J. China Coal Soc.* 38 (02), 226–232.

Feng, Y. (2013). *Research and application of fracture propagation mechanism of hydraulic fracturing in hard and difficult roof of coal mine*. Beijing: Graduate School of China Coal Research Institute.

Gao, F. (2021). Influence of hydraulic fracturing of strong roof on mining-induced stress-insight from numerical simulation. *J. Min. Strata Control Eng.* 3.

Gao, F., Kang, H., and Li, J. (2021). Numerical simulation of fault-slip rockbursts using the distinct element method. *Tunn. Undergr. Space Technol.* 110, 103805. doi:10.1016/j.tust.2020.103805

Gao, F., Stead, D., and Coggan, J. (2014). Evaluation of coal longwall caving characteristics using an innovative UDEC Trigon approach. *Comput. Geotechnics* 55, 448–460. doi:10.1016/j.compgeo.2013.09.020

Guo, X., Zhao, Z., Gao, X., Wu, X., and Ma, N. (2019). Analytical solutions for characteristic radii of circular roadway surrounding rock plastic zone and their application. *Int. J. Min. Sci. Technol.* 29, 263–272. doi:10.1016/j.ijmst.2018.10.002

Guo, Y., Yang, C., Jia, C., Xu, J., Wang, L., and Li, D. (2014). Research on hydraulic fracturing physical simulation of shale and fracture characterization methods. *Chin. J. Rock Mech. Eng.* 33 (01), 52–59.

Hou, Z., Yang, C., Wang, L., and Lei, P. (2016). *Hydraulic fracture propagation of shale horizontal well by large-scale true triaxial physical simulation test*, 37. Chongqing: Rock and Soil Mechanics.

Jia, C., and Hu, C. (2020). Instability mechanism and control technology of longwall entries driving along the gob in a thick coal seam. *J. Min. Strata Control Eng.* 2 (4), 38–45.

Jiang, L., Wang, P., Zhang, P., Zheng, P., and Xu, B. (2017). Numerical analysis of the effects induced by normal faults and dip angles on rock bursts. *Comptes Rendus Mécanique* 345, 690–705. doi:10.1016/j.crme.2017.06.009

Jiang, L., Zhang, P., Chen, L., Hao, Z., Sainoki, A., Mitri, H. S., et al. (2017). Numerical approach for goaf-side entry layout and yield pillar design in fractured ground conditions. *Rock Mech. Rock Eng.* 50, 3049–3071. doi:10.1007/s00603-017-1277-0

Kang, H., Jiang, P., Wu, Y., and Gao, F. (2021). A combined "ground support-rock modification-destressing" strategy for 1000-m deep roadways in extreme squeezing ground condition. *Int. J. Rock Mech. Min. Sci.* 142, 104746. doi:10.1016/j.ijrmms.2021.104746

Kang, H., Lou, J., Gao, F., Yang, J., and Li, J. (2018). A physical and numerical investigation of sudden massive roof collapse during longwall coal retreat mining. *Int. J. Coal Geol.* 188, 25–36. doi:10.1016/j.coal.2018.01.013

Kang, H., Wu, L., Gao, F., Lv, H., and Li, J. (2019). Field study on the load transfer mechanics associated with longwall coal retreat mining. *Int. J. Rock Mech. Min. Sci.* 124, 104141. doi:10.1016/j.ijrmms.2019.104141

Kang, H., Wu, Y., Gao, F., Jiang, P., Cheng, P., Meng, X., et al. (2016). Mechanical performances and stress states of rock bolts under varying loading conditions. *Tunn. Undergr. Space Technol.* 52, 138–146. doi:10.1016/j.tust.2015.12.005

Kang, H., Yang, J., Gao, F., and Li, J. (2020). Experimental study on the mechanical behavior of rock bolts subjected to complex static and dynamic loads. *Rock Mech. Rock Eng.* 53, 4993–5004. doi:10.1007/s00603-020-02205-0

Kang, H., Yuan, G., Gao, F., and Lou, J. (2021). Experimental study on the performance of different meshes under quasi-static loading. *Rock Mech. Rock Eng.* 55, 249–258. doi:10.1007/s00603-021-02651-4

Li, C., Zuo, J., Xing, S., Du, W., and Chuai, X. (2022). *Failure behavior and dynamic monitoring of floor crack structures under high confined water pressure in deep coal mining: A case study of Hebei*, 139. China: Engineering Failure Analysis.

Lian, X., Zhang, W., Li, C., and Guo, X. (2021). Application of discrete data extreme value distribution in the analysis of mine pressure rule. *Arab. J. Geosci.* 14, 2011. doi:10.1007/s12517-021-08352-0

Liu, H., Guo, L., and Zhao, X. (2020). Expansionary evolution characteristics of plastic zone in rock and coal mass ahead of excavation face and the mechanism of coal and gas outburst. *Energies* 13, 984. doi:10.3390/en13040984

Lu, C.-P., Dou, L.-M., Zhang, N., Xue, J.-H., Wang, X.-N., Liu, H., et al. (2013). Microseismic frequency-spectrum evolutionary rule of rockburst triggered by roof fall. *Int. J. Rock Mech. Min. Sci.* 64, 6–16. doi:10.1016/j.ijrmms.2013.08.022

Lu, C.-P., Liu, G.-J., Liu, Y., Zhang, N., Xue, J.-H., and Zhang, L. (2015). Microseismic multi-parameter characteristics of rockburst hazard induced by hard roof fall and high stress concentration. *Int. J. Rock Mech. Min. Sci.* 76, 18–32. doi:10.1016/j.ijrmms.2015.02.005

Ma, N., Ji, M., Zhiqiang, Z., and Xiaofei, G. (2019). Mechanical mechanism and evolution of X-shaped conjugate shear fractures-seism. *J. China Coal Soc.* 44 (6), 1647–1653.

Mondal, D., and Roy, P. N. S. (2019). Fractal and seismic b-value study during dynamic roof displacements (roof fall and surface blasting) for enhancing safety in the longwall coal mines. *Eng. Geol.* 253, 184–204. doi:10.1016/j.enggeo.2019.03.018

Nierobisz, A. (2017). Identification of load to dog heading support during a rockburst. *J. Min. Sci.* 52, 1129–1142. doi:10.1134/s1062739116061662

Ranjith, P. G., Zhao, J., Ju, M., De Silva, R. V. S., Rathnaweera, T. D., and Bandara, A. K. M. S. (2017). Opportunities and challenges in deep mining: A brief review. *Engineering* 3, 546–551. doi:10.1016/j.eng.2017.04.024

Ren, J., Zhang, W., and Ma, J. (2022). Experimental study on butterfly shape of failure zone and fractal characteristics of rock burst. *Eng. Fail. Anal.* 140, 106636. doi:10.1016/j.engfailanal.2022.106636

Shan, R., Li, Z., Wang, C., Wei, Y., Bai, Y., Zhao, Y., et al. (2021). Research on the mechanism of asymmetric deformation and stability control of near-fault roadway under the influence of mining. *Eng. Fail. Anal.* 127, 105492. doi:10.1016/j.engfailanal.2021.105492

Shichang, S., Yongzheng, W., Yukai, F., and Penghao, Z. (2021). Experimental study on shear mechanical properties of anchored rock mass under impact load. *J. Min. Strata Control Eng.* 3 (4), 26–33.

Wang, S., and Li, X. (2017). Dynamic distribution of longwall mining-induced voids in overlying strata of a coalbed. *Int. J. Geomech.* 17 (6), 04016124. doi:10.1061/(asce)gm.1943-5622.0000820

Wang, S., Li, X., and Wang, D. (2016). Void fraction distribution in overburden disturbed by longwall mining of coal. *Environ. Earth Sci.* 75, 151. doi:10.1007/s12665-015-4958-6

Wang, S., Li, X., and Wang, S. (2017). Separation and fracturing in overlying strata disturbed by longwall mining in a mineral deposit seam. *Eng. Geol.* 226, 257–266. doi:10.1016/j.enggeo.2017.06.015

Wang, Y., Tu, M., Fu, B., and Bu, Q. (2020). Study on the distribution of side abutment pressures and ground support for double-used entries in deep mining. *J. Min. Strata Control Eng.*

Wu, Y., Gao, F., Chen, J., and He, J. (2019). Experimental study on the performance of rock bolts in coal burst-prone mines. *Rock Mech. Rock Eng.* 52, 3959–3970. doi:10.1007/s00603-019-01794-9

Wu, Y., and Kang, H. (2017). Pressure relief mechanism and experiment of directional hydraulic fracturing in reused coal pillar roadway. *J. China Coal Soc.* 42 (5), 1130–1137.

Xie, J., Xu, J., and Wang, F. (2018). Mining-induced stress distribution of the working face in a kilometer-deep coal mine—A case study in tangshan coal mine. *J. Geophys. Eng.* 15, 2060–2070. doi:10.1088/1742-2140/aabc6c

Xie, L. X., Lu, W. B., Zhang, Q. B., Jiang, Q. H., Chen, M., and Zhao, J. (2017). Analysis of damage mechanisms and optimization of cut blasting design under high *in-situ* stresses. *Tunn. Undergr. Space Technol.* 66, 19–33. doi:10.1016/j.tust.2017.03.009

Xie, S., Pan, H., Zeng, J., Wang, E., Chen, D., Zhang, T., et al. (2019). A case study on control technology of surrounding rock of a large section chamber under a 1200-m deep goaf in Xingdong coal mine, China. *Eng. Fail. Anal.* 104, 112–125. doi:10.1016/j.engfailanal.2019.05.039

Yang, J. H., Jiang, Q. H., Zhang, Q. B., and Zhao, J. (2018). Dynamic stress adjustment and rock damage during blasting excavation in a deep-buried circular tunnel. *Tunn. Undergr. Space Technol.* 71, 591–604. doi:10.1016/j.tust.2017.10.010

Yongzheng, W. (2018). *Study on de-stressing mechanism of directional hydraulic fracturing to control deformation of reused roadway in longwall mining with two gateroad layout and its onsite practices*. Beijing: Graduate School of China Coal Research Institute.

Yuanjie, W., Gang, X., Fabing, C., and Yangpo, L. (2022). Mining pressure weakening mechanism by ground fracturing and fracturing evaluation of hard rock strata. *J. Min. Strata Control Eng.* 4 (2), 15–23.

Zhang, W., Li, C., Jin, J., Qu, X., Fan, S., and xin, C. (2021). A new monitoring-while-drilling method of large diameter drilling in underground coal mine and their application. *Measurement* 173, 108840.

Zhang, W., Ma, N., Ma, J., Li, C., Ren, J., and Jiang, B. (2020). Mechanism of rock burst revealed by numerical simulation and energy calculation. *Shock Vib.* 2020, 1–15. doi:10.1155/2020/8862849

Zhang, W., Qu, X., Li, C., Xu, X., Zhang, S., Jin, G., et al. (2019). Fracture analysis of multi-hard roofs based on microseismic monitoring and control techniques for induced rock burst: A case study. *Arab. J. Geosci.* 12, 784. doi:10.1007/s12517-019-4972-1

Zhao, K., Jiang, P., Feng, Y., and Sun, X. (2021). Investigation of the characteristics of hydraulic fracture initiation by using maximum tangential stress criterion. *J. Min. Strata Control Eng.*

Zhao, Z. (2014). *Mechanism of surrounding rock deformation and failure and control method research in large deformation mining roadway*. Beijing): China University of mining and technology.

Zhu, S., Jiang, F., Wang, X., Jiang, Y., Ning, T., and Sun, S. (2019). Energy accumulation characteristics and rockburst mechanism of surrounding rock at heading face of extra-thick coal seam. *Chin. J. Geotechnical Eng.* 41 (11), 2071–2078.

Ziyi, F., Yongliang, L., Hao, S., and Xiaolei, C. (2022). Characteristics and control measures of unsymmetric deformation of roadways within weakly-cemented soft rock. *J. Min. Strata Control Eng.* 4 (2), 44–53.

frontiers | Frontiers in Earth Science

TYPE Original Research
PUBLISHED 12 January 2023
DOI 10.3389/feart.2022.1062738

OPEN ACCESS

EDITED BY
Fangtian Wang,
China University of Mining and Technology, China

REVIEWED BY
Bangyou Jiang,
Shandong University of Science and Technology, China
Xuejie Deng,
China University of Mining and Technology Beijing, China

*CORRESPONDENCE
Leiming Zhang,
zhangleiming@stu.xust.edu.cn

SPECIALTY SECTION
This article was submitted to Structural Geology and Tectonics, a section of the journal Frontiers in Earth Science

RECEIVED 06 October 2022
ACCEPTED 31 October 2022
PUBLISHED 12 January 2023

CITATION
Zhang L, Lai X and Bai R (2023), Study of the response characteristics of the water–force coupling action of hard coal bodies in steeply inclined coal seams.
Front. Earth Sci. 10:1062738.
doi: 10.3389/feart.2022.1062738

Study of the response characteristics of the water–force coupling action of hard coal bodies in steeply inclined coal seams

Leiming Zhang[1,2]*, Xingping Lai[1,2] and Rui Bai[3]

[1]School of Energy Engineering, Xi'an University of Science and Technology, Xi'an, China, [2]Key Laboratory of Western Mines and Hazards Prevention, Ministry of Education of China, Xi'an, China, [3]National Energy Group Ningxia Coal Industry Co., Ltd. Qingshuiying Coal Mine, Lingwu, China

Study of the pre-blast weakening of hard-top coal water injection is especially important to solve problems related to the low recovery rate of coal resources and frequent dynamic disasters due to the low degree of fragmentation of hard-top coal during high-stage fully mechanized top-coal caving in steeply inclined coal seams. With the application of rock mechanical tests and numerical simulations, this study carries out mechanical property testing on natural and water-saturated coal samples, investigates the effect of moisture on coal sample mechanical properties in meso-scale, and quantifies the degradation of coal samples under moisture due to mollification. It also reveals the interaction between water and acoustic emission signals based on the statistics of acoustic emission count and energy. A numerical model is established to analyze coal sample internal stress distribution features before and after water injection in macro-scale. Moreover, the detailed mitigating measures for top-coal water injection for engineering practice are designed. The results demonstrate that the mechanical properties of coal samples are significantly affected by moisture-induced degradation. The failure and collapse degrees of water-saturated samples are generally larger than those of natural samples. When the water content is higher, the acoustic emission count and energy of the coal sample are smaller—presenting a negative correlation. The internal stress of coal samples before and after water injection differs significantly. When subjected to water, the top-coal stress releases and transfers, and the peak value is significantly reduced. This study has verified in macro- and meso-scales that top coal can be fully weakened under water–force coupling. The findings of this study are of practical significance for safe and efficient mining and provide a reference for presplit weakening of hard-top coal during horizontal sublevel fully mechanized top-coal caving in steeply inclined coal seams.

KEYWORDS

top-coal presplit, fully mechanized caving mining, coupling effect, water-injection weakening, steeply inclined coal seams

Introduction

Coal will remain the main integral energy in China for a long time. The Urumqi mining area in the west of China is rich in coal resources and is a strategic energy reserve area (Qian, et al., 2018; Zhang, et al., 2020; Lai, et al., 2022). However, the Urumqi mining area typically has 45°–87° steeply inclined coal seams, and consequently the mining process and technology of this steep lamination are very complex. High-stage horizontal sublevel fully mechanized caving mining is mostly adopted in current practice (Shi and Gao, 2003; Wang, 2018; Lai, et al., 2020; Wu, et al., 2020). Along with the mining process, problems such as the low degree of hard-top coal breakage and difficulty in releasing from the coal outlet are increasingly becoming prominent. This results in low top-coal recovery rate and the collapse of top coal in the goaf, which can easily induce a dynamic disaster. This seriously restricts the safe and efficient mining of these mines. Therefore, an investigation of advanced pre-crack weakening technology for the hard-top coal of steeply inclined coal seams is urgently required.

In recent years, many scholars at home and abroad have carried out a lot of basic theoretical research on the pretreatment and weakening technology of the hard-top coal of steeply inclined coal seams. In terms of the special occurrence features of steeply inclined coal seams, Ju et al. (2006) studied the appearance law and dynamic pressure influence characteristics of steeply inclined coal seams in Huating Coal Mine. Dai et al. (2006) applied the similarity simulation method to reveal the characteristics and laws of strata and surface movement induced by deep mining of steeply inclined coal seams. Li (2018) proposed a technical scheme and implementation approach of fully mechanized caving mining in a hard extra-thick seam in the Yushen Mining Area. Wu and Shi (1990) discussed the release rule and mine pressure development rule of top coal that is broken by the steep seam using a simulation test rack. Lai et al. (2009) investigated a roof collapse during the mining of steeply inclined coal seams in Weihuliang Coal Mine and effectively prevented the occurrence of a dynamic disaster. Meanwhile, pre-cracking technology of hard-top coal in a fully mechanized caving face has also been investigated. Xie et al. (1999) and Wang et al. (2000) discussed a pre-loosening blasting crushing technical scheme in a hard-thick seam and proved its good performance in application. Deng et al. (2004) investigated the mechanism of fracture development and propagation in coal samples during the water–force coupling fracturing process and conducted experiments on the relationship between fracture initiation and propagation of a coal sample under water pressure and the permeability of the coal sample, revealing the mechanical mechanism of hydraulic coal breaking. Suo (2001) implemented a comprehensive weakening method of pre-water injection and deep-hole blasting in a hard-top coal workface at Honghui No.1 Mine, which effectively solved the problem of large caving blocks in the top coal. Aiming at the special conditions of a hard seam at Datong Yungang Coal Mine, Yang (2014) adopted the combined weakening measure of water injection-explosion to fully combine the respective advantages of water injection and blasting measures. A set of weakening methods and measures suitable for a fully mechanized caving hard-top coal workface have been proposed. For example, Cui et al. (2015) studied steep ultra-thick coal rock, and designed and implemented a coupling–cracking scheme for steeply inclined coal seams. Their field practice results show that, after taking the coupling–cracking measurement, the cavitability, fragmentation degree, and recovery rate of top coal were significantly improved and the frequency of dynamic disasters was significantly reduced.

These scholars have actively explored and studied mining pressure development, mining technology, and pre-crack weakening technology for steeply inclined coal seams but mainly focused on the design parameter and scheme optimization of the pre-crack weakening scheme of hard-top coal. From these studies, it can also be found that whether using single water injection weakening or water injection-blasting coupled pre-blast weakening, it is clear that water-injection treatment is a key and necessary measure in the process of pre-blast weakening. Meanwhile, the occurrence of steeply inclined coal seams is more complicated. There is no research on the pre-blast and weakening technology for the hard-top coal of steeply inclined coal seams. In particular, the weakening-damage features of water-injection weakening and the response relationship between water injection and stress need to be studied further. In view of this, the authors took the north mining area of the Wudong Coal Mine as the background. Rock mechanics test and numerical calculation were used to study the response features of steeply inclined coal seams in the water–force coupling at macro- and micro-scales. The stress distribution law of the coal sample and the strength degradation and destruction of a coal sample under moisture-induced degradation are investigated. A specific top coal water-injection weakening scheme was proposed based on the actual situation in the field to provide rational guidance for the pre-blast and weakening of hard-top coal during horizontal sublevel fully capped caving in steeply inclined coal seams with similar conditions.

Engineering background

Wudong Coal Mine is located in Midong District, Urumqi City, Xinjiang, which is located on the border of Bogda Mountain and Jungar Basin, with a mine field area of about 20 km^2. The coal seams' dip angle in the mine's north mining area is 43°–51°, which means that they are steeply inclined coal seams. Currently, 43# and 45# coal seams are mainly mined. The average thickness of the two coal seams is 28.28 m and 21.21 m, respectively, and the dip angles are both 45°. The coal seam structure is simple and contains a small amount of carbonaceous mudstone or siltstone intercalated gangue. The occurrence characteristics of coal seams in the north mining area of the mine are shown in Figure 1.

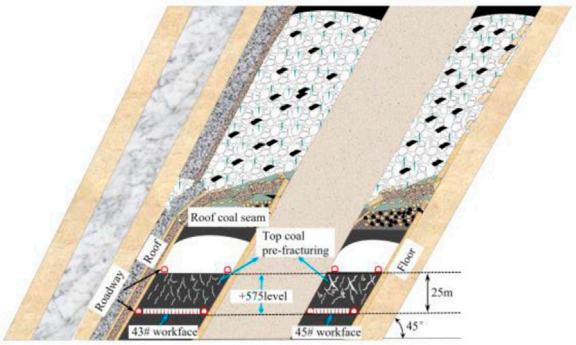

FIGURE 1
Occurrence characteristics of coal seams in the north mining area of Wudong Coal Mine.

The mine adopts the horizontal sublevel fully mechanized caving mining method. At present, the mining has been advanced to +575 level 43# and 45# seams in the north mining area. The workface has average widths of 33 m and 30.6 m, and the height of the design phase is 25 m. In the on-site mining and caving process, hard-top coal cannot be fully broken under the action of mine pressure and support disturbance, which leads to a large block size that exceeds the coal drawing port size and often causes plugging. This results in low recovery rate of the top coal, poor economic benefits, and is a serious threat to safety in production. Therefore, in the case of horizontal sublevel fully mechanized caving mining in this seam, a reasonable measurement should be adopted to pre-blast and weaken the hard-top coal so as to improve the caving ability of the top coal.

Coal sample physical and mechanical parameters test plan

Test protocol and sample preparation

The coal samples required for this test were taken from the +575 level 43# coal and 45# coal working faces in the north mining area of Wudong Coal Mine. According to the test requirements and the national standard "Method for Determination of Physical and Mechanical Properties of Coal and Rock," it is processed into Φ50 mm × 100 mm, Φ50 mm × 50 mm, and Φ 50 mm × 25 mm standard cylindrical samples. The machining accuracy is that the non-parallelism of the two ends is ≤0.05 mm, the diameter deviation of the upper and lower ends is ≤0.3 mm, and the axial deflection angle is ≤0.25°. The surface of the sample is smooth and defect-free.

To fully understand the physical and mechanical parameters, and the degradation of the steep coal sample under the effect of water, this test comprised 12 groups. Uniaxial length test, tensile test, and variational shear test on natural and water-saturated samples were carried out, and five samples were prepared for testing in each group to eliminate individual errors. The seam number rules and schemes are listed in Table 1, where 43-and 45-are samples of 43# and 45# seams, respectively. The state of the specific coal sample is treated as follows:

1) Natural state sample: Put the sample in a desiccator with water at the bottom. The bottom of the sample should be 20 mm above the water surface to maintain a certain humidity.
2) Water-saturated sample: The free soaking method was used, where the sample was put inside a container and water was added three times, with an interval of 2 h each time until the water surface was 20 mm higher than the specimen. After being soaked for 48 h, the sample was taken out of the container and the surface moisture was wiped dry. The sample was defined as a water-saturated sample and wrapped with plastic wrap for the experiment.

According to the physical parameters of the coal samples, the average densities of the 43# and 45# seams in Wudong Coal Mine are 1,315.03 kg/m^3 and 1,317.37 kg/m^3, and the average wave velocities are 1,513 m/s and 1,538 m/s, respectively. The average natural absorption rates of seams of 43# and 45# coal samples are 2.67% and 2.73%, respectively.

Test system

The uniaxial axial strength of the coal sample was determined by the SAS-2000 single triaxial rock mechanical loading system,

TABLE 1 Specimen use and size.

Usage	Number	Water-contained state	Diameter/mm	Height/mm	Quantity
Uniaxial compressive test	C43-1~5, C45-1~5	Nature	50	100	20
	C43-6~10, C45-6~10	Saturate			
Tensile strength test	T43-1~5, T45-1~5	Nature	50	25	20
	T43-6~10, T45-6~10	Saturate			
Variable angle shear test	S43-1~4, S45-1~4	Nature	50	50	20
	S43-5~10, S45-5~10	Saturate			

FIGURE 2
Test system diagram.

which can monitor the axial and radial strain at the same time. The DS5 multi-channel acoustic emission system is equipped to monitor the acoustic emission signal generated in the compression process of the coal sample in real-time, including rising count, amplitude, and energy. The sample frequency was set at 1 MHz, the acoustic emission signal detection threshold was set at 40 dB, and two AE sensors were fixed in the middle of the sample. The tensile and shear strengths were measured by using the HCT-605A tester. The test system is shown in Figure 2.

Coal sample test results and analysis

Analysis of uniaxial compression test results

In this study, uniaxial compressive tests were carried out on the coal samples with different moisture conditions taken from 43# seam and 45# seam. The detailed compressive strength and deformation parameters were obtained, and the mean values were taken for further analysis. As can be observed in the test results in Table 2, the uniaxial compressive strengths of samples of 43# and 45# seams degraded by 19.6% and 17.4%, respectively, under the influence of moisture. The elastic moduli of both samples were 15.3% under the influence of moisture.

Figure 3 shows the stress–strain curves of the experimentally obtained data. As indicated, coal samples of 43# and 45# seams of Wudong Coal Mine exhibited consistent stress–strain curves. The curves consisted of compaction stage, elastic stage, yield failure stage, and post-rupture stage. Coal samples underwent compaction and elasticity stages for a long time before failure. After reaching peak strength, the bearing capacity rapidly decreased (Zhang, et al., 2021; Liu, et al., 2022; Xue, et al., 2022).

Although stress–strain curves of natural and water-saturated coal samples showed the same trend, they were slightly different at the yield stage. The stress of natural coal samples increased continuously with the strain at the yield stage. When the stress reached the ultimate yield strength, the specimen did not fail immediately but demonstrated an abrupt reduction before growth as the strain kept increasing. During the experiment, it was observed that the sample was still able to bear the load despite the generation of the fracture, but the outer layer was broken and fell off, similar to wall caving. When subjected to continuous loading, the failure plane occurred and developed along the fracture of the specimen and continued until the end of the experiment. The water-consume-saturated coal samples had a relatively short yield stage and immediately failed upon reaching the ultimate strength, which was closely related to the existence of water. This happened because the secondary extension of fracture was blocked due to pore pressure and the incompressibility of fracture water. Finally, the specimen failed rapidly, which was accompanied by significant strength decline (Yao, et al., 2015; Lai, et al., 2021; Zhang, et al., 2021).

As shown in Figure 3, under uniaxial loading, natural coal samples mainly displayed a mixed tension–shear failure mode, where the vertical tensile fractures and certain shear fractures were significantly developed inside and the specimens were quite complete after loading. The water-saturated coal samples experienced a penetrating splitting shear failure, with an "X" shaped conjugate shear failure surface inside. The overall fracture degree of the samples was higher, and the crack propagation was more abundant.

The experimental results demonstrate that moisture-induced degradation was significant, which caused softening of the coal sample because of the reduction in the cohesion between fracture particles under the influence of water. In particular, the peak strength and elastic modulus of the samples presented a downward trend and the overall mechanical properties were weakened.

TABLE 2 Test results of compressive strength and deformation parameters of 43# and 45# coal seam in Wudong Coal Mine.

Number	Water-contained state	Average uniaxial compressive strength/MPa	Average elastic modulus/GPa	Average Poisson's ratio
C43	Nature	13.81	1.317	0.324
	Saturate	11.10	1.115	0.384
C45	Nature	13.59	1.324	0.328
	Saturate	11.22	1.122	0.383

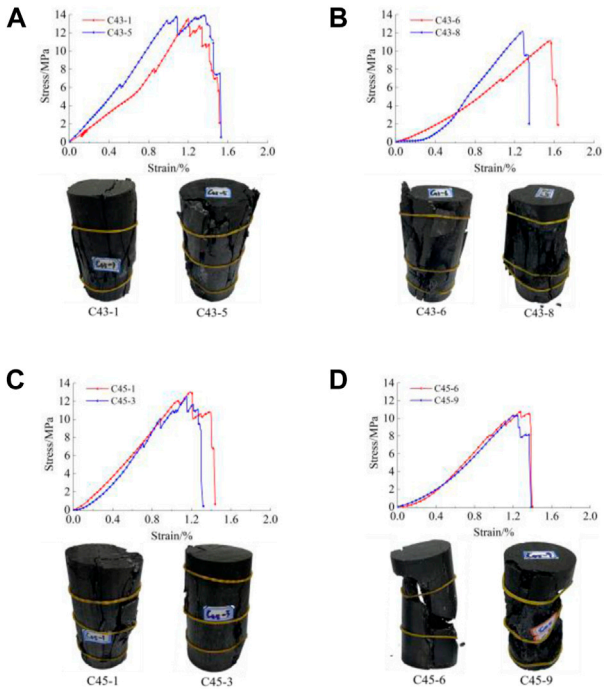

FIGURE 3
Typical uniaxial compression stress–strain curves and failure characteristics of 43# and 45# coal samples under natural and water saturation conditions. **(A)** Natural state of 43# coal samples. **(B)** Water-saturated state of 43# coal samples. **(C)** Natural state of 45# coal samples. **(D)** Water-saturated state of 45# coal samples.

Comparing the failure patterns of natural and water-saturated coal samples shows that the failure and broken blocks of water-saturated coal samples were generally more serious than those of natural samples. Therefore, in the implementation of the top-coal pre-blast scheme, water injection can soften the top coal in advance and change the crushing degree of the hard-top coal, which is of practical significance in terms of reducing the fragment size of the top coal and improving the recovery rate.

Analysis of the tensile strength test results

The results of the tensile strength test are shown in Table 3. The average tensile strengths of natural and water-saturated coal samples in 43# seam are 1.467 and 1.105 MPa, respectively. Meanwhile, the average tensile strengths of natural and water-saturated coal samples in 45# seam are 1.459 and 1.127 MPa, respectively. Moisture has a significant impact on the tensile strength of the coal samples. In particular, the tensile strengths of the coal samples obtained from 43# and 45# seams degraded by 24.68% and 22.76%, respectively, due to the softening effect of the water.

TABLE 3 Wudong Coal Mine 43#, 45# seam tensile strength test results.

Number	C43		C45	
Water-contained state	Nature	Saturate	Nature	Saturate
Average tensile strength/MPa	1.467	1.150	1.459	1.127

Figure 4 illustrates the fracturing features of the coal samples. In the Brazilian splitting experiment, an approximately vertical failure surface was generated along the primary joint of the coal sample, and the sample split into two halves along the failure surface. The main failure plane developed along the internal joints of the water-saturated coal sample, fracturing occurred locally, and the degree of fragmentation was significant.

Analysis of the shear strength test results

The shear strength test results of natural and water-saturated coal samples are shown in Table 4. According to the test results,

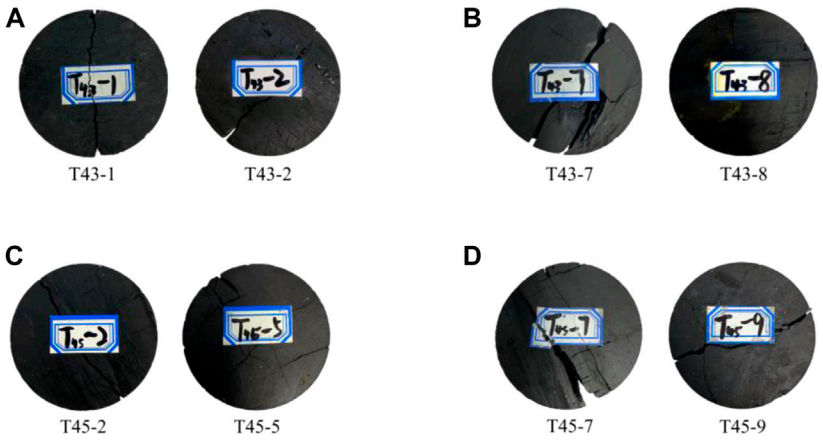

FIGURE 4
Typical coal samples splitting failure characteristics of 43# and 45# coal samples under natural and water-saturated conditions. **(A)** Natural state of 43# coal samples. **(B)** Water-saturated state of 43# coal samples. **(C)** Natural state of 45# coal samples. **(D)** Water-saturated state of 45# coal samples.

TABLE 4 Wudong Coal Mine 43#, 45# seam shear strength test results.

Number	Shear angle	P_s/ kN	σ/ MPa	τ/ MPa	Number	Shear angle	P_s/ kN	σ/ MPa	τ/ MPa
S43-1	60	5.654	1.124	1.947	S43-6	30	39.312	13.588	7.845
S43-2	60	7.044	1.412	2.446	S43-7	30	44.504	15.313	8.841
S43-3	45	21.130	5.960	5.960	S43-8	45	12.333	3.457	3.457
S43-4	45	29.779	8.332	8.332	S43-9	45	19.971	5.639	5.639
S43-5	60	3.688	6.387	6.040	S43-10	45	13.450	3.789	3.789
S45-1	45	17.813	5.026	5.026	S45-6	60	5.170	1.026	1.777
S45-2	30	63.562	21.882	12.633	S45-7	60	6.139	1.230	2.130
S45-3	30	69.569	24.257	14.005	S45-8	30	45.185	15.532	8.967
S45-4	30	65.835	22.827	13.179	S45-9	30	26.564	9.140	5.277
S45-5	60	9.511	1.921	3.328	S45-10	60	8.858	1.761	3.051

normal stress and shear stress were obtained by substituting the failure load Ps of the coal sample when it was cut into halves into Eqs 1, 2. The regression curves of normal stress and shear stress of natural and saturated coal samples under different shear angles were obtained by fitting, and Eq. 3 was used to calculate the angle of internal friction and cohesion C of coal samples (test data S43-5 and S45-9 with larger deviations were eliminated in the fitting process). The fitting results are shown in Figure 5.

$$\sigma = \frac{P_s}{A}\left(\cos\alpha + f\sin\alpha\right) \quad (1)$$

$$\tau = \frac{P_s}{A}\left(\sin\alpha - f\cos\alpha\right) \quad (2)$$

$$\tau = \sigma\tan\varphi + C \quad (3)$$

In this formula, σ is the normal stress, MPa; τ is the shear stress, MPa; P_s is the failure load of the sample, N; A is the contact area, mm^2; α is the sample placement angle, °; f is the friction coefficient of the roller, f =1/nd, n is the number of rollers; d is the diameter of the roller, mm; φ is the internal friction angle of the coal sample, °; and C is the cohesive force of the coal sample, MPa.

According to Figure 5, the shear stress along the shear plane of natural and water-saturated coal samples before failure increases with the normal stress. The cohesion of the two coal samples was 2.522 Mpa and 2.007 Mpa, respectively, and the

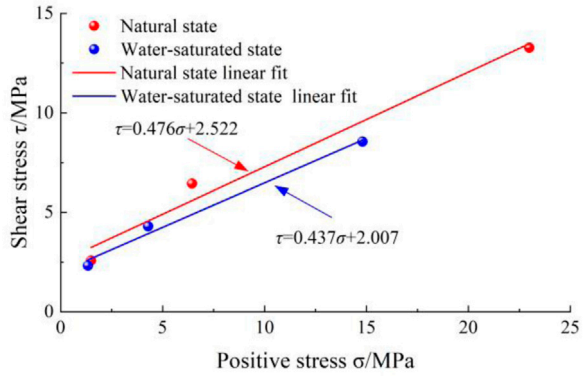

FIGURE 5
Shear strength curve of the coal samples.

degradation degree was 20.4%. The internal friction angles were 25.5° and 23.6°, respectively, and the deterioration degree was 7.5%. Hence, it could be concluded that moisture led to a severe degradation of the shear strength of the coal sample. Figure 6 shows the shear failure features of natural and water-saturated coal samples. As observed, both coal samples experienced shear failure along the shear plane, and the distributions of failure cracks on the surface were slightly different due to the different moisture conditions. The shear fractures of natural coal samples were mainly found near the shear plane, and the samples were mostly broken into halves along the shear plane, with a low degree of fragmentation. The shear surface of water-saturated coal samples sometimes deviated from the shear plane, and multiple shear fractures occurred near the shear surface, with a plentiful and high degree of fragmentation.

Analysis of acoustic emission characteristics

The acoustic emission signal was generated during the uniaxial loading on the coal sample. Based on the analysis of rising count and energy parameter, the acoustic emission evolution law and micro-failure features of the coal sample during loading were used to investigate acoustic emission features of natural and water-saturated coal samples. Specialized software was used to process acoustic emission parameters, such as rising count, accumulated rising count, and energy and accumulated energy, and the acoustic emission features of the coal sample under water–force coupling effect were analyzed (Qin, et al., 2012; Xia, et al., 2015; Zhang Y, et al., 2018). The rising count refers to the number of times that the acoustic emission signal exceeded the set detection threshold (40 dB), reflecting the number of microfractures inside the sample. Energy refers to the elastic energy released by the internal micro-fracture development of the coal sample, reflecting the degree of fragmentation. The acoustic emission and testing machine time were normalized during data processing to facilitate their synchronous analysis.

Figure 7 shows the stress, rising count, accumulated rising count, stress, energy, and accumulated energy curves under uniaxial loading of natural and water-saturated coal samples in +575 level in the north mining area in Wudong Coal Mine. As

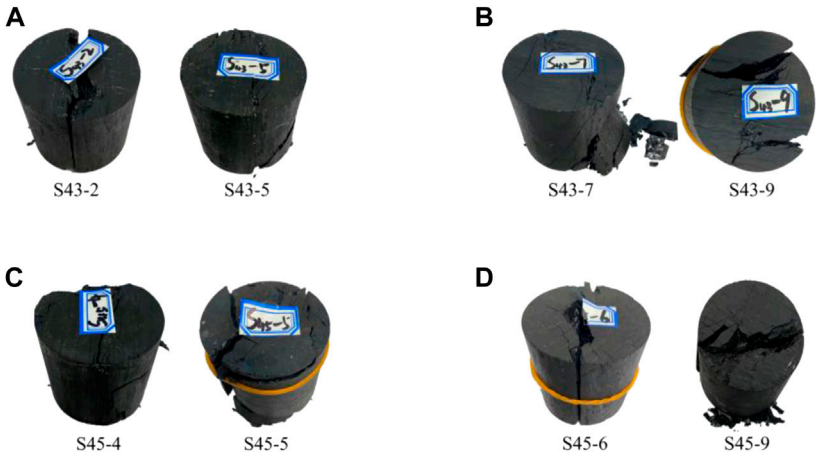

FIGURE 6
Typical coal shear failure characteristics of 43# and 45# coal samples under natural and water-saturated conditions. **(A)** Natural state of 43# coal samples. **(B)** Water-saturated state of 43# coal samples. **(C)** Natural state of 45# coal samples. **(D)** Water-saturated state of 45# coal samples.

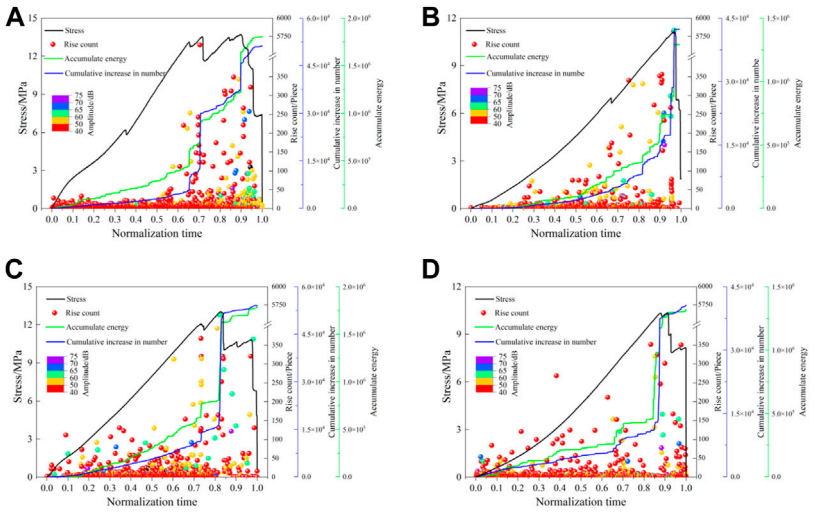

FIGURE 7
Typical coal AE characteristics of 43# and 45# coal samples under natural and water-saturated conditions. **(A)** AE characteristics in natural state of C43-5. **(B)** AE characteristics in water-saturated state of C43-6. **(C)** AE characteristics in natural state of C45-1. **(D)** AE characteristics in water-saturated state of C45-9.

observed, the acoustic emission features of natural and water-saturated samples in 43# and 45# seams did not differ much, and the acoustic emission count of each significantly increased before the peak load was achieved. Furthermore, the accumulated rising count and accumulated energy showed sharp growth, which happened because the internal fracture of the sample developed continuously and the elastic energy kept releasing at the elastic stage. Meanwhile, we found that there were differences in the details of the natural and water-saturated samples. The accumulated rising count and accumulated energy of the water-saturated samples were lower than those of natural samples. In addition, the moisture condition had a negative correlation with the acoustic emission count and energy of the coal sample (i.e., when the water content was higher, the acoustic emission count and energy became lower). This happened because the initiation and propagation of the fracture were hindered by the existence of incompressible water in fractures of the water-saturated coal samples. In addition, the absorption of the acoustic emission signal from moisture and the attenuation and disappearance of micro-elastic wave generated during the fracture development resulted in the inability to detect an acoustic emission signal due to the overly low amplitude. By statistical calculation, the low amplitude events (40–45 dB) of the natural samples obtained from 43# and 45# seams accounted for 76.43% and 72.58% of the total events, while in water-saturated samples, the percentages were 66.89% and 61.33%, respectively. This further verifies the absorption and inhibition effect of moisture on weak acoustic emission signals.

Stress distribution law of a coal body under water deterioration

In the horizontal sub-mining process of steeply inclined coal seams, the stress distribution in the top coal will change because of the collapse evolution of the roof and energy release, as well as the moisture-induced degradation. In this section, a numerical calculation model will be established, and the physical and mechanical parameters of 43# and 45# coal samples in natural and saturated state obtained from experiments will be used to investigate the stress variation laws before and after water injection. The mechanism of water injection to weaken the coal body will be further elaborated, and the top coal stress distribution features in steeply inclined coal seams after water injection will be studied to reveal the coupling characteristics of water–force coupling features in horizontal sublevel fully mechanized caving mining for the hard-top coal of steeply inclined coal seams.

3D numerical model construction and mining plan

FLAC^{3D} is widely used in the research and analysis of geotechnical and mine excavation projects because it can better simulate deformation problems such as stress, deformation, and displacement caused by excavation activity or external load disturbance. The FLAC^{3D} numerical calculation model of steep seam workface mining was established based on the geological data and the parameters of the north mining area of Wudong

TABLE 5 Physical and mechanical parameters of the main coal rocks in the northern mining area of Wudong Coal Mine.

Lithology	Bulk modulus/GPa	Shear modulus/GPa	Tensile strength/MPa	Friction angle/(°)	Cohesion/MPa	Density kg/m^3
Loess layer	0.45	0.44	0.30	22	5.42	1790
Ovulocyte layer	6.17	4.50	0.96	24	6.22	2,500
Siltstone	15.85	10.95	3.89	30	11.62	2,600
Fine sandstone	19.57	14.07	3.17	30	13.38	2,600
43# coal	**1.25**	**0.50**	**1.47**	**25.5**	**2.52**	**1,315**
43# coal full of water	**1.60**	**0.40**	**1.15**	**23.6**	**2.01**	**1,367**
45# coal	**1.28**	**0.50**	**1.46**	**25.5**	**2.52**	**1,317**
45# coal full of water	**1.60**	**0.41**	**1.13**	**23.6**	**2.01**	**1,354**
Carbonaceous peat	4.50	2.20	1.86	28	2.75	2,400
Argillaceous chalkstone	8.12	3.40	1.71	26	3.60	2,100

The bold values are the result of the previous rock mechanics tests, so they are specifically indicated for ease of distinction.

Coal Mine, which were collected by field investigation. The physical and mechanical parameters of the coal seams were obtained by a rock mechanics experiment. The specific parameters are shown in Table 5.

The mining sequence of 45# coal seam and 43# coal seam was simulated according to the historical mining sequence of the north mining area of Wudong Coal Mine. The numerical model was established until the surface with the size of 600 m × 350 m × 96 m (L × W × H), and the total of 128,020 elements and 135,681 nodes were divided. The numerical calculation model of the north mining area of Wudong Coal Mine is shown in Figure 8. The displacement boundary was applied to both sides and the bottom of the model, while displacement was free in the vertical direction. It should be noted that the stress field in the north mining area of Wudong Coal Mine plays a dominant role in horizontal tectonic stress. The maximum main stress was about 1.5–2 times larger than the gravitational stress, the gradient crustal stress of 0.025 MPa/m was applied in the vertical direction of the model, and the gradient crustal stress of 0.05 MPa/m was applied in the left-hand and right-hand directions (dip) and the front and back directions (strike), respectively.

According to the historical mining sequence, each level of steeply inclined coal seams was excavated in stages, and the survey lines were arranged along the strike in the top coal seam of 43# and 45# seams to extract the vertical stress of the top coal in the process of excavation. The top-coal stress distribution before and after water injection and mining in 43# coal seam and 45# coal seam at +575 level was analyzed.

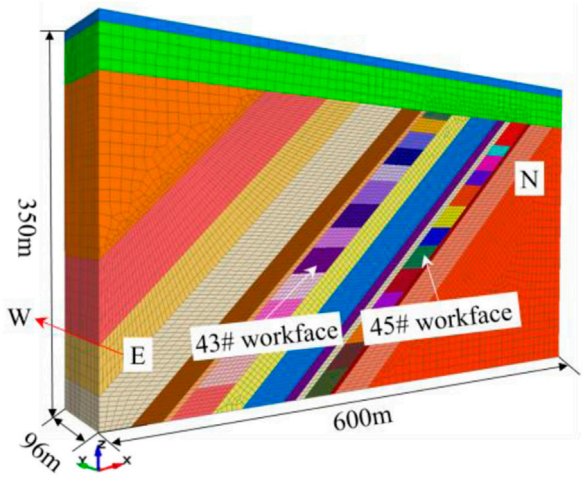

FIGURE 8
Numerical calculation model of Wudong Coal Mine North Mining Area.

Numerical calculation results and analysis

Figure 9 illustrates the vertical stress of different seams. As observed, the internal stress of 45# and 43# seams before and after water injection differed greatly: the maximum vertical stresses of 45# seam, which was located in the south upper corner, were 11.7 MPa and 7.21 MPa before and after water injection, respectively; the maximum vertical stresses of 43# seam, which was also located in the south upper corner, were 13.9 MPa and 8.47 MPa before and after water injection, respectively. This indicates that water injection caused the maximum stress to transfer downward, and the stress concentration area was significantly reduced with more uniform distribution. According to the internal stresses of the coal samples obtained from 43# and 45#, the stress of 43# seam was slightly larger than that of 45# seam. This happened because the force of the 43# coal seam roof on the 43# coal seam was larger than the force of the middle rock column on the upper left-hand of the 45# coal seam.

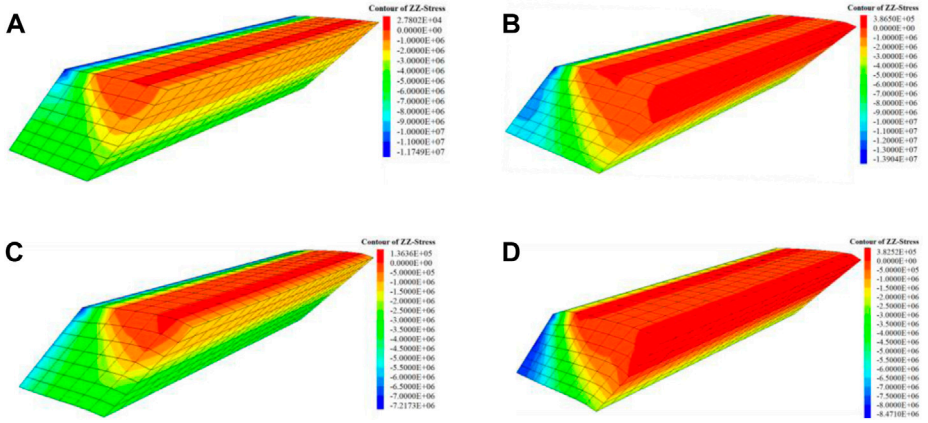

FIGURE 9
+575 level 45#, 43# coal seam stress distribution characteristics. **(A)** No water injection in 45#coal. **(B)** No water injection in 43#coal. **(C)** Water injection in 45#coal. **(D)** Water injection in 43#coal.

To quantitatively study the change of the internal stress and workface advanced support pressure of the top coal after water injection, two measuring points were arranged in the central position of the 45# and 43# seams along the advancing direction (y = 48 m and 96 m) to monitor the evolution law of the top-coal stress with the advancing degree. The measuring line was arranged in the middle of the floor of the 45# and 43# seams along the advancing direction to monitor the workface advanced support pressure. The stress evolution law of the internal measurement point of the top coal and the bottom plate of the 45# and 43# top coal is shown in Figure 10.

As observed in Figures 10A,B, the top-coal internal stress was significantly reduced after water injection. This indicates that top coal was fully weakened. As the advance continued, the vertical stress of each monitoring site presented an increasing trend, except for the advance at 28.8–38.4 m and 76.8–86.4 m with reduced stress. This happened because under this advancement, the monitoring sites had already reached within the reduction zone of advanced support pressure. Additionally, the top-coal stress of 43# seam was lower than that of 45# seam. This happened because 45# coal seam was first mined at the +575 level, and the mining in 45# coal seam played a similar role as mining in the protective layer in 43# coal seam, which effectively released the top-coal stress of 43# seam. Therefore, it not only improved the release rate of top coal but also reduced the outburst risk of the seam.

Figures 10C,D shows the evolution laws of floor advanced support pressures of 45# and 43# workfaces. As observed, water injection not only had a great impact on floor advanced support pressure, but it also weakened the peak pressure. Specifically, the peak advanced support pressure of 45# seam after water injection was 50%–65% of that before water injection, while the advanced peak support pressure of 43# seam after water injection was 63%–72% of that before water injection. This further demonstrates the significant weakening effect of water.

Engineering design

According to the occurrence characteristics and actual production conditions of the steeply inclined coal seams of the fully mechanized caving face in the north mining area of Wudong Coal Mine, as well as the aforementioned results, this study found that when implementing the pre-blast scheme for the top coal of the +575 level coal workface in the north mining area of Wudong Coal Mine, the top-coal water-injection weakening measure can be used in advance to improve the crushing degree of the top coal and increase the caving. Therefore, it was designed to implement top-coal water-injection weakening measures 30 m ahead of the north roadway of the 45# coal seam working face at +575 level. The same drill hole was used for water injection and blasting, and high-pressure water was used to fracture the seam. The length of the sealing hole of the water-injection hole was 10 m, and the diameter of the hole was Φ113 mm. The range of water-injection pressure and the amount of water injected are given by the following calculation (Kang, et al., 2004; Zhang Q, et al., 2018; Wang, et al., 2020):

$$P_D = (0.4 - 0.5)H \tag{4}$$

$$P_0 = 156 - \frac{88}{(0.001H + 0.8)} \tag{5}$$

$$T = l \cdot a \cdot h \cdot \gamma \tag{6}$$

$$M_K = K \cdot T \cdot W \tag{7}$$

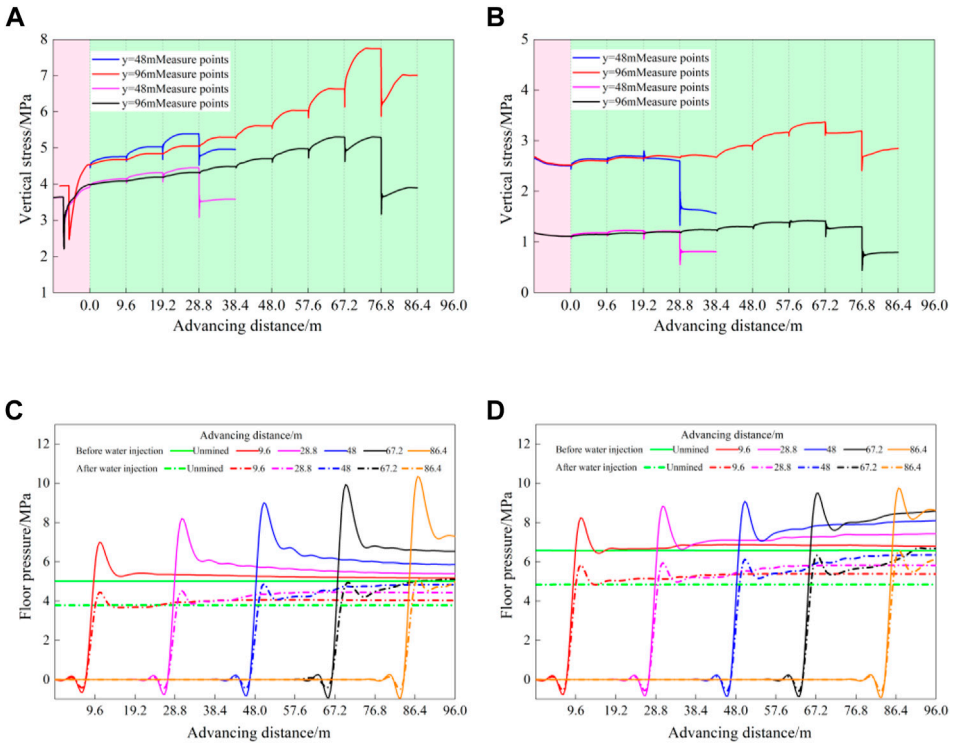

FIGURE 10
Stress evolution law of the internal measurement point of the 45# and 43# top coal and the floor. **(A)** Stress evolution law of 45# top coal. **(B)** Stress evolution law of 43# top coal. **(C)** Stress evolution law of 45# floor. **(D)** Stress evolution law of 43# floor.

In the formula, P_D is the formation pressure of the coal seam, kg/m^2; H is the burial depth of the coal seam, m; P_0 is the minimum pressure of water injection in the coal seam, MPa; l is water-injection length, m, take 20; a is borehole spacing, m, take 5; h is coal seam thickness, m, take 22; γ is coal density, t/m^3, take 1.316; M_K is the water injection amount of a single hole, t; T is the amount of wet coal borne by the borehole, t; W is the water absorption rate of the coal seam, %, to be taken as 2.7; and K is the coefficient of water imbalance, to be taken as 0.5 to 1.0.

The burial depth of the +575 level in the north mining area of Wudong Coal Mine is 260 m. The reference range of coal seam water-injection pressure is obtained by putting H=260 m into Eqs 4, 5 . The calculation results are P_D =10.4–11.7 MPa, P_0 =5.4 Mpa. According to the actual water injection situation of the 45# coal seam working face, the water-injection pressure of the coal seam is determined to be 10 Mpa. According to Eqs 6, 7, the water-injection volume is 39.09 tons.

Conclusion

1) Water-softening had a significant effect on the mechanical properties of the coal samples. Owing to the effect of water-softening, the deterioration degrees of uniaxial compressive strength of 43# and 45# coal seam coal samples were 19.6% and 17.4%, respectively, the deterioration degrees of elastic modulus were both 15.3%, and the deterioration degrees of tensile strength were 24.68% and 22.76%, respectively. In addition, the deterioration degree of cohesion was 20.4%, and the deterioration degree of internal friction angle was 7.5%.
2) The failure and the degree of broken pieces of water-saturated samples were generally more severe than those of natural samples. Moisture-induced degradation was obvious—the cohesion between fracture particles was destroyed due to water, causing the softening of the coal sample and worsening the overall mechanical properties.
3) Moisture condition was negatively correlated with acoustic emission count and energy. The accumulated rising count and accumulated energy of water-saturated samples were

lower than those of natural samples. This happened because of the existence of incompressible water in the fractures of the water-saturated coal samples, which hindered the initiation and propagation of fractures. Water exerted a repression effect on the absorption of weak acoustic emission signals, and part of the small elastic waves generated by fracture development attenuated and disappeared in the fracture water.

4) Numerical simulation studies showed that the internal stress of 45# and 43# coal bodies before and after water injection was evidently different. The water injection had a significant impact on the internal stress of the top coal and the advanced support pressure of the working surface base, which fully weakened the coal body. The stress in the coal body was released and transferred after water injection, the pressure peak was weakened, and the internal stress of the top coal and the advanced support pressure of the bottom plate was evidently reduced.
5) For the field project, we produced a specific water-injection weakening design. The design parameters are as follows: it was arranged 30 m ahead of the north lane of the working face; the length of the sealing hole of the water-injection hole was 10 m, the diameter of the hole was Φ113 mm, the water-injection pressure was 10 Mpa, and the water-injection volume per hole was 39.09 tons. By injecting water into the top coal of the working surface in advance to weaken it, the degree of crushing of the hard-top coal was changed, which was a significant development for the safe and efficient production of this steeply inclined working surface.

Data availability statement

The original contributions presented in the study are included in the article/Supplementary Material; further inquiries can be directed to the corresponding author.

Author contributions

LZ and XL conceived the research. LZ analyzed the data and wrote the manuscript. RB participated in the design of the study and verified the results. All authors have read and approved the final manuscript.

Funding

This research was funded by the National Natural Science Foundation of China (No. 52004201), Shaanxi Provincial Natural Science Basic Research Project Enterprise Joint Fund (No. 2019JLZ-04), and the Natural Science Foundation of Shaanxi Provincial Department of Education (No. 20JK0765).

Acknowledgments

We thank the National Natural Science Foundation of China (No. 52004201), Shaanxi Provincial Natural Science Basic Research Project Enterprise Joint Fund (No. 2019JLZ-04), and the Natural Science Foundation of Shaanxi Provincial Department of Education (No. 20JK0765) for its support of this study. We thank the academic editors and reviewers for their kind suggestions and valuable comments.

Conflict of interest

RB was employed by the National Energy Group Ningxia Coal Industry Co., Ltd. Qingshuiying Coal Mine.

The remaining authors declare that the research was conducted in the absence of any commercial or financial relationships that could be construed as a potential conflict of interest.

Publisher's note

References

Cui, F., Lai, X. P., Cao, J. T., and Shan, P. F. (2015). Strength deterioration study of coal and rock mass affected by coupled-crack. *Chin. J. Rock Mech. Eng.* 34 (2), 3633–3641. doi:10.13722/j.cnki.jrme.2014.0564

Dai, H. Y., Yi, S. H., Ju, W. J., Yan, Y. G., Yang, S. J., and Qiao, Z. D. (2006). Law of strata and surface movement due to horizontally-sliced mechanized top-caving mining at steep-inclined super-thick coal seam. *J. Univ. Sci. Technol. Beijing* 28 (5), 409–412. doi:10.13374/j.issn1001-053x.2006.05.022

Deng, G. Z., Wang, S. B., and Huang, B. X. (2004). Study on the behaviour of hydraulic crack propagation in coal and rock. *Chin. J. Rock Mech. Eng.* 23 (20), 3489–3493. doi:10.3321/j.issn:1000-6915.2004.20.018

Ju, W. J., Li, Q., Wei, D., and Dai, H. Y. (2006). Pressure character in caving steep-inclined and extremely thick coal seam with horizontally grouped top-coal drawing mining method. *J. China Coal Soc.* 31 (5), 558–561. doi:10.3321/j.issn:0253-9993.2006.05.002

Kang, T. H., Zhang, J. P., and Bai, S. W. (2004). Theoretical study and application of weakening top coal using water pre-infusion in fully mechanized sublevel caving mining. *Chin. J. Rock Mech. Eng.* 23 (15), 2615–2621. doi:10.3321/j.issn:1000-6915.2004.15.025

Lai, X. P., Bai, R., Cao, J. T., Shan, P. F., Fang, P. F., Fang, X. W., et al. (2021). Experimental study on mechanical and acoustic characteristics of interbedded rock specimens under cyclic loading. *J. Xi' Univ. Sci. Technol.* 41 (6), 955–963. doi:10.13800/j.cnki.xakjdxxb.2021.0601

Lai, X. P., Dai, J. J., and Li, C. (2020). Analysis on hazard characteristics of overburden structure in steeply inclined coal seam. *J. China Coal Soc.* 45 (1), 122–130. doi:10.13225/j.cnki.jccs.YG19.1405

Lai, X. P., Wang, N. B., Xu, H. D., Qi, T., Cao, J. T., and Jiang, D. H. (2009). Safety top-coal-caving of heavy and steep coal seams under complex environment. *J. Univ. Sci. Technol. Beijing* 31 (3), 277–280. doi:10.13374/j.issn1001-053x.2009.03.030

Lai, X. P., Zhang, L. M., Zhang, Y., Shan, P. F., Wan, P. F., and Mu, K. W. (2022). Research of the backfill body compaction ratio based on upward backfill safety mining of the close-distance coal seam group. *Geofluids* 2022, 1–11. Article ID 8418218. doi:10.1155/2022/8418218

Li, M. Z. (2018). *Research on key technology of fully mechanized caving mining with large mining height in hard and extra thick coal seam in Yushen mining area*. [Beijing: General Research Institute of Coal Science. [dissertation/master's thesis].

Liu, J., Xue, Y., Zhang, Q., Wang, H. M., and Wang, S. H. (2022). Coupled thermo-hydro-mechanical modelling for geothermal doublet system with 3D fractal fracture. *Appl. Therm. Eng.* 200, 117716. doi:10.1016/j.applthermaleng.2021.117716

Qian, M. G., Xu, J. L., and Wang, J. C. (2018). Further on the sustainable mining of coal. *J. China Coal Soc.* 43 (1), 1–13. doi:10.13225/j.cnki.jccs.2017.4400

Qin, H., Huang, G., and Wang, W. Z. (2012). Experimental study of acoustic emission characteristics of coal samples with different moisture contents in process of compression deformation and failure. *Chin. J. Rock Mech. Eng.* 31 (6), 1115–1120. doi:10.3969/j.issn.1000-6915.2012.06.004

Shi, P. W., and Gao, Z. N. (2003). The failure laws of surrounding rocks and overlying bed in the stereo special thickness seam mining. *J. China Coal Soc.* 28 (1), 13–16. doi:10.3321/j.issn:0253-9993.2003.01.003

Suo, Y. L. (2001). Study of pre-weakened method on the hard thick-top-coal in fully mechanized caving. *J. China Coal Soc.* 26 (6), 616–620. doi:10.3321/j.issn:0253-9993.2001.06.011

Wang, G., Fan, J. Y., Wang, W. R., and Xu, H. (2020). Research on slot spacing model for hydraulic slot-assisted directional fracturing of coal mass. *J. Min. Saf. Eng.* 37 (3), 622–631. doi:10.13545/j.cnki.jmse.2020.03.022

Wang, J. C., Bai, X. J., Wu, Z. S., and Xiong, D. H. (2000). Research on the fractured blocks of the top-coal in the longwall top-coal caving technique of the hard coal seam. *J. China Coal Soc.* 25 (3), 238–242. doi:10.13225/j.cnki.jccs.2000.03.005

Wang, J. C. (2018). Engineering practice and theoretical progress of top coal mining in China. *J. China Coal Soc.* 43 (1), 43–51. doi:10.13225/j.cnki.jccs.2017.4101

Wu, S. Q., and Shi, P. W. (1990). The study of rock pressure manifestation in steep seam. *J. Xi' Min. Inst.* 10 (2), 1–9. doi:10.13800/j.cnki.xakjdxxb.1990.02.001

Wu, Y. P., Yun, D. F., Xie, P. S., Wang, H. W., Lang, D., and Hu, B. S. (2020). Progress, practice and scientific issues in steeply dipping coal seams fully-mechanized mining. *J. China Coal Soc.* 45 (1), 24–34. doi:10.13225/j.cnki.jccs.YG19.0494

Xia, D., Yang, T. H., Xu, Tao., Wang, P. T., and Zhao, Y. C. (2015). Experimental study on AE properties during the damage process of water-saturated rock specimens based on time effect. *J. China Coal Soc.* 40 (S2), 337–345. doi:10.13225/j.cnki.jccs.2015.0440

Xie, H. P., Wang, J. C., Chen, Z. H., Xie, J. Q., Yan, Z. Y., and Tian, L. J. (1999). Study on top-coal blasting technique of full-mechanized caving in the hard thick coal seam. *J. China Coal Soc.* 24 (4), 16–20. doi:10.1088/0256-307X/15/12/024

Xue, Y., Liu, J., Ranjith, P. G., Gao, F., Xie, H. P., and Wang, J. (2022). Changes in microstructure and mechanical properties of low-permeability coal induced by pulsating nitrogen fatigue fracturing tests. *Rock Mech. Rock Eng.* doi:10.1007/s00603-022-03031-2

Yang, Z. W. (2014). *Research on combined weakened top coal technology of "water injection-blasting" in fully mechanized caving mining in Yungang Mine*. [dissertation/master's thesis]. Fuxin, China: Liaoning University of Engineering and Technology.

Yao, Q. L., Li, X. H., Zhou, J., Ju, M. H., Chong, Z. H., and Zhao, B. (2015). Experimental study of strength characteristics of coal specimens after water intrusion. *Arab. J. Geosci.* 8 (9), 6779–6789. doi:10.1007/s12517-014-1764-5

Zhang, Q., Ge, C. G., Li, W., Jiang, Z. B., Chen, J. X., and Li, B. G. (2018). A new model and application of coalbed methane high efficiency production from broken soft and low permeable coal seam by roof strata-in horizontal well and staged hydraulic fracture. *J. China Coal Soc.* 43 (1), 150–159. doi:10.13225/j.cnki.jccs.2017.1422

Zhang, Y., and Cao, S. G. (2021). Control of water-flowing fracture development with solid backfill mining: Designing a backfill body compression ratio for water resources protection. *Mine Water Environ.* 40 (4), 877–890. doi:10.1007/s10230-021-00821-y

Zhang, Y., Cao, S. G., Guo, S., Wan, T., and Wang, J. J. (2018). Mechanisms of the development of water conducting fracture zone in overlying strata during short wall block backfill mining: A case study in northwestern China. *Environ. Earth Sci.* 77 (14), 543. doi:10.1007/s12665-018-7726-6

Zhang, Y., Cao, S. G., Zhang, N., and Zhao, C. Z. (2020). The application of short-wall block backfill mining to preserve surface water resources in Northwest China. *J. Clean. Prod.* 261, 121232. doi:10.1016/j.jclepro.2020.121232

Zhang, Y., Liu, Y. Z., Lai, X. P., and Gao, J. M. (2021). Physical modeling of the controlled water-flowing fracture development during short-wall block backfill mining. *Lithosphere* 2021, 13. Article ID 2860087. doi:10.2113/2021/2860087

frontiers | Frontiers in Earth Science

TYPE Original Research
PUBLISHED 18 January 2023
DOI 10.3389/feart.2022.1090799

OPEN ACCESS

EDITED BY
Fangtian Wang,
China University of Mining and Technology, China

REVIEWED BY
Defu Zhu,
Taiyuan University of Technology, China
Wenlong Shen,
Henan Polytechnic University, China

*CORRESPONDENCE
Yun Zhang,
zhangyun@cumt.edu.cn

SPECIALTY SECTION
This article was submitted to Structural Geology and Tectonics, a section of the journal Frontiers in Earth Science

RECEIVED 06 November 2022
ACCEPTED 25 November 2022
PUBLISHED 18 January 2023

CITATION
Zhang Y, Liu Y, Liu J, Zhan R, He W, Tong L, Wan P and Bai L (2023), Control mechanism of the migration of heavy metal ions from gangue backfill bodies in mined-out areas.
Front. Earth Sci. 10:1090799.
doi: 10.3389/feart.2022.1090799

Control mechanism of the migration of heavy metal ions from gangue backfill bodies in mined-out areas

Yun Zhang[1]*, Yongzi Liu[1], Jia Liu[2], Rui Zhan[1], Wei He[1], Liang Tong[1], Peifeng Wan[1] and Licheng Bai[1]

[1]College of Energy Engineering, Xi'an University of Science and Technology, Xi'an, China, [2]State Key Laboratory of Eco-hydraulics in Northwest Arid Region, Xi'an University of Technology, Xi'an, China

In the process of solid backfill mining, the leaching of heavy metal ions from the gangue backfill body in the mined-out area can pose potential risk of polluting water resources in the mine. Accordingly, based on the environment of the gangue backfill body, the migration model of heavy metal ions from the gangue backfill body was established to reveal the pollution mechanism of water resources by the gangue backfill body in the mined-out area. The main factors that affect the migration of heavy metal ions were analyzed, and prevention and control techniques for the leaching and migration of heavy metal ions from gangue backfill bodies were proposed. Research showed that the heavy metal ions in gangue backfill bodies were subjected to the coupled action of seepage, concentration, and stress and then driven by water head pressure and gravitational potential energy to migrate downward along the pore channels in the floor, during which mine water served as the carrier. The migration distance of heavy metal ions increased with time. According to the migration rate, the migration process can be subdivided into three phases: the rapid migration phase (0–50 years), the slow migration phase (50–125 years), and the stable phase (125–200 years). It was concluded that the leaching concentration of heavy metal ions, the particle size of gangue, the permeability of floor strata, and the burial depth of coal seams were the main influencing factors of the migration of heavy metal ions. From the two perspectives of heavy metal ion leaching and migration, prevention and control techniques for the leaching and migration of heavy metal ions from gangue backfill bodies were proposed to protect water resources in mining area. The present study is of great significance to realizing utilization of solid waste in mines and protecting the ecological environment.

KEYWORDS

solid backfill mining, gangue backfill bodies, migration of heavy metal ions, pollution of water resources, environmental protection

Introduction

China's sustainable and rapid economic development has raised increasing demands for coal resources. Accompanied by constantly enhanced coal mining intensity, a great deal of gangue was abandoned and piled on the ground to form a gangue mountain (Zhang, et al., 2020; Yang, et al., 2021; Zhang, et al., 2021). According to incomplete statistics, gangue accumulation in China has exceeded six billion tons and has increased steadily at a speed of 0.68 billion tons per year, occupying approximately 13,000 hm^3 of land. This can cause serious waste of land resources and water pollution (Zhang, 2019; Zhang, et al., 2020; Wang, 2022). Meanwhile, because of the high carbon content in gangue, large amounts of harmful gases such as CO, CO_2, and SO_2 can be emitted after spontaneous combustion or slow oxidation of gangue, which then act as new carbon emission sources (Wang, et al., 2016; An, 2017; Liu, et al., 2022). In addition, the processing of waste gangue has also increased the economic cost of coal resource enterprises. In particular, the Dongqu Mine, owned by Xishan Coal & Electricity Group in China, annually produces approximately 150,0000 tons of waste gangue, which processing (at a current processing cost of 27.0 yuan per ton) would amount to about 40.5 million yuan, strongly affecting the enterprise's economic benefit (Liu, 2018; Liu, et al., 2020; Zhang, et al., 2020), Figure 1 shows the environmental damage caused by gangue accumulation in China. As China has paid increasing attention to environmental protection, China's coal industry has entered the stage of green mining. Moveover, the development of China's coal industry is divided into three phases, as shown in Figure 2. The 1970s and 1980s were in the efficient mining phase, China began to implement the fully-mechanized mining of coal resources; in the 1990s, for the safety and efficient mining phase, the theory of key stratum was proposed by Qian Minggao et al. (1996) to solve the safety problem of coal mining. Since the beginning of the 21st century, it is the green mining phase, the green technology of coal mining was proposed by Qian Minggao et al. (2003). This had also led to the ground treatment and emissions of waste gangue being controlled strictly. Solid backfill mining, as an environmentally friendly mining technique, can effectively utilize ground and underground gangue while controlling the movement of overlying strata (Zhang, et al., 2018; Zhang, et al., 2021; Lai, et al., 2022). However, after the large-scale backfill of gangue into the mined-out area, heavy metal ions from the gangue can be heavily leached and migrate under long-term leaching in mine water, posing a particular potential risk to the pollution of water resources in mines. Therefore, the prevention and management of water pollution in mines induced by gangue backfill bodies in mined-out regions have become a problem that urgently needs to be addressed.

Scholars have conducted a great deal of research on the environmental pollution induced by waste gangue accumulation and the gangue backfill materials of solid backfill mining. Concerning ecological pollution caused by the pile-up of gangue, Shang et al. (2022) measured and analyzed the contents of heavy metals in the soil around gangue mountains and found a high enrichment degree of heavy metals and severe pollution in soil. Based on mathematical statistics, Li et al. (2022) analyzed the distribution characteristics of heavy metals in the environment and soil around the gangue mountains. They concluded that the content of heavy metals dropped with increasing distance from gangue heaps. Employing a leaching test, Liu et al. (Liu, et al., 2005; Liu, et al., 2014) examined the effect of gangue accumulation on the surrounding water and found that the leaching water from gangue destroyed the ecological system of surface water, seriously affecting the subsistence of aquatic organisms. Concerning gangue backfill materials in solid backfill mining, Li et al. (Li, et al., 2020; Li, et al., 2020) measured the bearing compressive characteristics of gangue backfill materials and obtained the instant and creep compression deformation rules of gangue backfill materials during the loading process. By combining numerical simulations and compression tests, Zha et al. (2009) analyzed the effect of the non-linear deformation characteristics of gangue backfill bodies on strata movement and the impact of the grading characteristics of backfill gangue on compressive performance. Huang et al. (Huang, et al., 2019; Huang, et al., 2021) established the fractional viscoelastic creep model of the gangue backfill body and the fractal viscoelastic creep foundation beam model, they analyzed the secular deformation characteristics of the roof under solid backfill mining. However, pollution of water resources in mines induced by the gangue backfill body of solid backfill mining has been poorly investigated and still needs further exploration.

On that basis, this study analyzed the environment of the gangue backfill body, established the migration model of heavy metal ions from the gangue backfill body, and investigated the migration rules of heavy metal ions at different times. Finally, the water pollution mechanism of gangue backfill bodies in mined-out areas and the main influencing factors that affect the migration of heavy metal ions from gangue backfill bodies are revealed to propose prevention and control techniques for the leaching and migration of heavy metal ions. The present study is of great engineering and reference significance for the prevention and control of water resource pollution in mines, the development of backfill mining techniques, and the reasonable utilization of waste gangue in mines.

Analysis of water resource pollution mechanism induced by gangue backfill body in the mined-out area

During the solid backfill mining process, heavy metal ions from the gangue backfill body are constantly leached and migrate downward under the long-term leaching action of mine water, which can threaten the environmental safety of water resources

FIGURE 1
The environmental damage caused by gangue accumulation in China. **(A)** Gangue accumulation **(B)** Spontaneous combustion of gangue mountain **(C)** Pollution of water resources.

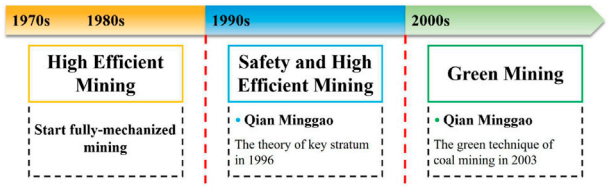

FIGURE 2
Development course of coal industry in China.

in the mine. Accordingly, this study aimed to establish a migration model of heavy metal ions from gangue backfill bodies and explore water resource pollution mechanisms.

Governing equations

(1) Basic assumptions

For the simplification of the calculation process, before the establishment of the migration model, the following basic assumptions can be made according to the migration characteristics of heavy metal ions:

1) Both floor strata and coal pillar are saturated porous elastomers with isotropic properties.
2) Heavy metal ions migrate with mine water as the carrier.
3) By ignoring convection, only the diffusion of heavy metal ions in the porous medium is considered.
4) Seepage is a kind of transient motion that satisfies generalized Darcy's law.

(2) Governing equation of the seepage field

Based on the above basic assumptions, heavy metal ions migrate from the gangue backfill body with mine water as the carrier. The mass conservation equation of seepage can be written as:

$$\frac{\partial}{\partial t}(\varepsilon\rho) + \nabla \cdot (\rho u) = Q_m, \tag{1}$$

where t is the time; ε is porosity; ρ is fluid density; Q_m is a the mass source term; and u is the flow rate of the fluid.

According to Darcy's law, the seepage under gravitational potential energy and head pressure of fluid can be written as:

$$u = -\frac{\kappa}{\mu}(\nabla p + \rho g), \tag{2}$$

where κ is permeability, μ is dynamic viscosity of fluid, p is pressure, g is gravitational acceleration.

(3) Governing equation of the concentration field

The floor strata and coal pillar can be regarded as a saturated porous elastomer with isotropic properties. The migration of heavy metal ions from the gangue backfill body should be combined with the fluid flow velocity in the governing equation of the seepage field. The following expression should be satisfied:

$$\frac{\partial(\varepsilon c_i)}{\partial t} + \nabla \cdot J + u \cdot \nabla c_i = R_i + S_i, \tag{3}$$

where c_i is the concentration of heavy metal ions, J is the diffusion flux, u is the Darcy velocity, R_i is the reaction rate expression, S_i is any source sink term.

Heavy metal ions migrate mainly in the format of molecular diffusion. The migration obeys Fick's second law, and the diffusion flux J can be written as:

$$J = -\frac{\varepsilon}{\tau_{F,i}} D_{F,i} \nabla c_i, \tag{4}$$

Where $D_{F,i}$ is the diffusion coefficient of fluid, $\tau_{F,i}$ is tortuosity.

(4) Governing equation of the stress field

Based on elastic mechanical theory, the properties of floor strata and coal pillars can change under the stress of the surrounding rock. The governing equation of the stress field can be written as follows:

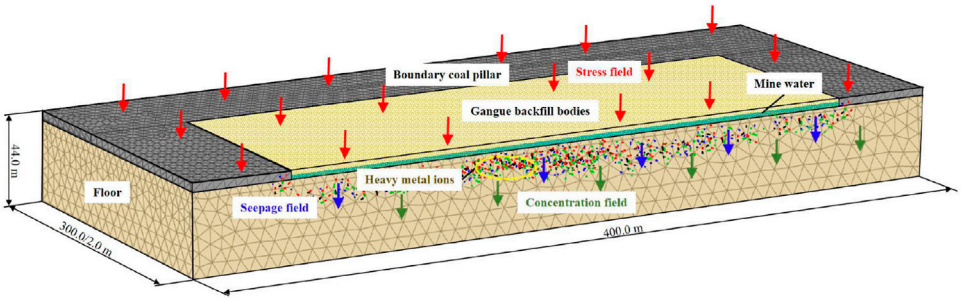

FIGURE 3
Numerical model.

$$\rho' \frac{\partial^2 v}{\partial t^2} = \nabla\sigma + F_v, \tag{5}$$

where ρ' is the density of porous media, v is the displacement, F_v is the volume force, and σ is the stress of surrounding rock.

The floor strata at a larger burial depth is subjected to greater stress on the surrounding rock, leading to a change in the permeability of the floor strata. The floor strata is mainly composed of sandstone in coal-measurement strata, and the relation between permeability and stress can be described as (He, et al., 2004):

$$\kappa = 2.3644 + 3.1137e^{-0.09605\sigma}, \tag{6}$$

where κ is permeability (unit: 10^{-3} μm^2); σ is surrounding rock stress (unit MPa).

Establishment and validation of the migration model of heavy metal ions from gangue backfill body

(1) Establishment of the model

Based on the technological characteristics of solid backfill mining, the migration model of heavy metal ions from gangue backfill body was established with COMSOL Multiphysics. The governing equations of the seepage, concentration, and stress fields can be solved with three specific modules: Darcy's law interface, the transport of diluted species in the porous media interface, and the solid mechanics interface. The model should be simplified considering the coupling among the seepage, concentration, and stress fields. Some size parameters of the model are described below. The overall size of the model is 400.0 m × 300.0 m × 44.0 m, the working face in solid backfill mining is 300.0 m × 200.0 m × 4.0 m, the depth of the floor strata is 40.0 m, and the width of the boundary coal pillar is 50 m. Finally, the established model was then divided into tetrahedral meshes, and the size was calibrated with fluid dynamics. Figure 3 shows the model details.

Based on the detailed condition of the environment of the backfill body, it can be assumed that a particular volume of mine water was filled in the mined-out region and that the gangue backfill body was soaked by mine water. Accordingly, the water head pressure was 4.0 m. By taking Mn ions as the research object, the leaching concentration was 3.2 × 10^{-}5 mol/L. The floor is composed of sandstone in terms of lithology, and the burial depth of the coal seam was 300.0 m. Accordingly, the migration of heavy metal ions from the gangue backfill body at different times can be simulated.

(2) Validation of the time step and the mesh

The solution precision of the migration model of heavy metal ions from gangue backfill body depends on the appropriate time step and mesh number. A time step that is too large can reduce the calculation precision, and if the time step is too small, the calculation time is too long (Tan, et al., 2022; Zhang, et al., 2022; Liu, et al., 2023), however, the mesh number is the opposite. Therefore, the time step was set as three values: 1, 5, and 25 years, the mesh number was set as three values: 85490, 205955 and 389112. The migration distances were calculated respectively for 25, 50, 75, 100, 125, 150, 175, and 200 years of operation, as shown in Figure 4.

The average calculation errors were as small as 5.3 and 1.0% when the time step was reduced from 25 to 10 to 1 year. The average calculation errors were as small as 15.8 and 1.5% when the mesh number was reduced from 85,490 to 205,955 to 389,112. The average error at the time step of 25 years and the mesh number of 85,490 exceeded 5.0%. At the time step of 1 year and the mesh number of 389,112, the calculation time was too long. In conclusion, the time step was set as 5 years and the mesh number was set as 205,955 for the model solution.

Analysis of the pollution of the underlying aquifer during the solid backfill mining process

Figure 5 displays the distribution cloud charts of the concentration of Mn ions at different times. Overall, the

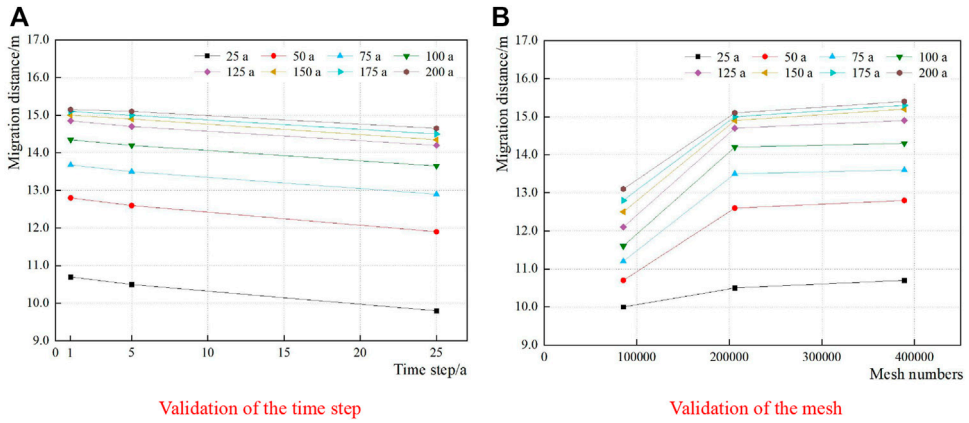

FIGURE 4
Validation of the time step and the mesh. **(A)** Validation of the time step **(B)** Validation of the mesh.

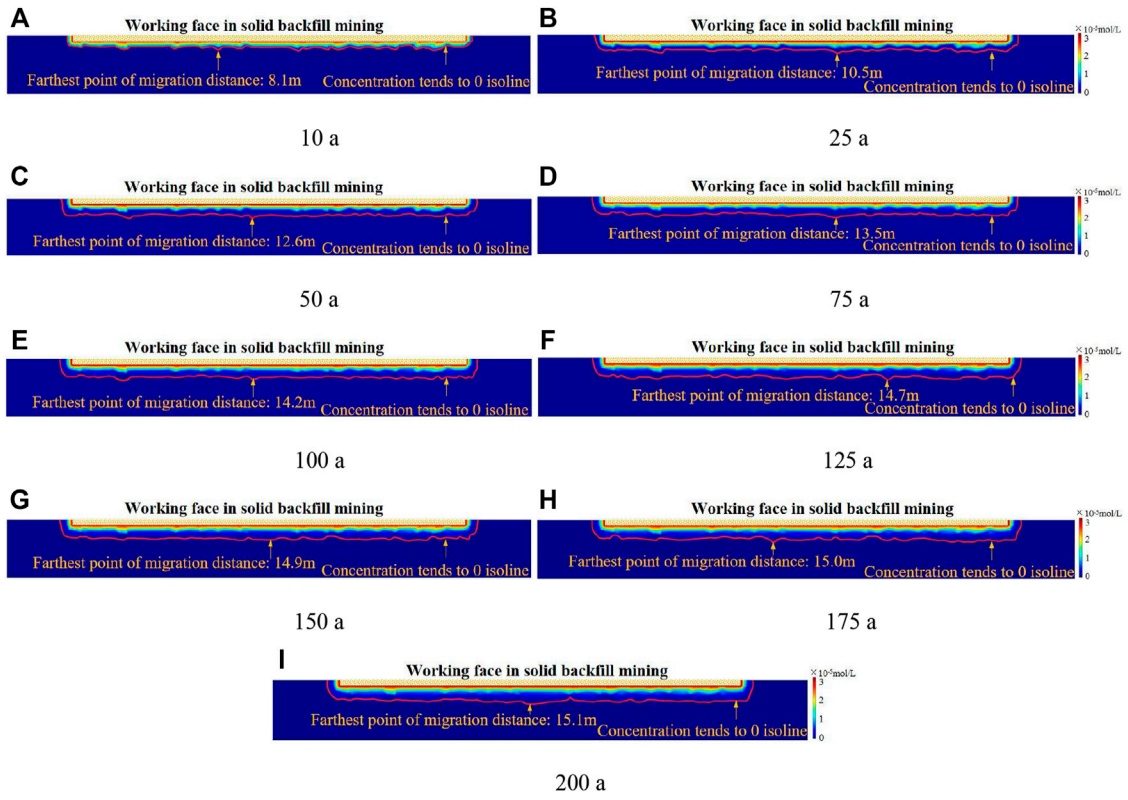

FIGURE 5
The distribution cloud charts of the concentration of Mn ions at different times. **(A)** 10 a **(B)** 25 a **(C)** 50 a **(D)** 75 a **(E)** 100 a **(F)** 125 a **(G)** 150 a **(H)** 175 a **(I)** 200 a.

concentration of Mn ions showed identical distribution patterns, which was highest at the interface between the gangue backfill body and the floor and infinitely close to the leaching concentration of Mn ions. Moreover, the concentration of Mn ions dropped gradually with the floor depth, suggesting a gradually weakened migration

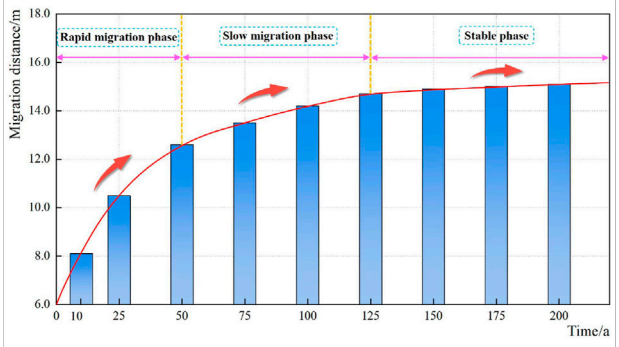

FIGURE 6
The histograms of the migration distances of Mn ions at different times.

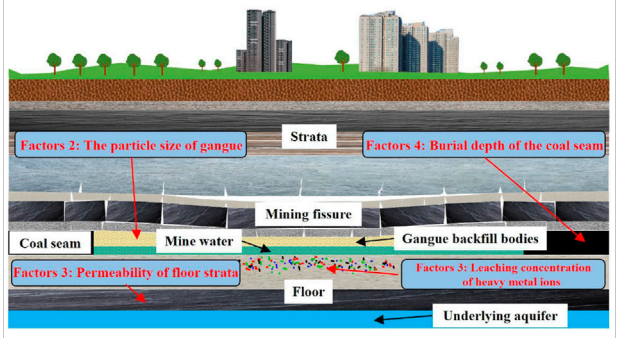

FIGURE 7
The environment where the gangue backfill body is located.

ability of heavy metal ions with the floor depth. The farthest point of the migration distance of heavy metal ions was always near the position below the center of the backfill mining working face. This is because some heavy metal ions on two sides of the working face can migrate toward the center, leading to a further migration distance of heavy metal ions at the center.

Figure 6 shows the histograms of the migration distances of Mn ions at different times. Overall, the migration distance of Mn ions increased with time. The migration distances of Mn ions at 10, 25, 50, 75, 100, 125, 150, 175, and 200 years were 8.1, 10.5, 12.6, 13.5, 14.2, 14.7, 14.9, 15.0, and 15.1 m, respectively. Based on the migration velocity of heavy metal ions, migration can be subdivided into three phases: the rapid migration phase (0–50 years), the slow migration phase (50–125 years), and the stable phase (125–200 years). The migration distance increased by 4.5 m as time increased from 10 to 50 years, with an increasing rate of 55.6%. In the second slow migration phase, the migration distance increased by 2.1 m and 16.7%. Finally, in the last stable phase (125–200 years), the migration distance increased by 0.4 m and 2.7%, respectively.

Based on the analysis of the migration rules of heavy metal ions after different times, it can be concluded that heavy metal ions were driven by the water head pressure and gravitational potential energy and then migrated constantly downward along the pore channels in the floor strata, during which mine water served as the carrier. With prolonged time, the migration distance of heavy metal ions increased constantly; however, on account of the concentration gradient, the migration ability weakened gradually, and the increasing trend of migration distance decreased. Conclusively, at a migration distance that is too large, heavy metal ions can enter the underlying aquifer, posing a certain pollution risk to water resources in mines.

Main controlling factors of the migration of heavy metal ions from gangue backfill body

Multiple factors codetermine the migration of heavy metal ions from gangue backfill bodies. Accordingly, by combining the environment of the gangue backfill body and the pollution mechanism of water resources by the gangue backfill body in the mined-out area, this study started from two perspectives—leaching and migration of heavy metal ions - and identified four main controlling factors that affect the migration of heavy metal ions. Figure 7 depicts the environment where the gangue backfill body is located.

Leaching concentration of heavy metal ions

The migration of heavy metal ions in the floor strata is subjected to the leaching concentration of heavy metal ions. The leaching concentration of heavy metal ions can be regarded as the fundamental factor that affects the migration of heavy metal ions from gangue backfill bodies. After being heavily leached, heavy metal ions can migrate downward along the floor. At a higher leaching concentration of heavy metal ions, the concentration gradient is more significant in migration, accompanied by enhanced migration ability. Accordingly, the migration rate can be accelerated, and the migration distance increases, posing a certain pollution risk to the underlying aquifer.

The particle size of gangue

During the solid backfill mining process, gangue particle size can determine the backfill quality and the final backfilling performance, which is connected with the leaching of heavy metal ions from the gangue backfill body. Under the same environmental conditions,

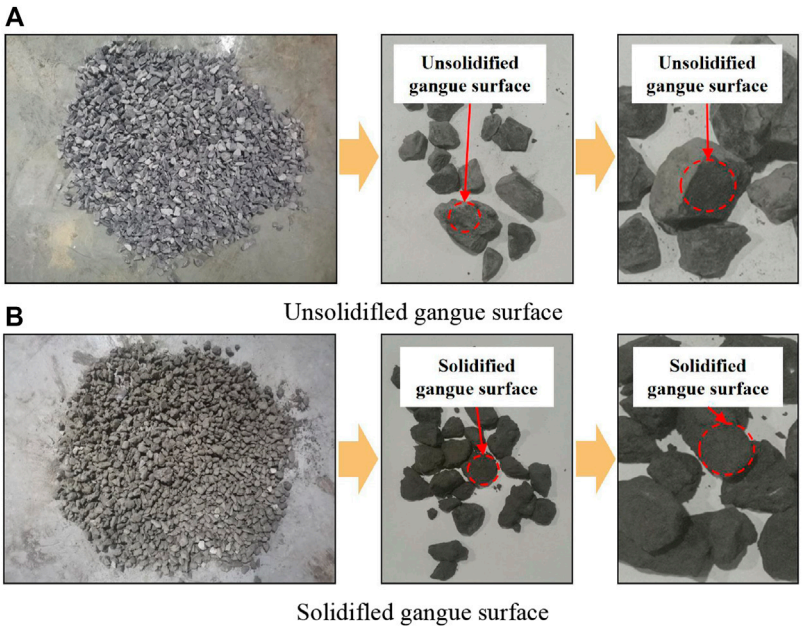

FIGURE 8
Comparison diagram of gangue surface before and after solidified. **(A)** Unsolidifled gangue surface **(B)** Solidifled gangue surface.

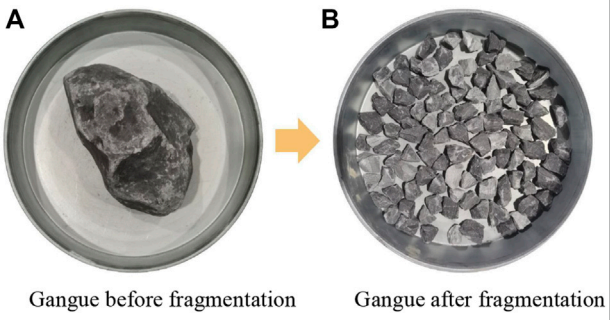

FIGURE 9
Comparison diagram before and after gangue fragmentation.
(A) Gangue before fragmentation **(B)** Gangue after fragmentation.

gangue with smaller particle sizes shows a larger specific surface area, corresponding to a larger contact area with mine water. After the long-term leaching of mine water, a more rapid reaction occurred on the gangue surface. Therefore, the leaching concentration and migration distance of heavy metal ions increased.

Permeability of floor strata

The permeability of the floor strata is also an essential factor that affects the migration of heavy metal ions from the gangue backfill body and is even the main factor. After leaching of the gangue backfill body, heavy metal ions constantly migrated downward along the pore channels in the floor strata with mine water as the carrier. On the other hand, the permeability of the floor strata is an essential factor that reflects the number of pores in the floor strata and can directly determine the migration distance of heavy metal ions. A greater number of pores can be found at a higher permeability of the floor strata, and more channels can be provided for the migration of heavy metal ions, thereby leading to a larger migration distance.

Burial depth of the coal seam

The burial depth of the coal seam can also impose a certain effect on the migration of heavy metal ions from the gangue backfill body. However, compared with the permeability of the rock strata, the burial depth of the coal seam can indirectly affect the permeability of the floor strata by affecting the stress on the surrounding rock, which can further affect the migration of heavy metal ions from the gangue backfill body. Based on the theory of rock mechanics, the floor strata was subjected to higher stresses at a deeper burial depth of the coal seam. Accordingly, pores in the floor strata were constantly closed, and the permeability constantly dropped, decreasing both the migration channels of heavy metal ions and the migration distance.

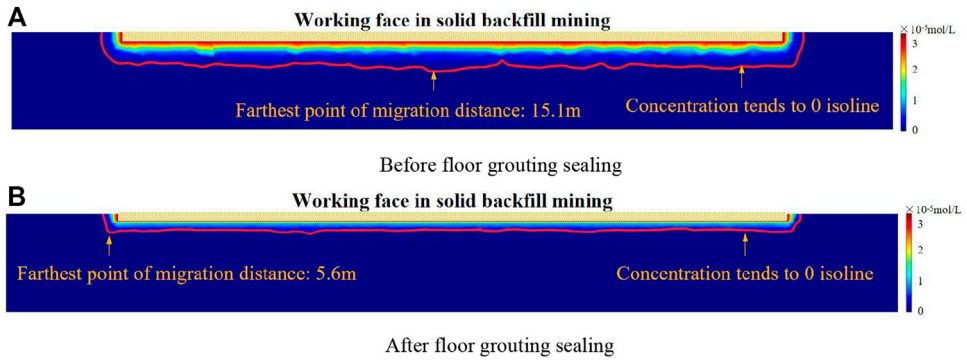

FIGURE 10
The distribution cloud diagram of Mn ion concentration before and after floor grouting sealing. **(A)** Before floor grouting sealing **(B)** After floor grouting sealing.

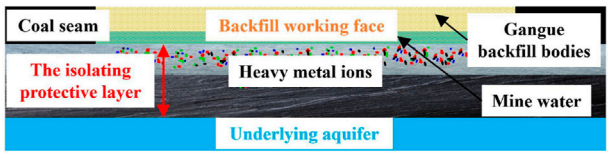

FIGURE 11
Layer relationship diagram.

Prevention and control technique for leaching and migration of heavy metal ions from gangue backfill body

Based on the above analyses of the migration mechanism of heavy metal ions and the main controlling factors, this study started from two perspectives—prevention and control of both leaching and migration of heavy metal ions—and the prevention and control technique for leaching and migration of heavy metal ions from gangue backfill bodies was proposed, as follows.

Gangue surface solidification technique

During the solid backfill mining process, gangue, as a backfill material, can be thrown to the mined-out area by the throw gangue machine; then, after long-term leaching in mine water, many heavy metal ions are leached. Accordingly, this study started from the prevention and control of the leaching of heavy metal ions and proposed the gangue surface solidification technique for reducing the contact area between gangue and mine water, as shown in Figure 8.

The gangue surface solidification technique refers to spraying the prepared cement onto the surface of gangue during the throwing process of gangue by the throw gangue machine; accordingly, gangue can be coated by cement to establish a separation barrier between gangue and mine water, thereby leading to a decline in the contact area between gangue and mine water. Heavy metal ions can thus be solidified into gangue to lower the leaching of heavy metal ions.

Control technique of gangue particle size

According to the above analysis of the main controlling factors of the migration of heavy metal ions, gangue particle size is a core factor that affects the filling ratio in the solid backfill mining process. Meanwhile, gangue particle size is also essential in determining heavy metal ions' leaching. The gangue before and after fragmentation is compared in Figure 9. After crushing into small gangue fragments with small sizes, the surface area can increase obviously, and the contact between gangue and mine water also increases, which can increase the leaching concentration of heavy metal ions and the migration distance. Therefore, the gangue particle size control technique was proposed to reduce heavy metal ions' leaching concentration while maintaining the filling ratio.

The particle size control technique attempts to choose gangue with large particle sizes as the backfill material while ensuring that the filling ratio satisfies the requirements. Accordingly, both the specific surface area of the gangue backfill body and the contact area between the gangue backfill body and mine water can be reduced, which can inhibit the leaching of heavy metal ions and lower the migration distance, thereby achieving an effective balance between the backfill efficiency and pollution prevention of water resources.

Grouting sealing technique for floor

Based on the analysis results of the pollution of the underlying aquifer during the solid backfill mining process, it can be found that heavy metal ions, as the pollution source, mainly migrate in pore and fracture channels inside the floor strata. Accordingly, a floor grouting sealing technique was proposed from the perspective of the prevention and control of the migration of heavy metal ions, to change the floor permeability. During the solid backfill mining process, many fractures appear in floor strata under mining-induced dynamic loads, which can enhance the permeability of floor strata. The increase in pore channels required for migrating heavy metal ions can lead to a rise in migration distance. The floor grouting sealing technique aims to drill and inject slurry into the fractures in the floor for sealing to reduce the permeability of the floor strata and inhibit the migration of heavy metal ions.

To explore the prevention and control effect of the migration of heavy metal ions with floor grouting sealing, the distributions of the concentration of Mn ions before and after grouting sealing were analyzed, as shown in Figure 10. After grouting and sealing, the permeability of the floor strata deceased, and the migration distance of Mn ions was 5.6 m, which was reduced by 63.0% compared with the value before floor grouting and sealing (15.1 m). Therefore, floor grouting and sealing techniques can effectively prevent the migration of heavy metal ions from gangue backfill bodies.

Discussion

Based on previous research results, once the migration distance of heavy metal ions exceeds the thickness of the isolating protective layer during the solid backfill mining process, heavy metal ions enter the underlying aquifer and cause pollution to water resources in the mine. The isolating protective layer refers to the strata between the backfill working face and the underlying aquifer, as shown in Figure 11.

Therefore, according to the position relation among the isolating protective layer, the underlying aquifer, and the backfill working face, the following formula allows one to judge whether the gangue backfill body polluted the underlying aquifer or not:

$$h\alpha \le H, \tag{7}$$

If Eq. 7 is satisfied, heavy metal ions fail to enter the underlying aquifer, and prevention and control measures should not be adopted; otherwise, heavy metal ions will migrate toward the underlying aquifer and cause particular pollution to water resources in mines. Some prevention and control techniques for the leaching and migration of heavy metal ions should be adopted to prevent the leaching and migration of heavy metal ions, improve the environment in the working face, and achieve the goal of water pollution control in the mine.

Conclusion

Based on the results obtained, the following conclusions were drawn:

1) In the solid backfill mining process, heavy metal ions in the gangue backfill body were subjected to the coupling action of seepage, concentration, and stress and then driven by water head pressure and gravitational potential energy to migrate downward along the pore channels in the floor strata, during which mine water served as the carrier. Thus can pose a potential pollution risk to water resources in mines.
(2) The migration distance of heavy metal ions increased with time. According to the migration rate, the whole migration process can be divided into three phases: the rapid migration phase (0–50 years), the slow migration phase (50–125 years), and the stable phase (125–200 years).
3) It can be concluded that the main influencing factors of the migration of heavy metal ions are the leaching concentration of heavy metal ions, the particle size of gangue, the permeability of the floor strata, and the burial depth of the coal seam. Moreover, from the two perspectives of heavy metal ion leaching and migration, prevention and control techniques for the leaching and migration of heavy metal ions from gangue backfill bodies were proposed to protect water resources in mining area.
4) By combining the location relation among the isolating protective layer, the underlying aquifer and the backfill working face, and the migration distance of heavy metal ions, it can be judged whether the underlying aquifer was polluted by heavy metal ions to determine whether to adopt the prevention and control technique for leaching and migration for preventing the leaching and migration of heavy metal ions. Zhang and Cao, 2021.

Data availability statement

The original contributions presented in the study are included in the article/supplementary material, further inquiries can be directed to the corresponding author.

Author contributions

YZ and YL conceived of the research. YZ analyzed the data and wrote the paper. JL, RZ, WH, LT, PW, and LB participated in the design of the study and verified the results. All authors have read and approved the final manuscript.

Funding

This research was funded by the National Natural Science Foundation of China (No. 52004201 and No. 51874284), and China Postdoctoral Science Foundation (No. 2020M683677XB and No. 2021T140551).

Acknowledgments

We would like to extend my gratitude to the College of Energy Engineering Xi'an University of Science and Technology China for providing us the platforms to complete this project. We thank the academic editors and reviewers for their kind suggestions and valuable comments.

Conflict of interest

The authors declare that the research was conducted in the absence of any commercial or financial relationships that could be construed as a potential conflict of interest.

Publisher's note

All claims expressed in this article are solely those of the authors and do not necessarily represent those of their affiliated organizations, or those of the publisher, the editors and the reviewers. Any product that may be evaluated in this article, or claim that may be made by its manufacturer, is not guaranteed or endorsed by the publisher.

References

An, Y. L. (2017). Environmental behaviors of the whole life cycle of coal and their effects on land resources. [dissertation/doctoral's thesis]. [Xuzhou, China]: China University of Mining and Technology.

He, Y. L., and Yang, L. Z. (2004). Testing study on variational characteristics of rockmass permeability under loading-unloading of confining pressure. *Chin. J. Rock Mech. Eng.*, (3): 415–419. doi:10.3321/j.issn:1000-6915.2004.03.010

Huang, P., Spearing, S., Ju, F., Vishwanath, K., Wang, Z. W., and Ning, P. (2019). Control effects of five common solid waste backfilling materials on *in situ* strata of gob. *Energies*, 12(1): 154. doi:10.3390/en12010154

Huang, P., Zhang, J. X., Guo, Y. M., Li, M., and Zhang, Q. (2021). Viscoelastic effect of deep gangue bacfill body and time-dependent defrmation characteristics of roof in deep mining. *J. China Univ. Min. Technol.*, 50(3): 489–497. doi:10.13247/j.cnki.jcumt.001280

Lai, X. P., Zhang, L. M., Zhang, Y., Shan, P. F., Wan, P. F., and Mu, K. W. (2022). Research of the backfill body compaction ratio based on upward backfill safety mining of the close-distance coal seam group. *Geofluids*, vol. 2022, 8418218. doi:10.1155/2022/8418218

Li, J. F. (2022). Study on temporal and spatial characteristics of heavy metal pollution in coal gangue piles in mining area. *Multipurp. Util. Mineral Resour.*, (2): 181–186. doi:10.3969/jissn.1000-6532.2022.02.032

Li, M., Zhang, J. X., Meng, G. H., Gao, Y., and Li, A. L. (2020). Testing and modeling creep compression of waste rocks for backfill with different lithologies. *Int. J. Rock Mech. Min. Sci.*, 125: 1–10. doi:10.1016/j.ijrmms.2019.104170

Li, M., Zhang, W. Q., Li, A. L., Zhu, C. L., Song, W. J., and Hu, Q. (2020). Experimental study on time-dependent compressive deformation of gangue backfilling materials. *J. Min. Saf. Eng.*, 37(1): 147–154. doi:10.13545/j.cnki.jmse.2020.01.016

Liu, J. G., Li, X. W., and He, T. (2020). Application status and prospect of backfill mining in Chinese coal mines. *J. China Coal Soc.*, 45(1): 141–150. doi:10.13225/j.cnki.jccs.YG19.1063

Liu, J., Xue, Y., Fu, Y., Yao, K., and Liu, J. Q. (2023), Numerical investigation on microwave-thermal recovery of shale gas based on a fully coupled electromagnetic, heat transfer, and multiphase flow model. *Energy*,263: 126090. doi:10.1016/j.energy.2022.126090

Liu, L., Wang, S. M., Zhu, M. B., Zhang, B., Hou, D. Z., Xu, C., et al. (2022). CO_2 storage-cavern construction and storage method based on functional backfill. *J. China Coal Soc.*, 47(3): 1072–1086. doi:10.13225/j.cnki.jccs.xr21.1558

Liu, Z. B., and Su, H. M. (2014). Release of arsenic from coal and coal gangue. *Environ. Prot. Chem. Industry*, 34(2): 101–104. doi:10.3969/j.issn.1006-1878.2014.02.002

Liu, Z. B., Zhang, Y. J., and Wang, J. (2005). Research of influence of leaching water of gangue on environments. *J. Liaoning Tech. Univ. Nat. Sci.*, (2): 280–283. doi:10.3969/j.issn.1008-0562.2005.02.041

Lu, J. B. (2018). Gangue filling technology and economic benefit analysis in Dongqu coal mine. *Shanxi Metall.*, 41(6): 137–138+165. doi:10.16525/j.cnki.cn14-1167/tf.2018.06.50

Qian, M. G., Miao, X. X., and Xu, J. L. (1996). Theoretical study of key stratum in ground control. *J. China Coal Soc.*, 21(3): 2–7. :doi:10.13225/j.cnki.jccs.1996.03.001

Qian, M. G., Xu, J. L., and Miao, X. X. (2003). Green technique in coal mining. *J. China Univ. Min. Technol.*, 32(4): 5–10. doi:10.3321/j.issn:1000-1964.2003.04.001

Shang, Y., and Sang, N. (2022). Pollution characteristics and phytotoxicity of heavy metals in the soil around coal gangue accumulation area. *Environ. Sci.*, 43(7): 3773–3780. doi:10.13227/j.hjkx.202106016

Tan, S. F., Li, J. W., Zhang, Z. H., He, Y., and Wang, N. F. (2022). Simulation study on the influence of spin on ignition process of two-phase in solid rocket motor. *J. Aerosp. Power*, 37(7): 1503–1515. doi:10.13224/j.cnki.jasp.20210327

Wang, S. B., Luo, K. L., Wang, X., and Sun, Y. Z. (2016). Estimate of sulfur, arsenic, mercury, fluorine emissions due to spontaneous combustion of coal gangue: An important part of Chinese emission inventories. *Environ. Pollut.*, 209: 107–113. doi:10.1016/j.envpol.2015.11.026

Wang, Y. T. (2022). Status and prospect of harmless disposal and resource comprehensive utilization of solid waste of coal gangue. *Coal Geol. Explor.*, 50(10): 54–66. doi:10.12363/issn.1001-1986.21.11.0614

Yang, K., Wei, Z., Zhao, X. Y., He, X., Zhang, J. Q., and Ji, J. S. (2021). Theory and technology of green filling of solid waste in underground mine at coal power base of Yellow River Basin. *J. China Coal Soc.*, 46(S2): 925–935. doi:10.13225/j.cnki.jccs.st21.0284

Zha, J. F., Guo, G. L., Liu, Y. X., and Wu, B. (2009). The noninear features of waste deformation and its impaction on strata movement. *J. China Coal Soc.*, 34(8): 1071–1075.

Zhang, H., Zhang, Q., Zuo, X., Wu, Z. Y., Fan, W. C., Liu, H. J., et al. (2021). Design and application of mining-sparating-backfilling system for mining ecological and environmental protection. *J. China Univ. Min. Technol.*, 50(3): 548–557. doi:10.13247/j.cnki.jcumt.001287

Zhang, Q., Miao, W. P., Liu, Q. S., Li, C., and Zhang, W. F. (2022). Research on pitch control strategy and aerodynamic performance of vertical axis wind turbine. *Acta Energiae Solaris Sin.*, 43(10): 296–303. doi:10.19912/j.0254-0096.tynxb.2021-0234

Zhang, Q., Yang, K., Zhang, H., Xia, K. Q., and Zhang, Q. (2021). Research on weakening law and quantitative characterization of strata behavior in solid filling mining. *J. China Univ. Min. Technol.* 50(3): 479–488. doi:10.13247/j.cnki.jcumt.001279

Zhang, Y., and Cao, S. G. (2021). Control of water-flowing fracture development with solid backfill mining: Designing a backfill body compression ratio for water resources protection. *Mine Water Environ.*, 40(4): 877–890. doi:10.1007/s10230-021-00821-y

Zhang, Y., Cao, S. G., Lai, X. P., Shan, P. F., Zhang, N., Zhao, C. Z., et al. (2020). Analysis on the mechanical properties of water-conducting fractures development during the shortwall block mining. *J. China Coal Soc.*, 45(S2): 551–560. doi:10.13225/j.cnki.jccs.2019.1833

Zhang, Y., Cao, S. G., and Wang, J. J. (2018).Mechanisms of the development of water-conducting fracture zone in overlying strata during shortwall block backfill mining: A case study in northwestern China. *Environ. Earth Sci.*, 77(14): 543. doi:10.1007/s12665-018-7726-6

Zhang, Y., Cao, S. G., Zhang, N., and Zhao, C. Z. (2020). The application of short-wall block back fill mining to preserve surface water resources in Northwest China. *J. Clean. Prod.*, vol. 261, 121232. doi:10.1016/j.jclepro.2020.121232

Zhang, Y. (2019). The mechanism of developmental behavior of water-conducting fracture in the overlying strata of short-wall block mining and the control technology in Western China. [dissertation/doctoral's thesis]. [Xuzhou, China]: China University of Mining and Technology.

frontiers | Frontiers in Earth Science

TYPE Original Research
PUBLISHED 18 January 2023
DOI 10.3389/feart.2022.1039478

OPEN ACCESS

EDITED BY
Yun Zhang,
Xi'an University of Science and Technology, China

REVIEWED BY
Rui Gao,
Taiyuan University of Technology, China
Baoxu Yan,
Xi'an University of Science and Technology, China
Wenlong Shen,
Henan Polytechnic University, China
Liang Xin,
Xi'an University of Technology, China

*CORRESPONDENCE
Shenggen Cao,
caoshenggen@126.com

SPECIALTY SECTION
This article was submitted to Structural Geology and Tectonics, a section of the journal Frontiers in Earth Science

RECEIVED 08 September 2022
ACCEPTED 03 November 2022
PUBLISHED 18 January 2023

CITATION
Che C, Cao S, Zhao C, Du S, Li J and Liu Y (2023), Research on cemented artificial pillars to replace protective inter-block coal pillars and stope failure laws. *Front. Earth Sci.* 10:1039478. doi: 10.3389/feart.2022.1039478

Research on cemented artificial pillars to replace protective inter-block coal pillars and stope failure laws

Chiyuan Che[1,2], Shenggen Cao[1,2]*, Changzheng Zhao[1,2], Shuyu Du[1,2], Jiang Li[1,2] and Yang Liu[1,2]

[1]State Key Laboratory of Coal Resources and Safe Mining, China University of Mining and Technology, Xuzhou, China, [2]School of Mines, China University of Mining and Technology, Xuzhou, China

Replacing protective inter-block coal pillars (PICPs) with cemented artificial pillars is proposed here to address low coal recovery rates. The use of cemented artificial pillars also reduces resource waste when PICPs are used in the short-wall block mining (SBM) process. A coal mine test area in northern Shaanxi, China, was employed as the study site. Artificial pillar replacement techniques were developed based on the layout characteristics of a typical SBM workface. High-strength cemented backfill materials for artificial pillars were manufactured using innovative material ratio testing, and the optimum ratios for backfill materials are discussed. A cusp catastrophe model of an artificial pillar was then developed and used to deduce the conditions and critical widths necessary to generate catastrophic instability of an artificial pillar. This theoretical analysis was validated using FLAC3D simulations. Using the test site conditions, the simulations revealed that when an artificial pillar had a width of 14 m, the destruction of the pillar and associated stope was gradual and would not cause catastrophic instability. Field monitoring performed at the test site verified the theoretical analysis and numerical simulation results, confirming that it was feasible to replace PICPs with cemented artificial pillars.

KEYWORDS

coal pillar recovery, cemented artificial pillar, backfill materials, catastrophe theory, stope failure laws

1 Introduction

China produces huge amounts of coal (Fu et al., 2021). The associated high-intensity longwall mining has resulted in numerous irregular blocks and residual coal pillars being left behind over the years of operation (Zhang et al., 2018). Due to mining economics, surface environmental concerns, and other factors, the mining of residual coal areas (e.g., 'under three' pressed coal, slope pressed coal) has been limited (Zhang Y. L. et al., 2021). As a new development in mining, the short-wall block mining (SBM) method provided an effective technical solution for coal resource mining (Zhang et al., 2020; Zhang Y. et al., 2021). In the SBM process, protective inter-block coal pillars (PICPs) are part of the support system and these

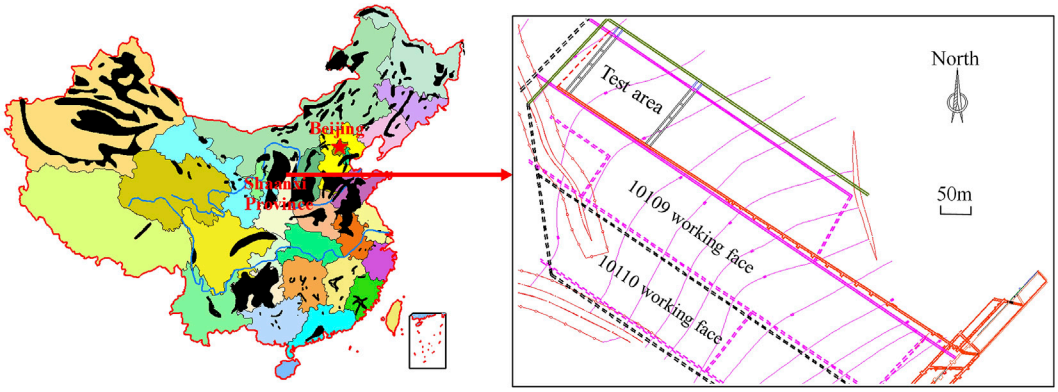

FIGURE 1
Details of the test area used in this study.

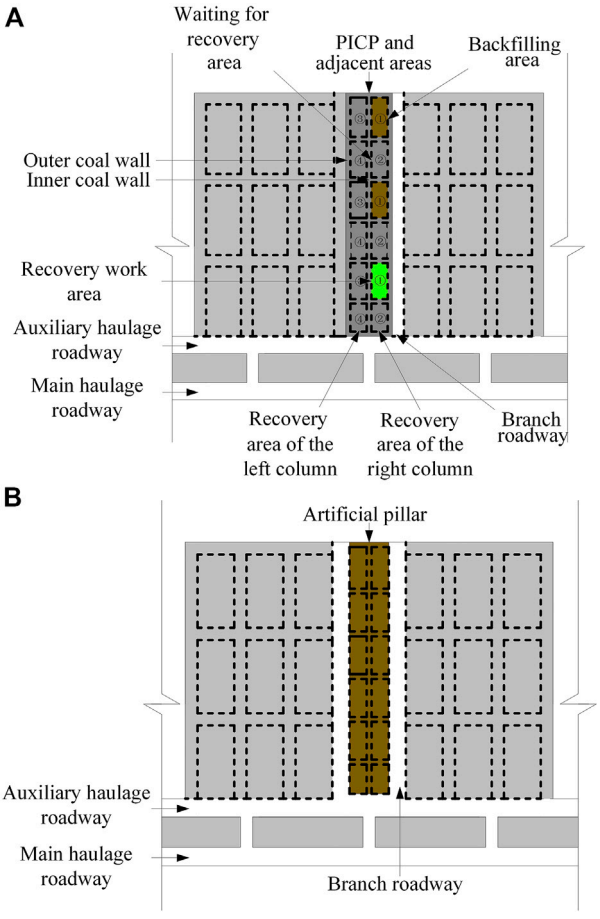

FIGURE 2
PICP replacement technique. **(A)** Recovery sequence of PICP; **(B)** completed recovery of PICP.

aid in controlling the distortion and destruction of the wall rock. However, the SBM method has a low recovery rate due to the PICPs being permanently left in the goaf after mining.

In one recent SBM study, Cao et al. (2014) determined the failure conditions of isolated coal pillars in a Datong coal mine by combining data from field-drilled peep-holes with theoretical derivations. Zhou et al. (2014) studied mine pressure behavior in an SBM working face layout based on force analysis of the PICPs and roof movement. Jiang et al. (2016) used an iterative approximation algorithm to obtain a model of the load-displacement energy of a hard roof in a short-wall block stope. Zhang et al. (2017) employed regression analysis to determine the nonlinear effect of the SBM method's stope parameters on the development height of overburden cracks.

Studies on coal pillar recovery have also recently been carried out. For instance, Zhou et al. (2019) proposed the use of a sand-based backfilling body to recover the remaining coal pillars and analyzed the principles involved in the use of sand-based backfilling bodies to maintain the stability of the stope. Ma et al. (2017) proposed the use of solid backfill to replace the coal pillars in the lower part of an industrial square to provide effective surface-subsidence control. Sun et al. (2018) proposed the cemented paste backfilling method to recover short-strip coal pillars and studied the stability conditions of the impermeable layer. However, there have been few published results describing the recovery of PICPs generated by the SBM method, hence further analysis and exploration are needed.

To fill this gap in the literature, we here propose to maximize coal recovery through the use of cemented artificial pillars to replace PICPs. The artificial pillar replacement technology for PICPs was designed to be compatible with the features of a typical SBM working face layout. The optimal composition and characteristics of the high-strength cemented backfill material for artificial pillar construction were determined through innovative materials ratio testing. A cusp catastrophe model of an artificial pillar was developed and used to determine the necessary conditions and critical widths to prevent catastrophic instability of the artificial pillars. The theoretical analysis was verified using FLAC3D numerical simulations of the dynamic failure process of the artificial pillar and stope. Field monitoring was

TABLE 1 Details of the 16 mixing ratios used in this study.

Mixing ratio	Cement	Fluvial sand	Fly ash	Coal gangue	Steel fiber	Water
A1	1	3.2	0.8	2	0.206	1.272
A2	1	2.4	1.6	2	0.211	1.272
A3	1	1.6	2.4	2	0.215	1.273
A4	1	3.2	0.8	2	0.416	1.308
A5	1	2.4	1.6	2	0.425	1.310
A6	1	1.6	2.4	2	0.435	1.312
A7	1	3.2	0.8	2	0.630	1.346
A8	1	2.4	1.6	2	0.644	1.352
A9	1	1.6	2.4	2	0.659	1.352
A10	1	3.2	0.8	2	0	1.235
A11	1	2.4	1.6	2	0	1.235
A12	1	1.6	2.4	2	0	1.235
A13	1	4	0	2	0.201	1.283
A14	1	4	0	2	0.407	1.307
A15	1	4	0	2	0.620	1.345
A16	1	4	0	2	0	1.235

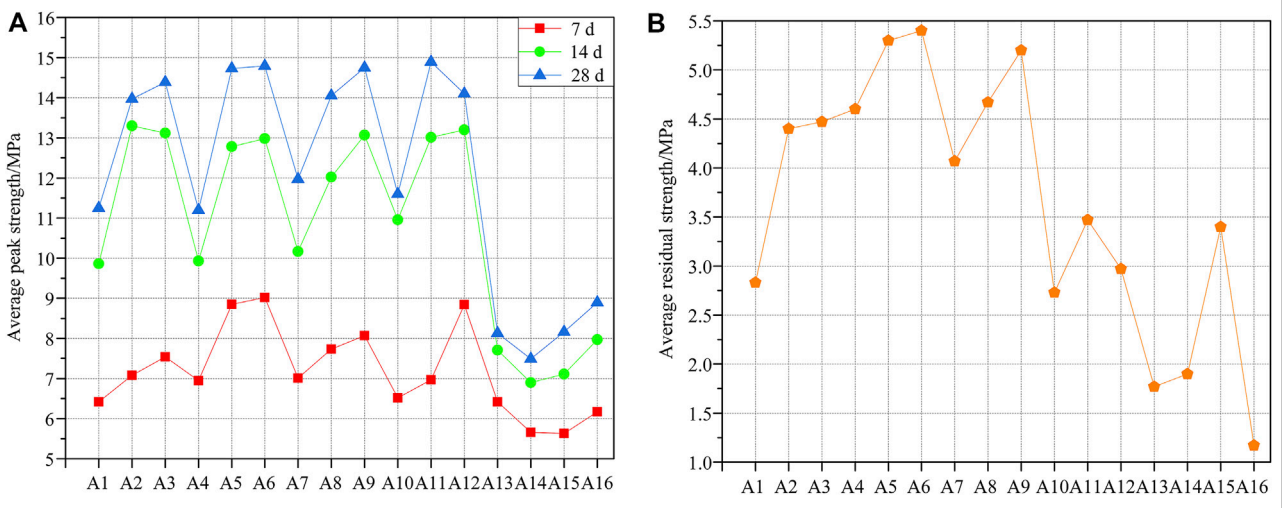

FIGURE 3
Results of the UCS tests. **(A)** Average peak strength at each measurement time (days 7, 14, and 28); **(B)** uniaxial compressive residual strength at day 28.

done to further confirm the theoretical analysis and numerical simulation results.

2 Engineering background

2.1 Test area

The test area selected was located in northern Shaanxi Province, China, and had a simple coal strata structure. The main coal mining seam at the site had five layers, and the No. 2 mining layer was used, with an average dip angle of about 2°. The test area was located 143 m underground where the height of the coal stratum was 4 m (Figure 1). The area dimensions were 152 m × 108 m. The roof was composed of mudstone and sandstone (18.0 m) and was relatively stable. The roof upward included mudstone (5.0 m), sandstone (5.2 m), mudstone (16.7 m), sandy shale (14.1 m), fine sandstone (5.0 m), mudstone (3.3 m), coarse sandstone (31.0 m), mudstone (10.7 m), and loess strata (34.0 m). The

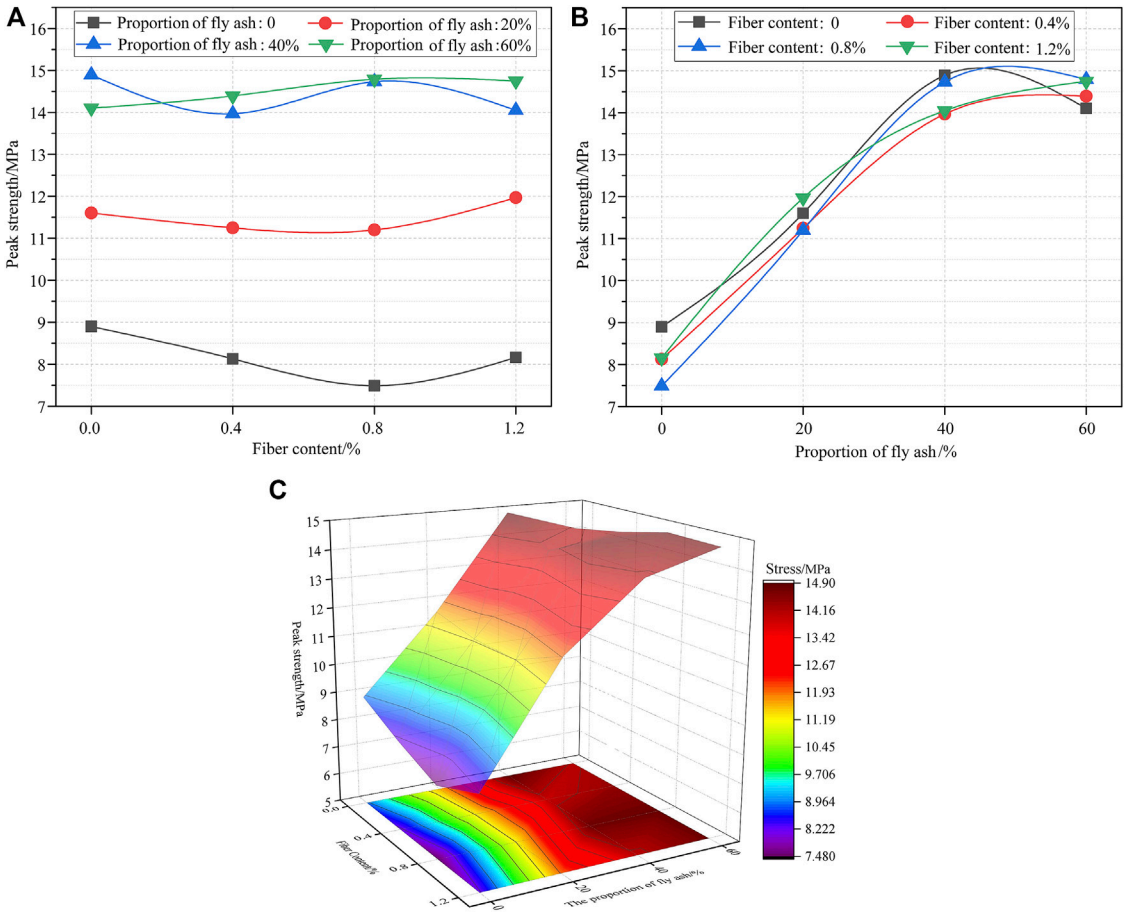

FIGURE 4
Effect of steel fiber and fly ash content on peak strength. **(A)** Steel fiber content; **(B)** proportion of fly ash; **(C)** interaction between steel fiber and fly ash.

stability of the roof, floor, and roadway of the adjacent working face in the test area was good, so the SBM method was adopted in that area. Two blocks were designed for mining, and the middle of the two blocks was the retained area of a PICP.

2.2 PICP replacement

The PICP and adjacent areas within the test area were divided into two columns of several recovery areas on the left and right of the site (Figure 2A). The inner and outer coal walls were left around the recovery area as backfilling retaining walls. The thickness of the inner and outer coal walls was 1.2 m. After digging the main haulage roadway and auxiliary haulage roadway in the testing area, a branch roadway with a width of 4.3 m (set according to the width of the continuous miner) was dug close to the right side of the PICP.

To reduce stress concentration, 'leaping' mining was then carried out in the recovery area of the right column of the PICP through a retreat mining sequence, and each recovery area was backfilled after mining. The excavation and recovery equipment used were continuous miners (Zhou et al., 2014). After all recovery areas of the right coal pillar were fully mined, another branch roadway with a width of 4.3 m was dug close to the PICP. The recovery areas in the left column were then mined one by one using the same process and sequence as the recovery areas in the right column. The recovery sequence is shown in Figure 2A. The strength of the backfill materials increased very slowly over 28 days of curing; therefore, the 28-day strength was taken as the final strength of the backfill materials and, the recovery areas in the left and right columns were backfilled and left standing for 28 days. The inner and outer coal walls were then recovered. Finally, the overall artificial pillar was obtained by backfilling the empty area formed after the inner coal wall was recovered (Figure 2B).

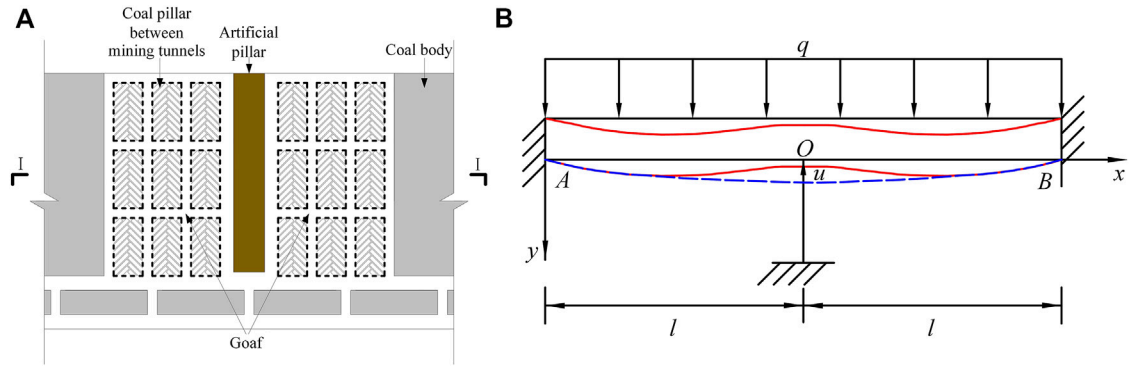

FIGURE 5
The goaf after block mining and the proposed mechanical model of the system. **(A)** The goaf after block mining; **(B)** mechanical model of the rock beam-artificial pillar system.

3 Matching experimental and mechanical property measurements of cemented backfilling materials

3.1 Experimental design and uniaxial compressive strength (UCS) tests

We employed uniaxial compressive strength (UCS) as the final target property in determining the optimum composition of the backfill materials. In the cemented backfill body, the cementitious materials were Portland cement (grade 42.5) and low-calcium secondary fly ash; fine aggregate (continuous graded fluvial sand with 0–4.75 mm particle size); and coarse aggregate (5–10 mm continuous graded coal gangue). The added concatenators were 25 mm × 0.65 mm crimped steel fiber (tensile strength >600 MPa, density of 7850 kg/m^3). Tap water was used for mixing the ingredients.

To ensure sufficient liquidity of the slurry for transport and to produce reliable strength in the backfilling body, the mass fraction of the slurry concentration was set to 85% in accordance with multiple earlier tests (Li, 2021). The variable factors in the proportioning scheme of the backfill material mixtures were the proportion of fly ash in the sum of fluvial sand and fly ash, and the proportion of steel fiber. Each variable factor was divided into four levels, which means that a total of 16 mixing ratios were set (Table 1). A group of nine samples of cemented backfill materials, with each sample having dimensions of 100 mm × 100 mm × 100 mm, were produced for each of the 16 mixing ratios. The sample was taken out from the mold 12 h later and cured in a curing box at a temperature of 20 ± 2°C and a relative humidity of 95% until the specified age was reached. We used the mechanical testing and simulation electro-hydraulic servo rock loading system (loading rate of 0.6 mm/min) to test the unconfined uniaxial compression mechanical properties of the backfill material samples as they cured on day 7, day 14, and day 28.

3.2 Tests results

3.2.1 Peak strength and residual strength

The peak strength at each measurement time and the residual strengths on day 28 are shown in Figure 3. Among the 16 mixing ratios, the 28-day peak strength values of samples of the A5, A6, A9, and A11 ratios all reached 14.7 MPa or more, showing good compressive properties (Figure 3A). The peak strength of mixing ratio A6 at 7 d was the highest, reaching 9.02 MPa (Figure 3B). Because of the addition of steel fiber to the A6 mixture, the bonding force between the steel fiber and the backfill materials improved their residual strength (Li, 2021; Ran et al., 2021), and mixture A6 had the highest residual strength at 5.4 MPa.

3.2.2 Effect of steel fiber and fly ash content on peak strength

As shown in Figures 4A,C, the steel fiber content had only a small effect on the peak strength compared to the fly ash, which had a large effect, showing that when the proportion of fly ash was larger, the peak strength was higher (Figures 4B,C). When the proportions of steel fiber and fly ash were 0.8% and 60%, respectively, the peak strength was the highest. Therefore, through comprehensive analysis of the influence of steel fiber and fly ash on peak strength, we concluded that the strength and durability of artificial pillar backfilling materials was optimal when the proportion of steel fiber and fly ash were 0.8% and 60%, respectively.

Based on the above results, we determined that the mixture ratio in A6 was optimal for these tests. The mass ratios of the ingredients in this mixture were: cement (1), fluvial sand (1.6), fly ash (2.4), coal gangue (2), steel fiber (0.435), and water (1.312). The strength of the 28-day cured mixture was used as the final strength.

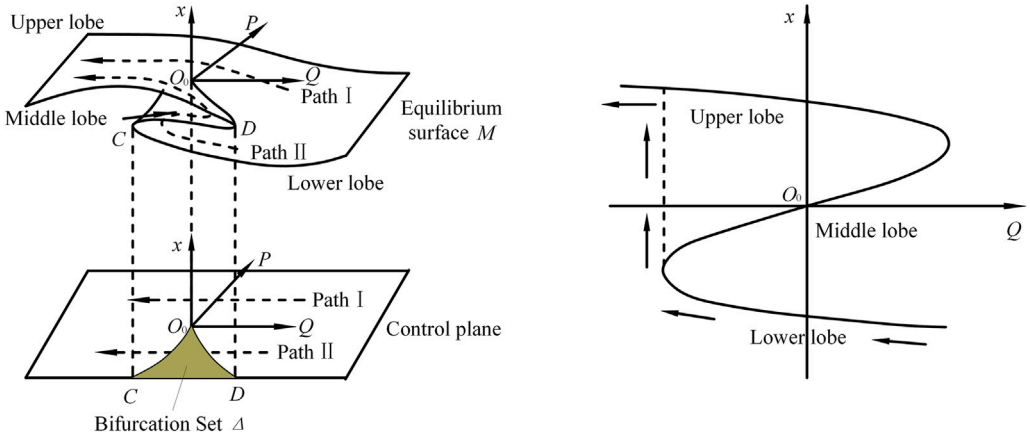

FIGURE 6
Equilibrium surface and control plane of the system.

4 Catastrophe theory analysis of artificial pillar instability

The instability and failure of an artificial pillar are affected by geological conditions and its own anti-failure performance, which is a discontinuous mutation process with sudden, instantaneous seismic activity and significant destruction. This process corresponds to the sudden jump, divergence, and lag characteristics described by catastrophe theory (Shi et al., 2020). This theory can effectively explain artificial pillar instability, and we used it to analyze the stability characteristics of artificial pillars used to replace PICPs.

4.1 Mechanical model of a rock beam-artificial pillar system

The goaf shown in Figure 5A is formed by mining in blocks on the two sides of an artificial pillar. If the size of the coal pillars between mining tunnels is too small, they will eventually degrade and fail to support the roof (Cao et al., 2014); thus, we will not consider the influence of coal pillars between mining tunnels. According to the theory of material mechanics, it is assumed that the floor is not deformed, and the roof is deemed to be a rock beam of length $2l$, which is always kept within its elastic range during the forced flexural displacement process. The flexural stiffness of the rock beam is given by EI, where $E = E_0/1 - \mu_0{}^2$, $I = BH^3/12$, and B and H represent the roof width and thickness, respectively. The un-mined coal body is considered to be rigid. The artificial pillar is relatively narrow, and its supporting effect per unit length on the roof is deemed to be the support force. The gravity of the rock beam and its overlying strata is regarded as load q, and the roof subsidence is u. The rock beam is firmly embedded in the coal body on both sides so that the whole structure constitutes a clamped beam. The mechanical model is summarized in Figure 5B, which was drawn by cutting the position in Figure 5A I-I (Qin et al., 2006; Zhang et al., 2011).

4.2 Cusp catastrophe model of the artificial pillar

The bending displacement energy, V_s, of the rock beam, the compressive displacement energy, V_e, of the artificial pillar, and the energy of the bending displacement process of the rock beam, V_p, constitute the total potential energy V (Xia et al., 2019; Shun et al., 2021), which is expressed as follows:

$$V = V_s + V_e - V_p \tag{1}$$

According to the mechanical analysis presented in the previous section, and existing research results (Zhou et al., 2018a; Shi et al., 2020), the total potential energy equation based on elastic mechanics theory is:

$$V = \frac{EI}{2}\int_0^{2l} f''(x)^2 dx + k_0 \int_0^u u \exp\left[-\left(\frac{u}{u_0}\right)^m\right] du - q\int_0^{2l} f(x)dx$$
$$= \frac{\pi^4 EI}{8l^3}u^2 + k_0 u_0 \left\{u_0 - (u_0 + u)\exp\left[-\left(\frac{u}{u_0}\right)^m\right]\right\} - qlu \tag{2}$$

where $k_0 = E'b/h$ is the stiffness of the artificial pillar ($E' = E_0'/1 - \mu'$), u_0 is the deformation at the peak strain of the artificial pillar ($u_0 = h\varepsilon_0$), and m is the index of curve homology.

According to the static equilibrium condition, the equation of the equilibrium surface, M, of $V = 0$ with u as the state variable can be obtained by:

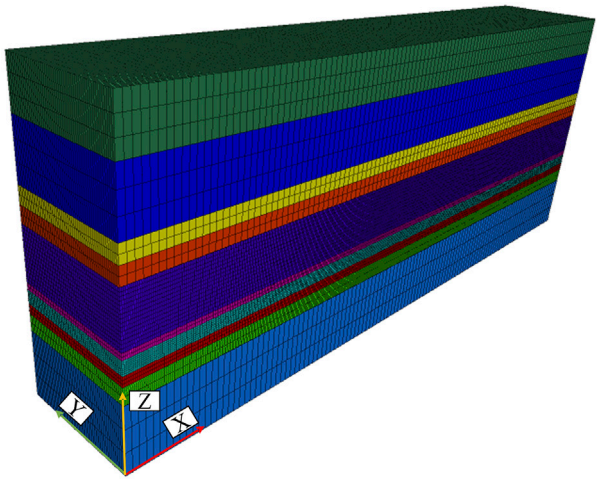

FIGURE 7
Three-dimensional numerical simulation model.

$$V' = \frac{\pi^4 EIu}{4l^3} + k_0 u \exp\left[-\left(\frac{u}{u_0}\right)^m\right] - ql = 0 \tag{3}$$

At the cusp of the equilibrium surface, there is:

$$V'' = \frac{k_0}{u_0}\left(2 - \frac{u}{u_0}\right)\exp\left[-\left(\frac{u}{u_0}\right)^m\right] = 0 \tag{4}$$

According to this relation, it can be found at the cusp that $u = u_1 = 2u_0$.

A Taylor expansion is now performed at the cusp with respect to the state variable u_1, and the third term is intercepted to obtain:

$$V' = k_0 u_1 \exp\left[-\left(\frac{u}{u_0}\right)^m\right] - \frac{\pi^4 EI}{4l^3}(b - u_1) - ql + \left\{k_0\left(1 - \frac{u_1}{u}\right)\exp\left[-\left(\frac{u}{u_0}\right)^m\right] + \frac{\pi^4 EI}{4l^3}\right\}(u - u_1) + \left\{\frac{k_0}{2u_0}\left(\frac{u_1}{u_0} - 2\right)\exp\left[-\left(\frac{u}{u_0}\right)^m\right]\right\}(u - u_1)^2 + \left\{\frac{k_0}{6u_0^2}\left(3 - \frac{u_1}{u_0}\right)\exp\left[-\left(\frac{u}{u_0}\right)^m\right]\right\}(u - u_1)^3 = 0 \tag{5}$$

The state parameter x, where $x = (u - u_1)/u_1$, and the control parameters P and Q are then introduced, where equation M is given by:

$$x^3 + Px + Q = 0 \tag{6}$$

Among which:

$$P = \frac{3}{2}(k - 1) \tag{7}$$

$$Q = \frac{3}{2}(1 + k - \xi) \tag{8}$$

$$k = \frac{\pi^4 EI/4l^3}{k_0 \exp\left(-\frac{m+1}{m}\right)} = \frac{k_2}{k_1} \tag{9}$$

$$\xi = \frac{ql \exp\left(\frac{m+1}{m}\right)}{k_0 u_1} \tag{10}$$

where k is the stiffness ratio, and ξ is a geometrical mechanical parameter.

Taking the first derivative of M, the singular value equation is expressed as:

$$3x^2 + P = 0 \tag{11}$$

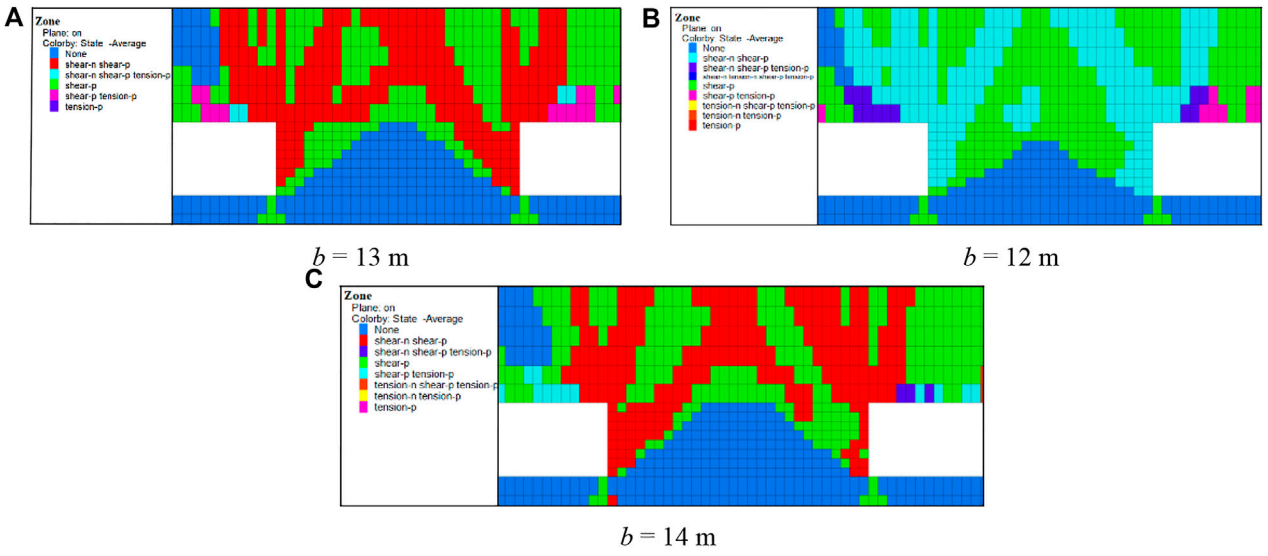

FIGURE 8
Distribution of plastic zones with different widths of artificial pillars **(A)** b = 13 m; **(B)** b = 12 m; **(C)** b = 14 m.

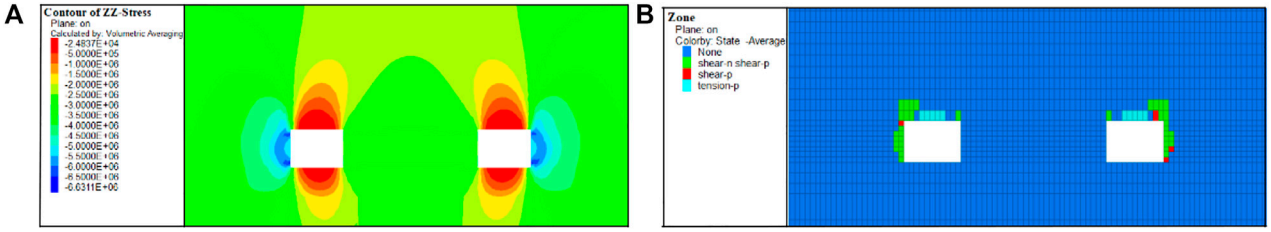

FIGURE 9
Distribution of vertical stress and plastic zones in branch roadways and the artificial pillar. **(A)** Vertical stress distribution of the branch roadway and artificial pillar; **(B)** distribution of plastic zones of the branches and artificial pillar.

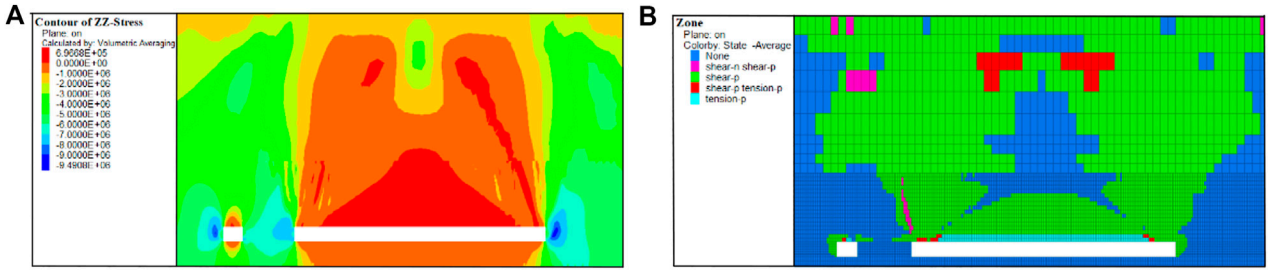

FIGURE 10
Distribution of vertical stress and plastic zones after mining block 1. **(A)** Vertical stress distribution after mining block 1; **(B)** plastic zone distribution after mining block 1.

By eliminating x in combination with Eqs 6, 11, the bifurcation set Δ is given by:

$$\Delta = 4P^3 + 27Q^2 = 0 \tag{12}$$

As shown in Figure 6, when the three-dimensional coordinate points controlled by P, Q, and x change continuously along path I, the system is stable; at this time, $\Delta > 0$. When the coordinate points change continuously along path II, there is a leap from the lower lobe to the upper lobe, and the system is mutational; at this time, $\Delta < 0$. When the system is in a boundary pattern, $\Delta = 0$ (Zhou et al., 2018b; Ma et al., 2019; Wang et al., 2021).

Substituting Eqs 7, 8 into Eq. 12, we get:

$$\Delta = 4\left[\frac{3}{2}(k-1)\right]^3 + 27\left[\frac{3}{2}(1+k-\xi)\right]^2 = 0 \tag{13}$$

According to this relation, ξ and k determine the stability of the system. When $k < 1$, $\Delta < 0$, the system exhibits catastrophic instability. Therefore, the necessary condition for the catastrophic instability of an artificial pillar is expressed by:

$$k = \frac{\pi^4 EI/4l^3}{k_0 \exp\left(-\frac{m+1}{m}\right)} = \frac{k_2}{k_1} < 1 \tag{14}$$

According to this equation, k_1 can be altered to improve the anti-failure capability and avoid catastrophic instability by changing the bearing capacity of the artificial pillar and determining a reasonable width. The bearing capacity of the artificial pillar was determined through the backfill materials ratio tests presented in Section 3. Here, we determine a reasonable artificial pillar width appropriate to the conditions of the test area used in this study. According to the boundary pattern of catastrophe, $\Delta = 0$ and Eq. 14, the critical width of the artificial pillar to eliminate catastrophic instability can be obtained by:

$$b = \frac{\pi^4 EIh/4l^3}{E' \exp\left(-\frac{m+1}{m}\right)} \tag{15}$$

In the test area used in this study, the roof thickness was 18 m, the elastic modulus of the roof rock was $E_0 = 20.33$ GPa, the Poisson's ratio of the roof was 0.22, and the roof span was 76 m. In addition, the elastic modulus E'_0 of the A6 backfill materials group was 1.15 GPa, and the Poisson's ratio μ' of backfill materials was 0.35. The A6 backfill mixture ratio samples had obvious strain softening characteristics, and their homology index, m, was 1, and the height of the artificial pillar reached 4 m. Therefore, we calculated that the critical width of an artificial pillar in the test area when catastrophic instability occurred would be 13 m.

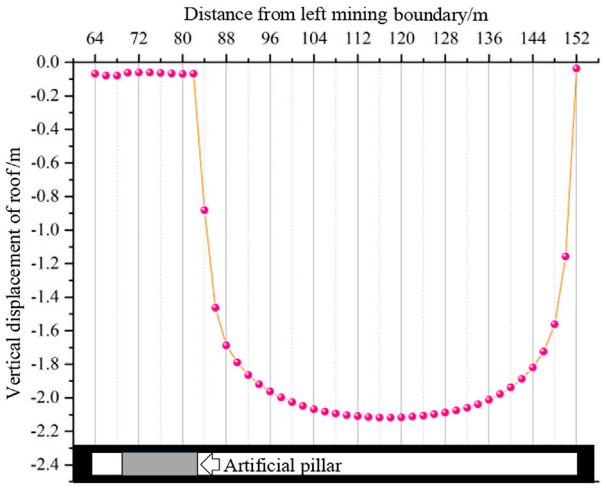

FIGURE 11
Stope roof subsidence after mining block 1.

5 Stope failure: Numerical simulation and field verification

5.1 Numerical simulation analysis of stope failure laws

The FLAC3D (version 5.0) model was set up according to the field conditions of the test area. The model was then simplified to a horizontal model, with X, Y, and Z dimensions of 232 m × 40 m × 91 m, respectively (Figure 7). A 40 m coal body was set on the boundary of the model to reduce the edge effect. The mining length of the test area was 152 m, and the lengths of blocks 1 and 2 varied according to the width of the artificial pillar. To speed up numerical calculations, the weight of the rock strata applied at the height of 84 m from the top of the model to the surface had an equivalent load of 1.77 MPa. The Mohr-coulomb failure criterion was used in the constitutive model. According to the calculations above, the critical width of the catastrophic instability of the artificial pillar was 13 m, so the widths of the artificial pillars were set to 13 m, 12 m, and 14 m for comparative analysis of the stope failure laws.

5.1.1 Analysis of the failure characteristics of the artificial pillars

The plastic zone of the artificial pillars after mining the blocks is shown in Figure 8. There is still a 2 m-wide elastic zone at the top of the artificial pillar when its width is 13 m, and the width of the elastic zone accounts for about 15% of the width of the artificial pillar. Although influenced by the unit division of the FLAC3D grid, the results are close to the theoretical derivation in Cao et al. (2014) that stipulated that catastrophic instability can occur when the width of the elastic area of a PICP is less than 14% of the total width of the coal pillar.

When the width of the artificial pillar is 12 m, the top is connected by the plastic zone, and it is very likely to experience catastrophic instability. However, when the width of the artificial pillar is 14 m, the large area is in the elastic zone, and only two sides of the artificial pillar experience compression-shear failure. Thus, the numerical simulation illustrates the failure characteristics of the artificial pillar, which verify the theoretical analysis presented above. The analysis confirms that an artificial pillar width of 13 m is the critical width for catastrophic instability under the conditions of the test area.

5.1.2 Analysis of stope failure laws

When the width of the artificial pillar was set to 14 m, the dynamic evolution process of stope deformation and failure was simulated for three cases: (1) after artificial pillar replacement of the PICP; (2) after the mining of block 1; and (3) after the mining of block 2.

5.1.2.1 Stope failure laws after artificial pillar replacement of the PICP

Figure 9 shows the distribution of the vertical stress and plastic zones in branch roadways and an artificial pillar after replacing the PICP. A rock mass without mining is usually in the elastic deformation state before roadway excavation (Qian et al., 2010). The excavation of the branch roadway and recovery pillar then redistributes the original rock stress. The stress is mostly concentrated in the upper and lower ends of the branch roadway, and the maximum vertical stress reaches 6.63 MPa. The roof of the branch roadway is damaged by tensile and shear stress, but the overall damage of the branch roadway is small.

5.1.2.2 Stope failure laws after mining block 1

After mining block 1 (Figure 10), the immediate roof was in a state of tensile failure in a large area of the stope, and the basic roof plastic zone developed into an inverted funnel shape, while the whole overlaying rock showed failure in the shape of a saddle. Under the influence of mining in block 1, the vertical stress concentration of the left branch roadway increased and the maximum vertical stress reached 9.49 MPa. The roof tensile stress of the branch roadway increased continuously. The mining of block 1 aggravated the destruction of the coal wall and roof of the branch roadway. The artificial pillar only produced a small range of stresses concentrated on one side of the goaf and a small range of shear failure occurred on the immediate upper roof of the artificial pillar. However, the artificial pillar suffered no damage.

Measuring points were arranged along the roof from the branch roadway on the left side of the artificial pillar to the mining boundary of the right goaf to monitor stope roof subsidence. As shown in Figure 11, there was only a little movement in the roof of the branch roadway after mining in block 1 as a result of the load from the overlying rock. After mining block 1, the roof on the branch roadway on the left side of the artificial pillar sank only slightly; the sinking curve of the goaf

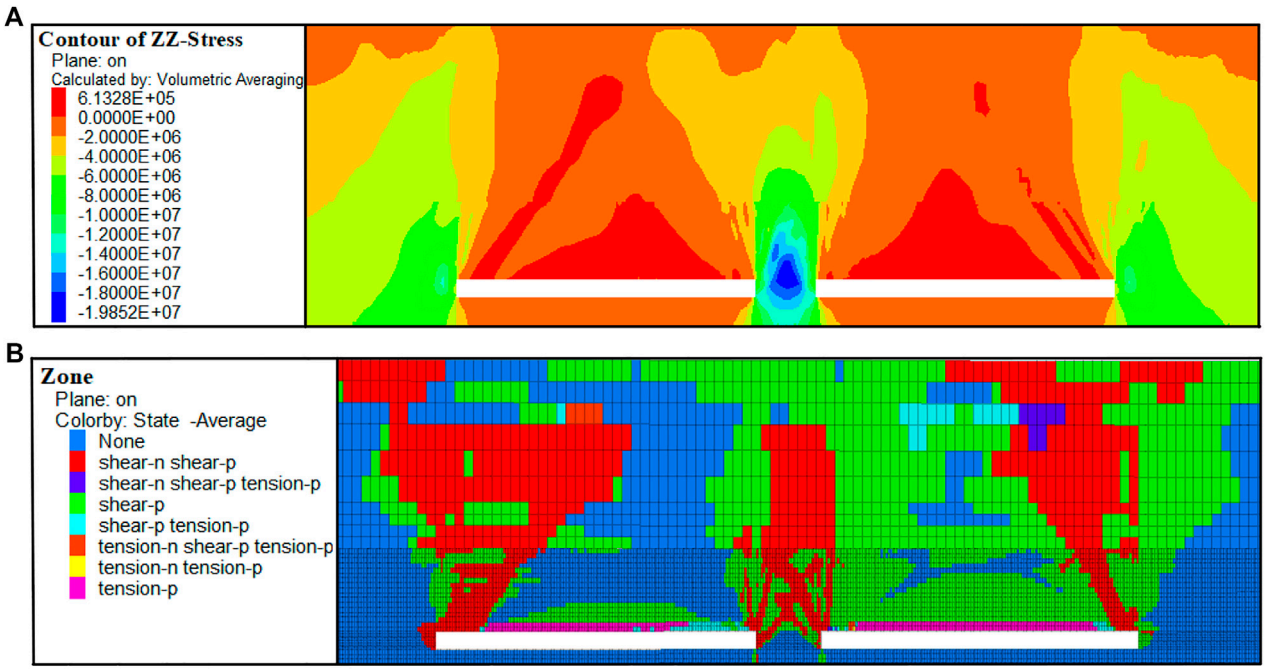

FIGURE 12
Distribution of vertical stress and plastic zones after mining block 2. **(A)** Vertical stress distribution after mining block 2; **(B)** plastic zone distribution after mining block 2.

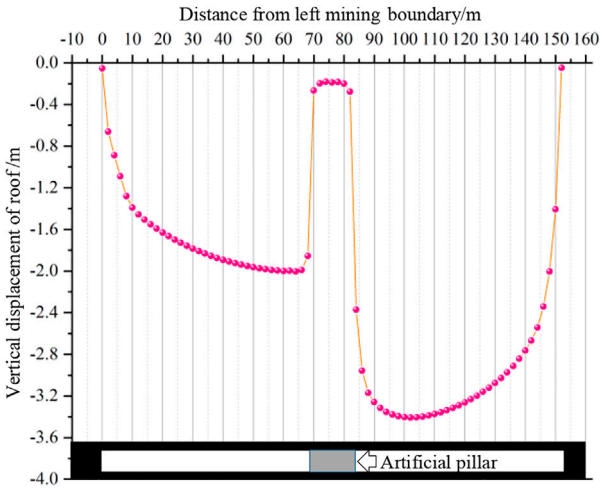

FIGURE 13
Stope roof subsidence after mining block 2.

roof had a single peak of parabolic shape. The maximum sinking position was near the roof span of the goaf 118 m to the left of the mining boundary, and the peak subsidence was 2.12 m. After the mining of block 1, the roof gradually began to break, but the branch roadway and artificial pillar retained good stability.

5.1.2.3 Stope failure laws after mining block 2

The stress on the stope was redistributed after mining block 2, and an artificial pillar-boundary coal-rock cooperative supporting system was formed (Figure 12). The stope stress was mostly concentrated in the roof's upper artificial pillar and the top of the artificial pillar. The abutment pressure exerted by the overlying rock on the artificial pillar presented a bell-shaped distribution, and the maximum vertical stress reached 19.85 MPa. A large area inside the artificial pillar remained in the elastic state without failure. The overlying strata failure degree of block 1 was much greater than that of block 2, and the overlying strata failure of the stope as a whole presented a large saddle shape.

Measuring points were arranged along the left mining boundary to the right mining boundary to monitor the vertical displacement of the stope roof after mining in block 2, as shown in Figure 13. After mining block 2, the stope roof sank significantly. The maximum sinking position of the right goaf shifted from 118 m to 102 m away from the left mining boundary (Figure 11). The maximum sinking position was close to the artificial pillar, and the maximum sinking distance was 3.41 m. The maximum sinking position of the left goaf appeared in the roof of the left side branch roadway of the original artificial pillar, 5 m away from the artificial pillar, and the maximum subsidence was 2 m. The maximum subsidence position of the left and right goaf was close to the artificial pillar. As the artificial pillar limited the roof subsidence of the whole stope, the artificial

FIGURE 14
Artificial pillar backfilling system.

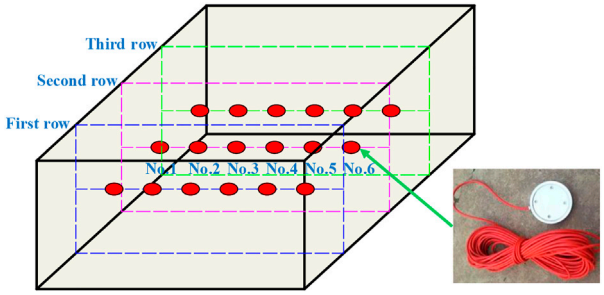

FIGURE 15
Earth pressure cells layout.

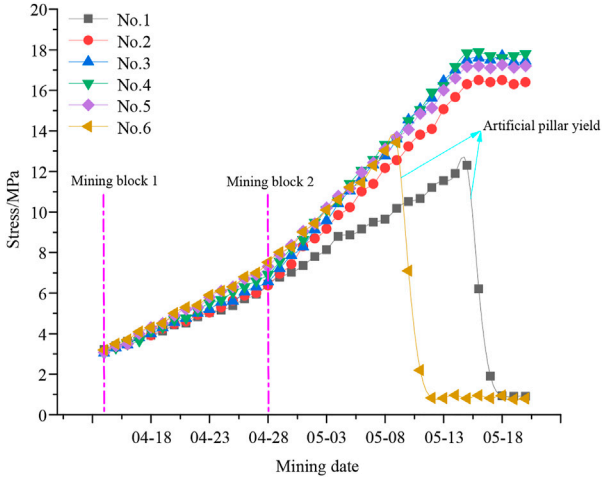

FIGURE 16
Artificial pillar stress–mining date-change curve.

pillar bore a large load, and further compression deformation occurred. The roof subsidence of the whole goaf was large and gradually showed a trend toward collapse. The movement of the overlying strata dominated after the PICP was replaced by the artificial pillar of the new cemented backfill material, and this was consistent with SBM. Although the stability of the artificial pillar was affected by mining disturbance, roof breaking, and subsidence in the goaf, its failure only started after mining block 2 and the failure was a gradual process that significantly contributed to the overall stability of the stope.

From the results of the simulations, we know that the damage to the artificial pillar, the roof of the goaf, and the surrounding rock of the stope followed similar laws, indicating that it was the block mined later that affected the stability of the previously formed goaf and artificial pillar, and that the stability of the stope was greatly affected by the mining. However, a reasonable width for the artificial pillar was effective in decreasing the damage caused by mining.

5.2 Field engineering verification

As shown in Figure 14, the artificial pillar backfilling system used as a test case in the coal mine consisted of systems for weighing and transporting the dry materials, mixing them, and conveying the slurry. The weighing system consisted of a transfer bin and a support. The transfer bin was installed on the support, and the weight loss of the support was determined. The main body of the conveying system for the dry materials was a plate chain conveyor. Its switch was connected to the weight sensors of the support for accurate measurement and stable feeding. The water required to be added to the slurry mixing system for slurry preparation was measured by using a tank with a controlled water height. The slurry mixing system was an intermittent operation two-axle forced mixer. A slurry transfer tank was arranged below the mixer to hold the prepared backfilling slurry. The slurry prepared by the mixing system was put into the transfer tank of the slurry conveying system and transported to the underground artificial pillar backfilling area at a constant speed through a conveying pump. The slurry conveying capacity was 30–50 m^3/h.

Earth pressure cells were installed during the artificial pillar pouring process to monitor its internal stresses. These could be

used to determine whether instability failure of the artificial pillar occurred. Three rows of earth pressure cells with a height of 2 m were arranged in the middle column of the artificial pillar. The height of each earth pressure cell was 2 m, the spacing between each earth pressure cell was 2 m, and a total of 18 cells were installed (No. 1-6 from left to right in Figure 15). A stress-mining date-change curve of the artificial pillar was then drawn using the monitoring data of the second row of earth pressure cells as it was relatively complete (Figure 16).

Figure 16 shows that the stress of the artificial pillar increased during the mining of block 1, and the artificial pillar did not yield until after mining was completed. With the mining of block 2, the stress concentration degree in the artificial pillar also rose. Affected by the mining of block 2, the stress at the No. 6 monitoring point decreased sharply. Therefore, it can be inferred that the artificial pillar began to yield on the side close to block 1, but the yield range did not spread to monitoring point 5. Thus, the yield range was within 4 m. With further mining at block 2, the phenomenon of a sudden stress drop also occurred at the No. 1 monitoring point, indicating that the artificial pillar began to yield on the side close to block 2, and the yield range in the artificial pillar was further expanded. It can be inferred that the yield width was less than 8 m as no sharp decline in stress occurred at monitoring points 2-5. The artificial pillar with a width of 14 m still had an elastic area of at least 6 m without catastrophic instability occurring. Therefore, an artificial pillar with a width of 14 m was reasonable for the conditions in the test area. The field monitoring results verified the theoretical derivation and numerical simulation results presented above.

6 Conclusion

1) This work addresses the low coal-recovery rate and the waste of resources caused by PICPs in SBM by replacing them with artificial cemented pillars. A coal mine test area in northern Shaanxi Province, China, was employed to test the design and operation of an artificial pillar replacement system for PICPs.
2) Using innovative materials ratio tests, appropriate combinations of cemented backfill materials for constructing artificial pillars with reliable strengths were obtained. Their peak strength and residual strength values reached 14.7 and 5.4 MPa, respectively. The optimum mixture mass ratio was cement (1), fluvial sand (1.6), fly ash (2.4), coal gangue (2), steel fiber (0.435), and water (1.312).
3) A cusp catastrophe model of an artificial pillar was established, and the necessary conditions for catastrophic instability were deduced as the stiffness ratio, $k < 1$. The critical width of an artificial pillar in the test area to avoid catastrophic instability was calculated to be 13 m.
4) FLAC3D numerical simulations were used to verify the catastrophe theory analysis. The simulation results showed that when the width of the artificial pillar was 14 m, the failure of the pillar and stope progressed gradually, and no sudden instability occurred. Field monitoring results in the test area verified the theoretical derivation and numerical simulation results, confirming that it was feasible to replace PICPs with cemented artificial pillars with widths of 14 m.

Data availability statement

The original contributions presented in the study are included in the article/Supplementary Materials. Further inquiries can be directed to the corresponding author.

Author contributions

All authors listed have made a substantial, direct, and intellectual contribution to the work and have read and approved it for publication.

Funding

This study was supported by the National Natural Science Foundation of China (51874284, 52274143).

Conflict of interest

The authors declare that the research was conducted in the absence of any commercial or financial relationships that could be construed as a potential conflict of interest.

Publisher's note

All claims expressed in this article are solely those of the authors and do not necessarily represent those of their affiliated organizations, or those of the publisher, the editors and the reviewers. Any product that may be evaluated in this article, or claim that may be made by its manufacturer, is not guaranteed or endorsed by the publisher.

References

Cao, S. G., Cao, Y., and Jiang, H. J. (2014). Research on catastrophe instability mechanism of section coal pillars in block mining. *J. Min. Saf. Eng.* 31 (6), 907–913. doi:10.13545/j.issn1673-3363.2014.06.013

Fu, Q., Yang, K., Liu, Q. J., Liu, S., He, X., and Lyu, X. (2021). Optimization of barrier pillar design in longwall mining with top coal caving in spontaneous combustion coal seam. *Geofluids* 2021, 1–15. doi:10.1155/2021/2749373

Jiang, H. J., Cao, S. G., Zhang, Y., and Wang, C. (2016). Analytical solutions of hard roof's bending moment, deflection and energy under the front abutment pressure before periodic weighting. *Int. J. Min. Sci. Technol.* 26 (1), 175–181. doi:10.1016/j.ijmst.2015.11.027

Li, J. (2021). "Research and application of bearing characteristics of strong-toughness cemented backfilling materials,". Master Thesis (Xuzhou (Jiangsu): China University of Mining and Technology). doi:10.27623/d.cnki.gzkyu.2021.000375

Ma, C. Q., Li, H. Z., and Zhang, P. P. (2017). Subsidence prediction method of solid backfilling mining with different filling ratios under thick unconsolidated layers. *Arab. J. Geosci.* 10 (23), 511–512. doi:10.1007/s12517-017-3303-7

Ma, S. W., Luo, Z. Q., Hu, J. H., Ren, Q. F., Qin, Y. G., and Wen, L. (2019). Determination of intervening pillar thickness based on the cusp catastrophe model. *Adv. Civ. Eng.* 2019, 1–11. doi:10.1155/2019/8253589

Qian, M. G., Shi, P. W., and Xu, J. L. (2010). *Mining pressure and strata control*. Xu Zhou, China: China University of Mining and Technology Press, 197.

Qin, S. Q., Jiao, J. J., Tang, C. A., and Li, Z. G. (2006). Instability leading to coal bumps and nonlinear evolutionary mechanisms for a coal-pillar-and-roof system. *Int. J. solids Struct.* 43 (25-26), 7407–7423. doi:10.1016/j.ijsolstr.2005.06.087

Ran, J. L., Li, T. C., Chen, D. H., Shang, L. M., Li, W. T., and Zhu, Q. W. (2021). Mechanical properties of concrete reinforced with corrugated steel fiber under uniaxial compression and tension. *Structures* 34, 1890–1902. doi:10.1016/j.istruc.2021.08.135

Shi, X. Z., Ke, W. Y., Gou, Y. G., Huo, X. F., and Kan, Z. H. (2020). Optimization of strip pillar size in upper chamber of long-span stope. *J. Min. Saf. Eng.* 37 (06), 1084–1093. doi:10.13545/j.cnki.jmse.2020.06.00

Shun, P., Xu, X. D., Zhou, Y. J., Zang, G. C., and Wang, J. (2021). Investigation of instability and blasting caving technology of composite support structure in the goaf of gypsum mine. *Geotech. Geol. Eng. (Dordr).* 39 (6), 4377–4391. doi:10.1007/s10706-021-01769-0

Sun, Q., Zhang, J. X., and Zhou, N. (2018). Study and discussion of short-strip coal pillar recovery with cemented paste backfill. *Int. J. Rock Mech. Min. Sci.* 104, 147–155. doi:10.1016/j.ijrmms.2018.01.031

Wang, X. R., Guan, K., Yang, T. H., and Liu, X. G. (2021). Instability mechanism of pillar burst in asymmetric mining based on cusp catastrophe model. *Rock Mech. Rock Eng.* 54 (3), 1463–1479. doi:10.1007/s00603-020-02313-x

Xia, K. Z., Chen, C. X., Zhou, Y. C., Liu, X. M., Zheng, Y., and Pan, Y. C. (2019). Catastrophe instability mechanism of the pillar-roof system in gypsum mines due to the influence of relative humidity. *Int. J. Geomech.* 19 (4), 06019004. doi:10.1061/(asce)gm.1943-5622.0001378

Zhang, Q. L., Cao, X. G., Wang, Y. L., and Liu, H. Q. (2011). Stability analysis of stope roof-pillar based on cusp catastrophe model. *China Saf. Sci. J.* 21 (10), 52–57. doi:10.16265/j.cnki.issn1003-3033.2011.10.022

Zhang, Y., Cao, S. G., Guo, S., Wan, T., and Wang, J. J. (2018). Mechanisms of the development of water-conducting fracture zone in overlying strata during shortwall block backfill mining: A case study in northwestern China. *Environ. Earth Sci.* 77 (14), 543–617. doi:10.1007/s12665-018-7726-6

Zhang, Y., Cao, S. G., Lan, L. X., Gao, R., and Yan, H. (2017). Analysis of development pattern of a water-flowing fissure zone in shortwall block mining. *Energies* 10 (5), 734. doi:10.3390/en10050734

Zhang, Y., Cao, S. G., Zhang, N., and Zhao, C. Z. (2020). The application of short-wall block backfill mining to preserve surface water resources in northwest China. *J. Clean. Prod.* 261, 121232. doi:10.1016/j.jclepro.2020.121232

Zhang, Y., Liu, Y. Z., Lai, X. P., and Gao, J. M. (2021a). Physical modeling of the controlled water-flowing fracture development during short-wall block backfill mining. *Lithosphere* 2021 (4), 2860087. doi:10.2113/2021/2860087

Zhang, Y. L., Wang, B. K., Zhang, X. F., and Li, F. Q. (2021b). Forty years' development and future prospect on mechanized short-wall mining technology with continuous miner in China. *J. China Coal Soc.* 46 (01), 86–99. doi:10.13225/j.cnki.jccs.2020.1632

Zhou, M. P., Cao, S. G., and Jiang, X. J. (2014). The law of rock pressure in the stope with blocking mining by the continuous miner. *J. Min. Saf. Eng.* 31, 413–417. doi:10.13545/j.issn1673-3363.2014.03.013

Zhou, N., Yan, H., Jiang, S. Y., Sun, Q., and Ouyang, S. Y. (2019). Stability analysis of surrounding rock in paste backfill recovery of residual room pillars. *Sustainability* 11 (2), 478. doi:10.3390/su11020478

Zhou, Y. J., Li, M., Xu, X. D., Li, X. T., Ma, Y. D., and Ma, Z. G. (2018a). Research on catastrophic pillar instability in room and pillar gypsum mining. *Sustainability* 10 (10), 3773. doi:10.3390/su10103773

Zhou, Y. J., Xu, X. D., Li, X. T., Li, M., and Yang, Y. G. (2018b). Study on catastrophe instability of support system in gypsum goaf based on energy dissipation theory. *Adv. Civ. Eng.* 2018, 1–9. doi:10.1155/2018/4293584

frontiers | Frontiers in Earth Science

TYPE Original Research
PUBLISHED 30 January 2023
DOI 10.3389/feart.2022.1098674

OPEN ACCESS

EDITED BY
Yun Zhang,
Xi'an University of Science and Technology, China

REVIEWED BY
Yang Xiao,
Xi'an University of Science and Technology, China
Nan Zhou,
China University of Mining and Technology, China

*CORRESPONDENCE
Tianqi Song,
songtianqi2023@163.com

SPECIALTY SECTION
This article was submitted to Structural Geology and Tectonics, a section of the journal Frontiers in Earth Science

RECEIVED 15 November 2022
ACCEPTED 09 December 2022
PUBLISHED 30 January 2023

CITATION
Gu W, Zhu L and Song T (2023), Research on key parameters of pipeline transportation of waste rock treatment in underground residual space. *Front. Earth Sci.* 10:1098674. doi: 10.3389/feart.2022.1098674

Research on key parameters of pipeline transportation of waste rock treatment in underground residual space

Wenzhe Gu[1,2], Lei Zhu[2] and Tianqi Song[2]*

[1]School of Energy and Mining Engineering, China University of Mining and Technology (Beijing), Beijing, China, [2]China Coal Energy Research Institute Co, Ltd, Xi'an, China

As the key link of coal gangue slurry filling, slurry pipeline transportation is an important guarantee to realize the slurry mixing and safe transportation of gangue from solid powder. To realize the underground excavation gangue of the Huangling No. 2 coal mine without raising the ground, the slurry filling technology is proposed to transport the slurry made by gangue through the pipeline and fill it into the goaf. The phase composition and microstructure characteristics of underground excavation gangue in the Huangling No. 2 coal mine were analyzed by X-ray diffraction and an electron microscope scanning test, the slurry-forming properties of gangue powder with different particle sizes and gradations were studied, and the influence of gangue slurry concentration on its rheological properties was analyzed. The experimental results show that the gangue powder crushed using a cage crusher can be made into stable slurry when the particle grading size is the natural crushing gradation with the upper limit of particle size less than 3 mm. The viscosity of the slurry is positively correlated with the concentration. When the concentration is below 70%, the increase in viscosity is small, and when the concentration is above 70%, the increase in viscosity is significant. It is determined that the concentration of the Huangling No. 2 coal mine slurry is 70%. Based on the determination of slurry preparation parameters, the simulation analysis of slurry pipeline transportation was carried out, the influence of design velocity on the velocity distribution of the pipeline section and the variation law of slurry concentration was explored, and the design velocity of the project is determined to be 1.5 m/s. The engineering practice shows that the slurry preparation parameters are reasonable. The crushing and pulping of gangue under the ground and the safe transportation of a 6 km pipeline are realized, which provides a reference for similar engineering projects.

KEYWORDS

slurry pipeline transportation, gangue slurry filling technology, particle size and grading, design velocity, gangue disposal

1 Introduction

Gangue slurry filling is a technical method of crushing gangue into powder to produce slurry, which is transported through a pipeline and injected into the goaf of the working face. It can effectively solve the problem of green disposal of gangue faced by the coal industry (Matousek, 2002; Senapati and Mishra, 2017; Wang et al., 2018; Cruz et al., 2019), and its technical key lies in the reasonable determination of the main parameters of gangue slurry pulping and pipeline transportation, to ensure the long-distance safe transportation of slurry (Chen et al., 2015). The slurry pipeline transportation technology can use the small pipeline to complete the efficient transportation and backfilling of gangue, which has little impact on the normal production of underground coal mines (Qi et al., 2018; Wu et al., 2018; Rao et al., 2020; Wu et al., 2022). This technology has been continuously applied in engineering practice with its unique technical advantages (Hz et al., 2017; Singh et al., 2017), but it still needs to be continuously developed and improved to adapt to the transportation of different materials and different working conditions. Therefore, scholars at home and abroad have conducted many experiments and research studies.

Jaworska-Jóźwiak (2021) studied the influence of solid concentration on the shear stress and viscosity of lime slurry, obtained the variation characteristics of shear stress with concentration in different concentration ranges, and pointed out that the determination of the boundary concentration above which the increase in shear stress is exponential is a fundamental guideline in determining the transport parameters of fine-dispersive lime slurry. Through this method, the transportation efficiency and water consumption of the slurry pipeline transportation system are greatly improved. Singh et al. (2015) investigated the effect of particle size, solid concentration, and temperature on the rheology of the coal–water slurry through rheological and settlement experiments; the relationship between the slurry concentration and apparent viscosity of the coal–water mixture under different particle-size conditions was obtained, the transformation characteristics of the coal–water mixture state were analyzed, and the rheological model was obtained by fitting the change in the flow behavior of coal slurries. Feng et al. (2022) found that the flow velocity directly affects the transportation properties and then affects the pipe blockage and wear during the pipeline transportation of backfill slurry. Through experiments, the movement characteristics of solid materials in slurry at different flow rates were studied. The research results provide a reference for determining the reasonable flow rate of backfill slurry pipeline transportation. Li MZ (Senapati and Pothal, 2017; Li et al., 2018; Cheng et al., 2020; Li et al., 2020) analyzed the influence of the interaction between particles of different sizes on the particle dynamics, studied the influence of adding finer particles on the transport characteristics of the slurry in pipelines, and obtained the relationship between the main parameters of slurry and the movement law of solid particles during pipeline transportation.

The aforementioned scholars have carried out detailed studies on the function relationship of key parameters in the process of slurry pipeline transportation, which enriched the technical system of slurry pipeline transportation. Based on the previous research results, taking the second-phase slurry filling project of the Huangling No. 2 coal mine as the background, this study determined the key parameters of gangue slurry preparation on the basis of mastering the basic physical and chemical characteristics of gangue and slurry through on-site gangue sampling, physical and chemical analysis, slump and rheological experiments and determined the core parameters of slurry pipeline transportation through numerical simulation and analysis. The research results provide support for the industrial application of the grouting filling project for the green disposal of gangue in the Huangling No. 2 coal mine.

2 Engineering background

The Huangling No. 2 coal mine is located in Yan'an City, Shaanxi Province. The designed production capacity of the mine is 10.0 Mt/a. and the underground roadway excavation produces gangue of 0.2 Mt/a. As the minefield is located in the Huangling National Forest Park Reserve, to avoid environmental pollution caused by the ground discharge of gangue, the mine plans to use the method of gangue slurry filling to convert the gangue into slurry and inject it into the goaf.

The gangue slurry filling project of the Huangling No.2 coal mine is divided into two phases. The first phase of the project arranges the crushing and pulping system near the roadway of the working face. The gangue excavated underground was transported to the crushing and pulping system by car. After converting it into slurry, it was transported and injected into the goaf of the working face by the pipeline. The advantage of this arrangement is that the slurry pipeline transmission distance is short, usually less than 3 km, but the filling system only serves one working face, and its position will move continuously with the continuity of the working face. At present, the Huangling No. 2 coal mine has completed the first phase of the project, which has successfully verified the feasibility of slurry filling technology. Now the coal mine plans to carry out the second phase of the project. The second phase adopts a centralized layout, and the filling system is arranged near the gangue bin at the bottom of the shaft to make it serve the whole mine. However, this centralized layout mode has the disadvantage of a long slurry transportation distance, up to 6 km. Therefore, to ensure the success of the project, it is necessary to study the key parameters of gangue slurry preparation and pipeline transportation in detail. The system layout of phase II is shown in Figure 1.

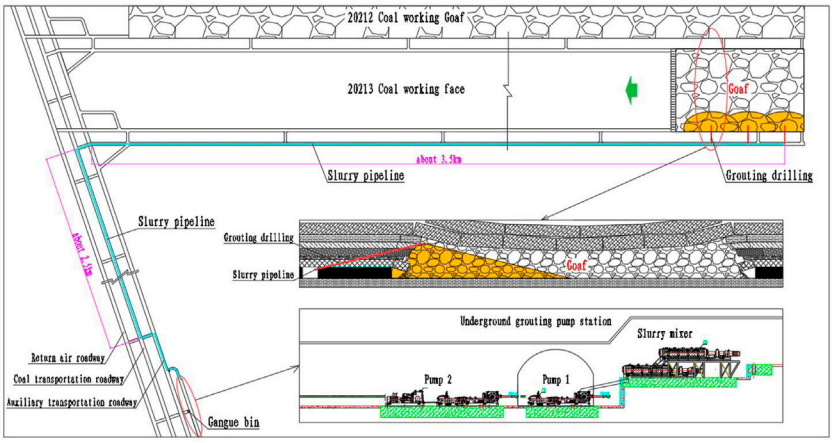

FIGURE 1
Slurry filling system layout of phase II in the Huangling No. 2 coal mine.

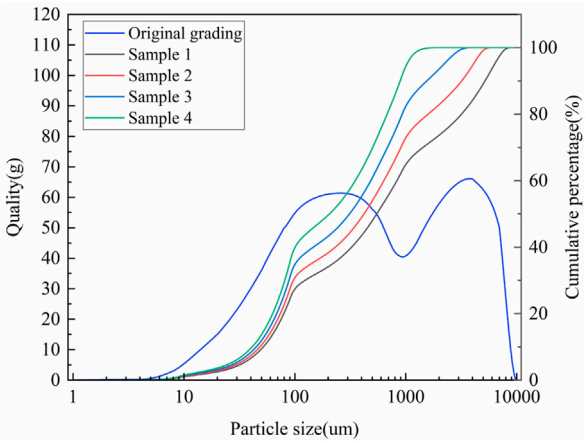

FIGURE 2
Particle size distribution curve of the gangue sample.

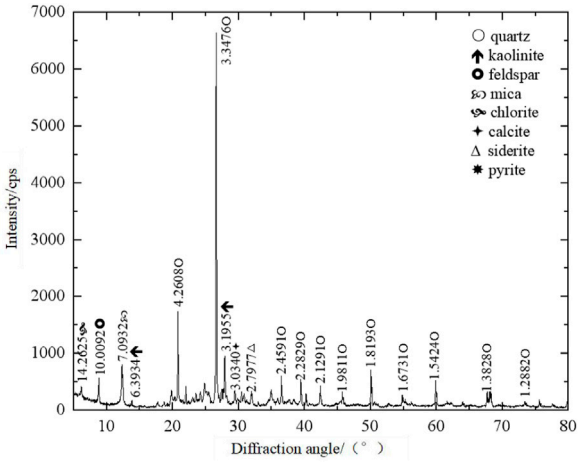

FIGURE 3
X-ray diffraction pattern of coal gangue.

3 Experiment on physicochemical properties and parameter determination of gangue slurry

3.1 Analysis of material source and physicochemical properties

3.1.1 Material source

To ensure the accuracy and credibility of the experimental results, the gangue used in this experiment was taken from the gangue bin of the Huangling No. 2 coal mine through field sampling. The particle size of the sampled gangue is −200 mm. Before the experiment, it was crushed to a particle size of −8 mm using a double-toothed roll crusher and a cage crusher. Combined with the actual situation of the project, the method of controlling the upper limit was used to change the particle size gradation of gangue powder, and the particle size and gradation within the limit were not adjusted. The powder with the upper limit of −8 mm, −5 mm, −3 mm, and −1.25 mm is named sample 1, sample 2, sample 3, and sample 4, respectively. Statistics of the particle size distribution curves of the four groups of gangue powder samples are shown in Figure 2.

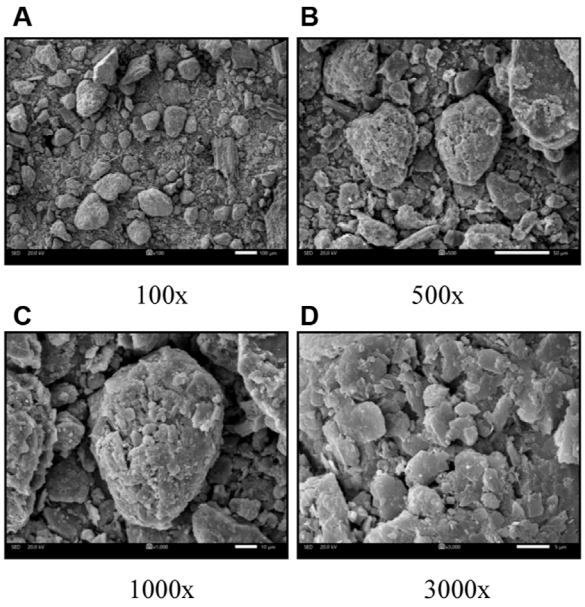

FIGURE 4
SEM scanning picture. **(A)** 100x, **(B)** 500x, **(C)** 1,000x, and **(D)** 3,000x.

3.1.2 Physicochemical properties of gangue powder

The composition of gangue powder is tested using an X-ray diffractometer, and the test results are shown in Figure 3.

According to the standard powder diffraction data of various substances provided by the National Data Center of the Powder Diffraction Federation (TCPDS-ICDD), a comparative analysis was carried out according to the standard analysis method. The analysis results are as follows: the phase composition mainly includes quartz, kaolinite, some feldspar, mica, and a small amount of chlorite, calcite, siderite, pyrite, and other minerals.

To characterize the appearance of the crushed gangue particles, the scanning electron microscope test was carried out on them. Under the condition of high magnification (shown in the 1,000x picture), it can be seen that there are some cracks on the surface and the surface is uneven, as shown in Figure 4.

Combined with the test results of the X-ray diffraction energy spectrum, the gangue contains more kaolinite (flaky) and other minerals, and a small amount of "large" particles are wrapped by a large number of small particle sizes and flaky particles. In the pulping process, flaky kaolin minerals can be used as fine particles to wrap and suspend the gangue with large particle size, which is conducive to ensuring the stability of the slurry and realizing long-distance stable transportation (Sadrossadat et al., 2020).

3.2 Slump test of gangue slurry

To study the influence of the particle size and gradation of crushed gangue powder on the quality of slurry preparation, four groups of gangue samples with different particle sizes and gradations were configured into slurry with the concentration of 65%, 70%, and 75% respectively. No other additives or curing agents are added to the gangue slurry. The fluidity and stability of the configured slurry were studied through a slump experiment. The experiment process and results are shown in Figure 5, 6.

The experiment results show that the slump of sample 1 is 283 mm at the concentration of 65%, and the stability and fluidity of the slurry are relatively good, but the distribution of large particles in the slurry can be clearly seen from the diffused slurry. When the concentration increases to 70% and 75%, there is an obvious material accumulation shape in the middle of the slump experiment, which indicates that the stability of the slurry is poor, easy to precipitate, and insufficient to form a stable and fluid slurry. The experiment results of sample 2 are better than those of sample 1. However, when the slurry concentration reaches 75%, there is also an obvious precipitation and accumulation due to the large solid material particles. When the upper limit of the particle size of gangue is reduced to less than 3mm, the experimental results of samples 3 and 4 show that the stability of the gangue slurry is good, the slurry basically remains homogeneous in the diffusion process, and there is no obvious accumulation of large particles in the middle. Therefore, it is considered that the gangue powder with particle grading of samples 3 and 4 can be made into stable slurry (Lee et al., 2009; Zhou et al., 2021).

Through the analysis of the four groups of gangue slump experiments with different particle sizes and gradations, the results show that the larger the content of coarse particles in the slurry, the worse its stability because the coarse particles are easily precipitated in the slurry flow process and cannot form a stable slurry (Vlasak and Chara, 2011; Li et al., 2022; Matoušek et al., 2022). When the particle grading size of the gangue powder is the natural crushing gradation with the upper limit of particle size less than 3 mm, it can be configured into slurry with good stability, that is, samples 3 and 4 meet the requirements of pulping. Therefore, to ensure the stability of the slurry and reduce the crushing cost of the gangue as much as possible, sample 3 is determined to be used as the gangue powder of the project, that is, it is determined to use the natural crushing gradation gangue powder with the upper limit of particle size of 3 mm for pulping.

3.3 Analysis of the rheological properties of gangue slurry

On the basis of determining the particle size and gradation of the gangue powder, the gangue slurry with a mass concentration

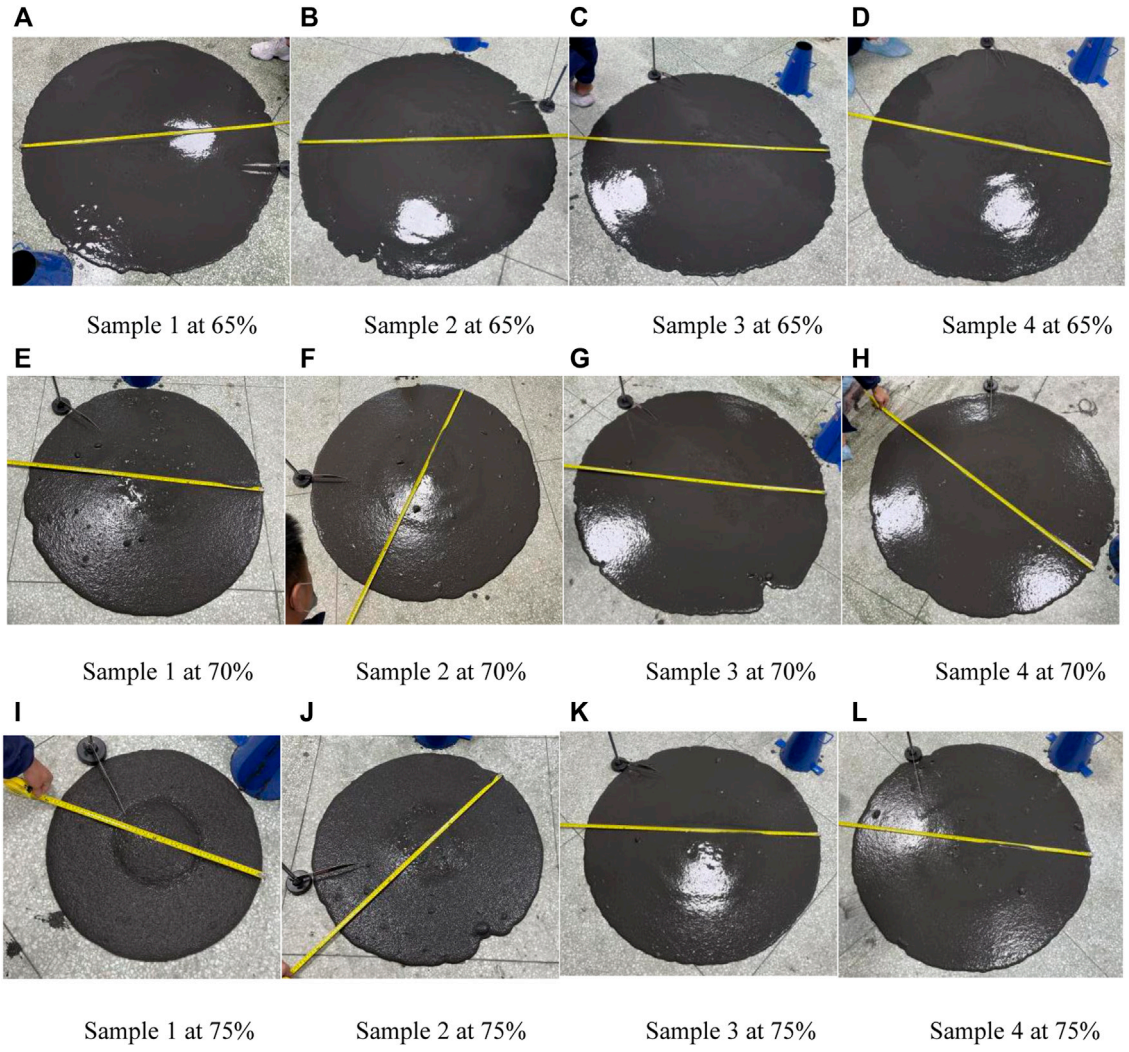

FIGURE 5
Slump test of gangue slurry with different concentrations. **(A)** Sample 1 at 65%, **(B)** sample 2 at 65%, **(C)** sample 3 at 65%, **(D)** sample 4 at 65%, **(E)** sample 1 at 70%, **(F)** sample 2 at 70%, **(G)** sample 3 at 70%, **(H)** sample 4 at 70%, **(I)** sample 1 at 75%, **(J)** sample 2 at 75%, **(K)** sample 3 at 75%, and **(L)** sample 4 at 75%.

of 66%–76% was prepared, and the rheological properties of the gangue slurry were tested using an Anton Paar rheometer. The test was conducted in the shear mode. The rheological characteristic curves of slurries with different concentrations are sorted out according to the experimental test results, as shown in Figure 7.

It can be seen from Figure 7 that the shear stress of gangue slurry generally shows an increasing trend with the increase in the shear rate. When the slurry concentration is in the range of 66%–74%, the increase in the shear stress of slurry is gentle with the increase of shear rate. When the slurry concentration reaches 76%, the shear stress increases obviously with the increase in the shear rate. At the same shear rate, when the slurry concentration is less than 70%, the shear stress increases slightly with the increase of the slurry concentration. When the slurry concentration is less than 70%, the shear stress increases obviously with the increase in the slurry concentration.

The experimental results show that the higher the concentration, the greater the shear stress and shear rate required for the elastoplastic state transition of the slurry under the same particle size gradation. It can be seen from the analysis that the greater the concentration of coal gangue slurry is, the greater the force between the particles in the gangue slurry is, and the gangue particles are firmly bonded. Therefore, a larger shear force and shear rate are required to change the elastic state. The smaller the concentration of coal gangue slurry is, the weaker the internal structure of the slurry is and the easier it is to cause the coarse particles of the gangue to sink, causing

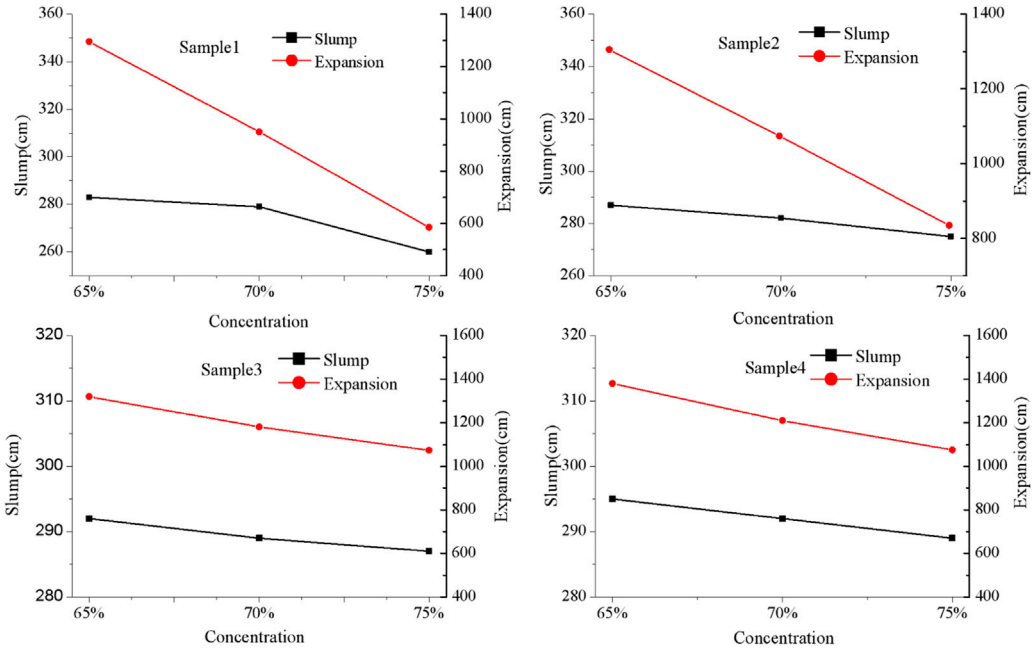

FIGURE 6
Slump test results of gangue slurry.

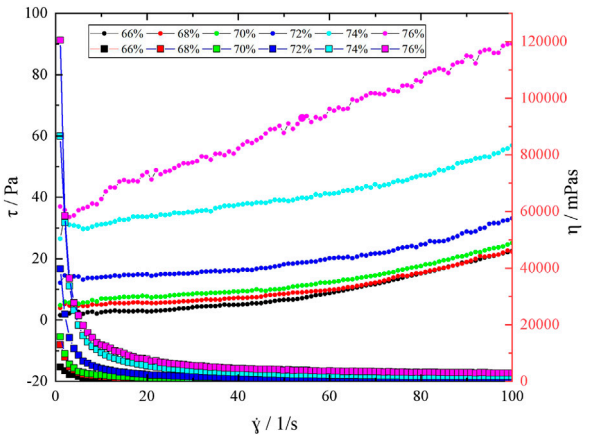

FIGURE 7
Rheological characteristic curve of gangue slurry with different concentrations.

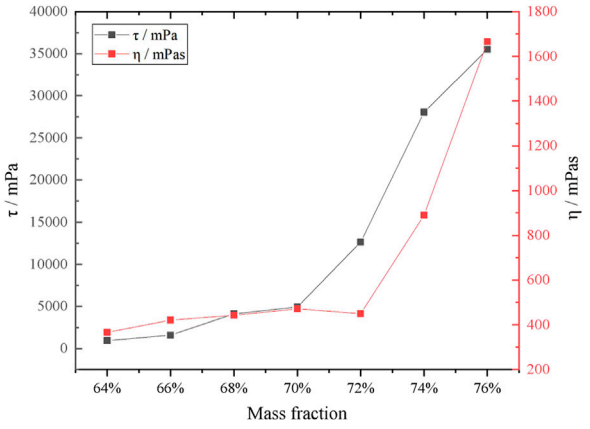

FIGURE 8
Relationship between the shear stress and viscosity of slurry with concentration.

segregation. According to the rheological experimental data, the relationship between the shear stress and viscosity of the slurry with different concentrations is drawn, as shown in Figure 8.

Figure 8 shows that the plastic viscosity and yield stress of gangue slurry generally increase with the increase in concentration (Singh et al., 2020). However, the changes in different concentration ranges are different. In the range of 66–70%, the plastic viscosity of the slurry increases slowly with the increase in the concentration. When the slurry concentration is greater than 70%, the plastic viscosity of the slurry increases rapidly with the increase in the concentration. In the range of 66–72%, the yield stress of the slurry increases slowly with the increase in the concentration. When the slurry

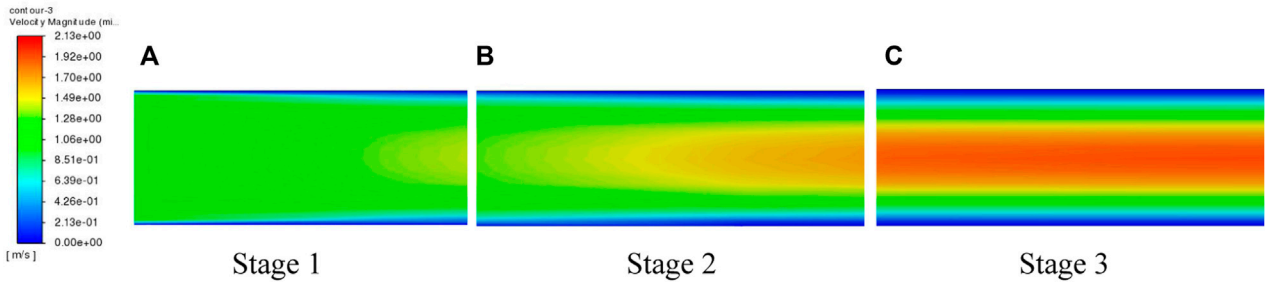

FIGURE 9
Velocity distribution cloud diagram in the pipeline section. **(A)** Stage 1. **(B)** Stage 2. **(C)** Stage 3.

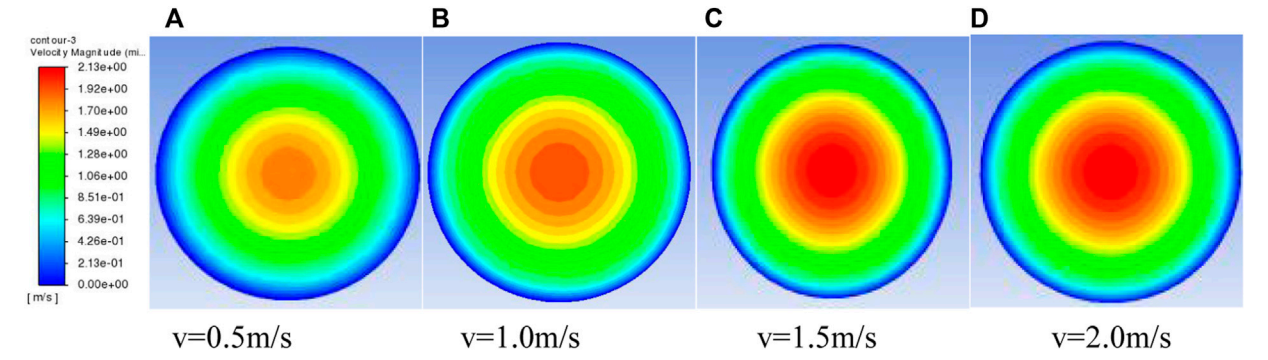

FIGURE 10
Velocity distribution cloud diagram of the pipeline section under different flow velocities. **(A)** v=0.5 m/s. **(B)** v=1.0 m/s. **(C)** v=1.5 m/s. **(D)** v=2.0 m/s.

concentration is greater than 72%, the yield stress of the slurry increases rapidly with the increase in the concentration. After the slurry concentration continues to increase to a certain extent, minor changes will have a significant impact on the viscosity. In order to ensure the safe transportation of the slurry, the concentration of the slurry prepared in this test is determined to be 70%.

4 Numerical simulation analysis of slurry pipeline transportation

The gangue slurry shows complex mechanical phenomena in the process of pipeline transportation. At present, there is no accurate method to describe the flow characteristics of slurry in the pipeline (Gao et al., 2020). To study the internal particle migration law during the pipeline transportation of gangue slurry, Ansys Fluent software is used to simulate the pipeline transportation of high-concentration gangue slurry, study the micro-velocity distribution law of gangue slurry during pipeline transportation, and analyze the solid particle settlement law, so as to reasonably design the transportation velocity and ensure the safe operation of the system.

4.1 Establishment of the experimental model

The Euler model is selected as the calculation model of this experiment, and the model is set as the standard K-εModel (Rathore et al., 2021). The geometric model is set according to the actual transportation conditions of the Huangling No. 2 coal mine, and an additional 4-km horizontal pipeline is set, that is, the total length of the model pipeline is 10 km, and the pipeline diameter is 99 mm.

The flow medium in the pipeline is the solid–liquid two-phase flow mixed with water and gangue particles. The liquid phase and solid phase are set at the inlet of the pipeline, in which the water density is 1,000 kg/m^3 and the gangue density is 2,340 kg/m^3. The particle-size grading of the gangue powder and the viscosity of the slurry are set according to the experimental test results.

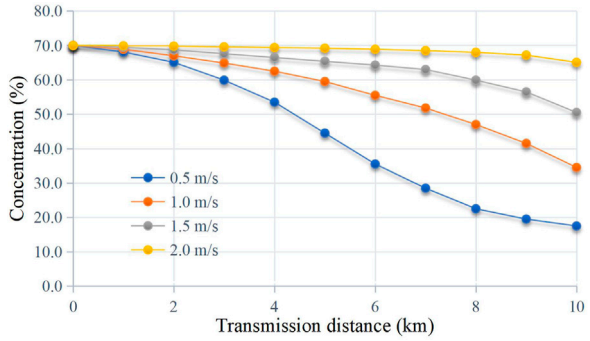

FIGURE 11
Concentration variation diagram of slurry under different flow velocities.

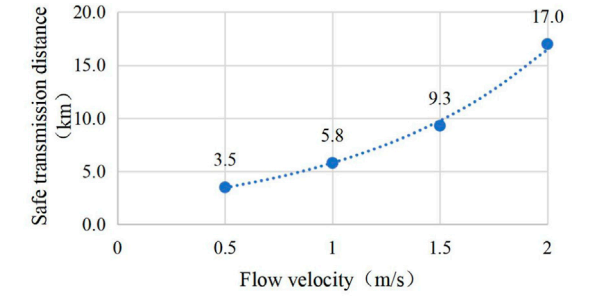

FIGURE 12
Relationship between safe transmission distance and design velocity.

This numerical simulation takes the gangue slurry with 70% concentration as the basic condition, and takes the slurry inlet velocity as the main factor to simulate the movement law of slurry in the pipeline during the transportation at the velocity of 0.5 m/s, 1.0 m/s, 1.5 m/s, and 2.0 m/s, respectively, so as to reasonably determine the transportation velocity of the industrial project.

To master the velocity, concentration distribution and change characteristics of the slurry in the pipeline under different working conditions, the velocity, concentration, and other data in the whole pipeline are monitored to analyze the stability of slurry pipeline transportation.

4.2 Analysis of experimental results

4.2.1 Velocity distribution law of the pipeline section

4.2.1.1 Velocity distribution characteristics under different conveying distances

The velocity distribution cloud maps at different positions in the model are extracted. The maps show that the cross-section velocity of the pipeline experiences the process from uniformity to stratification and then to stability in the process of slurry pipeline transportation, which can be roughly divided into three stages. Stage 1: the velocity in the pipeline section is evenly distributed, stage 2: the velocity increases in the center of the pipeline, and stage 3: the velocity distribution in the pipeline is stable, as shown in Figure 9.

Due to the same inlet velocity, the slurry flow velocity in the pipe section at the initial stage of transportation is basically uniform. With the increase of the conveying distance, the influence of friction between the slurry and pipe wall on the slurry movement gradually appears, resulting in the decrease in slurry velocity around the pipe wall. On the condition that the flow is constant, the velocity of the slurry in the center of the pipeline increases gradually, and finally, the velocity of the pipeline section is relatively stable.

4.2.1.2 Velocity distribution characteristics of the pipeline section in equilibrium state

The velocity distribution cloud diagram of the pipeline section when the velocity of the gangue slurry reaches the equilibrium state at different initial velocities during pipeline transportation is shown in Figure 9. It can be seen from Figure 10 that ① the conveying speed of the slurry in the pipeline section is distributed in a concentric circle, and the velocity distribution in the vertical and horizontal directions inside the pipeline is basically symmetrical. The velocity of slurry at the center of the pipeline is higher and that at the pipe wall is lower. ② According to the velocity distribution of slurry at the pipeline section, the section velocity of slurry is divided into a middle-flow core area and non-flow core area. When the inlet velocity increases from 0.5 m/s to 2.0 m/s, the range of the flow core area gradually increases, and the range of the low-velocity area near the pipe wall gradually decreases.

In the process of slurry pipeline transportation, when the transportation velocity is greater than the critical velocity, the slurry mainly moves in suspension, and the slurry stability is good. When the transportation velocity is less than the critical velocity, the slurry obviously has stratified movement and the solid particles in the bed will settle, which is not conducive to the safe transportation of the slurry.

According to the simulation calculation results, the slurry transportation velocity data at 0.05 d from the center line of the pipeline to the bottom are extracted after the slurry transportation velocity distribution in the pipeline section is stable under different design flow velocity conditions. The data show that when the inlet velocity increases from 0.5 m/s, 1.0 m/s, and 1.5 m/s to 2.0 m/s, the flow velocities at the measuring points near the pipe wall are 0.05 m/s, 0.06 m/s, 0.19 m/s, and 0.38 m/s, respectively, and the flow velocity at the pipe wall increases significantly.

To sum up, the design velocity of slurry pipeline transportation directly affects the movement state of slurry in

FIGURE 13
Actual picture of filling operation.

the pipeline (Pinto et al., 2014; Singh et al., 2019). The larger the conveying speed, the larger will be the flow core area, and the slurry mainly moves in suspension. The smaller the conveying speed, the larger will be the non-flow core area, and the smaller the velocity of slurry near the pipe wall, the more obvious the slurry movement. Due to the settlement characteristics of gangue slurry, the stability is relatively low. Therefore, the conveying speed should be guaranteed during the conveying process. Considering the numerical simulation results and similar engineering experience, it is preliminarily determined that the slurry conveying speed should be greater than 1.0 m/s.

4.2.2 Velocity distribution law of the pipeline section

Whether the gangue slurry can be stably transported in the pipeline mainly depends on the movement state of the slurry (Chen et al., 2017). Ideally, the slurry transportation velocity is greater than the critical velocity to ensure that the slurry is in a turbulent state. However, according to the simulation results of slurry pipeline transportation velocity distribution, the velocity of slurry in the pipeline section will be redistributed due to the friction of the pipe wall. Even if the transportation velocity is greater than the critical velocity, the velocity of the slurry near the pipe wall during the transportation is relatively low. Therefore, the slurry near the pipe wall will have a push movement. During the push movement, the solid particles in the slurry will settle. With the increase of the transportation distance, the range of the push layer will continue to stack, which will eventually lead to the change in the slurry concentration in the pipeline (Calderon-Hernandez et al., 2020).

According to the calculation results, combined with the identification method of slurry quasi-homogeneous flow in engineering applications, the slurry mass concentration data at the top of the pipe (0.92 D from the bottom of the pipe) under different inlet speeds and different transportation distances are extracted, as shown in Figure 11.

Figure 11 shows that the slurry concentration changes during pipeline transportation, the concentration at the top of the pipeline gradually decreases, and the concentration at the bottom gradually increases. In general, the slurry shows sedimentation during transportation. With the increase in the transportation distance, the slurry settlement becomes more obvious. Under the same transportation distance, when the transportation speed increases from 0.5 m/s to 2.0 m/s, the smaller will be the change in the slurry concentration at the top of the pipeline, indicating that the stability of slurry transportation is better.

The ideal state of slurry pipeline stable transportation is homogeneous flow, but it is difficult to realize in practical engineering, so pseudo-homogeneous flow is usually used to judge whether the slurry can be transported safely. According to the engineering design standard for long-distance pipeline transportation of slurry, the pseudo-homogeneous flow needs to meet the requirements of $C/C_a \geq 0.8$ (where C is the concentration at 0.92 Dn from the inner bottom of the pipe; C_a is the concentration at 0.5 Dn from the inner bottom of the pipe). By calculating the numerical simulation results according to this standard, the safe transportation distance of slurry at each transportation speed can be obtained, as shown in Figure 12. It can be

seen that when the inlet speed is 0.5 m/s, 1.0 m/s, 1.5 m/s, and 2.0 m/s, the safe transmission distance is 3.5 km, 5.8 km, 9.3 km, and 17.0 km, respectively.

4.2.3 Determination of design velocity

Through the aforementioned analysis, it can be seen that the design velocity of slurry pipeline transportation has a direct impact on the velocity distribution and settlement characteristics of the slurry. To ensure that the slurry is in a turbulent state and reduce the risk of pipe blockage caused by coarse particle deposition during slurry transportation, it is recommended that the transportation speed should be greater than 1.0 m/s by comprehensively considering the numerical simulation results and similar engineering experience. On this basis, by analyzing the settlement characteristics of slurry pipeline transportation, the safe transportation distance under each flow velocity is simulated and calculated. Combined with the actual working conditions of the project—the transportation distance is about 6 km—the transportation velocity of the slurry pipeline in the Huangling No. 2 coal mine is determined to be 1.5 m/s.

5 Engineering practice

According to the research results, the Huangling No. 2 coal mine has completed the construction of an underground filling system. The excavated gangue is crushed from −300 mm to −3 mm through the three-level crushing system of a single-toothed roll crusher, a toothed roll crusher, and a squirrel cage crusher. Then, the unqualified powder of + 3 mm is removed by the relaxation screen with a hole diameter of 3 mm, and the gangue powder of −3 mm under the screen enters the horizontal mixer and is mixed with water into slurry with a mass concentration of 70%. Finally, the qualified slurry is pumped to the filling working face at a flow rate of 1.5 m/s through a slurry pipe with a diameter of 100 mm. Field operations are shown in Figure 13.

During field operation, through real-time monitoring of key positions of the slurry transmission pipeline, the data show that the pipeline pressure is normal. Before and after each operation, the underground staff carried out the clean water flushing process. During the whole joint commissioning process, there was no slurry sedimentation and pipe blockage, which was successfully applied.

6 Conclusion

Based on the second-phase grouting project of the Huangling No. 2 coal mine, to ensure the safe transportation of the gangue slurry to the working face and realize the filling of underground goaf, this paper systematically studies the key parameters of coal gangue slurry preparation and pipeline transportation through on-site sampling, laboratory experiments, and numerical simulation, combined with theoretical analysis. The main findings are as follows:

1) The coal gangue particle size grading with the upper limit of crushing particle size of 3 mm can be made into stable slurry, and the viscosity of the slurry is positively correlated with the concentration. When the concentration is below 70%, the viscosity growth is small, and when the concentration is above 70%, the viscosity growth significantly increased.
2) The transportation velocity of coal gangue slurry is distributed in concentric circles along the radial direction of the pipeline. The flow velocity of the pipeline section can be divided into the flow core zone with higher velocity in the middle and the non-flow core zone with lower velocity near the pipe wall. With the increase in the inlet velocity, the velocity near the pipe wall increases and the stability of slurry transportation increases. At the same time, with the increase in the conveying distance, the slurry sedimentation characteristics become increasingly prominent.
3) During the industrial test of grouting filling in the Huangling No. 2 coal mine, the upper limit of the gangue particle size is 3 mm, the slurry concentration is 70%, and the pipeline transportation speed is 1.5 m/s. The stability of slurry transportation is good during field operation.

Data availability statement

The original contributions presented in the study are included in the article/Supplementary Material; further inquiries can be directed to the corresponding author.

Author contributions

LZ contributed to the conception of the study and helped perform the analysis with constructive discussions. WG performed the experiment and contributed significantly to analysis and manuscript preparation; TS performed the data analyses and wrote the manuscript.

Funding

This work was supported by the Key Science and Technology Projects of China Coal Group “Research on theory, technology and equipment of four-dimensional collaborative backfill of slurry pipeline in mining overburden fracture area of coal mine” (ZMYXM*CK-023).

Conflict of interest

Authors LZ and TS are/were employed by China Coal Energy Research Institute Co., Ltd.

The remaining author declares that the research was conducted in the absence of any commercial or financial relationships that could be construed as a potential conflict of interest.

Publisher's note

References

Calderon-Hernandez, J. W., Sinatora, A., de Melo, H. G., Chaves, A. P., Mano, E. S., Leal Filho, L. S., et al. (2020). Hydraulic convey of iron ore slurry: Pipeline wear and ore particle degradation in function of pumping time. *Wear* 203272, 450–451. doi:10.1016/j.wear.2020.203272

Chen, D., Jiang, X., Lv, S., Lv, G., Ma, Z., Yan, J., et al. (2015). Rheological properties and stability of lignite washery tailing suspensions. *Fuel* 141, 214–221. doi:10.1016/j.fuel.2014.10.067

Chen, X., Zhou, J., Chen, Q., Shi, X., and Gou, Y. (2017). CFD simulation of pipeline transport properties of mine tailings three-phase foam slurry backfill. *Minerals* 7 (8), 149–168. doi:10.3390/min7080149

Cheng, H., Wu, S., and Zhang, X. (2020). Effect of particle gradation characteristics on yield stress of cemented paste backfill. *Int. J. Min. Metall. Mat.* 27 (1), 10–17. doi:10.1007/s12613-019-1865-y

Cruz, N., Forster, J., and Bobicki, E. R. (2019). Slurry rheology in mineral processing unit operations: A critical review. *Can. J. Chem. Eng.* 97 (7), 2102–2120. doi:10.1002/cjce.23476

Feng, G., Wang, Z., Qi, T., Du, X., Guo, J., Wang, H., et al. (2022). Effect of velocity on flow properties and electrical resistivity of cemented coal gangue-fly ash backfill (CGFB) slurry in the pipeline. *Powder Technol.* 396, 191–209. doi:10.1016/j.powtec.2021.10.050

Gao, R., Zhou, K., Zhou, Y., and Yang, C. (2020). Research on the fluid characteristics of cemented backfill pipeline transportation of mineral processing tailings. *Alexandria Eng. J.* 59 (6), 4409–4426. doi:10.1016/j.aej.2020.07.047

Hz, A., Ldgsb, C., Jkd, E., Pena-Polo, F., and Bencomo, A. (2017). Heavy oil slurry transportation through horizontal pipelines: Experiments and CFD simulations. *Int. J. Multiph. Flow* 91, 130–141. doi:10.1016/j.ijmultiphaseflow.2016.04.013

Jaworska-Jóźwiak, B. (2021). Influence of solids concentration on solid-liquid transportation in a lime production plant. *WSEAS Trans. Appl. Theor. Mech.* 16, 28–36. doi:10.37394/232011.2021.16.4

Lee, Seong W., HuCui, J., and Huang, Yan H. (2009). Particle characteristics and analysis using a laser-based phase Doppler particle analyzer (PDPA) and statistical method. *Part. Sci. Technol.* 27 (3), 553–561. doi:10.1080/02726350903328845

Li, M. Z., He, Y. P., Liu, W. H., Huang, C., and Jiang, R. h. (2020). Effect of adding finer particles on the transport characteristics of coarse-particle slurries in pipelines. *Ocean. Eng.* 218 (5), 108160. doi:10.1016/j.oceaneng.2020.108160

Li, M. Z., He, Y. P., Liu, Y. D., and Huang, C. (2018). Effect of interaction of particles with different sizes on particle kinetics in multi-sized slurry transport by pipeline. *Powder Technol.* 338 (6), 693–702. doi:10.1016/j.powtec.2018.07.088

Li, Z., Guo, L., Zhao, Y., Peng, X., and Kyegyenbai, K. (2022). A particle size distribution model for tailings in mine backfill. *Metals* 12 (4), 594. doi:10.3390/met12040594

Matoušek, V., Chára, Z., Konfršt, J., and Novotny, J. (2022). Experimental investigation on effect of stratification of bimodal settling slurry on slurry flow friction in pipe. *Exp. Therm. Fluid Sci.* 132, 110561. doi:10.1016/j.expthermflusci.2021.110561

Matousek, V. (2002). Pressure drops and flow patterns in sand-mixture pipes. *Exp. Therm. Fluid Sci.* 26 (6), 693–702. doi:10.1016/s0894-1777(02)00176-0

Pinto, T. S., Junior, D. M., Slatter, P. T., and Leal Filho, L. (2014). Modelling the critical velocity for heterogeneous flow of mineral slurries. *Int. J. Multiph. Flow* 65, 31–37. doi:10.1016/j.ijmultiphaseflow.2014.05.013

Qi, C., Chen, Q., Fourie, A., Zhao, J., and Zhang, Q. (2018). Pressure drop in pipe flow of cemented paste backfill: Experimental and modeling study. *Powder Technol.* 333, 9–18. doi:10.1016/j.powtec.2018.03.070

Rao, N. D., Thatoi, D. N., and Biswal, S. K. (2020). Rheological study and numerical analysis of high concentration iron ore slurry pipeline transportation. *Mater. Today Proc.* 22, 3197–3202. doi:10.1016/j.matpr.2020.03.457

Rathore, R. K., Gupta, P. K., and Kumar, N. (2021). Numerical investigation of zinc tailings slurry flow field in a horizontal pipeline. *Mater. Today Proc.* 45, 2702–2706. doi:10.1016/j.matpr.2020.11.541

Sadrossadat, E., Basarir, H., Luo, G., Karrech, A., Durham, R., Fourie, A., et al. (2020). Multi-objective mixture design of cemented paste backfill using particle swarm optimisation algorithm. *Miner. Eng.* 153, 106385. doi:10.1016/j.mineng.2020.106385

Senapati, P. K., and Mishra, B. K. (2017). Feasibility studies on pipeline disposal of concentrated copper tailings slurry for waste minimization. *J. Institution Eng.* 98 (3), 277–283. doi:10.1007/s40032-016-0309-y

Senapati, S., and Pothal, J. K. (2017). Some studies on rheological and pipeline transportation of concentrated limestone-water slurry. *Int. J. Fluid Mech. Res.* 44 (4), 349–356. doi:10.1615/interjfluidmechres.2017017172

Singh, M. K., Kumar, S., and Ratha, D. (2020). Computational analysis on disposal of coal slurry at high solid concentrations through slurry pipeline. *Int. J. Coal Prep. Util.* 42 (2), 116–130. doi:10.1080/19392699.2017.1346632

Singh, M. K., Kumar, S., Ratha, D., and Kaur, H. (2017). Design of slurry transportation pipeline for the flow of muti-particulate coal ash suspension. *Int. J. Hydrogen Energy* 42 (30), 19135–19138. doi:10.1016/j.ijhydene.2017.04.259

Singh, M. K., Ratha, D., Kumar, S., and Kumar, D. (2015). Influence of particle-size distribution and temperature on rheological behavior of coal slurry. *Coal Prep.* 36 (1), 44–54. doi:10.1080/19392699.2015.1049265

Singh, V., Kumar, S., and Mohapatra, S.Thapar Institute of Engineering and Technology, Patiala, Punjab, 147004, India; National Institute of technology, Jamshedpur, India (2019). Modeling of erosion wear of sand water slurry flow through pipe bend using CFD. *J. Appl. Fluid Mech.* 12 (3), 679–687. doi:10.29252/jafm.12.03.29199

Vlasak, P., and Chara, Z. (2011). Effect of particle size distribution and concentration on flow behavior of dense slurries. *Part. Sci. Technol.* 29 (1), 53–65. doi:10.1080/02726351.2010.508509

Wang, S. Y., Wu, A. X., Ruan, Z. E., Yin, S. h., Wang, Y., Wang, S.-Y., et al. (2018). Simulation of long-distance pipeline transportation properties of whole-tailings paste with high sliming. *J. Cent. South Univ. Sci. Technol.* 49 (10), 141–150. doi:10.1007/s11771-018-3724-9

Wu, A., Ruan, Z., and Wang, J. (2022). Rheological behavior of paste in metal mines. *Int. J. Min. Metall. Mat.* 29 (4), 717–726. doi:10.1007/s12613-022-2423-6

Wu, A. X., Yang, Y., Cheng, H. Y., Chen, S. M., and Han, Y. (2018). Status and prospects of paste technology in China. *Chin. J. Eng.* 40 (5), 517. doi:10.13374/j.issn2095-9389.2018.05.001, No.

Zhou, N., Du, E., Zhang, J., Zhu, C., and Zhou, H. (2021). Mechanical properties improvement of Sand-Based cemented backfill body by adding glass fibers of different lengths and ratios. *Constr. Build. Mater.* 280 (1), 122408. doi:10.1016/j.conbuildmat.2021.122408

frontiers | Frontiers in Earth Science

TYPE Original Research
PUBLISHED 30 January 2023
DOI 10.3389/feart.2022.1110093

OPEN ACCESS

EDITED BY
Lishuai Jiang,
Shandong University of Science and Technology, China

REVIEWED BY
Xuelong Li,
Shandong University of Science and Technology, China
Xuesheng Liu,
Shandong University of Science and Technology, China

*CORRESPONDENCE
Junling Hou,
houjunling2022@163.com

SPECIALTY SECTION
This article was submitted to Structural Geology and Tectonics, a section of the journal Frontiers in Earth Science

RECEIVED 28 November 2022
ACCEPTED 09 December 2022
PUBLISHED 30 January 2023

CITATION
Hou J, Li C, Yuan L, Li J and Liu F (2023), Study on green filling mining technology and its application in deep coal mines: A case study in the Xieqiao coal mine.
Front. Earth Sci. 10:1110093.
doi: 10.3389/feart.2022.1110093

Study on green filling mining technology and its application in deep coal mines: A case study in the Xieqiao coal mine

Junling Hou[1]*, Chuiyu Li[2], Lin Yuan[3], Junbin Li[4] and Fei Liu[4]

[1]School of Vanadium and Titanium, Panzhihua University, Panzhihua, China, [2]School of Civil Engineering and Architecture, Anhui University of Science and Technology, Huainan, China, [3]Sichuan Geotechnical Intelligent Measurement Technology Co, Ltd, Panzhihua, China, [4]Huainan Mining (Group) Co., Ltd, Huainan, China

Due to the gradual depletion of shallow mineral resources at present, mines are now gradually entering the deep mining stage. To promote the safe and efficient green mining of deep coal resources and sustainable energy development, and to improve the production efficiency of paste filling mining, the research group has performed this study on the green filling mining technology and application of the working face. Taking working face 1241 (3) of the Xieqiao coal mine as the engineering background, the selection and experiment of filling materials were carried out, and the gangue, fly ash and cement produced by the Xieqiao coal mine were used as the filling aggregate. Next, the strength changes before and after paste filling was obtained by theoretical calculation. The strength at the early stage of filling was no less than 0.13 MPa, and that at the late stage of filling was no less than 2 MPa. Based on previous experimental research and theoretical calculation, the mixing pumping process of paste material ratio and the gangue crushing process were determined, and the filling pipeline system was designed. Then, based on the traditional coal mining technology, a filling mining technology of working face was designed and optimized. The field application of the research results shows that after the goaf of the working face had been filled, the ground pressure behavior of the coal wall of the working face was significantly weakened, and the stability of the surrounding rock of the working face was effectively controlled. Therefore, the method achieved good results, effectively controlled the stability of surrounding rock in goaf, and provided a theoretical basis and data support for realizing safe, efficient and green mining of deep coal resources. The results of this study bear important significance and application value.

KEYWORDS

sustainable development, deep mining, green mining, filling mining, deep coal mine

Introduction

Coal mines are the main energy sound in China, accounting for about 70% of the primary energy structure. In the foreseeable future, the status of coal as the main energy source in China is not expected to change. Coal is an important basic industry related to the national economic lifeline and energy security. With the gradual depletion of shallow coal resources, resource development continues to deepen. The mining of coal resources in wells several km deep has gradually become the new normal of development (De-Wei and Hai-Dong, 2019; Liu and Li, 2019). The theory and technology of synergistic and high-efficiency mining with low ecological damage of deep resources is one of the key scientific problems in the future development of mineral resources at depths of 1,000–2000 m (Min et al., 2022). Previous practice shows that filling mining can effectively control strata movement and prevent surface subsidence. Filling mining is the fundamental way in which to achieve safe, efficient and green mining of deep coal and associated resources (Li et al., 2020).

Scholars have studied the ground mine pressure behavior of the comprehensive mining working face under the goaf, and proposed that the high support pressure of the coal pillar affects the stability of the surrounding rock of the working face here, which is prone to deformation and piecing (Xing et al., 2020; Pang et al., 2021). According to the mechanical model of the compression bar stability, the critical stress required for the instability of the coal wall and wall spalling at different layer heights was obtained in Reference (Zhang et al., 2020). Scholars have also studied the filling degree of goaf caused by equivalent direct roof fall backwardness in shallow buried large mining height working faces. This method divides filling into the full filling type and general filling type (Qing et al., 2019; Wang et al., 2019). According to the deformation characteristics of filling body, scholars determined four different mining affected areas, including early strength area, roof cutting area, old roof rotation area, and masonry beam stability structure formation area (Li et al., 2022a). In addition, the high-speed vortex pulping system was designed. After optimization, the pulping effect of the filling system was stable, and the filling sedimentation reduction effect was good (Sun et al., 2019; Acharya and Kharel, 2020). In view of the spatial distribution of the strength of tailings backfill with different grades, it is found that the strength of tailings backfill with different grades will gradually increase from top to bottom in the vertical direction (Chu et al., 2019; Petrov, 2019). Scholars have also optimized the filling mining process, by proposing overburden rock migration control technologies such as prevention and control of pipeline plugging and secondary filling (Liu et al., 2020a; Li et al., 2022b). They established a coordinated bearing model of filling, surrounding rock and coal pillar, and clarified the mechanism of their joint control on the bearing capacity of overlying strata (Li et al., 2020; Liu et al., 2021a). Scholars have also clarified the control mechanism of key overlaying strata on surface subsidence. Research and development partial filling mining technologies include strip filling in mined-out areas, subsequent filling in short wall caving areas, and overburden isolation grouting filling (Liu et al., 2021b; Ic et al., 2021; Pang et al., 2021). Scholars have studied the cause of surface subsidence in filling mining, and observed that it was mainly caused by the amount of roof and floor movement before filling and the amount of filling body compression (Liu et al., 2019; Zhang et al., 2019; Lin et al., 2021). Finally, scholars have studied the surrounding rock control mechanism of gob side entry retaining in deep big high mining with filling, and proposed the performance optimization of high-water material filling bodies, which ensures the stability of the size and structure of the reserved roadway (Sun et al., 2019; Liu et al., 2020b; Li et al., 2021; Cascone et al., 2022; Li et al., 2022c; Wang et al., 2022; Zhou et al., 2022).

For green filling mining in coal mines, scholars throughout the world have performed much work and obtained numerous research results. However, the selection of filling materials, construction technology and field application for green filling mining in deep coal mines must still be studied. In this paper, comprehensive research methods such as field investigation, theoretical analysis, numerical simulation, model construction, process optimization and field application are used to carry out the filling mining of deep coal mines from the aspects of determination of filling material parameters, selection of filling materials, process optimization and field application. This paper takes working face 1241 (3) of the Xieqiao coal mine of Anhui Huainan Mining Group as the engineering background, and proposes the high-efficiency production technology and application of filling mining. The results of this study bear important theoretical guidance and application significance for green mining.

Basic conditions of the working face

Working face 1241 (3) of the Xieqiao coal mine is located in the fourth stage of 13–1 coal seam in the east of the west wing Group C mining area. The western part of the working face begins from the system roadway of the Group C mining area in the west wing, ends at fault F10 in the east, and begins at transport groove 1231 (3) in the north, and ends at the contour line of −610 m in the south. The upper part of working face 1231 (3) has been mined, yet the underlying strata 11–2 coal seam has not been excavated.

The 13–1 coal seam assignment in working face is stable, while the floor of the coal seam fluctuates slightly along the groove direction. According to the track, transport groove, cut coal thick spot and drilling coal thickness, the thickness of the coal seam on this working face is in the range of 4.5–6.7 m, with an average coal thickness of 5.1 m. The 13–1 coal seam is dominated by semi-bright briquette coal, which is black in

color, large in size, and flaky in texture; it is shiny with grease, contains siderite, and a layer of mudstone with dirt bands is locally developed. The working face can be mined to a length of 257 m, inclined length of 100 m, and mining height control in the range of 2.7–3.6 m.

The comprehensive analysis is based on ground exploration drilling data and actual measurement data of working face 1231 (3), west wing track stone door, west wing belt stone door, and other measured data. The 13–1 coal seam in this working face is generally in a southward inclined monoclinal structure. There are two faults affecting this working face, and there is no collapse column or magmatic rock intrusion phenomenon.

Strength calculation of the filling body

Early strength of the filling body

The production of the coal mine filling working face is generally carried out alternately according to the process of "mining-filling." To ensure the stability of the filling body, the working face should continue to advance after the solidification of the filling body in the previous cycle has become stable. That is, to say, the paste filling slurry is required to achieve condensation and solidification within 6–8 h, and has a strength which plays a supporting role on the roof on the basis of ensuring self-stability. Otherwise, it is necessary to extend the solidification waiting time of the paste filling material until it reaches the required strength, before it can be removed and isolated for the following cycle of coal mining. The strength of the paste filling body to meet the requirements of isolated demolition is usually called early strength.

The basic role of the early strength of the paste filling body involves two aspects. The first is to ensure that the new solidified paste filling body remains stable without damage under the action of self-weight stress, and the other is to bear the weight of the rock that may be unstable under the direct roof.

The self-weight stress of the filling body is used to determine the strength required for the self-stabilization of the filling body, as shown in Formula Eq. 1:

$$\sigma_{c1} = \gamma_f \cdot h_f, \tag{1}$$

Where $\sigma c1$ is the self-stability strength of filling body, MPa; γf is the paste bulk density, MN/m3; hf—filling height, m.

The unstable part of the rock under the direct roof shall be considered according to the rock gravity of the caving arch height in the area to be filled. The support height of the filling body is about half of the width of the area to be filled (i.e., filling step).

Therefore, the early strength of paste filling body can be calculated by Formula Eq. 2:

$$\sigma_{c,6\sim8h} \geq \gamma_f \cdot h_f + 0.5\gamma_r \cdot b_f, \tag{2}$$

Where $\sigma_{c,\ 6\sim8h}$ is the early strength of filling body, MPa; γ_r is the direct roof rock bulk density, MN/m^3; and b_f is the filling step, m.

The Xieqiao coal mine adopts the 3–5 m large step distance for all paste filling. According to the maximum filling step distance of 5 m, the bulk density of the filling body is 0.02 MN/m^3, the direct roof rock bulk density is 0.025 MN/m^3, and the filling body height is 3.6 m. The early strength of the paste filling material should not be less than 0.13 MPa.

Strength at the late stage of the filling body

After the working surface has been pushed, the goaf is completely filled with the filling body to control the strata movement. This is the full mining and full filling method. The filling body in this method is always in a triaxial stress state under the combined action of roof, floor and surrounding rock. Therefore, the full mining and full filling method can use the Coulomb-Moore strength criterion to calculate the strength at the late stage of filling body σ_1, as shown in Formula Eq. 3:

$$\sigma_1 = \frac{1+\sin\varphi}{1-\sin\varphi}\sigma_3 + 2c\frac{\cos\varphi}{1-\sin\varphi}, \tag{3}$$

Where σ_3 is the minimum principal stress; c is the cohesive force of materials; and φ is the internal friction angle of the material.

For the goaf filling body of the Xieqiao coal mine, σ_3 takes the horizontal stress, c=0.2 MPa, φ=41°. After calculation, when the mining depth is about 600 m, the triaxial compressive strength of the filling body under full mining and full filling condition is 3.2 MPa.

Three theories can be used to calculate the load of the filling pillar: effective area theory, pressure arch theory, and Wilson's two-zone constraint theory. As the effective area method is simple and can meet the engineering requirements, it has been widely applied. According to the effective area theory, the weight of the overlying strata over the mined-out width is transferred to the width of the left filling pillar. Therefore, the load P on the filling column can be calculated by Formula Eq. 4, as follows:

$$P = \gamma H(1-\rho), \tag{4}$$

Where ρ=A/(W+A); γ is the average capacity of the overburden, MN/m^3; H is the average mining depth, m; ρ is the recovery rate; A is the width of the filling pillar, m; and W is the mining breadth, m.

The strength of the filling pillar reflects the bearing capacity of the overlying strata, which acts as the basis for the stability of the filling pillar. According to the rock mechanics, the strength of the filling pillar is related to the strength of the filling block, and also depends on factors such as the size of the filling pillar, mining method, and load change. Therefore, the strength of the

filling block tested in the laboratory cannot be directly used to evaluate the overall strength of the on-site filling pillar, and it is necessary to perform appropriate parameter conversion between the laboratory filling block and on-site filling pillar. At present, the overall strength of the filling pillar can adopt the calculation formula related to the width height ratio proposed by Bieniawski (Liu et al., 2021b), as shown in Formula Eq. 5:

$$\sigma_s = \sigma_c\left[0.64 + 0.36\left(\frac{W}{h}\right)\right]^n, \quad (5)$$

Where σc is the uniaxial compressive strength of the filling block tested in the laboratory, MPa; when W/h>5, n = 1.4; and when W/h<5, n = 1.

Since the filling surface of coal mine is a large area of filling and the height of coal seam is limited, the width-height ratio of filling pillar is much larger than 5. The parameter n in the above formula is 1.4, and the formula then becomes Formula Eq. 6:

$$\sigma_s = \sigma_c\left[0.64 + 0.36\left(\frac{W}{h}\right)\right]^{1.4}. \quad (6)$$

According to the principle of coal pillar stability, the stability of filling pillar should conform to the relationship of Formula Eq. 7:

$$\sigma_s = FP, \quad (7)$$

Where F is the safety factor, available from 1.2 to 2.0.

According to the above analysis, the strength at the late stage of the laboratory filling block required for filling can be deduced according to the formula, as shown in Formula Eq. 8:

$$\sigma_c = \frac{F\gamma H(1-p)}{\left[0.64 + 0.36\left(\frac{W}{h}\right)\right]^{1.4}} \quad (8)$$

It can be seen from the formula that the uniaxial strength of the filling body is greater than 1.93 MPa.

In the test of paste filling material in the Xieqiao coal mine, the uniaxial test strength of the filling body should be not less than 2 MPa.

Selection and experiment of filling materials

Selection of filling materials

Paste filling mining is a green mining method, that is, used to process coal gangue, coal fly ash and other solid waste on the ground into paste slurry with no critical velocity, and no need for dehydration. It uses a filling pump and gravity action to transport the paste slurry underground through a pipeline, thus filling the goaf quickly. To make gangue and other materials into qualified paste slurry, the proportion of fine particles less than 0.08 mm must reach more than 15%. Otherwise, the paste will undergo layered bleeding, which in severe cases will cause pipe blocking accidents, in which case the paste pipeline transportation system cannot operate normally.

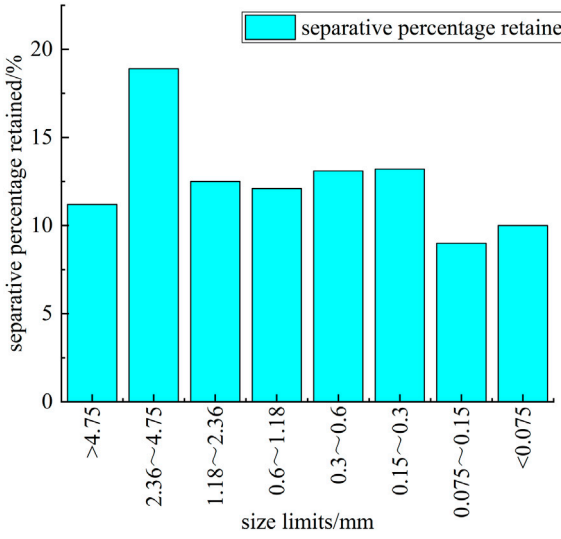

FIGURE 1
Particle grade of the crushed gangue.

At the beginning of filling, the important process of slurry pushing water should be carried out, so as to avoid the plugging accident of phase change of paste caused by free falling accelerated motion in drill holes for filling. In such a case, the paste will produce water-solid separation, and the bottom of the hole will undergo graded stiffening. In other words, it is necessary to fill the drilling filling pipeline with water, and control the flow velocity near the outlet of the filling pipeline, so that the first batch of paste slurry can be transported from the ground to the underground at a safe speed. In the process of slurry pushing water, the front of the paste pipeline will inevitably be diluted by the contact pipeline water, and this part of the paste diluted by water must not precipitate; if it does, it will also cause plugging accidents. The solution to this is that a small amount of paste in contact with pipeline water is made of fine particle material, usually with fly ash paste, i.e., fly ash, cement, and water mixed in equal proportion. Similarly, at the end of the filling, the paste must be flushed out of the filling pipe with water, and a small amount of fly ash paste must also be addded.

To solve the problem of difficult discharge of gangue in the Xieqiao coal mine, coal gangue is chosen as the paste filling aggregate, and the coal fly ash and cement are produced by the mine.

Filling material experiment

1) Physicochemical analysis of filling materials

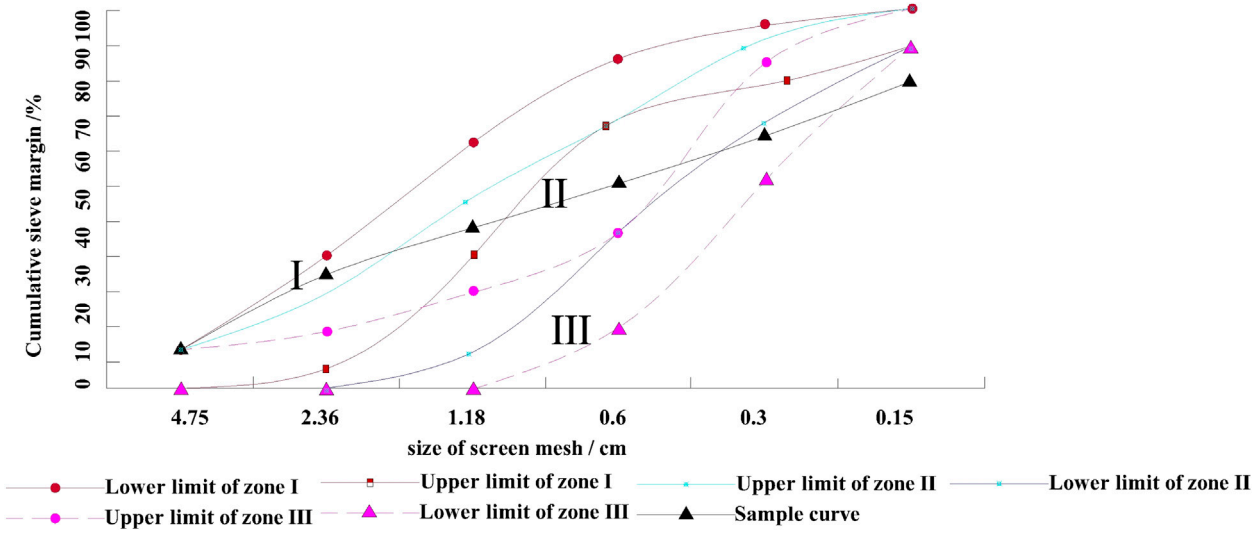

FIGURE 2
Partition diagram of particle curve of the crushed gangue.

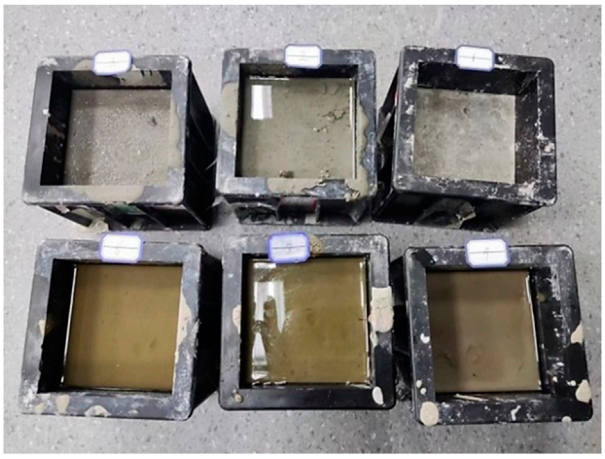

FIGURE 3
Filling paste curing diagram.

Using coal gangue as the filling aggregate, unprocessed washed gangue and raw gangue cannot meet the requirements in production since, as a filling aggregate, it must be crushed to a size fraction with a maximum particle size of about 15 mm. Figure 1 shows the particle grade of crushed gangue, and Figure 2 is the curve partition diagram of the broken gangue particles.

It can be seen from the curve partition diagram that the gangue of the Xieqiao coal mine after crushing is mainly distributed in zone II. According to the national standard for fly ash for cement and concrete (GB1596-2017), the standard consistency water demand ratio of grade II fly ash must exceed 105%, and the residual amount of 0.045 mm square hole sieve must not exceed 30%. The standard for grade III is 45%. To ensure the performance of filling slurry, fly ash should be sampled and analyzed when entering the field, to ensure that the fly ash is not lower than the grade III standard.

2) Mechanical experiment of backfill

After determining the filling materials, the research group carried out indoor test experiments on the strength of the filling body to determine whether the strength of the filling body could meet the needs of the field working face. The prepared filling paste material is shown in Figure 3. To reduce the influence of accidental errors on the experimental results, three groups of filling paste strength tests were carried out in this study. First, the filling paste was made. After full curing, the standard sample was removed with a coring machine, and it was placed in the mechanical testing system for testing.

The filling material after being damaged under compression is shown in Figure 4, and the stress-strain curve of the filling body is shown in Figure 5. It can be seen from Figure 4 that the failure mode of filling body under compression is basically the same as that of ordinary rock. The results show that the paste filling material has similar properties with rock after hardening. It can be seen from Figure 5 that the peak strengths of the hardened filling paste materials are 3.68, 3.71, and 3.58 MPa, respectively, with an average of 3.65 MPa. This exceeds the theoretical calculation value of 2 MPa, and the results meet the requirements of goaf filling at the working face. In addition, the filling body also has a certain post peak strength, which plays a significant role in controlling the stability of the goaf.

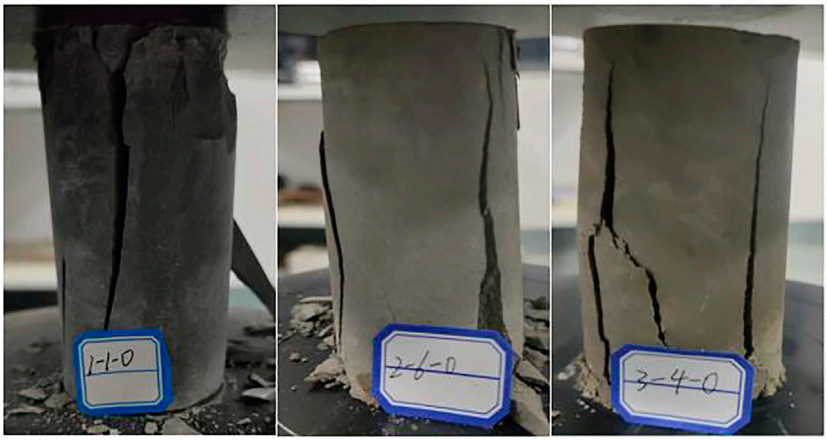

FIGURE 4
Morphology of the filling material after damage.

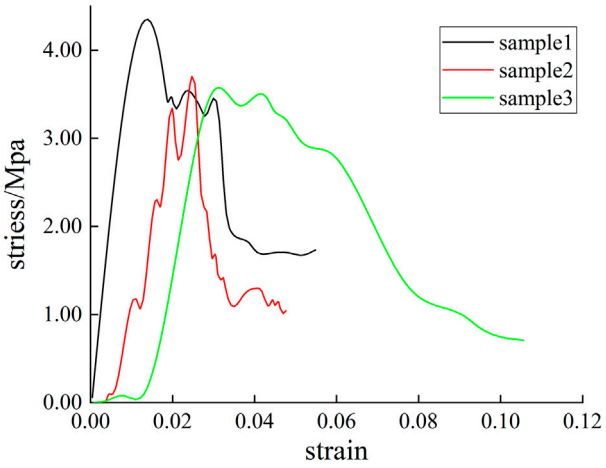

FIGURE 5
Stress strain curve of the filling body.

In summary, the filling materials obtained in this study are highly consistent with the rock materials in terms of strength and properties, and can meet the needs of goaf filling in deep coal mines.

Process design of the filling mining face

Process design of filling system

1) System

The filling system of the Xieqiao coal mine consists of a ground filling station, filling pipeline and filling working face.

Ground filling station: The ground filling station is the production line of paste slurry, including the preparation, storage, transportation, batching, mixing, pumping, automatic control, and other links of raw materials. Automatic control is the central command system that ensures the reliable operation of the filling station. The paste filling system includes much equipment and complex technology, and is closely related to the production of the working face. It requires a highly automated control system as a guarantee.

Filling pipeline: This is the delivery means of paste slurry, including ground pipeline, underground pipeline and working surface pipeline along the control gate valve.

Filling face: The key devices of the filling face are the filling hydraulic support and shearer, which act as the key links affecting its efficiency and safety.

The filling system process mainly includes the mixing pumping process and gangue crushing process.

2) Proportioning mixing pumping process

The mixing pumping system adopts a double system arrangement, and the two systems run simultaneously. The flow chart of the designed mixing pumping process is shown in Figure 3. All of the materials after batching and weighing are added to the mixer and stirred into qualified paste, then added to the filling pump, then through the filling pipeline the materials are transported to the filling face to be filled. To ensure the safety and reliability of the system, two filling pumps were set up, with one as a backup, as shown in Figure 6:

3) Gangue crushing process

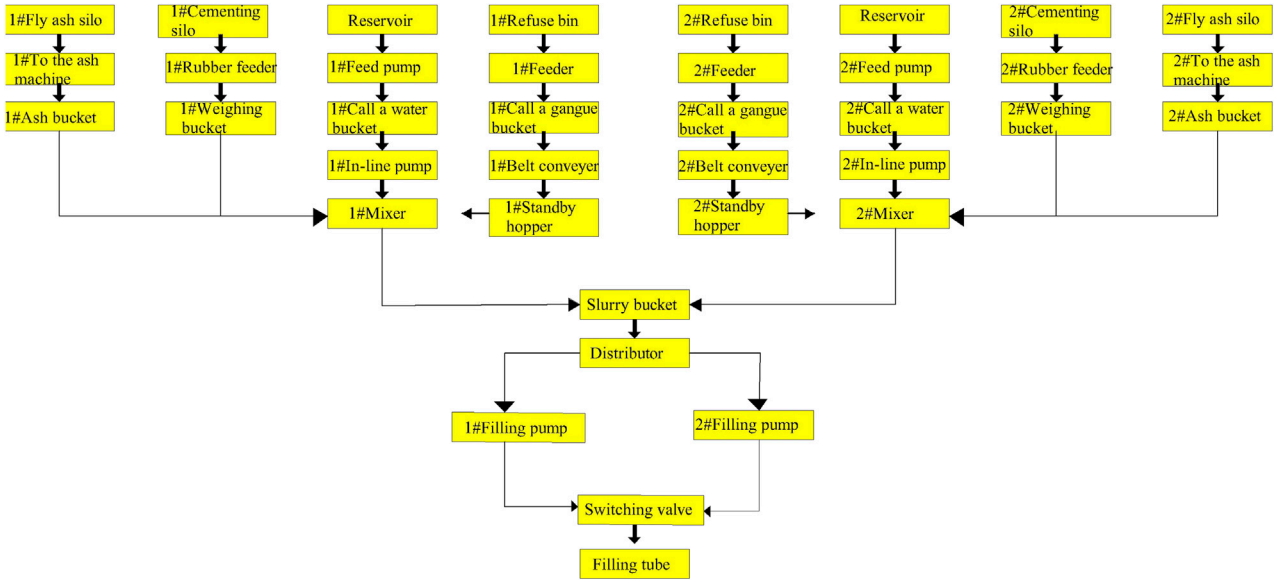

FIGURE 6
Flow diagram of the proportioning mixing pumping process.

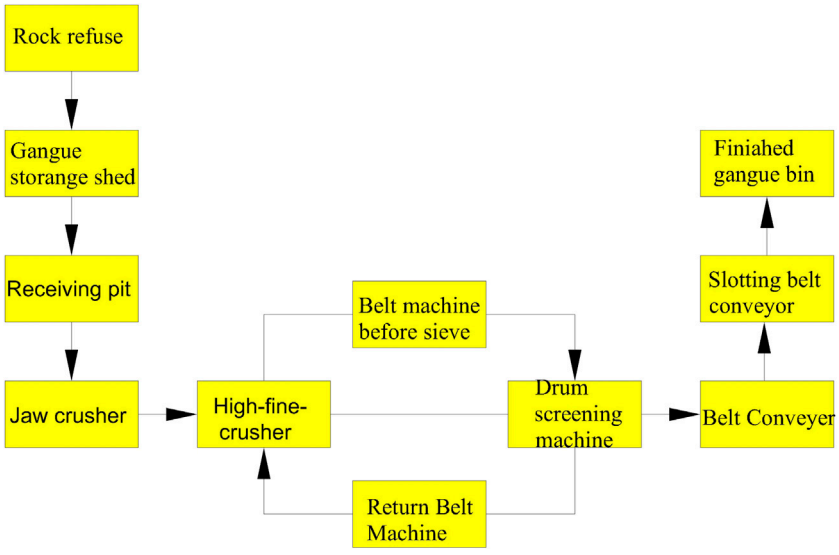

FIGURE 7
Process flow diagram of the gangue crushing system.

Mine gangue was adopted for the filling of the Xieqiao coal mine. The maximum particle size of gangue designed to enter the filling system was 500 mm. The maximum particle size of gangue after crushing processing needed to be controlled within 15 mm, and the gangue powder with particle size less than 0.08 mm was controlled at about 15%. Therefore, the gangue design adopted two-stage crushing processing, and the process flow is as shown in Figure 7:

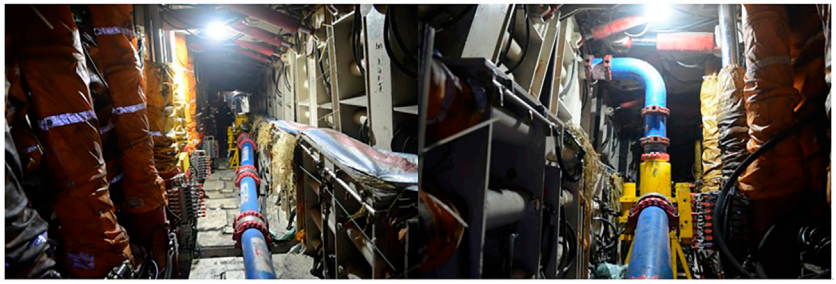

FIGURE 8
Site layout of the paste filling pipeline.

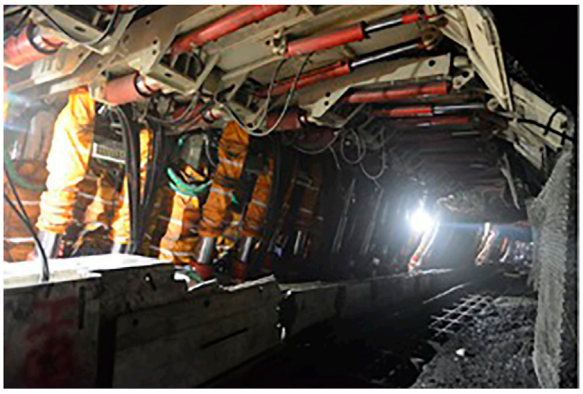

FIGURE 9
Special paste filling support for the filling working face.

Filling pipeline system design

1) Filling pipeline system composition

The function of paste filling pipeline system is to safely transport the paste filling material to the goaf under the action of pumping pressure or self-weight pressure of the filling pump. The filling pipeline system is mainly composed of the ground filling pipeline, filling drilling riser, filling trunk pipeline system, pipeline pressure online detection system, filling working face pipeline system, drainage pipeline, and its supporting valve group.

2) Filling pipeline path

The working face groove filling pipeline was arranged in the transportation groove and installed near the non-production side. The pipeline diameter was 219 mm and the wall thickness was 12 mm.

According to the field conditions of the Xieqiao coal mine and the opinions of mine owner, the filling path of filling working face 1241 (3) was determined as follows:

Ground filling station (filling pump) → ground pipeline 140 m → drilling pipeline 635 m → hole bottom chamber 5 m → −610 west wing track stone 523 m → transport groove 1241 (3) contact lane 50 m → transport groove 1241 (3) 400 m → working face 1241 (3) 100 m. The distribution valve was set up in the filling working face to fill the goaf. The filling pipeline system designed in this paper is mainly designed for the mining system of deep coal mines, which can fully meet the working requirements from the ground to the filling face, and can be optimized and adjusted according to different needs.

Along the pipeline are arranged in the floor, a fixed device is set, the spacing of which did not exceed 15 m, and paste filling pipeline field layout is shown as in Figure 8.

Filling mining process

The coal seam in the working face was stable, with an average thickness of 5.1 m. The design adopted a single-strike long-wall comprehensive mechanized filling mining method, with backward mining in the area, and a filling method to deal with the goaf. Because the mine filling mining area was mainly concentrated at the late stage of CoalSeams in No.6 (with a coal thickness of about 3 m), the comprehensive rate of filling support multi coal seam adaptability, and the comprehensive efficiency of filling mining, the first filling face of working face 1241 (3) selection model for ZC5600/20/38 paste filling mining support. The mining thickness was set to 3.5 m, with top coal mining, as shown in Figure 9. The hydraulic support can adapt to multi seam mining, and can be adjusted according to the occurrence conditions of coal seams, thus improving the comprehensive efficiency of filling mining.

The filling mining area adopted long wall and fully mechanized filling mining method. The filling test of mining face 1241 (3) adopted

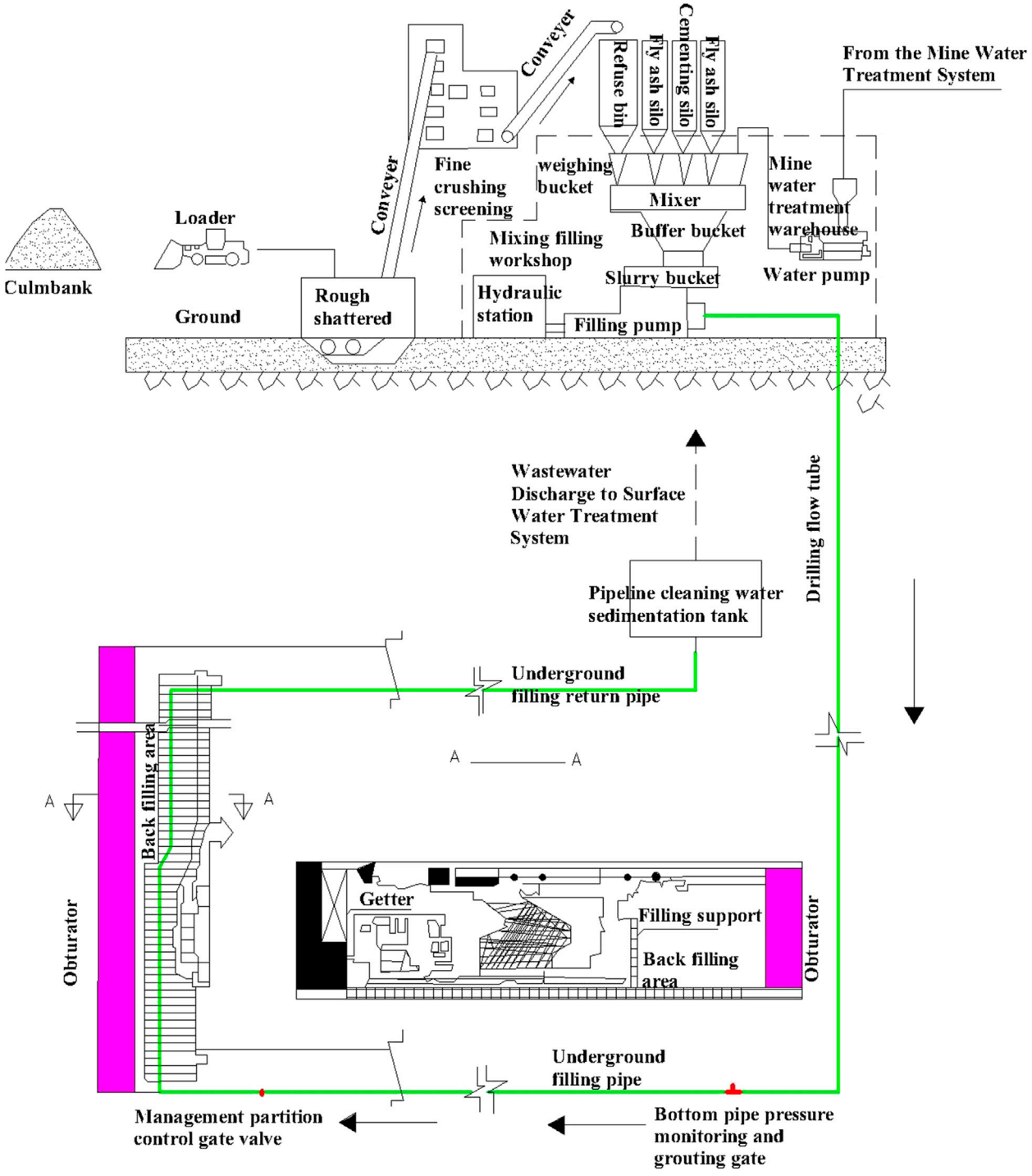

FIGURE 10
Process flow chart of the paste filling mining.

long wall, comprehensive mechanized paste filling mining, with single knife circulation footage 0.8 m, a mining height of 3.5 m, the top coal set at 1.3 m, and single-class footage of 1.6 m. Five classes (40 h) were taken to complete a filling cycle, with a filling step 3.2 m, among which there were two classes of production, one class of isolation, one class of filling, and one class of solidification overhaul.

TABLE 1 Surface deformation after filling in the working face goaf.

Structure	Surface deformation value				
	Sink/mm	Inclination/mm.m^{-1}	Strike dip/mm.m^{-1}	Propensity level/mm.m^{-1}	Strike level/mm.m^{-1}
Tanghaizi Village	160	-0.1–0.5	-0.7–0.6	-0.3–0.2	-0.9–0.3
Railway line	140	-0.4–0	-0.6–0.5	-0.1–0	-0.7–0.3
Lumber mill	0	0	0	0–0.1	0
Air shaft	10	0	0–0.1	0	0–0.1

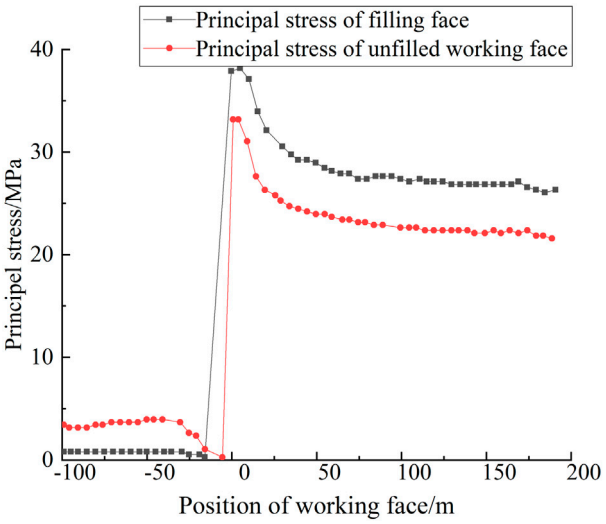

FIGURE 11
Distribution law of principal stress in the filling face and unfilled face.

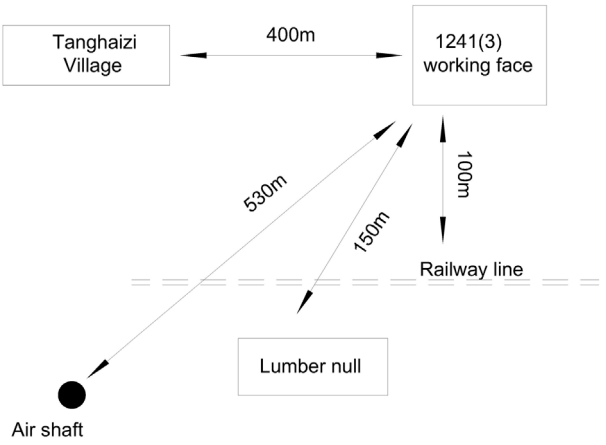

FIGURE 12
Horizontal position relationship between the filling face and surface buildings.

The working face adopted special paste filling support, and the single mining-filling circulation process was as follows: cutting coal → hanging net → moving support → pushing conveyor → filling area isolation → filling → solidification overhaul, as shown in Figure 10. A charge-back cycle is completed every 40 h. Compared with the traditional coal mining process, the process increased the filling area isolation, filling, solidification maintenance, and other processes.

Field application

Using the FLAC3D numerical simulation method, the distribution law of principal stress before and after filling in the goaf of the working face was simulated and analyzed. It can be seen from Figure 11 that there was a significant difference between the goaf filled and unfilled in the working face. After the goaf of the working face had been filled, the abutment pressure at the coal wall of the working face decreased significantly, and the stress concentration coefficient was about 2.2. When the goaf was not filled, the stress concentration factor at the coal wall was about 2.5. It can be seen from the figure that, after the goaf of the working face had been filled, the ground pressure appearance of the coal wall of the working face was significantly weakened, and the stability of the surrounding rock of the working face was effectively controlled.

It can be seen from Figure 12; Table 1 that, after the goaf had been treated by the filling method, the deformation values of the surface buildings were within the safe range. The results show that the filling of the goaf could not only effectively weaken the ground pressure appearance of the working face, but also effectively controlled the surface subsidence.

It can be concluded that the field application of the research results has achieved good results, effectively controlled the stability of surrounding rock in the goaf and the subsidence of the surface, and provided a theoretical basis and data support to achieve safe, efficient and green mining of deep coal resources, which bears important significance and promotion and application value.

Based on the above analysis, it can be concluded that the stress of coal wall before and after filling is obvious. Due to the existence of filling body, the ground pressure manifestation of the working face is significantly weakened, which provides favorable conditions for the stability control of the working face.

Conclusion

In this paper, the comprehensive research methods of indoor experiment, theoretical analysis and field application were used to carry out the research on green filling mining in deep coal mines. The study determines the filling materials and optimizes the filling mining technology of deep coal mines, which provides theoretical and data support for the filling mining of deep coal mines, and has important significance and value. The following main conclusions were obtained.

1) Taking working face 1241 (3) of the Xieqiao coal mine as the engineering background, this paper adopted the methods of indoor test and theoretical analysis to carry out the selection and experiment of filling materials. The minimum strengths of the filling body in the early and late stages were 0.13 and 2 MPa, respectively. The self-produced gangue, fly ash and cement of the Xieqiao coal mine were selected as the filling aggregate.
2) Based on the technical conditions of coal seam occurrence and mining in the Xieqiao coal mine, a single-strike longwall comprehensive mechanized filling mining technology was proposed. A safe and efficient filling mining technique was designed, and the supporting equipment for filling mining was improved, including the hydraulic support of the working face and the filling pipeline equipment.
3) The field application of the research results shows that, after the goaf of the working face had been filled, the ground pressure behavior of the coal wall of the working face was significantly weakened, and the stability of the surrounding rock of the working face was effectively controlled. The study has thus achieved good results, effectively controlled the stability of surrounding rock in goaf, and provided a theoretical basis and data support for achieving safe, efficient and green mining of deep coal resources. This bears important significance and application value.

Data availability statement

The original contributions presented in the study are included in the article/supplementary material, further inquiries can be directed to the corresponding author.

Author contributions

Data curation,JH and CL Formal analysis, LY; Investigation, JL and FL All authors have read and agreed to the published version of the manuscript.

Conflicts of interest

YL was employed by the company Sichuan Geotechnical Intelligent Measurement Technology Co, Ltd, Panzhihua.

JL and LF were employed by the company Huainan Mining (Group) Co., Ltd.

The remaining authors declare that the research was conducted in the absence of any commercial or financial relationships that could be construed as a potential conflict of interest.

Publisher's note

References

Acharya, B. S., and Kharel, G. (2020). Acid mine drainage from coal mining in the United States – An overview. *J. Hydrology* 588, 125061. doi:10.1016/j.jhydrol.2020.125061

Cascone, T., Chelvanambi, M., and Wargo, J. A. (2022). Immunotherapy response-associated akkermansia: Canary in a coal mine. *Trends Immunol.* 43, 337–339. doi:10.1016/j.it.2022.03.007

Chu, W., Xiong, W., Ge, Z., and Cheng, Q. (2019). Predicting mine water inflow and groundwater levels for coal mining operations in the pangpangta coalfield, China. *Environ. Earth Sci.* 78 (5).

De-Wei, X. U., and Hai-Dong, L. I. (2019). Study on hydrogeological characteristics and water filling factors of wulasu mining area in dongsheng coalfield. *Ground Water*.

Ic, A., Ey, B., and Aoy, C. (2021). Sodium silicate effect on setting properties, strength behavior and microstructure of cemented coal fly ash backfill. *Powder Technol.* 384.

Li, H., Guo, K., and Guo, G. (2022). Strata and surface influence range of deep coal mining for mine land reuse. *Environ. Earth Sci.* 81, 68. doi:10.1007/s12665-022-10174-6

Li, L., Xie, D., Wei, J., Yin, H., Zhang, W., Man, X., et al. (2020). Analysis and control of water inrush under high-pressure and complex karstic water-filling conditions. *Environ. Earth Sci.* 79 (21), 493. doi:10.1007/s12665-020-09242-6

Li, S., Wang, J., Zhang, J., and Zhang, M. (2022). Effects of mining and reclamation on the spatial variability of soil particle size distribution in an underground coalmine area: A combination method using multi-fractal and joint multi-fractal theories. *Environ. earth Sci.* 81 (4), 117. doi:10.1007/s12665-022-10257-4

Li, X. L., Chen, S. J., Wang, S., Zhao, M., and Liu, H. (2021). Study on *in situ* stress distribution law of the deep mine taking Linyi Mining area as an example. *Adv. Mater. Sci. Eng.* 9 (4), 5594181–5594211. doi:10.1155/2021/5594181

Li, X. S., Peng, J., Xie, Y. L., Li, Q., Zhou, T., Wang, J., et al. (2022). Influence of high-temperature treatment on strength and failure behaviors of a quartz-rich

sandstone under true triaxial condition. *Lithosphere* 2022, 3086647. doi:10.2113/2022/3086647

Lin, H., Yang, R., Lu, B., Li, Y., Fang, S., Fan, Z., et al. (2021). Overlying strata movement law of continuous mining and continuous backfilling cemented-fill mining. *Environ. earth Sci.* 80, 688. doi:10.1007/s12665-021-09993-w

Liu, H., Zhang, M., Su, L., Chen, X., and Sun, A. (2021). A boundary model of terrain reconstruction in a coal-mining subsidence waterlogged area. *Environ. Earth Sci.* 80 (5), 187. doi:10.1007/s12665-021-09508-7

Liu, S., Fu, M., Jia, H., and Li, W. (2019). Shear characteristics of cuneiform reaming anchorage bolts in coal mine roadways. *Rock Mech. Rock Eng.* 52 (6), 1931–1943. doi:10.1007/s00603-018-1670-3

Liu, S., and Li, W. (2019). Indicators sensitivity analysis for environmental engineering geological patterns caused by underground coal mining with integrating variable weight theory and improved matter-element extension model. *Sci. Total Environ.* 686 (10), 606–618. doi:10.1016/j.scitotenv.2019.04.393

Liu, S. M., Li, X. L., Wang, D. K., and Zhang, D. M. (2020). Investigations on the mechanism of the microstructural evolution of different coal ranks under liquid nitrogen cold soaking. *Energy Sources A: Recovery Util. Environ. Eff.*, 1–17. doi:10.1080/15567036.2020.1841856

Liu, W., Liu, S., Tang, C., Qin, W., and Zhang, J. (2020). Evaluation of surface water quality after mine closure in the coal-mining region of guizhou, China. *Environ. Earth Sci.* 79 (18), 427. doi:10.1007/s12665-020-09167-0

Liu, Z., Dong, S., Wang, H., Wang, X., Nan, S., and Liu, D. (2021). Macroscopic and mesoscopic development characteristics of the top strata of middle ordovician limestone in the hanxing mining area. *Environ. Earth Sci.* 80 (16), 526–617. doi:10.1007/s12665-021-09859-1

Min, X., Xu, D., Hu, X., and Li, X. (2022). Changes in total organic carbon and organic carbon fractions of reclaimed minesoils in response to the filling of different substrates. *J. Environ. Manag.* 312, 114928. doi:10.1016/j.jenvman.2022.114928

Pang, L., Liu, W., Zheng, Q., Du, Y., Meng, X., and Li, X. (2021). Evaluation and analysis of metal mine filling based on numerical simulation and actual measurement. *Environ. Earth Sci.* 80, 505. doi:10.1007/s12665-021-09844-8

Petrov, P. (2019). Chemical and physicochemical parameters of recultivated embankments of maritsa-iztok mine in relation to development of soil formation process. *Nat. Rev. Neurosci.* 20 (2).

Qing, Z., Zheng, X., and Shao, M. (2019). Changes of solute transport characteristics in soil profile after mining at an opencast coal mine site on the loess plateau, China. *Sci. Total Environ.* 665, 142–152. doi:10.1016/j.scitotenv.2019.02.035

Sun, W., Xiao, E., Krumins, V., Dong, Y., Li, B., Deng, J., et al. (2019). Comparative analyses of the microbial communities inhabiting coal mining waste dump and an adjacent acid mine drainage creek. *Microb. Ecol.* 78, 651–664. doi:10.1007/s00248-019-01335-5

Wang, S., Li, X. L., and Qin, Q. Z. (2022). Study on surrounding rock control and support stability of Ultra-large height mining face. *Energies* 15 (18), 6811. doi:10.3390/en15186811

Wang, Z., Li, H., and Tang, R. (2019). Network analysis of coal mine hazards based on text mining and link prediction. *Int. J. Mod. Phys. C* 30 (07), 1940009–1940034. doi:10.1142/s0129183119400096

Xing, Y., Wang, J., Shaheen, S. M., Feng, X., Rinklebe, J., Zhang, H., et al. (2020). Mitigation of mercury accumulation in rice using rice hull-derived biochar as soil amendment: A field investigation. *J. Hazard. Mater.* 388, 121747. doi:10.1016/j.jhazmat.2019.121747

Zhang, J., Chen, L., Chen, Y., Ge, R., Shi, X., Zhou, K., et al. (2020). Discrimination of water-inrush source and evolution analysis of hydrochemical environment under mining in renlou coal mine, anhui province, China. *Environ. Earth Sci.* 79 (2), 61. doi:10.1007/s12665-019-8803-1

Zhang, J., Liu, J., and Wang, X. (2019). Research on risk assessment index system of coal mine occupational disease based on unascertained measure theory. *Basic & Clin. Pharmacol. Toxicol.* 125.

Zhou, X. M., Wang, S., Li, X. L., Meng, J., Li, Z., Zhang, L., et al. (2022). Research on theory and technology of floor heave control in semicoal rock roadway: Taking longhu coal mine in Qitaihe mining area as an Example. *Lithosphere* 2022 (11), 3810988. doi:10.2113/2022/3810988

frontiers | Frontiers in Earth Science

TYPE Original Research
PUBLISHED 30 January 2023
DOI 10.3389/feart.2022.1097551

OPEN ACCESS

EDITED BY
Yun Zhang,
Xi'an University of Science and Technology, China

REVIEWED BY
Baoxu Yan,
Xi'an University of Science and Technology, China
Xuesheng Liu,
Shandong University of Science and Technology, China

*CORRESPONDENCE
Pengfei Jiang,
jiangpengfei@tdkcsj.com

SPECIALTY SECTION
This article was submitted to Structural Geology and Tectonics, a section of the journal Frontiers in Earth Science

RECEIVED 14 November 2022
ACCEPTED 09 December 2022
PUBLISHED 30 January 2023

CITATION
Yao Y, Jiang P, Zhou N and Du E (2023), Study on deformation control of overlying strata in short-wall coordinated filling mining of thick coal seam under aquifer.
Front. Earth Sci. 10:1097551.
doi: 10.3389/feart.2022.1097551

Study on deformation control of overlying strata in short-wall coordinated filling mining of thick coal seam under aquifer

Yinan Yao[1,2], Pengfei Jiang[3]*, Nan Zhou[1,2] and Erbao Du[1,2]

[1]State Key Laboratory of Coal Resources and Safe Mining, China University of Mining and Technology, Xuzhou, Jiangsu, China, [2]School of Mines, China University of Mining and Technology, Xuzhou, Jiangsu, China, [3]Coal Mining Branch, China Coal Research Institute, Beijing, China

The mining of coal resources and the protection of water resources are often in opposition, and this contradiction is more prominent in the mining of thick coal seams due to the difficulty of controlling the overburden deformation. Based on the mining conditions of thick coal seam under the main aquifer of a coal mine in the water shortage area of Northwest China, this paper puts forward the short-wall coordinated filling mining (SCFM) of thick coal seam. The stress analysis of the overall structure consisting of the top and bottom plates, coal pillars and filler at each stage of the mining process was carried out, the length of the short-walled working face suitable for this coal mine was derived, and the key parameters for the mining of the three pan areas of the mine were designed. The analysis results show that the sensitivity of the maximum tensile stress in the roof to the length of the working face is better than the filling rate in the case of short-walled working face arrangement. When the design coal mine working face length is 40 m and the filling rate is 95%, the overburden fissure development height can be controlled to 58.45 m after the whole area of three pan area is retrieved. It is verified by the downhole injection method that the requirement of non-conducting aquifer is satisfied after using SCFM. The research in this paper is of great significance to achieve safe and efficient recovery of coal resources and water conservation under strongly water-rich rock formations.

KEYWORDS

water protection mining, short-wall coordinated filling mining, overburden deformation, fracture development, engineering design

1 Introduction

With its inherent characteristics, coal resources will remain an important source of energy supply for some time in the future, but due to its endowment characteristics and mining methods, most of the mines are facing the problem of massive groundwater loss and ecological environment damage caused by mining activities (Zhang et al., 2014; Fan et al., 2019; Yao et al., 2020). For ecologically fragile areas where water resources are scarce, the decline in groundwater level due to the breakage of aquifers after mining will

make the ecological damage on the surface more serious, and currently backfill mining is widely used as a form of green mining to protect the loss of groundwater resources brought about by the impact of mining (Shen et al., 2021; Zhang et al., 2021). However, it is more difficult to control the overburden for thick seam mining, and the traditional filling mining method often faces the contradiction between the overburden control effect and mining efficiency. Too long working face will result in poor overburden control, while too short will affect mining efficiency (Wen et al., 2019; Tai et al., 2020; Chen et al., 2022). Therefore, the SCFM technology is proposed to control the overburden deformation by reducing the size of the working face together with the filling body filling, which provides a new way for "water conservation mining" (Chi et al., 2019). Systematic study of the influencing factors of overburden deformation of thick coal seam mining under water-bearing seams and establishment of the design process of SCFM parameters are of great significance to improve the safety of thick coal seam mining under water-bearing seams and protect groundwater resources.

Aiming at the filling mining of thick coal seam under aquifer, Deng et al. (2017) proposed a filling mining method of upward slicing longwall-roadway cemented backfilling, and studied the compression performance of cemented backfill materials with different mixing ratios and curing time. The recovery rate and safety of thick coal seam under aquifer are greatly improved by filling mining in layered roadway (Deng et al., 2017). Wen et al. (2022) comparatively analyzed the traditional longwall mining and longwall paste filling mining of thick coal seam, and obtained the key parameters such as mining thickness and filling rate under the critical state of water inrush (Wen et al., 2022). Bai et al. (2018) focused on the effect of backfilling mining under shallow thick coal seams on controlling groundwater loss and reducing surface subsidence, and obtained the optimal ratio of backfilling materials and slurry concentration (Bai et al., 2018).

For the study of the development height of hydraulic fracture zone by backfill mining, Xu et al. (2022) proposed a new method of water-preserved coal mining with long-wall continuous mining and partial filling, and studied the influence of multiple factors on the development height of water flowing fractured zone by analytic hierarchy process, and established a prediction model (Xu et al., 2022). Li et al. (2017) measured and numerically analyzed the development of water-conducting fracture zone in fully mechanized solid filling mining under aquifer, which provided design basis for fully mechanized solid filling (Li et al., 2017). Zhang et al. (2020) studied the controlling effect of short-wall block filling mining method on the development of water flowing fracture and strata movement, established the mechanical development model of water flowing fracture zone, and deduced the development height of water flowing fracture zone (Zhang et al., 2020). Wang (2015) studied the law of water-conducting fracture development in the overburden rock of the Wangerville backfill coal mining method, which provides help to determine reasonable mining parameters for backfill coal mining under water bodies (Wang, 2015).

In summary, there are many analysis and parameter design of overburden control effect of longwall face filling and roadway mining filling, but there is a lack of research on short-wall working face collaborative filling mining and controlling the development of overlying strata deformation and fracture, especially the design of SCFM and the development height of water flowing fractured zone with the whole area mining as the research background.

In this paper, for the requirements of safe mining of coal resources and water resources protection under strong water-bearing strata, the research content of SCFM to control overburden deformation is proposed, and the deformation characteristics of overburden during backfill mining are analyzed in detail to provide reference for similar mines to achieve safe mining of coal resources and water resources protection.

2 Short-wall coordinated filling mining technology

2.1 Engineering background

The study mine is located at the junction of Gansu and Shaanxi provinces in the Yellow River Basin, which is a coal-rich and water-scarce area. The design production capacity of the mine is 5.0 Mt/a, the main mining is 4$^{\#}$ coal, the average buried depth is 925.17 m, and the average thickness of the coal seam is 6.67 m. It is a thick coal seam, most of which can be mined, and the structure is simple. The distribution of coal-water dual resources in China and the assignment of coal seams and aquifers in the studied mines are shown in Figures 1A, B, respectively. There are a total of 8 water-bearing rock layers in the overlying rock strata of this coal mine, among which the water-bearing layer of Luohe Group is a strong water-bearing layer, which has a great impact on the mine production. According to the already mined second panel (with similar geological conditions with the third panel) monitoring data show, the average water level of the aquifer in the upper section of the Luohe Formation decreased by 34.95 m during the mining period, and the maximum water inflow of the working face reached 3499.8 m^3/h, with the change curves shown in Figures 1C, D. Therefore, it is very urgent to change the existing mining methods and mining parameters and develop a set of technology suitable for thick coal seam mining under strong aquifer in this mine.

2.2 Short-wall coordinated filling mining

In response to the serious water gushing at the working face during the production of this coal mine, which brings problems

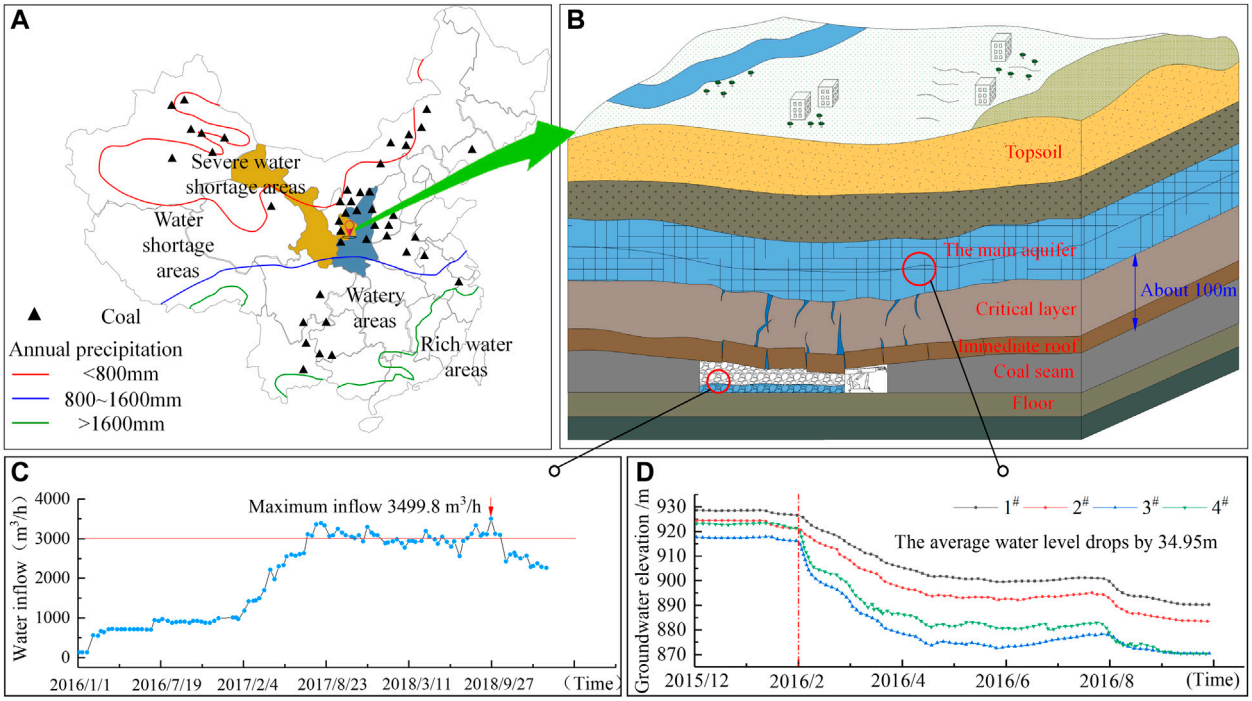

FIGURE 1
Basic information of the mine, **(A)** China coal-water dual resource distribution map, **(B)** Diagram of coal seam and aquifer assignment, **(C)** Working surface water gushing curve graph, **(D)** Water level variation curve of the aquifer in the upper section of the Luohe Formation.

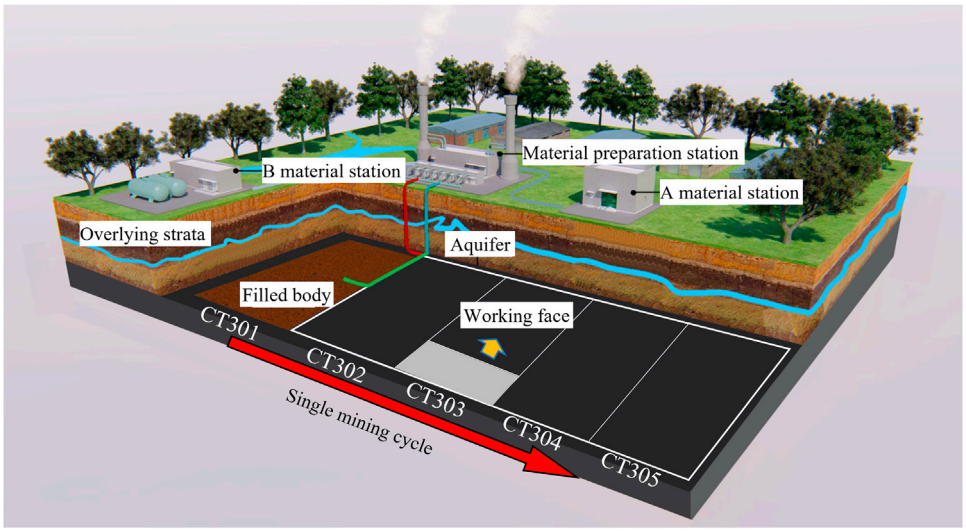

FIGURE 2
The principle diagram of SCFM technology.

to the mine's safety production and water resources protection, the method of SCFM of thick coal seams under strong water-bearing seams is proposed. Ordinary fully mechanized working face length according to the different coal thickness is usually 100–200 m, SCFM than the general fully mechanized mining face length is shorter, usually less than 100 m, for the control of

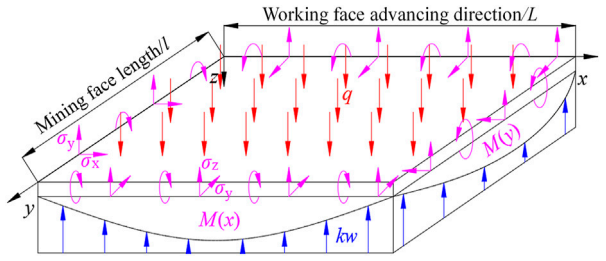

FIGURE 3
Simplified mechanical model of roof in SCFM.

overburden deformation has a certain effect, with high water material filling can be more effective limit overburden deformation space (Wang et al., 2016; Li et al., 2017; Deng et al., 2020). As shown in Figure 2, the SCFM takes a certain number of working faces as a mining cycle (five working faces are taken as an example in the figure). The first step is to form a face production system and finish mining the first face CT301. The second step is to start mining the CT303 face after spacing the coal pillars (i.e., CT302 face) at a certain distance from the first face already mined, and at the same time to fill the CT301 already mined. Step 3: Repeat the above steps after spacing the coal pillar (i.e., CT304 working face) by a certain distance to mine CT305 working face while filling the mined CT303 working face. Step 4: When the mining cycle reaches the designed number of working faces, fill the last working face and start back mining the skipped working faces (i.e., CT302, CT304 working faces) in the order of mining and filling as above until the whole cycle is completed. For the entire mining area, the mining area can be divided into several mining cycles and steps one through four can be repeated to complete the entire area.

3 Key factors of overburden deformation control

The overburden deformation and fracture development after coal seam mining in the working face are mainly affected by factors such as coal seam mining height, working face size, goaf filling rate, lithologic structure, coal seam burial depth and geological structure (Liu et al., 2018; Feng et al., 2021). The mining height is generally determined by the occurrence state of the coal seam, and the size of the working face and the filling rate of the goaf become the main controllable factors. In order to intuitively analyze the damage of the main controllable factors to the roof of the filling coal mining face, the stress model of the roof of the SCFM established to analyze its stress characteristics.

For the study mine, the advance length is determined by the occurrence conditions of coal seams. In most cases, it is greater than 1000 m. The thickness of the immediate roof and the main roof in the overlying strata is about 5 m, and the length of the short-wall working face is generally less than 100 m, preliminary estimate is 50–100 m, according to the definition of thin plate model, short wall face length of 25–400 m can be regarded as thin plate model (Li et al., 2014; Feng et al., 2017). The roof of the overlying strata in the short-wall filling stope can be regarded as a thin plate model, and the filling material is regarded as an elastic foundation. In order to ensure that it does not break under the constraints of the working face size and the filling body, it can be seen as a four-sided clamped plate supported by the high-level rock layer above and supported by the filling body below. The mechanical model of the elastic thin plate is established as shown in Figure 3.

The roof of short-wall filling stope deforms under the joint constraints of working face size and filling body. According to the solution method of elastic mechanics thin plate problem, the internal force problem is transformed into the solution of thin plate deflection equation. The deflection equation of elastic thin plate surface expressed by double sine series is calculated:

$$w(x,y)=\sum_{m=1,3\ldots}^{\infty}\sum_{n=1,3\ldots}^{\infty}A_{mn}\sin\frac{m\pi x}{L}\sin\frac{n\pi y}{l} \tag{1}$$

In the formula, L is the length of the advancing direction of the working face; l is the length of working face; A_{mn} is the generalized coordinate of the bending surface of elastic thin plate. The system composed of stope roof and elastic foundation is regarded as a whole and solved by virtual work principle:

$$w(x,y)=\sum_{m=1,3\ldots}^{\infty}\sum_{n=1,3\ldots}^{\infty}\frac{\frac{Ll}{mn\pi^2}4q+\frac{m\pi}{l}LE_m+\frac{n\pi}{L}lF_n}{\frac{Ll\pi^4}{4}D\left(\frac{m^2}{L^2}+\frac{n^2}{l^2}\right)^2+\frac{klL}{4}}\sin\frac{m\pi x}{L}\sin\frac{n\pi y}{l} \tag{2}$$

In the formula, the coefficients of bending moment $M(x)$ and $M(y)$ in the form of E_m and F_n Fourier series, $\begin{cases}M(x)=\sum_{m=1,3\ldots}^{\infty}E_m\sin\frac{m\pi x}{L}\\ M(y)=\sum_{n=1,3\ldots}^{\infty}F_n\sin\frac{n\pi y}{l}\end{cases}$; D is bending rigidity; q is uniform load. According to the meanings of elastic modulus, filling rate and elastic foundation coefficient, we can solve the equation of elastic foundation coefficient of the filling body as a function of the filling rate of the mining area $k=\frac{\sigma_0}{h_1(1-\varphi)}$, where σ_0 is the initial stress on the coal seam, h_1 is the mining thickness of the coal seam, and φ is the filling rate of the mining area. By substituting k into Eq. 2, the bending moment expressed by Fourier series appears on the fixed edge, and the plane stress component corresponding to the plate is Eq. 3. By substituting the bending moment $M(x)$ and $M(y)$ in the form of Fourier series into Eq. 3, the maximum tensile stress Eq. 4 on the roof can be obtained, in which σ_x, σ_y and τ_{xy} are the tensile stress of the roof in x and y directions and the shear stress component corresponding to the roof respectively.

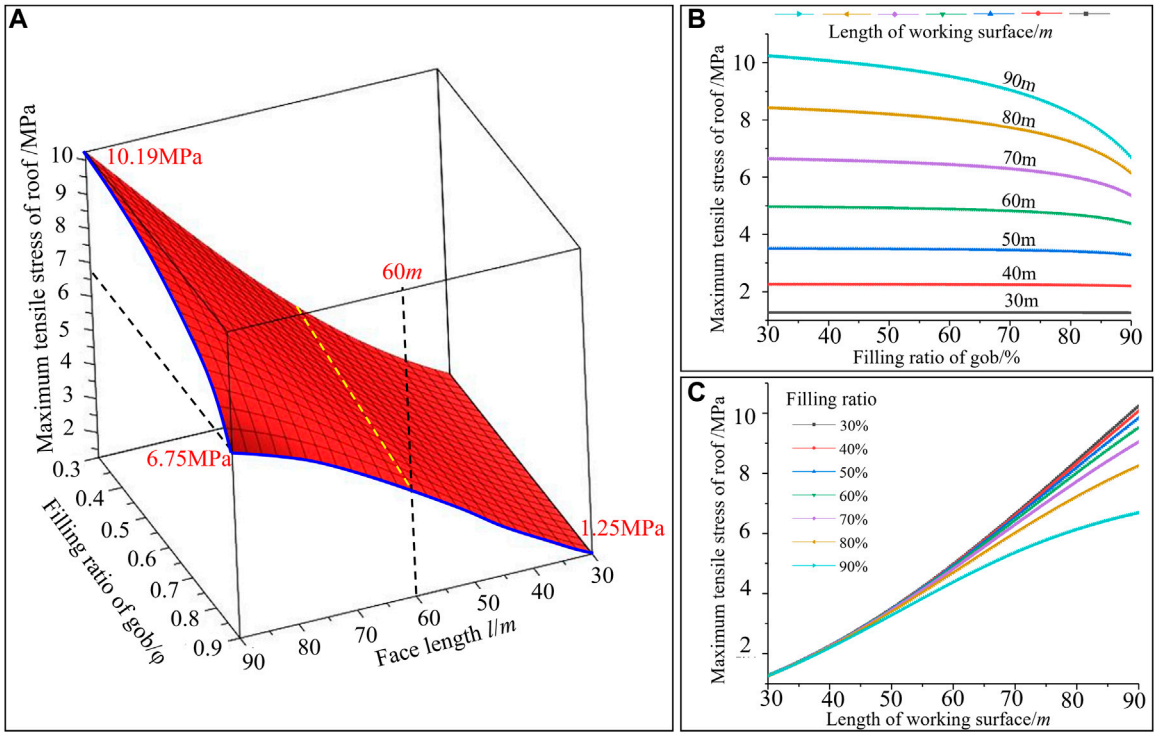

FIGURE 4
Influencing factors of maximum tensile stress of roof, **(A)** The relationship between the maximum tensile stress of the roof and the length of the working face and the filling rate, **(B)** Filling rate, **(C)** Length of working surface.

$$\begin{cases} \sigma_x = \dfrac{12M(x)z}{h^3} \\ \sigma_y = \dfrac{12M(y)z}{h^3} \\ \tau_{xy} = \dfrac{12M(xy)z}{h^3} \end{cases} \tag{3}$$

$$\begin{cases} \sigma_{x\max} = \dfrac{6M(x)}{h^2} = \dfrac{6}{h^2}\sum\limits_{m=1,3\ldots}^{\infty} E_m \sin\dfrac{m\pi x}{L} \\ \sigma_{y\max} = \dfrac{6M(y)}{h^2} = \dfrac{6}{h^2}\sum\limits_{n=1,3\ldots}^{\infty} F_n \sin\dfrac{n\pi y}{l} \end{cases} \tag{4}$$

In order to control the roof without cracks, the critical condition of $\begin{cases} \sigma_{x\max} \le [\sigma_t] \\ \sigma_{y\max} \le [\sigma_t] \end{cases}$ must be satisfied. The coefficients of bending moment $M(x)$ and $M(y)$ expressed by Fourier series can be solved :

$$\begin{cases} \sum\limits_{m=1,3\ldots}^{\infty}\sum\limits_{n=1,3\ldots}^{\infty} \dfrac{\dfrac{Ll}{mn\pi^2}4q + \dfrac{mn\pi}{l}LE_m + \dfrac{m^2\pi}{L}lF_n}{\dfrac{Ll\pi^4}{4}D\left(\dfrac{m^2}{L^2}+\dfrac{n^2}{l^2}\right)^2 + \dfrac{\sigma_0 lL}{4h(1-\varphi)}} = 0 \\ \sum\limits_{m=1,3\ldots}^{\infty}\sum\limits_{n=1,3\ldots}^{\infty} \dfrac{\dfrac{Ll}{mn\pi^2}4q + \dfrac{n^2\pi}{l}LE_m + \dfrac{mn\pi}{L}lF_n}{\dfrac{Ll\pi^4}{4}D\left(\dfrac{m^2}{L^2}+\dfrac{n^2}{l^2}\right)^2 + \dfrac{\sigma_0 lL}{4h(1-\varphi)}} = 0 \end{cases} \tag{5}$$

According to the geological conditions of the SCFM face in the third panel of the mine, the average thickness of the coal seam is 6.67 m, the average dip angle is 8°. The basic roof of the overlying strata is fine-grained sandstone, the bending stiffness D is 1.64×10^{12} N·m, the elastic modulus E is 14.3 GPa, the Poisson's ratio μ is 0.3, the thickness h is 3.79 m, the length L of the working face is 375 m, and the length of the working face is to be determined. The uniform load of the overlying strata of the basic roof q is calculated to be 0.17 MPa. In order to simplify the calculation of the plate model, the first two terms representing the Fourier coefficients of the fixed edge bending moment are selected and substituted into the above parameters to solve the Fourier coefficients E_1, E_3, F_1 and F_3 corresponding to the bending moment :

$$\begin{cases} E_1 = -\dfrac{(660.37\times(6.89\times10^{14}l^4\varphi - 3.51\times10^{16}l^4 + 1.81\times10^{20}l^2(\varphi-1) + 8.60\times10^{25}(\varphi-1))}{1.29\times10^{14}l^4\varphi - 4.33\times10^{15}l^4 + 1.30\times10^{19}l^2(\varphi-1) + 2.54\times10^{24}(\varphi-1)} \\ E_3 = \dfrac{(220.12\times(3.06\times10^{15}l^4\varphi + 4.50\times10^{15}l^4 + 9.77\times10^{20}l^2(\varphi-1) + 6.05\times10^{25}(\varphi-1))}{1.29\times10^{14}l^4\varphi - 4.33\times10^{15}l^4 + 1.30\times10^{19}l^2(\varphi-1) + 2.54\times10^{24}(\varphi-1)} \\ F_1 = -\dfrac{2.07\times10^{21}\times(20992l^2\varphi - 1.72\times10^5 l^4 + 1.30\times10^9 l^2(\varphi-1) + 9.11\times10^{13}(\varphi-1))}{(1.29\times10^{14}l^4\varphi - 4.33\times10^{15}l^4 + 1.30\times10^{19}l^2(\varphi-1) + 2.54\times10^{24}(\varphi-1))} \\ F_3 = 0 \end{cases} \tag{6}$$

Substituting Eq. 6 into Eq. 4, the relationship between the maximum tensile stress of roof and the length and filling rate of working face can be obtained. In order to intuitively analyze the

relationship between the maximum tensile stress of roof and the two, Eq. 7 is further processed and drawn into Figure 4.

$$\sigma_{t\max} = \frac{34.03l^2\left(6.89\times10^{14}l^4\varphi - 3.51\times10^{16}l^4 + 1.81\times10^{20}l^2(\varphi-1) + 8.60\times10^{25}(\varphi-1)\right)}{1.29\times10^{14}l^4\varphi - 4.33\times10^{15}l^4 + 1.30\times10^{19}l^2(\varphi-1) + 2.54\times10^{24}(\varphi-1)} + \frac{11.34l^2\left(3.06\times10^{15}l^4\varphi + 4.50\times10^{15}l^4 + 9.77\times10^{20}l^2(\varphi-1) + 6.05\times10^{25}(\varphi-1)\right)}{1.29\times10^{14}l^4\varphi - 4.33\times10^{15}l^4 + 1.30\times10^{19}l^2(\varphi-1) + 2.54\times10^{24}(\varphi-1)} \quad (7)$$

From the analysis in Figure 4A, it can be seen that when the filling rate is 90%, the maximum tensile stress of the roof decreases from 6.75 to 1.25 MPa during the reduction of the working face length from 90 m to 30 m, and the reduction rate reaches 81.48%. When the working face length is 90 m, the maximum tensile stress of the roof decreases from 10.19 to 6.75 MPa in the process of decreasing the filling rate from 30% to 90%, and the decrease is 33.95%. It is easy to know that the maximum tensile stress of the roof in the short-wall filling mining working face is more sensitive to the length of the working face than the filling rate of the goaf, i.e., the length of the working face has a greater influence on the maximum tensile stress of the roof.

From the analysis of Figures 4B, C, it can be seen that the maximum tensile stress in the roof slab decreases with the increase of the filling rate, but the reduction rate is affected by the length of the working face, and the critical value is roughly 60 m. When the working face length is greater than 60m, the effect of increasing filling rate on the reduction of maximum tensile stress in the roof is more obvious, and this effect increases with the increase of working face length. When the working face length is 60 m, 70 m, 80 m and 90 m respectively, the maximum tensile stress reduction of the roof corresponding to the increase of filling rate from 30% to 90% is 33.95%, 25.61%, 18.52%, and 8.40% respectively. In contrast, the maximum tensile stress of the roof plate decreases very little with the increase of the filling rate when the working face length is less than 60 m, and even remains basically unchanged.

At the same time, the maximum tensile stress in the roof increases significantly with the increase of the working face length regardless of the filling rate. However, when the filling rate is low, the roof tensile stress changes significantly with the length of the working face, and the increase slows down gradually with the increase of the filling rate. When the filling rate of the goaf is 60%, 70%, 80% and 90%, the increase of maximum tensile stress of the roof corresponding to the increase of the working face length from 40 m to 90 m is 352.38%, 328.57%, 290.48%, and 221.43% respectively.

To sum up, under the layout of short-wall filling mining face, the sensitivity of the maximum tensile stress of the roof to the length of the working face is better than the filling rate. In the design process of mining parameters, the length of the working face should be taken as the main factor to control the development of roof cracks, but the filling must be used to prevent the development of cracks caused by the slow deformation of the roof.

4 Working face design based on elastic foundation coefficient

It can be seen from the above section that the length of the working face plays a key role in controlling the maximum tensile stress of the roof in the main controllable factors of SCFM. According to the operation process of SCFM, taking five working faces of single mining cycle as an example, the stress analysis of the interaction system composed of coal body, filling body and roof in each mining step is carried out. It is easy to know that the deformation of overlying strata is always controlled by the three mining units of the current mining face and the left and right adjacent mining affected areas. Therefore, the design principle of working face length is that the roof control range of three working units should be greater than the stress concentration area. When the solid coal is recovered by filling, the combination of roof and filling body forms a coupling system of stress and deformation. In order to facilitate the analysis, the three operating units are regarded as the foundation synergy with different elastic coefficients to jointly control the roof subsidence.

In a single mining cycle, the supporting capacity of the overall structure composed of roof and floor, coal pillar and filling body to the overlying strata is related to the mining state of different stages of the working face. The following is an analysis of the three basic structures formed during the single mining cycle, and then the different states of the combination of coal pillar and filling body during the whole mining period are analyzed.

(1) Structure 1:

Structure 1 consists of a filling body and its two adjacent working faces, whose stress state under the action of roof and floor is shown in Figure 5. The filling body is in the stage of being compacted and sunk, and the small elastic foundation coefficient causes the stress of the two adjacent working faces to rise. The relationship between the three units and the roof is established by the elastic foundation theory, as shown in Eq. 8.

$$2\int_0^{L_1} k_1 w_1(x,y)dy + \int_{L_1}^{l+L_1} k w_2(x,y)dy = q_2(2L_1 + l) \quad (8)$$

In the formula, k_1 is the elastic foundation coefficient of coal pillar unit; k is the equivalent elastic foundation coefficient; q_2 is the load of coal pillar and filling body; w_1 and w_2 are the deformation of coal pillar and filling body unit; L_1 is the length of working face to be mined; l is the length of the mined face.

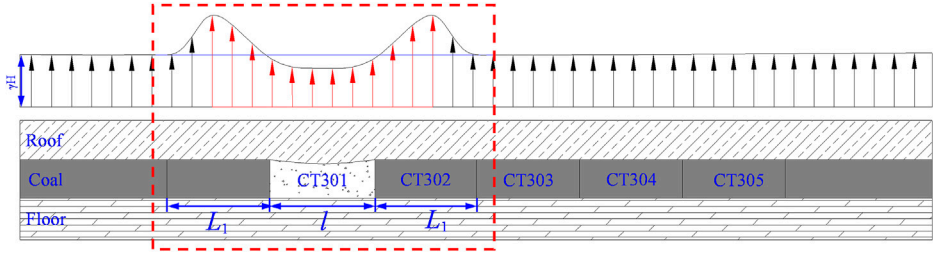

FIGURE 5
Structure 1 stress analysis diagram.

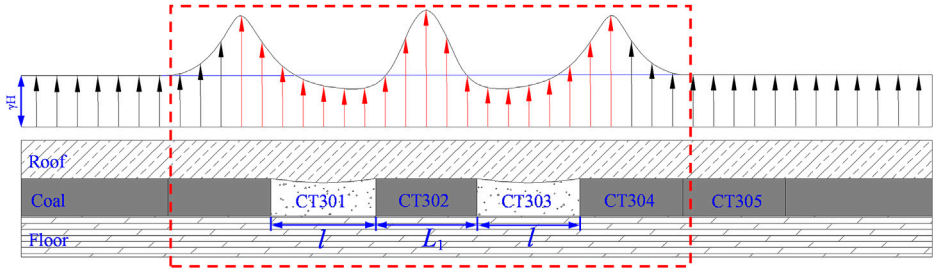

FIGURE 6
Structure 2 stress analysis diagram.

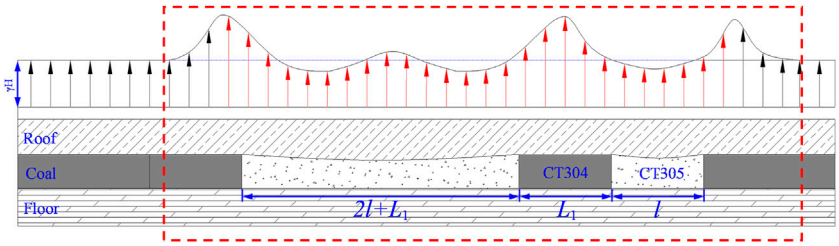

FIGURE 7
Structure 3 stress analysis diagram.

Solving Eq. 8, the relationship between the length of working face and elastic foundation coefficient can be expressed as:

$$L_1 = \frac{E_0}{q_2 h_1}\int_0^{L_1} w_1(x,y)dy \tag{9}$$

In the formula, E_0 is the elastic modulus of filling body; h_1 is the height of filling body.

(2) Structure 2:

Structure 2 is composed of two filling bodies sandwiched by a working face to be mined. The stress state of structure 2 under the action of roof is shown in Figure 6. The working face to be mined temporarily becomes the main bearing body in the structure at this stage, and the stress increases obviously. The relationship between the three units and the roof is established by the elastic foundation theory as shown in Eq. 10.

$$2\int_{L_1}^{l+L_1} kw_2(x,y)dy + \int_{L_1+l}^{2L_1+l} k_1 w_1(x,y)dy = q_2(2l+L_1) \tag{10}$$

By solving the Eq. 10, the relationship between the working face length and the elastic foundation coefficient in the case of structure two can be expressed as follows:

$$L_1 = \frac{E_0}{q_2 h_1}\int_{L_1+l}^{2L_1+l} w_1(x,y)dy \tag{11}$$

(3) Structure 3:

As shown in Figure 7, the third structure is a working face to be mined plus two asymmetric filling bodies, that is, the size of the filling areas on both sides is inconsistent, resulting in an asymmetric increase in the stress of the working face to be mined. The relationship between the three units and the roof is established by the elastic foundation theory as shown in Eq. 12.

$$\int_{L_1}^{2L_1+2l} kw_2(x,y)dy + \int_{2L_1+2l}^{3L_1+2l} k_1 w_1(x,y)dy + \int_{3L_1+2l}^{3L_1+3l} kw_2(x,y)dy = q_2(3l+2L_1) \tag{12}$$

Solving Eq. 12, the relationship between the length of working face and elastic foundation coefficient can be expressed as:

$$L_1 = \frac{E_0}{q_2 h_1}\int_{2L_1+2l}^{3L_1+2l} w_1(x,y)dy \tag{13}$$

From the process flow of SCFM, it can be seen that different mining stages in the mining area during the whole mining period are the combination of the above three conditions. By combining the above three conditions, the stress conditions of different stages in the whole mining process can be obtained, and then the influence of the length of the working face on the elastic foundation coefficient can be obtained, and the reasonable distance between the length of the working face L_1 and l can be analyzed. According to the elastic foundation coefficient and the force balance condition, in order to ensure that the stress appears within a reasonable range, the interval distance between the first and the fifth mining face is respectively (14)–(18).

$$L_1 = \frac{E_0}{q_2 h_1}\int_{0}^{L_1} w_1(x,y)dy \tag{14}$$

$$L_1 = \frac{E_0}{3q_2 h_1}\left[\int_{0}^{L_1} w_1(x,y)dy + \int_{L_1+l}^{2L_1+l} w_1(x,y)dy + \int_{2(L_1+l)}^{3L_1+2l} w_1(x,y)dy\right] \tag{15}$$

$$L_1 = \frac{E_0}{4q_2 h_1}\left[\int_{0}^{L_1} w_1(x,y)dy + \int_{L_1+l}^{2L_1+l} w_1(x,y)dy + \int_{2(L_1+l)}^{3L_1+2l} w_1(x,y)dy + \int_{3(L_1+l)}^{4L_1+3l} w_1(x,y)dy\right] \tag{16}$$

$$L_1 = \frac{E_0}{3q_2 h_1}\left[\int_{0}^{L_1} w_1(x,y)dy + \int_{L_1+3l}^{2L_1+3l} w_1(x,y)dy + \int_{2L_1+4l}^{3L_1+4l} w_1(x,y)dy\right] \tag{17}$$

$$L_1 = \frac{E_0}{2q_2 h_1}\left[\int_{0}^{L_1} w_1(x,y)dy + \int_{L_1+5l}^{2L_1+5l} w_1(x,y)dy\right] \tag{18}$$

From the above-mentioned analysis of the workface spacing distance elastic foundation expressions for each recovery step, it can be seen that the stress is greatest at the time of the fourth recovery operation and the highest requirements for workface spacing. And the structure consisting of the filling area and the working face to be mined varies with the size of the working face. When the length of the working face is not consistent, it is more conducive to the release of the support pressure, but it will have a negative impact on the mining process. In order to balance the requirements for overlying rock control and to coordinate the production process to improve mining efficiency, the distance with the highest requirements for workface spacing was chosen as the workface length. Substituting the specific parameters of the study mine in Section 2, and considering a certain safety factor, we get that the roof control range of the three operating units is larger than the stress concentration zone when the length of the fourth recovery operating face is 40 m.

5 SCFM overburden hydraulic conductivity fracture development

5.1 Overburden hydraulic conductivity fracture peak point analysis

Generally the overburden rock appears collapse, fracture, bending and other characteristics from bottom to top after the coal seam is retrieved, and the development height of the fracture zone is directly related to whether the overburden aquifer can be conducted (Miao et al., 2011; Liu et al., 2017). The rock strata in the range of fractured zone have the characteristics of maintaining the original layer state, but the hard rock strata in this range are easy to break and crack, which makes the water seepage phenomenon, while the soft rock strata have good toughness and allow large deformation, which has a good barrier effect on the seepage of water (Xie et al., 2021). After the rupture of the hard roof in the lower side, under the combined action of stress release and the weak rock layer above, the fracture of the overlying rock may terminate here. The critical breaking height of the soft rock layer in the overlying rock layer is regarded as the peak point of the development of water flowing fracture (Liu et al., 2019; Li et al., 2021).

The soft rock stratum is bent and sunk by the support of the coal walls on both sides, and the critical rupture position is related to the span between the coal walls. When the span is large, the maximum curvature of soft rock occurs above the side of coal wall. When the span is small, the maximum curvature of soft rock occurs right above the middle of the mining area. In this paper, the soft rock stratum is regarded as a fixed beam model, as shown

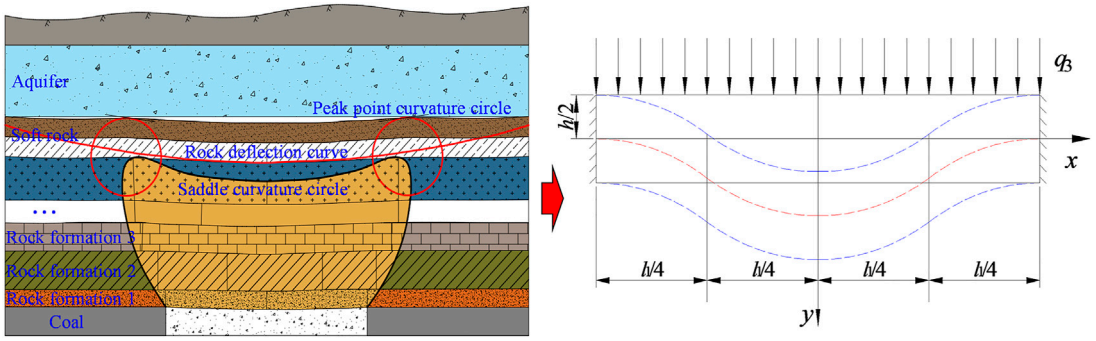

FIGURE 8
Mechanical model of solid support beam for overlying soft rock formations.

in Figure 8, and the peak point of overburden fracture development after the whole period of SCFM is analyzed.

The bending deflection equation of the fixed beam model is :

$$w_3 = a_1\left(1+\cos\frac{2\pi x}{l_1}\right)+a_2\left(1+\cos\frac{6\pi x}{l_1}\right)+\cdots+a_n\left(1+\cos\frac{(2n-1)2\pi x}{l_1}\right) \tag{19}$$

In the formula, w_3 and l_1 are the deflection and span of the fixed beam in the overlying weak rock stratum respectively. The effective load q_3, elastic modulus E_2 and inertia moment I to z axis of the weak strata of overlying strata are respectively brought into Eq. 19 to obtain:

$$w_3 = \sum_{i=1}^{n}\frac{q_3 l_1^4}{[(2n-1)2\pi]^3(2n-1)\pi E_2 I}\left(1+\cos\frac{(2n-1)2\pi x}{l}\right) \tag{20}$$

Based on the deformation deflection curve of the fixed beam obtained above, the maximum deflection of the fixed beam model of overburden rock is:

$$w_{3\max} = w_3|_{x=\frac{l_1}{2}} = \frac{4q_3 l_1^4}{\pi^4 E_2 I} = 0.041\frac{q_3 l_1^4}{E_2 I} \tag{21}$$

At the same time, the rotation angle equation of fixed beam is:

$$\theta = \frac{\mathrm{d}w_3}{\mathrm{d}x} = \sum_{i=1}^{n}\frac{-q_3 l_1^2}{(2n-1)^3\pi^3 E_2 h_2^3}\sin\frac{(2n-1)2\pi x}{l_1} \tag{22}$$

The curvature equation of fixed beam is:

$$\frac{1}{\rho} = \frac{\mathrm{d}^2 w_3}{\mathrm{d}x^2} = -\sum_{i=1}^{n}\frac{6q_3 l_1}{(2n-1)^2\pi^2 E_2 h_2^3}\cos\frac{(2n-1)2\pi x}{l_1} \tag{23}$$

In the formula, ρ is the radius of curvature of the soft rock layer. Under the condition of bending deformation of soft rock stratum, the smaller the radius of curvature, that is, the greater the curvature, the greater the tensile deformation. Therefore, the maximum value of the curvature equation of the clamped beam in the soft rock layer of Eq. 23 can be obtained and the deformation at this position (generally 2 mm/m) can still maintain the integrity of the entire soft rock layer, that is, the critical span can be obtained (Zhao et al., 2018; Li, 2019). The allowable limit span under the condition of maximum horizontal deformation of soft rock stratum is:

$$l_1 = \frac{2E_2 h_2^2}{375 q_3} \tag{24}$$

The distance from the upper and lower boundaries of the soft rock strata to the roof of the coal seam is the height of the water-conducting fracture development, and this position is the peak point at different positions of the water-conducting fracture development.

5.2 Overburden fracture development height under the whole area recovery condition

The dip direction of the third panel of the mine is more than 1000 m, and the distance from the boundary of the second and third panels to the boundary of the third and fourth panels is about 700 m in the strike direction. The number of working faces and mining size in the strike direction should be designed according to the allowable development height of the water flowing fracture in the overlying strata. The development height of the water flowing fracture must also meet the control requirements after the completion of the mining in the whole area.

The main aquifer in the third panel is the Luohe Formation aquifer, and the main aquifuge is the Anding Formation aquifuge. Through the analysis of drilling data, it can be seen that the thickness of the effective interval between the coal seam roof and the lower boundary of the Luohe Formation aquifer is 100 m, and the thickness of the Anding Formation aquifuge is about 35 m. Considering a certain safety factor, it is considered safe to control the

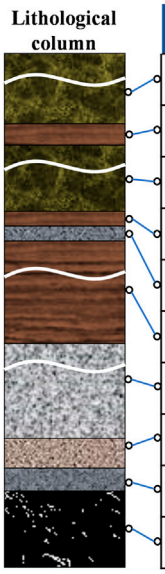

Lithological column	Name of stratum	Thickness /m	Density /kg·m^{-3}	Elastic modulus/MPa	Compressive strength/MPa	Tensile strength/MPa
	Sandy mudstone	17.24	2100	1080	25.1	3.10
	Coarse Sandstone	1.50	2590	19650	78	3.91
	Sandy mudstone	9.80	2100	1080	25.1	3.10
	Coarse Sandstone	1.00	2590	19650	78	3.91
	mudstone	1.00	2050	6840	30	2.37
	Coarse Sandstone	23.08	2590	19650	78	3.91
	medium grained sandstone	17.03	2380	21830	70	3.08
	fine-sandstone	3.79	2150	14270	50	3.20
	mudstone	1.25	2050	6840	30	2.37
	4#coal	6.67	1900	4830	10	0.87

FIGURE 9
Mechanical parameters of overlying rock layers in three panels.

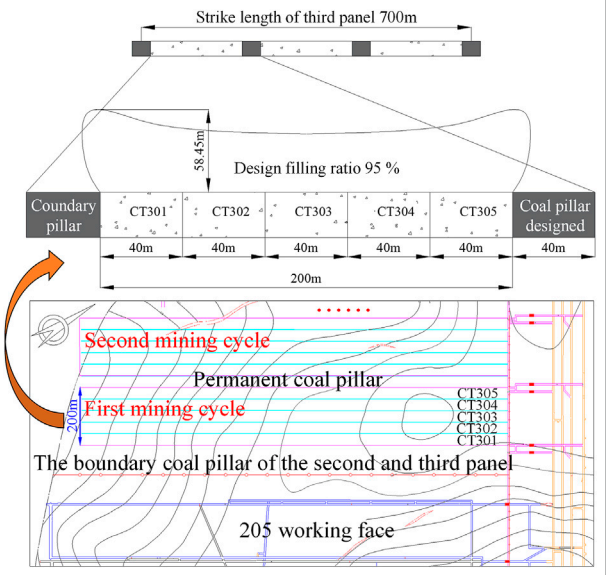

FIGURE 10
Parameter design diagram of the three-panel area of the mine.

development height of the overburden rock fracture within 65 m. The distribution of overlying soft rock strata in the third panel is shown in Figure 9.

According to the height of overburden deformation and fracture development in the mine can't exceed 65 m, it is concluded that the 9th layer of sandy mudstone in the overlying strata is the critical soft rock layer. The critical span obtained under the condition of critical tensile deformation is the maximum mining width allowed after the whole mining of the third panel. Through the Eq. 25, the load q_3 of the 9th layer of soft rock is 0.78 Mpa.

$$(q_3)_k = \frac{E_2 h_2^3 \sum_{k=1}^{s} h_k \gamma_k}{\sum_{k=0}^{s} E_k h_k^3} \tag{25}$$

Substitute the actual parameters of the 9th layer of soft rock formation into the above Eq. 24 and design the fixed beam according to the requirement that the width of the solid support beam is 1/2–1/3 of the height and the height is 1/10–1/12 of the span, and the load is the line load along the span direction, and take the maximum span of 200 m with certain safety factor. The strike distance of the whole mining area between the boundary coal pillars in the third panel is 693 m. It can be seen that the 9th soft rock layer will be destroyed and produce cracks after the whole mining area is mined. Therefore, according to the previous analysis, the third panel is designed as follows.

As shown in Figure 10, the strike length of the three-panel area of the study mine is approximately 700 m, which far exceeds the critical span of 200 m for the 9th soft rock layer, so the critical span of 200 m is used as a mining cycle, where each working face is 40 m long and divided into 5 working faces. In order to ensure that the overburden deformation fracture development is still within the control range after the mining range is increased, a

TABLE 1 Drilling design parameters.

Number	Inclination/°	Hole depth/m	Vertical depth/m	Horizontal distance/m
1#	50	130.54	100	83.91
2#	55	122.08	100	70.02
3#	60	115.47	100	57.74
4#	55	122.08	100	70.02

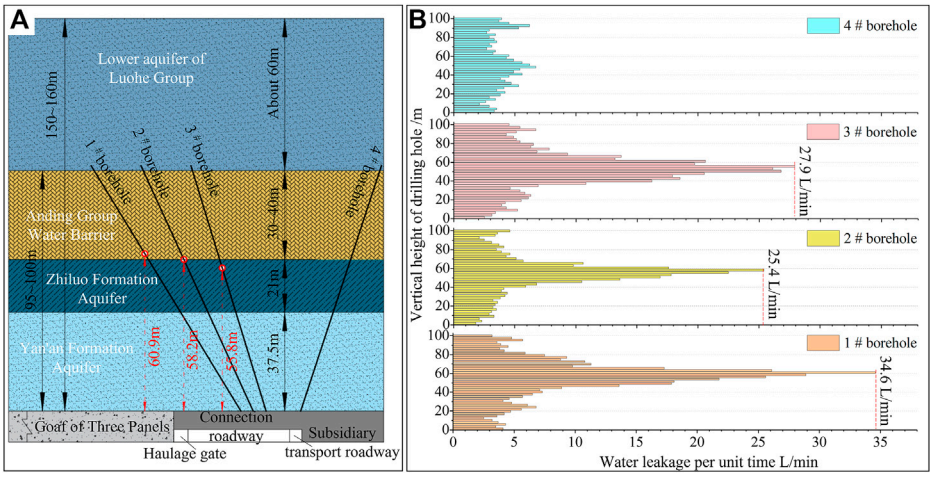

FIGURE 11
Upward hole segmented water injection method, **(A)** Borehole layout, **(B)** Unit time leakage water loss and borehole vertical height histogram.

distance of one working face length is spaced between two adjacent mining cycles, so that the cycle completes the design of the entire pan area recovery work, the calculated overburden hydraulic fracture development height is 58.45 m.

In order to verify the actual development height of the hydraulic fracture zone after the whole area has been re-mined, 2 months after the completion of filling and re-mining in the three pans, when the hydraulic fissure zone is fully developed to its maximum height, a drilling site is set up in the liaison road between the auxiliary transport roadway and the transport roadway on the outside of the stopping line of the first mining face in the three pans, and an inclined drilling hole is constructed in the direction of the goaf. Drill holes 1# to 3# are exploratory drill holes, avoiding the fall zone and penetrating diagonally to a certain height above the top boundary of the expected fissure zone. The drill hole 4# was drilled diagonally towards the coal pillar of the pan area and was a comparison drill hole not affected by mining. The parameters of drill holes 1–4# are shown in Table 1. The leakage per unit time of each section of borehole is measured by the method of segmented water injection into the inverted hole, and the development height of water flowing fractured zone is analyzed by the change of leakage. The borehole layout and the leakage per unit time are shown in Figure 11.

As shown in Figure 11, each section of 4# contrast borehole has different sizes of leakage, water injection leakage changes in the range of 2.1–6.7 L/min, in the drilling depth of 50–68 m and 110–113 m interval, the corresponding vertical height of 41–55.8 m, 90.2–92.6 m leakage showed two smaller peaks, the average leakage interval reached 5.64 L/min. The leakage in the contrast hole reflects the existence of primary cracks and certain permeability and water absorption when the rock layer is not broken and moved. The primary cracks and water absorption of the rock layer at the aquifer of Zhiluo Formation and the junction of the aquifuge of Anding Formation and the lower aquifer of Luohe Formation are larger than other rock layers. The net leakage can be obtained by subtracting the leakage of the corresponding section 4# background hole from the unit time leakage of each section of 1–3# borehole, so as to reduce the error caused by the primary fracture.

The maximum water loss per unit time of 1–3# boreholes is much larger than that of 4# comparative boreholes. The maximum

values are 34.6 L/min, 25.4 L/min and 27.9 L/min, respectively, and the corresponding vertical heights are 60.9 m, 58.2 m and 55.8m, respectively. It can be seen from the histogram of 1# hole leakage per unit time that when the vertical height is less than 19.5 m, the corresponding leakage is not much different from that of 4# contrast hole, indicating that the rock strata in this section may not be destroyed or in the compacted dense area. In the vertical height range of 19.5–60.9 m, the leakage shows an exponential upward trend until it reaches the maximum. This section should enter the water-conducting fracture zone, the gap is developed, and the rock mass is more damaged. After the vertical height of 60.9 m, the leakage decreases rapidly with the increase of the hole depth. After the vertical height of 65.5 m, the leakage has dropped below 10 L/min. The net leakage after subtracting the leakage of 4# contrast hole is less than 5 L/min on average. It shows that the development of water-conducting fractures caused by mining is small after the vertical height of 60.9 m.

The unit time leakage of 2# and 3# holes increases rapidly to the peak value from the vertical height of 41 m and 35 m respectively, and the distance to the fracture zone is farther than that of 1# hole. And the leakage volume decreases to 10 L/min near 77.1 m and 73.5 m deep (corresponding to a vertical height of 63 m) in both holes, which is about the junction of the water-bearing layer of the Zhiluo Formation and the water-insulating layer of the Anding Formation. This indicates that the development of the fracture has stopped below the water barrier of the Anding Group, and a comparison of the leakage in the latter part of the peak leakage per unit time in holes 2# and 3#, i.e., the leakage in the water barrier of the Anding Group, with the leakage in this section in the comparison holes also shows that the hydraulic fissures have not continued to develop upwards.

To sum up, through the comprehensive analysis of the leakage amount per unit time in 1–3# measurement boreholes and 4# comparison boreholes, it can be seen that the measured value of the development height of the hydraulic fissure zone in the whole area of the three pans after recovery is more in line with the calculated value, basically developing to the bottom of the water barrier of the stability group and stopping, none of them exceeds the safe hydraulic fissure zone height of 65 m.

6 Conclusion

(1) A model of the forces on the roof of a SCFM face was established to study the influence of two major controllable factors, namely the size of the working face and the infill rate, on the roof of an backfill coal mining face. The results show that the maximum tensile stress in the roof under the short-wall working face arrangement is more sensitive to the length of the working face than the filling rate, so the length of the working face should be the main factor in the design of the mining parameters to control the roof fracture development.

(2) Based on the elastic foundation coefficient, the length of the working face in a single mining cycle is designed. The whole SCFM process is always regarded as the process of controlling the deformation of the overlying strata by the three mining units of the current mining face and the left and right adjacent mining affected areas. Three basic structures composed of filling body, coal body and roof formed during a single mining cycle are constructed. Taking five working faces as examples, the stress of each step in a single mining cycle is analyzed. The results show that the fourth step of the mining cycle has the highest requirement for the working face interval. When the length of a single working face is designed to be 40 m, the roof control range of the three working units is greater than the stress concentration area.

(3) Taking the research mine as the engineering background, the layout of the SCFM working face in the whole area of the three panels was designed, and the development height of the water-conducting fracture under the condition of the whole mining area was calculated to be 58.45 m. Through the inverted hole water injection exploration method, it is verified that the actual development height of the water flowing fracture after mining and filling is close to the calculated value, and both exceed the safe height of 65 m.

Data availability statement

The original contributions presented in the study are included in the article/supplementary material, further inquiries can be directed to the corresponding author.

Author contributions

YY and ED wrote the manuscript. PJ and NZ revised the manuscript. YY and ED conducted the field experiments. YY, PJ, and NZ conceived the idea, carried out data analysis.

Funding

This work was funded by the Graduate Innovation Program of China University of Mining and Technology (grant number 2022WLKXJ048).

Acknowledgments

The authors would like to extend their thanks to the providers of the materials used in this study, and their appreciation to those who offered support for this study,

including CUMT and Coal Mining Branch, China Coal Research Institute.

Conflict of interest

The authors declare that the research was conducted in the absence of any commercial or financial relationships that could be construed as a potential conflict of interest.

Publisher's note

All claims expressed in this article are solely those of the authors and do not necessarily represent those of their affiliated organizations, or those of the publisher, the editors and the reviewers. Any product that may be evaluated in this article, or claim that may be made by its manufacturer, is not guaranteed or endorsed by the publisher.

References

Bai, E. H., Guol, W. B., Tan, Y., and Yang, D. M. (2018). The analysis and application of granular backfill material to reduce surface subsidence in China's northwest coal mining area. *PLoS One* 13, e0201112. doi:10.1371/journal.pone.0201112

Chen, L., Zhang, D. S., Fan, G. W., Zhang, S. Z., Wang, X. F., and Zhang, W. (2022). A new repeated mining method with preexisting damage zones filled for ultra-thick coal seam extraction - case study. *Front. Earth Sci.* 10, 1–14. doi:10.3389/feart.2022.835867

Chi, M. B., Zhang, D. S., Liu, H. L., Wang, H. Z., Zhou, Y. Z., Zhang, S., et al. (2019). Simulation analysis of water resource damage feature and development degree of mining-induced fracture at ecologically fragile mining area. *Environ. Earth Sci.* 78, 88. doi:10.1007/s12665-018-8039-5

Deng, X. J., Yuan, Z. X., Lan, L. X., De Wit, B. J., and Zhang, J. W. (2020). Roof movement and failure behavior when mining extra-thick coal seams using upward slicing longwall-roadway cemented backfill technology. *Adv. Mat. Sci. Eng.* 2020, 1–15. doi:10.1155/2020/5828514

Deng, X. J., Zhang, J. X., Zhou, N., De Wit, B., and Wang, C. T. (2017). Upward slicing longwall-roadway cemented backfilling technology for mining an extra-thick coal seam located under aquifers: A case study. *Environ. Earth Sci.* 76, 789. doi:10.1007/s12665-017-7120-9

Fan, L. M., Ma, X. D., Jiang, Z. Q., Sun, K., and Ji, R. J. (2019). Review and thirty years prospect of research on water-preserved coal mining. *Coal Sci. Technol.* 47, 1–30. doi:10.13199/j.cnki.cst.2019.07.001

Feng, J., Peng, H., Shuai, G., Meng, X., and Lan, L. X. (2017). A roof model and its application in solid backfilling mining. *Int. J. Min. Sci. Technol.* 27, 139–143. doi:10.1016/j.ijmst.2016.11.001

Feng, J., Wang, S. J., Hou, E. K., Ding, X., and Duan, H. J. (2021). Determining the height of water-flowing fractured zone in bedrock-soil layer in a jurassic coalfield in northern Shaanxi, China. *Adv. Civ. Eng.* 2021, 1–15. doi:10.1155/2021/9718802

Li, B. (2019). *Study on the characteristics of stress seepage of coal-rock mass and the influence of key strata under coal seam group mining with multiple protective layers*. Chongqing, China: Chongqing University. dissertation/doctor's thesis.

Li, M., Zhang, J. X., Deng, X. J., Ju, F., and Li, B. Y. (2017). Measurement and numerical analysis of water-conducting fractured zone in solid backfill mining under an aquifer: A case study in China. *Q. J. Eng. Geol. Hydrogeol.* 50, 81–87. doi:10.1144/qjegh2016-018

Li, M., Zhang, J. X., Jiang, H. Q., Huang, Y. L., and Zhang, Q. (2014). A thin plate on elastic foundation model of overlying strata for dense solid backfill mining. *J. China Coal Soc.* 39, 2369–2373. doi:10.13225/j.cnki.jccs.2013.1843

Li, X. B., Li, Q. S., Xu, X. H., Zhao, Y. Q., and Li, P. (2021). Multiple influence factor sensitivity analysis and height prediction of water-conducting fracture zone. *Geofluids* 2021, 1–10. doi:10.1155/2021/8825906

Liu, J. W., Sui, W. H., and Zhao, Q. J. (2017). Environmentally sustainable mining: A case study of intermittent cut-and-fill mining under sand aquifers. *Environ. Earth Sci.* 76, 562. doi:10.1007/s12665-017-6892-2

Liu, S. L., Li, W. P., and Wang, Q. Q. (2018). Height of the water-flowing fractured zone of the jurassic coal seam in northwestern China. *Mine Water Environ.* 37, 312–321. doi:10.1007/s10230-017-0501-1

Liu, Y., Yuan, S. C., Yang, B. B., Liu, J. W., and Ye, Z. Y. (2019). Predicting the height of the water-conducting fractured zone using multiple regression analysis and GIS. *Environ. Earth Sci.* 78, 422. doi:10.1007/s12665-019-8429-3

Miao, X. X., Cui, X. M., Wang, J. A., and Xu, J. L. (2011). The height of fractured water-conducting zone in undermined rock strata. *Eng. Geol.* 120, 32–39. doi:10.1016/j.enggeo.2011.03.009

Shen, Z. X., Zhang, Q., Chen, D. L., and Singh, V. P. (2021). Varying effects of mining development on ecological conditions and groundwater storage in dry region in Inner Mongolia of China. *J. Hydrol.* 597, 1–13. doi:10.1016/j.jhydrol.2020.125759

Tai, Y., Guo, S., and Lan, L. X. (2020). Reasonable gangue section length for disposing gangue pollutants in the new green mixed workface. *Bull. Eng. Geol. Environ.* 79, 1669–1682. doi:10.1007/s10064-019-01677-x

Wang, G. (2015). *Developing law of water-flowing fracture with wongawilli backfill in coal mines*. Beijing China: China university of mining and technology. dissertation/master's thesis.

Wang, X. F., Zhang, D. S., Sun, C. D., and Wang, Y. (2016). Surface subsidence control during bag filling mining of super high-water content material in the Handan mining area. *Int. J. Oil, Gas. Coal Technol.* 13, 87–102. doi:10.1504/ijogct.2016.078049

Wen, J. H., Cheng, W. M., Chen, L. J., Shi, S. S., and Wen, Z. J. (2019). A study of the dynamic movement rule of overlying strata combinations using a short-wall continuous mining and full-caving method. *Energy Sci. Eng.* 7, 2984–3004. doi:10.1002/ese3.474

Wen, P., Guo, W. B., Tan, Y., Bai, E. H., Ma, Z. B., Wu, D. T., et al. (2022). Paste backfilling longwall mining technology for thick coal seam extraction under buildings and above confined aquifers: A case study. *Minerals* 12, 470. doi:10.3390/min12040470

Xie, X. S., Hou, E. K., Wang, S. M., Sun, X. Y., Hou, P. F., Wang, S. B., et al. (2021). Formation mechanism and the height of the water-conducting fractured zone induced by middle deep coal seam mining in a sandy region: A case study from the xiaobaodang coal mine. *Adv. Civ. Eng.* 2021, 1–11. doi:10.1155/2021/6684202

Xu, Y. J., Ma, L. Q., Ngo, I., and Zhai, J. T. (2022). Prediction of the height of water-conductive fractured zone under continuous extraction and partial backfill mining method-A case study. *Sustainability* 14, 6582. doi:10.3390/su14116582

Yao, Q. L., Zheng, C. K., Tang, C. J., Xu, Q., Chong, Z. H., and Li, X. H. (2020). Experimental investigation of the mechanical failure behavior of coal specimens with water intrusion. *Front. Earth Sci.* 7, 1–13. doi:10.3389/feart.2019.00348

Zhang, J. X., Jiang, H. Q., Deng, X. J., and Ju, F. (2014). Prediction of the height of the water-conducting zone above the mined panel in solid backfill mining. *Mine Water Environ.* 33, 317–326. doi:10.1007/s10230-014-0310-8

Zhang, Y., Cao, S. G., Zhang, N., and Zhao, C. Z. (2020). The application of short-wall block back fill mining to preserve surface water resources in northwest China. *J. Clean. Prod.* 261, 121232. doi:10.1016/j.jclepro.2020.121232

Zhang, Y., Liu, Y. Z., Lai, X. P., and Gao, J. M. (2021). Physical modeling of the controlled water-flowing fracture development during short-wall block backfill mining. *Lithosphere* 2021, 1–15. doi:10.2113/2021/2860087

Zhao, H. F., Wang, X. H., Liu, Z. Y., Yan, Y. J., and Yang, H. X. (2018). Investigation on the hydraulic fracture propagation of multilayers-commingled fracturing in coal measures. *J. Pet. Sci. Eng.* 167, 774–784. doi:10.1016/j.petrol.2018.04.028

frontiers | Frontiers in Earth Science

TYPE Original Research
PUBLISHED 16 February 2023
DOI 10.3389/feart.2023.1120344

OPEN ACCESS

EDITED BY
Fangtian Wang,
China University of Mining and Technology, China

REVIEWED BY
Anxiu Liu,
Taiyuan University of Technology, China
Xiaolou Chi,
Anhui University of Science and Technology, China

*CORRESPONDENCE
Xiangang Hou,
xianganghou@126.com

SPECIALTY SECTION
This article was submitted to Structural Geology and Tectonics, a section of the journal Frontiers in Earth Science

RECEIVED 09 December 2022
ACCEPTED 08 February 2023
PUBLISHED 16 February 2023

CITATION
Qin T, Wang Y, Hou X and Duan Y (2023), A characterization method for equivalent elastic modulus of rock based on elastic strain energy.
Front. Earth Sci. 11:1120344.
doi: 10.3389/feart.2023.1120344

A characterization method for equivalent elastic modulus of rock based on elastic strain energy

Tao Qin, Yiwei Wang, Xiangang Hou* and Yanwei Duan

Key Laboratory of Mining Engineering of Heilongjiang Province College, Heilongjiang University of Science and Technology, Harbin, Heilongjiang, China

Energy is an internal variable during rock deformation and failure, and its dissipation and conversion law can reflect the rock's internal damage and deterioration state. Analysis of rock deformation and failure process from the perspective of energy is helpful to deeply understand the mechanism of rock damage, fracture and instability failure, and has important theoretical and practical significance for the stability evaluation and support control of surrounding rock. In this study, through single cyclic loading and unloading (SCLU) experiments, cyclic triaxial loading and unloading (CTLU) experiments and conventional triaxial compression (CTC) experiments, the equivalent elastic modulus method based on elastic strain energy is proposed to analyze the energy conversion of rock. The results show that the error of the elastic strain energy calculated by the strain energy formula method is generally higher than 10% with the secant and tangent modulus of the loading and unloading curve as input parameters. Taking the equivalent elastic modulus proposed in this study as an input parameter, more accurate elastic strain energy can be obtained by the strain energy formula. During the rock failure process, the equivalent elastic modulus shows a three-stage characteristic of increase, steady and decrease. The equivalent elastic modulus can be estimated by the quadratic function between the equivalent elastic modulus and confining pressure and axial strain. Under the same deformation and deviatoric stress, the elastic strain energy stored in rock increases with increasing confining pressure. The local maximum energy dissipation rate corresponds to stress drop, and the peak energy dissipation rate appears near the peak strength. High energy dissipation mainly occurs in a short time after peak strength, and energy release and dissipation are more sudden and severe under high confining pressure.

KEYWORDS

characterization method, equivalent elastic modulus, elastic strain energy, energy dissipation, sandstone

1 Introduction

The nature of rock mass deformation and failure is damage degradation and instability driven by energy. Energy is an internal variable in the whole process of rock mass deformation and failure, and its dissipation and conversion law can reflect the internal damage degradation state of rock mass (Xie et al., 2009; Peng et al., 2014). Under loading conditions, the transformation of rock from uniform deformation to local deformation, from disorderly failure to orderly failure, and from macroscopic homogeneity to macroscopic heterogeneity is accompanied by the transformation of

energy accumulation to energy dissipation (Wang et al., 2019). Taking underground mining as an example, the excavation and support change the original stress field, and the surrounding rock accumulates, dissipates and releases energy (Cai et al., 2019; Keneti and Sainsbury, 2020; Xiao et al., 2021). Partial input energy of the rock mass is transformed into elastic strain energy (releasable strain energy) and released during instability failure, and some energy is transformed into plastic energy corresponding to plastic deformation, surface energy corresponding to crack initiation and expansion, kinetic energy of the failure surrounding rock mass, acoustic emission (microseismic) and radiation energy, etc., (Lu et al., 2021; Meng et al., 2021; Shirani Faradonbeh et al., 2021). During the process of rock mass excavation, stress redistributes and strain energy accumulates in surrounding rock, and the gathered energy is easily released along the face of caving, resulting in damage and fracture of surrounding rock and even sudden instability of surrounding rock (Li et al., 2018; Jiang et al., 2020; Liu et al., 2021; Tu et al., 2021; Zhang et al., 2021). Revealing the deformation and failure mechanism of rock mass from the perspective of energy is one of the research hotspots in the field of rock mechanics.

Many scholars (Huang and Li, 2014; Gong et al., 2019; Zhang et al., 2019; Qin et al., 2020) have systematically carried out laboratory experiments to study the laws of rock energy conversion under different loading conditions such as cyclic loading and unloading test, conventional compression test, unloading test, etc., and achieved many beneficial research results. Currently, two methods are widely used in calculating and analyzing rock energy, especially elastic strain energy. Firstly, the area method is based on the stress-strain curve under cyclic loading and unloading (Gong et al., 2021; Xu et al., 2021; Ding et al., 2022; Gong et al., 2022). This method has high accuracy, but it is generally applicable to laboratory experiments that can obtain cyclic loading and unloading curves, and it is difficult to be popularized and applied to engineering rock masses. Secondly, the traditional strain energy formula method based on elasticity theory is simple and fast, but the calculation accuracy depends on the value of elastic modulus (Gong and Wang, 2022; Qiao et al., 2022). Therefore, how to establish a simple, fast and easy method to calculate the elastic strain energy of engineering rock mass needs further study.

In this study, the quantification method of energy in the process of rock deformation and failure and its applicable conditions were discussed. Based on the single cyclic loading and unloading (SCLU) experiments, the influence of the method of calculating elastic modulus on the elastic strain energy calculated by the strain energy formula method was analyzed. On this basis, cyclic triaxial loading and unloading (CTLU) experiments were performed, and an equivalent elastic modulus characterization method of rock based on elastic strain energy was established. Based on the proposed equivalent elastic modulus estimation formula, the evolution characteristics of elastic strain energy and energy dissipation were analyzed through conventional triaxial compression (CTC) experiments. The research results have important theoretical and practical significance for the mechanism analysis, stability evaluation and support control of surrounding rock in the stope.

2 Energy transformation and quantitative analysis during rock deformation and failure

2.1 Energy transformation during rock deformation and failure

The process of rock deformation and failure under load is accompanied by energy input, energy accumulation, energy dissipation and energy release. The energy transformation process of rock under external load is shown in Figure 1.

The change of rock state can be considered as the change from one energy balance state to another new energy balance state. If ignoring the temperature effect, part of the energy input by the external force working on the rock is accumulated in the form of elastic strain energy inside the rock, and this part of energy is reversible. The other part is mainly used for internal dissipated plastic strain energy and crack surface energy, released kinetic energy and friction heat energy.

In this study, the plastic strain energy is defined as irreversible internal dissipated energy which is not dissipated in the form of cracks. Before the macroscopic fracture, the kinetic energy released to the outside is mainly in the form of acoustic emission waves, while in the post-peak stage, it is mainly in the form of macroscopic movement of rock blocks. The frictional heat energy is the heat generated by the friction between rock substrates on both sides of the crack. During the process of rock deformation and failure, there are energy transformation processes such as external energy input, internal accumulation and dissipation, and release to the outside, and the specific bearing state corresponds to the specific energy transformation state.

2.2 Quantification of energy during rock deformation and failure

The total input energy can be separated into two parts: reversible elastic strain energy and irreversible dissipated energy, assuming that there is no heat exchange with the environment. The elastic strain energy is primarily stored in the rock during the pre-peak stage of rock deformation and failure, whereas the dissipated energy is primarily in the form of plastic deformation and damage energy dissipation. The elastic strain energy is primarily released in the rock during the post-peak period, and the energy is primarily used for macroscopic crack fracture, friction between rock substrates on both sides of the crack, and kinetic energy of fragments. According to the law of energy conservation, the energy relationship during the process of rock deformation and failure can be expressed as follows:

$$\boldsymbol{U} = \boldsymbol{U}^{d} + \boldsymbol{U}^{e} \tag{1}$$

where, U^d is dissipated energy density, hereinafter referred to as dissipated energy; U^e is the elastic strain energy density, hereinafter referred to as the elastic strain energy.

The input energy density can be calculated by the following formula:

$$\boldsymbol{U} = \int_0^{\varepsilon_1} \boldsymbol{\sigma}_1 d\boldsymbol{\varepsilon} + \int_0^{\varepsilon_2} \boldsymbol{\sigma}_2 d\boldsymbol{\varepsilon} + \int_0^{\varepsilon_3} \boldsymbol{\sigma}_3 d\boldsymbol{\varepsilon} \tag{2}$$

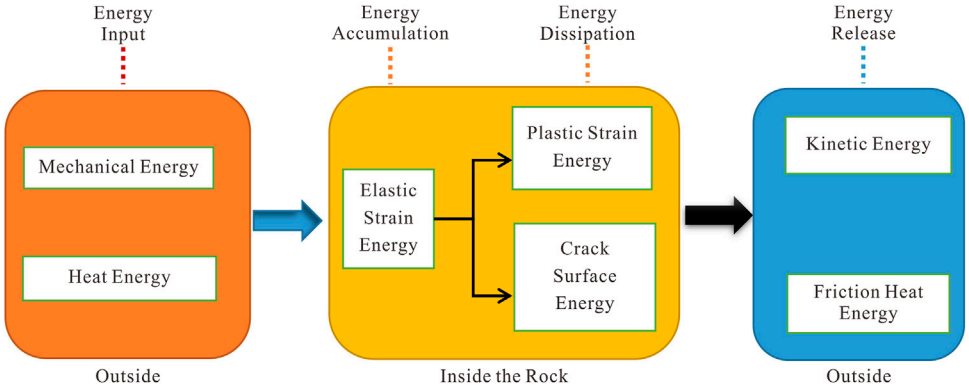

FIGURE 1
Energy transformation of rock under external load.

where, σ_1, σ_2 and σ_3 are the maximum principal stress, intermediate principal stress and minimum principal stress, respectively. ε_1, ε_2 and ε_3 are the strain corresponding to the principal stress.

Elastic strain energy and dissipated energy during the process of rock deformation and failure can be determined by the area method or strain energy formula method.

2.2.1 Area method

As shown in Supplementary Figure S1, the area below the loading curve is the total input energy, the area below the unloading curve is the elastic strain energy U^e, and the area between the loading curve and unloading curve is the dissipated energy U^d.

2.2.2 Strain energy formula method

In the strain energy formula method, the elastic strain energy is calculated through the elastic theory formula, and the total input energy is calculated by the integral of stress-strain curve, and the difference between the above two is the dissipated energy.

The elastic strain energy U^e can be expressed as:

$$U^e = \frac{1}{2}(\sigma_1\varepsilon_1 + \sigma_2\varepsilon_2 + \sigma_3\varepsilon_3) \tag{3}$$

From the Generalized Hooke's Law:

$$\begin{cases} \varepsilon_1 = \frac{1}{E}[\sigma_1 - \nu(\sigma_2 + \sigma_3)] \\ \varepsilon_2 = \frac{1}{E}[\sigma_2 - \nu(\sigma_1 + \sigma_3)] \\ \varepsilon_3 = \frac{1}{E}[\sigma_3 - \nu(\sigma_1 + \sigma_2)] \end{cases} \tag{4}$$

Substitute Eq. 4 into Eq. 3 to obtain:

$$U^e = \frac{1}{2E}[\sigma_1^2 + \sigma_2^2 + \sigma_3^2 - 2\nu(\sigma_1\sigma_2 + \sigma_2\sigma_3 + \sigma_1\sigma_3)] \tag{5}$$

Where, E and ν are elastic modulus and Poisson's ratio, respectively.

For the conventional triaxial compression test, the Eq. 5 can be written as:

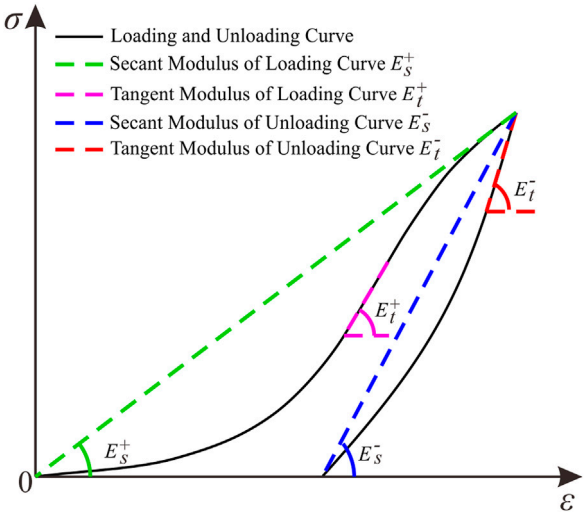

FIGURE 2
Schematic diagram of different calculation methods for elastic modulus.

$$U^e = \frac{1}{2E}[\sigma_1^2 + 2\sigma_3^2 - 2\nu(2\sigma_1\sigma_3 + \sigma_3^2)] \tag{6}$$

For the uniaxial compression test, the Eq. 5 can be written as:

$$U^e = \frac{\sigma_1^2}{2E} \tag{7}$$

3 Quantitative method of elastic modulus and its limitations

For loading and unloading tests, the elastic strain energy corresponding to each cycle can be calculated by the area method, but for monotonic loading tests, the elastic strain energy can only be calculated by the strain energy formula method. In this case, the elastic modulus has a very important influence on the

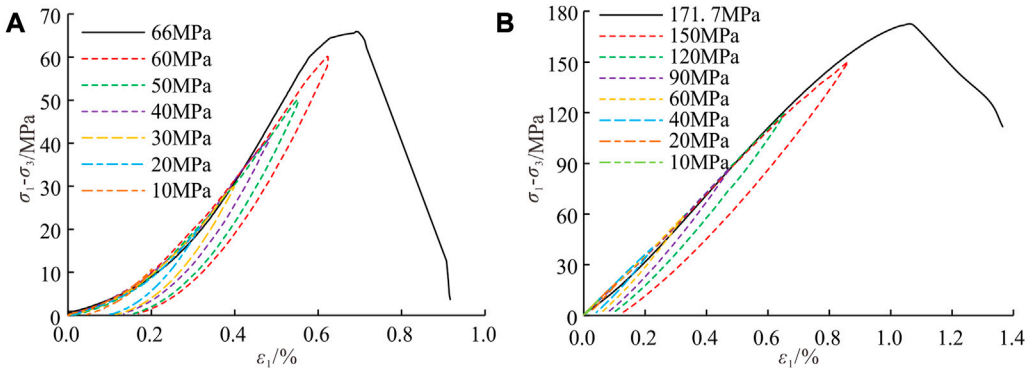

FIGURE 3
Stress-strain curves of sandstone under SCLU. **(A)** Confining pressure σ_3 = 0 MPa. **(B)** Confining pressure σ_3 = 20 MPa.

TABLE 1 Results of elastic strain energy calculated by different elastic modulus (σ_3 = 0 MPa).

Serial number	Area method	Strain energy formula method							
		SMLC E_s^+		TMLC E_t^+		SMUC E_s^-		TMUC E_t^-	
	U^e/(kJ/m^3)	U^e/(kJ/m^3)	Deviation/%	U^e/(kJ/m^3)	Deviation/%	U^e/(kJ/m^3)	Deviation/%	U^e/(kJ/m^3)	Deviation/%
1	6.44	10.78	67.4	5.95	7.6	8.49	31.9	5.14	20.3
2	16.02	30.47	90.2	17.99	12.3	22.52	40.6	14.12	11.9
3	31.01	59.68	92.5	35.83	15.5	43.10	39.0	26.47	14.6
4	54.25	99.11	82.7	62.49	15.2	72.20	33.1	43.29	20.2
5	73.22	133.76	82.7	90.88	24.1	99.45	35.8	60.68	17.1
6	100.51	184.40	83.5	128.39	27.7	137.67	37.0	86.10	14.3

TABLE 2 Results of elastic strain energy calculated by different elastic modulus (σ_3 = 20 MPa).

Serial number	Area method	Strain energy formula method							
		SMLC E_s^+		TMLC E_t^+		SMUC E_s^-		TMUC E_t^-	
	U^e/(kJ/m^3)	U^e/(kJ/m^3)	Deviation/%	U^e/(kJ/m^3)	Deviation/%	U^e/(kJ/m^3)	Deviation/%	U^e/(kJ/m^3)	Deviation/%
1	15.04	25.42	69.04	25.57	70.00	23.20	54.23	22.73	51.11
2	22.98	39.38	71.36	38.94	69.45	34.51	50.15	32.72	42.40
3	60.00	84.27	40.45	78.95	31.58	71.43	19.05	61.98	3.31
4	112.21	144.57	28.84	127.03	13.20	122.85	9.48	101.42	9.61
5	210.12	271.91	29.41	227.41	8.23	231.63	10.24	186.68	11.15
6	359.24	471.16	31.15	386.64	7.63	406.71	13.21	315.83	12.08
7	546.32	751.84	37.62	589.28	7.86	647.62	18.54	479.19	12.29

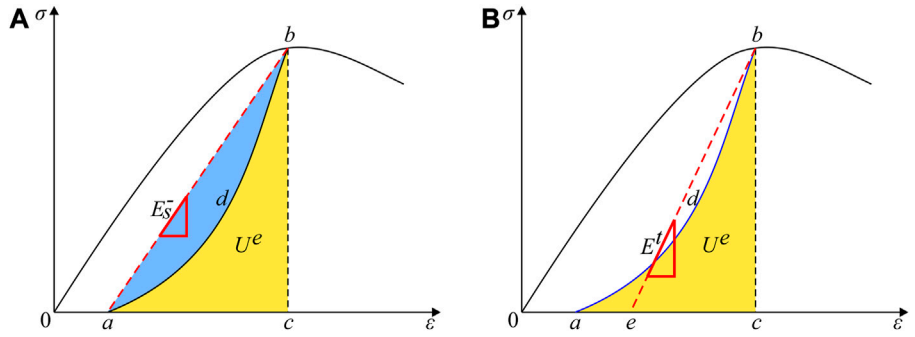

FIGURE 4
Schematic diagram of elastic strain energy and equivalent elastic modulus. **(A)** Elastic strain energy. **(B)** Determination of equivalent elastic modulus.

accuracy of the calculation results. Therefore, this section discusses the influence of several methods of calculating elastic modulus on theoretical calculation results of elastic strain energy.

3.1 Quantitative method of elastic modulus

As shown in Figure 2, the calculation methods of elastic modulus can mainly be concluded as follows:

Method 1: Secant modulus of loading curve (SMLC), denoted as E_s^+, is the slope of the secant line between the starting point of the loading and the upper limit stress point.

Method 2: Tangent modulus of loading curve (TMLC), denoted as E_t^+, is the slope of the straight line segment of the loading stress-strain curve.

Method 3: Secant modulus of unloading curve (SMUC), denoted as E_s^-, is the slope of the secant line between the starting point of unloading and lower limit unloading stress point.

Method 4: Tangent modulus of unloading curve (TMUC), denoted as E_t^-. It can be seen from the stress-strain curve in the unloading stage that the straight line segment of the unloading curve occurs within a period after the initial unloading moment. To avoid the calculation difference caused by the sudden change of stress and strain at the initial unloading moment, E_t^- is the slope of the straight line segment between the starting point of unloading and the point of 8–10 MPa below.

3.2 Limitations of quantitative methods of elastic modulus

3.2.1 Experimental scheme

The specimens adopted in this study are cylindrical yellow sandstone with Φ50 mm × H100 mm, in which quartz, potash feldspar and clay minerals account for 76.12%, 20.93% and 2.95%, respectively, with an average density of 2.10 g/cm^3 and no obvious joints on the surface, as shown in Supplementary Figure S2. The Sonic Viewer-SX ultrasonic wave velocity test system was used to screen the sandstone samples. The samples with similar wave velocities were selected for testing to reduce the dispersion of the samples. The loading device was TOP INDUSTRIE Rock 600–50 automatic servo rheometer. Two linear variable displacement transducer (LVDT) were used to collect axial strain, and annular electronic strain gauge was used to collect annular strain, as shown in Supplementary Figure S3.

In this study, single cyclic loading and unloading (SCLU) experiments, cyclic triaxial loading and unloading (CTLU) experiments and conventional triaxial compression (CTC) experiments were performed, which were discussed in more detail in Section 3.2.2, Section 4.2 and Section 5, respectively.

The SCLU experiments were carried out under confining pressure of 0 MPa and 20 MPa, i.e., single cyclic uniaxial loading and unloading (SCULU) experiments and single cyclic triaxial loading and unloading (SCTLU) experiments. Seven SCULU experiments were performed with the unloading stress of 10 MPa, 20 MPa, 30 MPa, 40 MPa, 50 MPa, 60 MPa and 70 MPa. For SCULU experiments, the specimens were loaded to the preset unloading stress with an axial loading rate of 0.5 MPa/s, and then the specimens were completely unloaded with an axial unloading rate of 0.5 MPa/s. In the seventh experiment, the rock specimen failed when it was loaded to 66.0 MPa, and the unloading stress-strain curve was not obtained. Eight SCTLU experiments were performed with the unloading deviatoric stress of 10 MPa, 20 MPa, 40 MPa, 60 MPa, 90 MPa, 120 MPa, 150 MPa, 180 MPa. For SCTLU experiments, the experimental procedure was as follows: (a) the hydrostatic pressure ($\sigma_1 = \sigma_2 = \sigma_3 = 20$ MPa) was applied with a loading rate of 0.5 MPa/s; (b) the specimens were loaded to the preset unloading deviatoric stress with an axial loading rate of 0.5 MPa/s; (c) the specimens were unloaded to deviatoric stress of 2 MPa (in order to prevent the separation of the rock specimens from the pressure head of the testing machine) with an axial unloading rate of 0.5 MPa/s. In the eighth experiment, the rock specimen failed when it was loaded to 171.7 MPa, and the unloading stress-strain curve was not obtained.

The CTLU experiments were performed under the confining pressure of 0 MPa, 5 MPa, 10 MPa, 15 MPa and 20 MPa. Firstly, the hydrostatic pressure ($\sigma_1 = \sigma_2 = \sigma_3$) was applied with a loading rate of 0.5 MPa/s. Then, the specimens were loaded to the preset unloading deviatoric stress and unloaded to deviatoric stress of 2 MPa with the same axial rate of 0.5 MPa/s. As shown in Supplementary Figure S4, the increment in the pre-peak stage and the decrement in the post-peak stage for cyclic stress were set to 10 MPa and 20 MPa respectively.

TABLE 3 Results of equivalent elastic modulus.

Cycles	σ_3 = 0 MPa			σ_3 = 5 MPa			σ_3 = 10 MPa			σ_3 = 15 MPa			σ_3 = 20 MPa		
	σ_1-σ_3/MPa	ε_1/%	*E*/GPa	σ_1-σ_3/MPa	ε_1/%	*E*/GPa	σ_1-σ_3/MPa	ε_1/%	*E*/GPa	σ_1-σ_3/MPa	ε_1/%	*E*/GPa	σ_1-σ_3/MPa	ε_1/%	*E*/GPa
1	11.1	0.18	9.4	10.1	0.08	14.1	11.6	0.07	18.4	12.6	0.08	20.8	9.9	0.05	21.5
2	20.7	0.28	11.7	20.8	0.15	16.2	20.3	0.12	19.0	22.1	0.13	21.3	19.9	0.11	22.1
3	31.0	0.37	13.8	30.8	0.22	17.5	31.7	0.19	20.1	34.6	0.21	22.2	29.5	0.16	22.7
4	41.2	0.45	15.3	39.6	0.27	18.6	40.0	0.23	21.0	43.6	0.26	22.4	40.4	0.22	23.0
5	51.7	0.53	16.3	50.2	0.33	19.8	50.1	0.29	21.8	54.6	0.32	22.6	51.3	0.28	23.3
6	60.9	0.61	16.6	60.2	0.39	20.4	60.5	0.34	22.6	66.0	0.38	23.0	60.6	0.33	23.5
7				70.3	0.45	21.3	70.5	0.39	23.1	76.9	0.43	23.3	70.2	0.38	23.7
8				80.5	0.51	21.6	80.3	0.44	23.4	87.5	0.49	23.5	80.0	0.42	23.8
9				89.8	0.56	21.8	90.5	0.49	23.5	98.7	0.55	23.6	90.2	0.47	24.0
10				100.4	0.64	21.9	100.1	0.54	23.7	109.1	0.60	23.7	101.9	0.54	24.1
11				109.9	0.71	21.7	110.1	0.59	23.8	120.0	0.66	23.7	109.8	0.58	24.1
12				97.0	0.94	20.1	120.0	0.65	23.7	130.8	0.72	23.5	119.9	0.64	24.1
13				82.0	1.05	18.6	129.2	0.71	23.6	140.8	0.78	23.4	130.1	0.69	24.1
14				60.5	1.12	17.0	139.7	0.78	23.6	152.3	0.86	23.1	140.0	0.76	24.0
15							117.3	1.03	22.3	159.9	0.92	22.7	151.5	0.83	23.9
16							100.0	1.07	22.0	114.5	*1.25*	21.3	138.9	1.06	22.8
17							83.2	1.13	21.3	95.2	1.29	20.9	137.0	1.15	22.6
18							58.2	1.21	20.2	75.4	1.35	20.7	123.2	1.18	22.4
19										55.2	1.38	20.5	102.2	1.22	22.1
20													80.2	1.24	21.9

10.3389/feart.2023.1120344

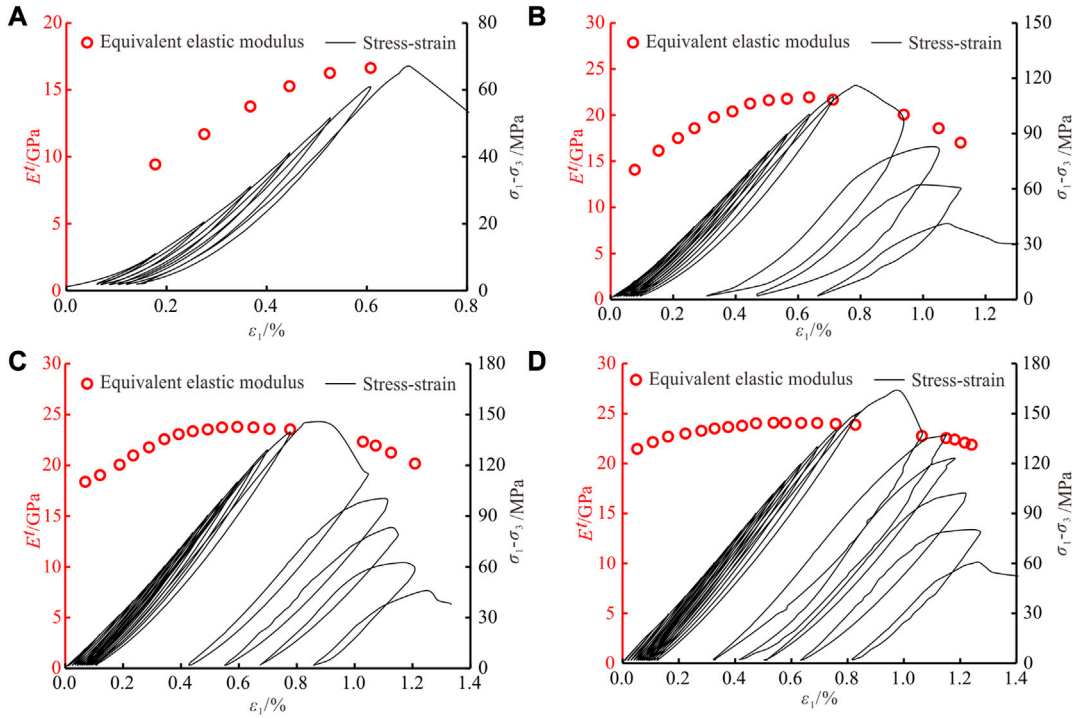

FIGURE 5
Evolution of equivalent elastic modulus under CTLU. **(A)** σ_3 = 0 MPa. **(B)** σ_3 = 5 MPa. **(C)** σ_3 = 10 MPa. **(D)** σ_3 = 20 MPa.

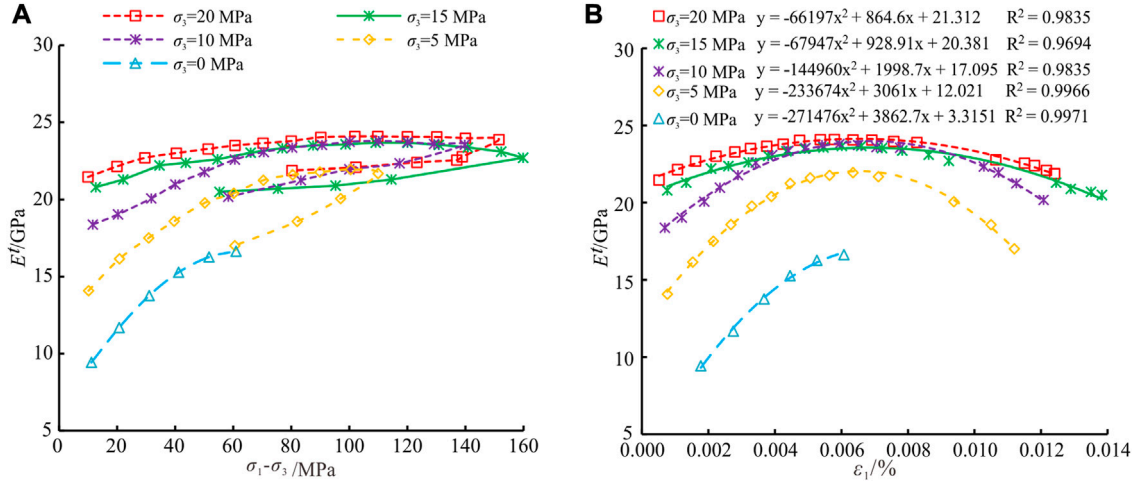

FIGURE 6
Equivalent elastic modulus under different confining pressure. **(A)** Relationship between equivalent elastic modulus and deviatoric stress. **(B)** Quadratic polynomial fitting of equivalent elastic modulus.

The CTC experiments were performed under the confining pressure of 0 MPa, 5 MPa, 10 MPa, 15 MPa and 20 MPa. The loading procedure was as follows: firstly, the hydrostatic pressure was applied with a loading rate of 0.5 MPa/s; then, the specimen was subsequently loaded to failure with an axial loading rate of 0.5 MPa/s.

3.2.2 Limitations of methods

As shown in Figure 3, the stress-strain curves of sandstone under uniaxial compression show obvious non-linear characteristics regardless of unloading at low-stress or high-stress levels, and the elastic modulus calculated by different methods are different. With the increase of confining pressure, the non-linear characteristics of stress-strain curve

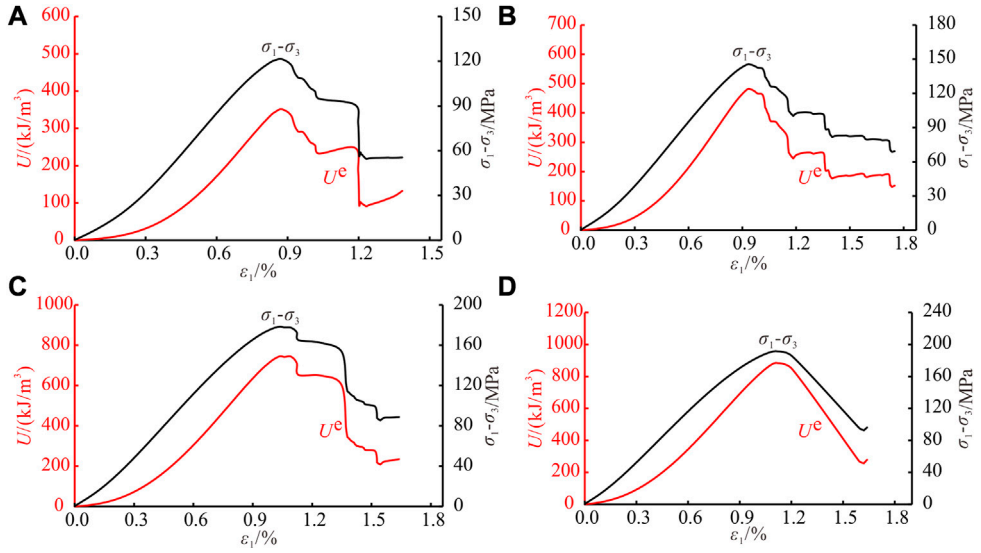

FIGURE 7
Evolution of elastic strain energy under CTC. **(A)** σ_3 = 5 MPa. **(B)** σ_3 = 10 MPa. **(C)** σ_3 = 15 MPa. **(D)** σ_3 = 20 MPa.

reduce, and the difference of calculated elastic modulus also decreases. Supplementary Tables S1, S2 list the elastic modulus in each SCLU experiment calculated by the abovementioned method. Under the same stress limit, the elastic modulus calculated by the four methods can be listed in descending order: TMUC E_t^-, TMLC E_t^+, SMUC E_s^-, and SMLC E_s^+.

In order to compare the accuracy of elastic strain energy calculated by different elastic modulus, the elastic strain energy was calculated by using the area method and strain energy formula method, respectively. Based on the results of the area method, the calculation deviation corresponding to different values of elastic modulus was obtained, as shown in Tables 1, 2. As can be seen from the tables, the calculation deviation of elastic strain energy using different elastic modulus is large. For SCULU experiment, the calculation deviation of elastic strain energy using SMLC E_s^+ is the largest, followed by SMUC E_s^-, and the deviation using TMLC E_t^+ or TMUC E_t^- is smaller. For SCTLU experiment, the deviation of elastic strain energy calculated by SMLC E_s^+ is obviously larger than the other three. The deviation of elastic strain energy calculated by the strain energy formula method using different elastic modulus is generally above 10% in the SCULU or SCTLU experiment. Therefore, in order to obtain more accurate elastic strain energy and provide more accurate basic data for analyzing energy conversion characteristics of rock, it is necessary to improve the quantitative method of elastic modulus.

4 Equivalent elastic modulus based on elastic strain energy and its evolution

4.1 Characterization method for equivalent elastic modulus based on elastic strain energy

As shown in Figure 4A, the main reasons for the calculation deviation of elastic strain energy can be concluded: the elastic strain energy calculated by SMUC E_s^- is the area of triangle *abc*, while the actual elastic strain energy is the area of cross-sectional area *adbca*, and the deviation is the blue area. The non-linear characteristic of stress-strain curve in the unloading stage is mainly due to the non-linear elastic properties of the sandstone. Sandstone is a kind of porous medium rock, and rock matrix under a certain stress level will show more obvious linear elastic properties, but its internal microcracks, microvoids will gradually open under unloading, leading to the reducement of effective bearing area and the decrease of elastic modulus. Its apparent phenomenon is non-linear characteristic of unloading curve, which is also the essential reason for the large error of elastic strain energy calculated using secant modulus.

Based on the above analysis, this study put forward the equivalent elastic modulus (the slope of the line be in Figure 4B based on elastic strain energy, defined as E^t. The elastic strain energy can be calculated through the area between the unloading stress-strain curve and the horizontal axis, then the equivalent elastic modulus can be calculated according to the formula of elastic strain energy. For uniaxial compression, the equivalent elastic modulus can be calculated as follows:

$$E^t = \frac{\sigma_1^2}{2U^e} \tag{8}$$

For triaxial compression, the elastic strain energy can be calculated through the axial and radial unloading curve, and the equivalent elastic modulus can be calculated as follows:

$$E^t = \frac{1}{2U^e}\left[\sigma_1^2 + \sigma_2^2 + \sigma_3^2 - 2\nu^t\left(\sigma_1\sigma_2 + \sigma_2\sigma_3 + \sigma_1\sigma_3\right)\right] \tag{9}$$

where, ν^t is the unloading Poisson's ratio obtained by the ratio of radial to axial strain increment at the unloading process (Huang and Li, 2014).

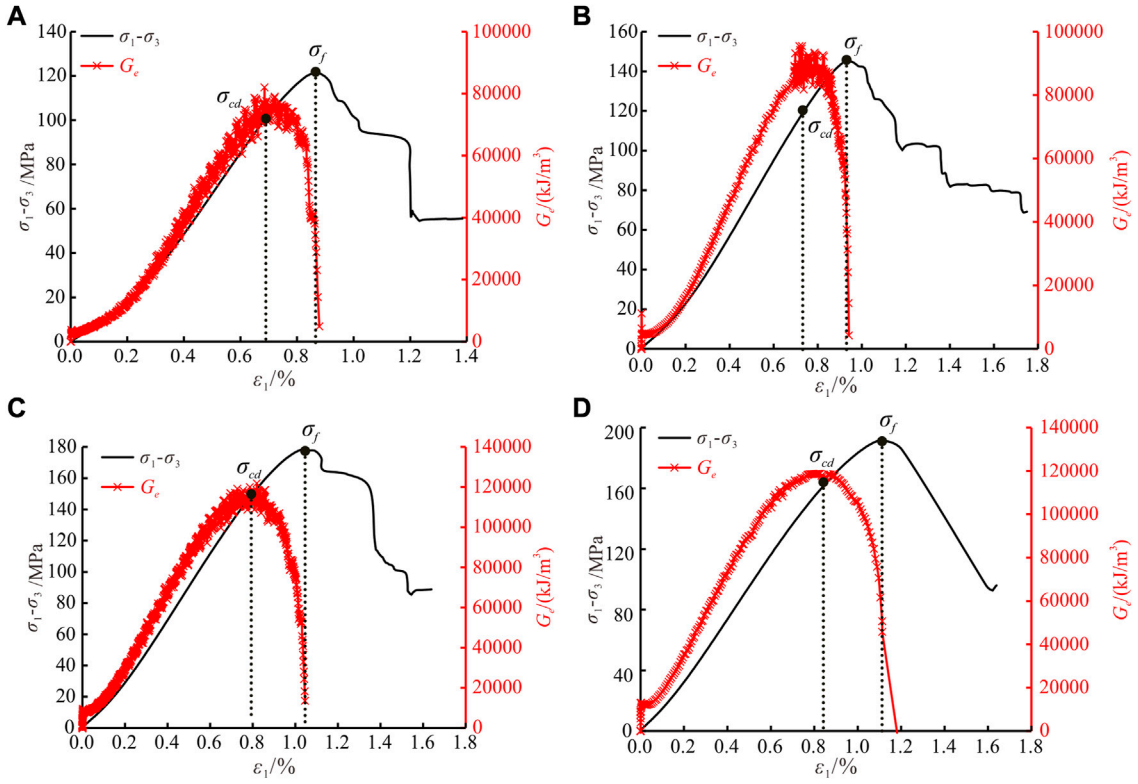

FIGURE 8
The elastic strain energy storage efficiency under CTC. **(A)** σ_3 = 5 MPa. **(B)** σ_3 = 10 MPa. **(C)** σ_3 = 15 MPa. **(D)** σ_3 = 20 MPa.

In this study, the characterization method for equivalent elastic modulus is proposed from the perspective of energy, which aims to better quantify the elastic strain energy stored in rock. It is essentially different from the elastic modulus defined by the stress-strain curve, and more suitable for the analysis of energy conversion law during rock failure.

4.2 Evolution law and estimation formula of equivalent elastic modulus

Based on the CTLU experiments, the equivalent elastic modulus proposed above (Formula 9) was used to determine the equivalent elastic modulus of rock under different confining pressure and cyclic limit stress, as shown in Table 3.

Figure 5 shows the change of equivalent elastic modulus under different confining pressure. Figure 5A shows that the post-peak unloading curve was not obtained under confining pressure of 0 MPa, and the equivalent elastic modulus increases gradually with the increase of cycles and axial strain. Theoretically, the storage capacity of elastic strain energy decreases after the specimen reaches the yield stage, leading to the decrease of the equivalent elastic modulus. The difference between peak stress and yield stress is less than cyclic stress increment (10 MPa) under confining pressure of 0 MPa, therefore the maximum stress of a cyclic loading is difficult to be exactly between the yield stress and peak stress, and the decrease of equivalent elastic modulus before the peak stress is not observed. It can be seen from Figures 5B–D that for triaxial cyclic loading and unloading tests, the equivalent elastic modulus shows a three-stage with the increase of cycles and axial strain, i.e., increasing, stabilizing and decreasing.

In order to further analyze the effect of confining pressure on the equivalent elastic modulus of rock, the evolution of equivalent elastic modulus for CTLU experiment under different confining pressure was shown in Figure 6. With the increase of confining pressure, the equivalent elastic modulus increases under the same deviatoric stress and axial strain, and the variation of equivalent elastic modulus decreases obviously with the increase of deviatoric stress and axial strain, indicating that the confining pressure has a strengthening effect on the elastic modulus of rock. It can be seen from Figure 6B that the quadratic polynomial fitting of equivalent elastic modulus with axial strain is fairly good, and the fitting formula can be used to estimate the equivalent elastic modulus of rock under different confining pressure and axial strain:

$$\begin{cases} E^t = -66197\varepsilon^2 + 864.6\varepsilon + 21.312 & \sigma_3 = 20MPa \\ E^t = -67947\varepsilon^2 + 928.9\varepsilon + 20.381 & \sigma_3 = 15MPa \\ E^t = -144960\varepsilon^2 + 1998.7\varepsilon + 17.095 & \sigma_3 = 10MPa \\ E^t = -233674\varepsilon^2 + 3061\varepsilon + 12.021 & \sigma_3 = 5MPa \\ E^t = -271476\varepsilon^2 + 3862.7\varepsilon + 3.315 & \sigma_3 = 0MPa \end{cases} \quad (10)$$

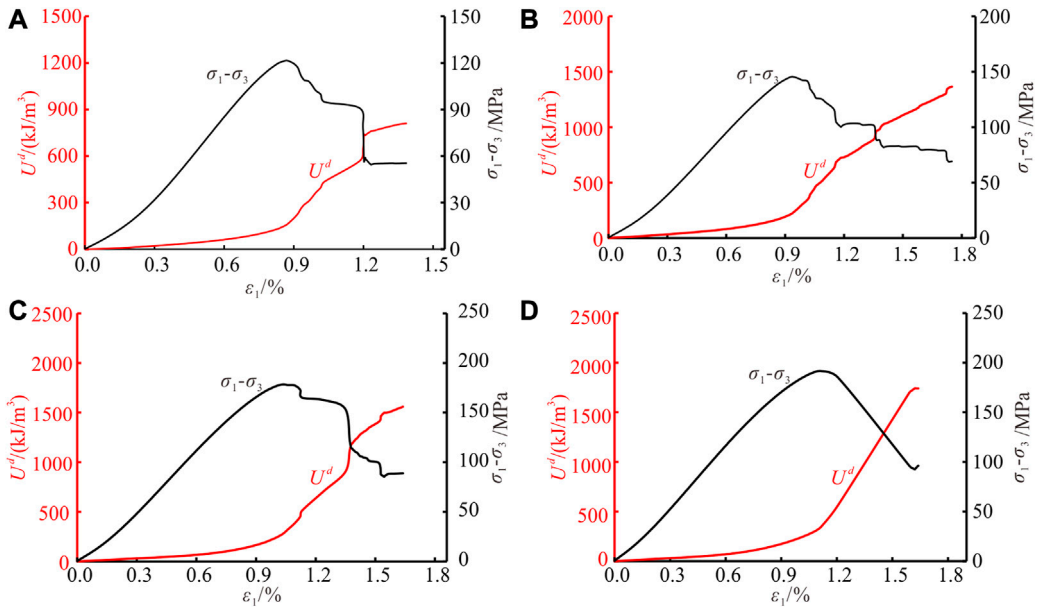

FIGURE 9
The curves of dissipated energy under CTC. **(A)** σ_3 = 5 MPa. **(B)** σ_3 = 10 MPa. **(C)** σ_3 = 15 MPa. **(D)** σ_3 = 20 MPa.

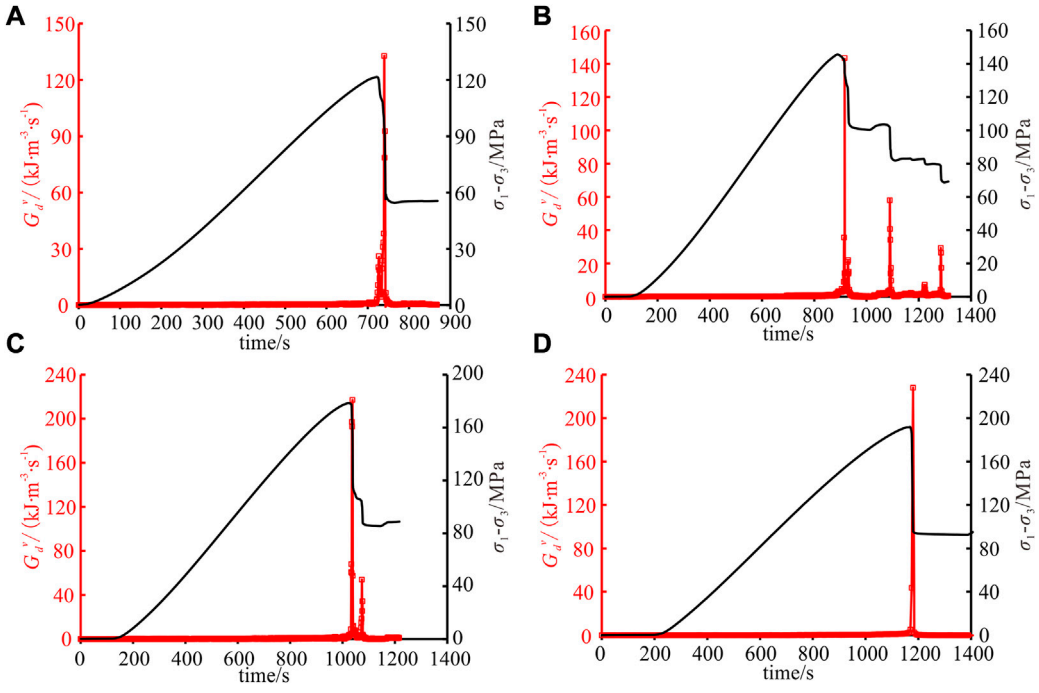

FIGURE 10
Evolution of energy dissipation rate under CTC. **(A)** σ_3 = 5 MPa. **(B)** σ_3 = 10 MPa. **(C)** σ_3 = 15 MPa. **(D)** σ_3 = 20 MPa.

5 Conversion characteristics of energy based on the equivalent elastic modulus

5.1 Characteristic stress of rock

Based on the CTC experiments, the characteristic stresses such as crack closure stress, crack initiation stress and crack damage stress of sandstone under different confining pressure were calculated from the perspective of the crack activity inside the rock (Diederichs et al., 2004). As shown in Supplementary Figures S5, S6, it can be seen that the crack initiation stress and crack damage stress increase with increasing confining pressure, while the effect of confining pressure on crack closure stress is obvious under low confining pressure. When the confining pressure increases to 10 MPa, the crack closure stress tends to be stable. This is mainly due to: there is a limit stress for original cracks and voids inside rock, i.e., when the stress reaches a certain limit, the cracks and voids fully closed. As shown in Supplementary Figure S6B, the normalized characteristic stress (characteristic stress/peak strength) is less affected by confining pressure, and the normalized crack closure stress, crack initiation stress and crack damage stress are stable at about 0.31, 0.65 and 0.81, respectively.

On the basis of the above analysis, the equivalent elastic modulus of sandstone under different confining pressures is used for the subsequent analysis of energy conversion process. It should be pointed out that in the subsequent energy analysis, the calculation of energy takes the hydrostatic stress state as the starting point. Although there is energy dissipation and transformation during the loading process from initial state to hydrostatic stress state, this part of energy is small and does not affect the overall law of energy dissipation and transformation during the process of rock failure. Therefore, this part of energy is not considered in this study.

5.2 Evolution characteristics of elastic strain energy

5.2.1 Evolution law of elastic strain energy

According to the theory of elasticity, the elastic strain energy depends only on elastic modulus and the final value of external load, and has nothing to do with the loading sequence. Based on the equivalent elastic modulus obtained in section 4, elastic strain energy is calculated according to stress-strain data collected during the CTC experiment, and the results are shown in Figure 7. Under constant confining pressure, elastic strain energy is only affected by elastic modulus and external load. Therefore, the curve of elastic strain energy is similar to the curve of stress. During sandstone deformation and failure process, the elastic strain energy gradually accumulates and increases with increasing external input energy, and reaches the maximum value at the peak strength, namely, the elastic energy storage limit. When the elastic strain energy accumulated inside the rock reaches this limit, the rock will show macroscopic fracture. The greater the energy storage limit of the rock, the less likely it is to be damaged driven by energy. In the post-peak stage, the elastic strain energy decreases as the axial stress decreases. Under the same stress, the elastic strain energy in the post-peak stage is bigger than pre-peak stage, the main reason is that the fractured rock contains a large number of microcracks, the elastic strain energy calculated by the equivalent elastic modulus includes the elastic strain energy accumulated in rock microcracks.

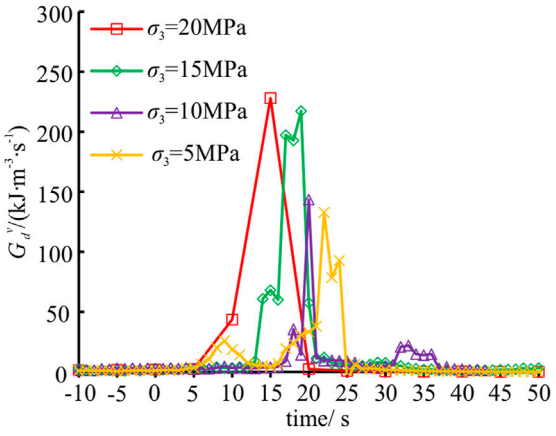

FIGURE 11
Energy dissipation rate near peak strength.

5.2.2 Effect of confining pressure on elastic strain energy storage efficiency

In order to analyze the storage characteristics of elastic strain energy in the pre-peak stage, the elastic strain energy storage efficiency G_e is defined as the stored elastic strain energy of unit strain, and is calculated as follows:

$$G_e = \frac{\Delta U^e}{\Delta \varepsilon_1} \tag{11}$$

Where, G_e is the elastic strain energy storage efficiency, kJ/m^3; ΔU^e is the change of elastic strain energy, kJ/m^3; $\Delta\varepsilon_1$ is the change of axial strain.

Figure 8 shows the curve of elastic strain energy storage efficiency under different confining pressure. It can be seen that the elastic strain energy storage efficiency first increases gradually, and reaches the peak at the crack damage stress. After crack damage stress, the elastic strain energy storage efficiency decreases gradually. The comparison of elastic strain energy storage efficiency under different confining pressure shows that the elastic strain energy storage efficiency increases with increasing confining pressure. For example, the peak elastic strain energy storage efficiency increases from 80,000 kJ/m^3 under σ_3 = 5 MPa to 140,000 kJ/m^3 under σ_3 = 20 MPa, i.e., the elastic strain energy storage efficiency increases by 75%. Elastic strain energy storage efficiency reflects the rock elastic strain energy transformation efficiency. Before the crack damage stress, rock is dominated by elastic deformation, and elastic strain energy storage efficiency increases with increasing axial stress and strain. After the crack damage stress, the internal cracks propagate quickly, rock is dominated by plastic deformation, and the elastic strain energy storage efficiency decreases.

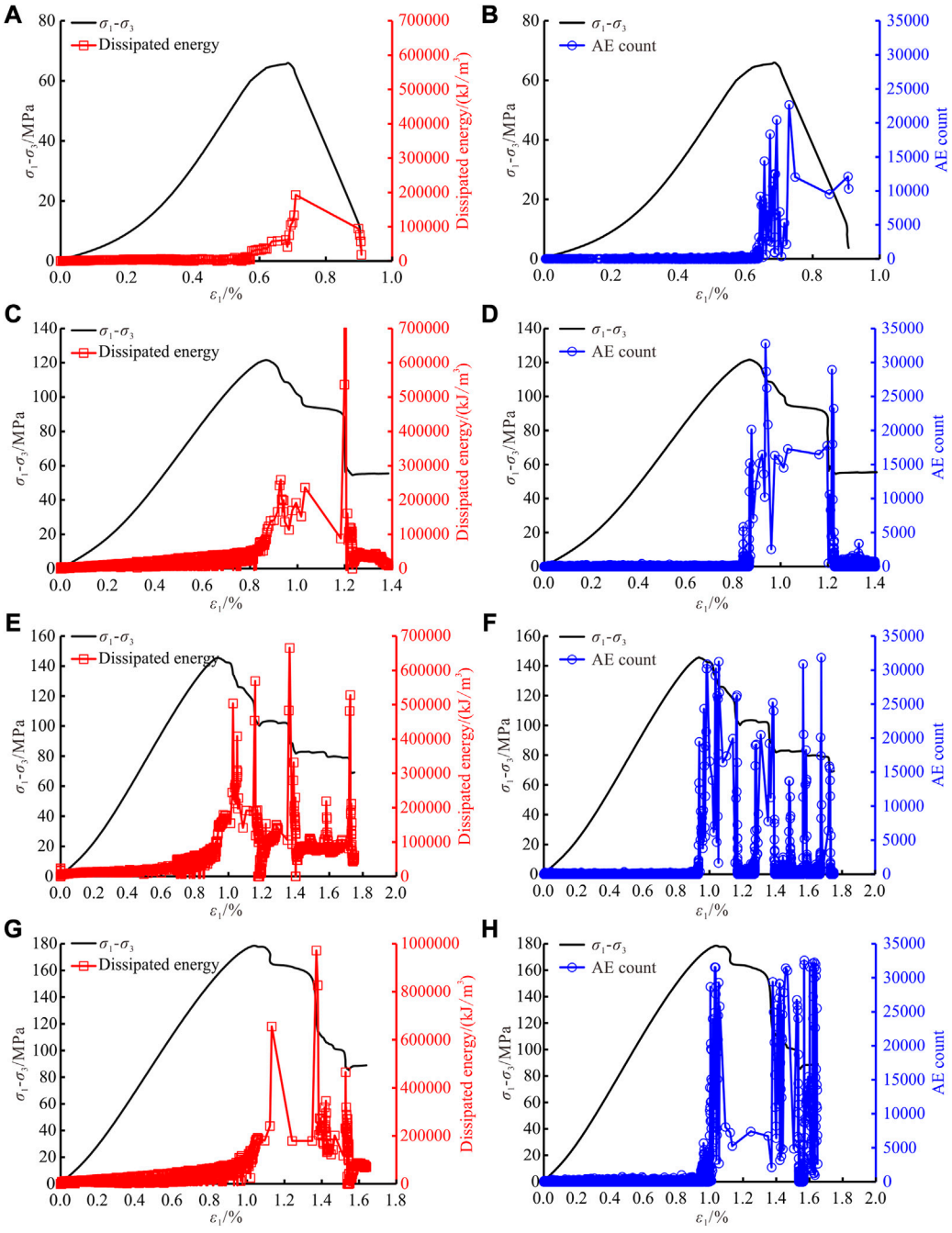

FIGURE 12
Evolution characteristics of dissipated energy and AE count. **(A)** Dissipated energy under σ_3 = 0 MPa. **(B)** AE count under σ_3 = 0 MPa. **(C)** Dissipated energy under σ_3 = 5 MPa. **(D)** AE count under σ_3 = 5 MPa. **(E)** Dissipated energy under σ_3 = 10 MPa. **(F)** AE count under σ_3 = 10 MPa. **(G)** Dissipated energy under σ_3 = 15 MPa. **(H)** AE count under σ_3 = 15 MPa.

5.3 Evolution characteristics of energy dissipation

For sandstone under compression, the process of internal primary microcrack closure, new crack initiation and propagation is always accompanied by energy dissipation, that is, the damage and fracture of rock are driven by energy. Therefore, this section will analyze the characteristics of energy dissipation under different stress states.

5.3.1 Evolution law of energy dissipation

Figure 9 shows the curve of energy dissipation under CTC. It can be seen that the dissipated energy increases continuously with the increase of rock deformation. In the pre-peak stage, the dissipated

energy is small, and the corresponding curve is relatively gentle and flat, i.e., the damage of rock develops steadily, and there is no sudden release and dissipation of energy. After reaching the peak strength, the dissipated energy increases rapidly with large-scale deformation and macroscopic fracture of rock. Furthermore, the dissipated energy increases suddenly to a certain extent at the stress drop point, i.e., when the local fracture occurs.

5.3.2 Characteristics of energy dissipation rate

To measure the speed of rock energy dissipation in different loading stages, this study introduces the energy dissipation rate G_d^v, namely, the dissipated energy per unit time, which can be calculated by the following formula (Wang et al., 2021):

$$G_d^v = \frac{\Delta U^d}{\Delta t} \tag{12}$$

Where, ΔU^d is the change of dissipated energy, kJ/m^3; Δt is the time increment, s.

Based on the above formula, the energy dissipation rate of rock under CTC is calculated, as shown in Figure 10. It can be seen that the local maximum energy dissipation rate appears at the stress drop point, and the peak energy dissipation rate appears near the peak strength. Outside the peak strength region, the energy dissipation rate is generally at a low level. Therefore, the energy dissipation rate can not only quantify the energy dissipation speed, but also can be used to evaluate the local failure and macroscopic failure of rock.

The above analysis demonstrated that high-rate energy dissipation is mainly concentrated near the peak strength, so the dissipated energy near the peak strength is listed in Figure 11. The time = 0 in the figure represents the moment of peak strength, the negative value represents the pre-peak stage and the positive value represents the post-peak stage. Figure 11 shows that the energy dissipation rate presents an obvious hysteresis effect and confining pressure effect.

(1) Hysteresis effect. Before the peak strength, the energy dissipation rate is at a low level. After reaching the peak strength, the energy dissipation rate increases rapidly to a higher level, i.e., the high-rate of energy dissipation lags behind the peak strength. Under CTC, the peak energy dissipation rate usually occurs within 10–30 s after the peak strength.

(2) Confining pressure effect. Before the peak strength, the energy accumulated in the rock increases as the confining pressure increases. After reaching the peak strength, the amount and rate of energy dissipation during the rock failure process increase correspondingly. For example, the peak energy dissipation rate increases from 132.9 kJ m^{-3}·s^{-1} under σ_3 = 5 MPa to 228.0 kJ m^{-3}·s^{-1} under σ_3 = 20 MPa. In addition, the hysteresis effect of energy dissipation rate gradually weakens as the confining pressure increases. For example, with the increase of confining pressure from 5 MPa to 20 MPa, the high-level energy dissipation rate gradually moves forward to the peak strength, and the lag time of peak energy dissipation rate decreases from 22 s to 15 s.

To summarize, energy release and dissipation of rock under load mainly occur in a short time after the peak strength. Under high confining pressure, energy release and dissipation are more sudden and severe, i.e., the engineering rock mass under high confining pressure will be easier to induce dynamic disasters.

5.3.3 Comparative analysis of energy dissipation and acoustic emission activities

During the process of rock deformation and fracture, the dissipation and release of energy are accompanied by elastic waves, namely, acoustic emission (AE). AE can reflect the process of energy dissipation inside rock, and AE energy is a part of dissipated energy. Based on this, this section analyzes the evolution characteristics of dissipated energy and AE count (Grosse and Ohtsu, 2008), as shown in Figure 12.

Figure 12 shows that there is a good correspondence between dissipated energy and AE count, i.e., the sudden increase of AE count corresponds to high dissipation of energy. In the pre-peak stage, the dissipated energy and AE count are both at a low level. Near the peak strength, the dissipated energy and AE count increase rapidly and reach a high level. In the post-peak stage, after the formation of the main fracture surface, cracks continue to initiate, propagate and coalesce, and acoustic emission activities are relatively active. When the local fracture occurs, an obvious stress drop appears with a sudden increase of AE count.

From the perspective of energy dissipation, it can be seen that there are many local maximum energy dissipation points corresponding to stress drop points near and after the peak strength. This is mainly due to the initiation and propagation of secondary fracture surfaces along with the development of principal fracture surface. The initiation and propagation of secondary fracture surfaces will lead to the reduction of rock bearing capacity and the occurrence of stress drop, resulting in a sharp increase of energy dissipation. In addition, there is a confining pressure effect on energy dissipation: the greater the confining pressure, the greater the energy dissipation at the peak strength. For example, the energy dissipation at peak strength increases from 1.9×10^5 kJ/m^3 under σ_3 = 0 MPa to 6.5×10^5 kJ/m^3 under σ_3 = 15 MPa. Therefore, when preventing and controlling dynamic disasters such as rock burst in the practice of underground mining engineering, it is necessary not only to pay attention to the inherent properties such as peak strength and brittleness index of surrounding rock mass, but also to analyze the stress state of surrounding rock mass, especially the surrounding rock mass under high confining pressure.

6 Conclusion

Based on the theory of energy balance and elasticity, energy transformation and quantification of energy for sandstone are discussed. In view of elastic strain energy quantification, the reasonable value of elastic modulus in the strain energy formula method is analyzed with reference to the calculation results of the area method, and then the characterization method for equivalent elastic modulus based on elastic strain energy is proposed. Through the CTLU experiments of sandstone under different confining pressure, the fitting quadratic function between equivalent elastic modulus, confining pressure and axial strain is determined. The

proposed equivalent elastic modulus is applied to analyze the evolution characteristics of elastic strain energy and energy dissipation. The following main points are concluded from this study.

(1) Taking the secant and tangent modulus of loading and unloading curve as input parameters respectively, the elastic strain energy under different confining pressure is calculated by using the strain energy formula method. Compared with the calculation results of area method, when the tangent modulus of loading curve or unloading curve is used as input parameter, the deviation of elastic strain energy calculated by the strain energy formula method is smaller, but the deviation is still generally higher than 10%.
(2) A characterization method for equivalent elastic modulus based on elastic strain energy is proposed to obtain more accurate calculation of energy when using the strain energy formula method. The elastic strain energy is calculated firstly by the area between the unloading stress-strain curve and the abscissa axis, and then the equivalent elastic modulus under specific confining pressure and axial strain is inversely calculated by using the theoretical calculation formula of elastic strain energy.
(3) The mechanical parameters such as elastic modulus, peak strength and residual strength show an obvious confining pressure effect, that is, they increase with increasing confining pressure. However, there are limit closure stress and limit closure amount. When the confining pressure increases to 10 MPa, the crack closure stress tends to be stable, but the crack initiation stress and crack damage stress increase with increasing confining pressure; The normalized characteristic stress is less affected by the confining pressure, that is, the normalized crack closure stress, crack initiation stress and crack damage stress are stable at about 0.31, 0.65 and 0.81, respectively.
(4) The elastic strain energy storage limit and elastic strain energy storage efficiency increase with increasing confining pressure. The local maximum energy dissipation rate point corresponds to an stress drop, and the peak energy dissipation rate appears near the peak strength. The energy dissipation rate presents hysteresis effect and confining pressure effect, i.e., high energy dissipation mainly occurs in a short time after the peak strength, and rock fracture and energy dissipation are more sudden and severe under high confining pressure.

Data availability statement

The original contributions presented in the study are included in the article/Supplementary Material, further inquiries can be directed to the corresponding author.

Author contributions

TQ and XH conceived and designed the study. YW and YD performed the experiments. TQ and XH wrote the original manuscript. XH and YW participated in the data analysis and manuscript modification.

Funding

This study was financially supported by the Scientific and technological key project of "Revealing the List and Taking Command" in Heilongjiang Province: Study on geological model and ventilation model of intelligent mining in extremely thin coal seam (2021ZXJ02A03), Intelligent mining demonstration of fully mechanized working face in extremely thin coal seam (2021ZXJ02A04). In addition, this study was also financially supported by the Fundamental Research Funds for the Higher Education Institutions of Heilongjiang Province (2022-KYYWF-0538) and the High Level Introduction of Talent Research Start-up Fund of Heilongjiang University of Science and Technology.

Acknowledgments

We would like to acknowledge the editors and reviewers for their comments and suggestions.

Conflict of interest

The authors declare that the research was conducted in the absence of any commercial or financial relationships that could be construed as a potential conflict of interest.

Publisher's note

Supplementary material

The Supplementary Material for this article can be found online at: https://www.frontiersin.org/articles/10.3389/feart.2023.1120344/full#supplementary-material

References

Cai, W., Dou, L. M., Si, G. Y., Cao, A. Y., Gong, S. Y., Wang, G. F., et al. (2019). A new seismic-based strain energy methodology for coal burst forecasting in underground coal mines. *Int. J. Rock Mech. Min. Sci.* 123, 104086. doi:10.1016/j.ijrmms.2019.104086

Diederichs, M. S., Kaiser, P. K., and Eberhardt, E. (2004). Damage initiation and propagation in hard rock during tunnelling and the influence of near-face stress rotation. *Int. J. Rock Mech. Min. Sci.* 41 (5), 785–812. doi:10.1016/j.ijrmms.2004.02.003

Ding, Z. W., Jia, J. D., Tang, Q. B., and Li, X. F. (2022). Mechanical properties and energy damage evolution characteristics of coal under cyclic loading and unloading. *Rock Mech. Rock Eng.* 55, 4765–4781. doi:10.1007/s00603-022-02884-x

Gong, F. Q., and Wang, Y. L. (2022). A new rock brittleness index based on the peak elastic strain energy consumption ratio. *Rock Mech. Rock Eng.* 55, 1571–1582. doi:10.1007/s00603-021-02738-y

Gong, F. Q., Yan, J. Y., Luo, S., and Li, X. B. (2019). Investigation on the linear energy storage and dissipation laws of rock materials under uniaxial compression. *Rock Mech. Rock Eng.* 52, 4237–4255. doi:10.1007/s00603-019-01842-4

Gong, F. Q., Zhang, P. L., Luo, S., Li, J. C., and Huang, D. (2021). Theoretical damage characterisation and damage evolution process of intact rocks based on linear energy dissipation law under uniaxial compression. *Int. J. Rock Mech. Min. Sci.* 146, 104858. doi:10.1016/j.ijrmms.2021.104858

Gong, F. Q., Ni, Y. X., and Ren, L. (2022). Effects of loading rate on rockburst proneness of granite from energy storage and surplus perspectives. *Rock Mech. Rock Eng.* 55, 6495–6516. doi:10.1007/s00603-022-02990-w

Grosse, C., and Ohtsu, M. (2008). *Acoustic emission testing: Basics for research-applications in civil engineering*. Berlin Heidelberg: Springer.

Huang, D., and Li, Y. R. (2014). Conversion of strain energy in triaxial unloading tests on marble. *Int. J. Rock Mech. Min. Sci.* 66, 160–168. doi:10.1016/j.ijrmms.2013.12.001

Jiang, L. S., Kong, P., Zhang, P. P., Shu, J. M., Wang, Q. B., Chen, L. J., et al. (2020). Dynamic analysis of the rock burst potential of a longwall panel intersecting with a fault. *Rock Mech. Rock Eng.* 53, 1737–1754. doi:10.1007/s00603-019-02004-2

Keneti, A., and Sainsbury, B.-A. (2020). Development of A Semi-Quantitative risk matrix for strain-burst hazard assessment – a numerical modelling approach in the absence of micro-seismic data. *Eng. Geol.* 279, 105893. doi:10.1016/j.enggeo.2020.105893

Li, Z. Y., Wu, G., Huang, T. Z., and Liu, Y. (2018). Study on shale energy evolution law and strength failure criterion under triaxial cyclic loading. *Chin. J. Rock Mech. Eng.* 37 (3), 662–670. doi:10.13722/j.cnki.jrme.2017.0927

Liu, X. B., Zhang, Z. Y., Ge, Z. L., Zhong, C. L., and Liu, L. (2021). Brittleness evaluation of saturated coal based on energy method from stress–strain curves of uniaxial compression. *Rock Mech. Rock Eng.* 54, 3193–3207. doi:10.1007/s00603-021-02462-7

Lu, Z. G., Ju, W. J., Gao, F. Q., Yi, K., and Sun, Z. Y. (2021). Bursting liability index of coal based on nonlinear storage and release characteristics of elastic energy. *Chin. J. Rock Mech. Eng.* 40 (8), 1559–1569. doi:10.13722/j.cnki.jrme.2020.1204

Meng, Q. B., Liu, J. F., Huang, B. X., Pu, H., Wu, J. Y., and Zhang, Z. Z. (2021). Effects of confining pressure and temperature on the energy evolution of rocks under triaxial cyclic loading and unloading conditions. *Rock Mech. Rock Eng.* 55, 773–798. doi:10.1007/s00603-021-02690-x

Peng, R. D., Ju, Y., Wang, J. G., Xie, H. P., Gao, F., and Mao, L. T. (2014). Energy dissipation and release during coal failure under conventional triaxial compression. *Rock Mech. Rock Eng.* 48 (2), 509–526. doi:10.1007/s00603-014-0602-0

Qiao, L., Hao, J. W., Liu, Z. Y., Li, Q. W., and Deng, N. F. (2022). Influence of temperature on the transformation and self-control of energy during sandstone damage: Experimental and theoretical research. *Int. J. Min. Sci. Technol.* 32, 761–777. doi:10.1016/j.ijmst.2022.02.008

Qin, T., Duan, Y. W., Sun, H. R., Wang, L., and Liu, H. L. (2020). Mechanical characteristics and energy dissipation characteristics of sandstone under triaxial stress conditions. *J. China Coal Soc.* 45 (S1), 255–262. doi:10.13225/j.cnki.jccs.2019.1393

Shirani Faradonbeh, R., Taheri, A., and Karakus, M. (2021). Failure behaviour of a sandstone subjected to the systematic cyclic loading: Insights from the double-criteria damage-controlled test method. *Rock Mech. Rock Eng.* 54, 5555–5575. doi:10.1007/s00603-021-02553-5

Tu, Q. Y., Cheng, Y. P., Xue, S., Ren, T., and Cheng, X. (2021). Energy-limiting factor for coal and gas outburst occurrence in intact coal seam. *Int. J. Min. Sci. Technol.* 31 (4), 729–742. doi:10.1016/j.ijmst.2021.05.009

Wang, F. T., Liang, N. N., and Li, G. (2019). Damage and failure evolution mechanism for coal pillar dams affected by water immersion in underground reservoirs. *Geofluids* 2019, 2985691–2985712. doi:10.1155/2019/2985691

Wang, A. W., Gao, G. S., Pan, Y. S., Song, Y. M., and Li, L. (2021). Impact liability and energy dissipation of prefabricated borehole coal samples. *J. China Coal Soc.* 46 (3), 959–972. doi:10.13225/j.cnki.jccs.2020.1364

Xiao, P., Li, D. Y., Zhao, G. Y., and Liu, H. X. (2021). New criterion for the spalling failure of deep rock engineering based on energy release. *Int. J. Rock Mech. Min. Sci.* 148, 104943. doi:10.1016/j.ijrmms.2021.104943

Xie, H. P., Li, L. Y., Peng, R. D., and Ju, Y. (2009). Energy analysis and criteria for structural failure of rocks. *J. Rock Mech. Geotechnical Eng.* 1 (1), 11–20. doi:10.3724/SP.J.1235.2009.00011

Xu, L., Gong, F. Q., and Liu, Z. X. (2021). Experiments on rockburst proneness of pre-heated granite at different temperatures: Insights from energy storage, dissipation and surplus. *J. Rock Mech. Geotechnical Eng.* 14 (5), 1343–1355. doi:10.1016/j.jrmge.2021.08.004

Zhang, Y., Feng, X. T., Zhang, X. W., Wang, Z. F., Sharifzadeh, M., and Yang, C. X. (2019). A novel application of strain energy for fracturing process analysis of hard rock under true triaxial compression. *Rock Mech. Rock Eng.* 52, 4257–4272. doi:10.1007/s00603-019-01868-8

Zhang, C., Wang, F. T., and Bai, Q. S. (2021). Underground space utilization of coalmines in China: A review of underground water reservoir construction. *Tunn. Undergr. Space Technol.* 107, 103657. doi:10.1016/j.tust.2020.103657

frontiers | Frontiers in Earth Science

TYPE Original Research
PUBLISHED 20 February 2023
DOI 10.3389/feart.2023.1115323

OPEN ACCESS

EDITED BY
Fangtian Wang,
China University of Mining and Technology, China

REVIEWED BY
Shizhong Zhang,
China University of Mining and Technology, China
Feng Wang,
Shandong University of Science and Technology, China

*CORRESPONDENCE
Baolin Jiang,
jiangbaolin_xust@foxmail.com

SPECIALTY SECTION
This article was submitted to Structural Geology and Tectonics, a section of the journal Frontiers in Earth Science

RECEIVED 03 December 2022
ACCEPTED 02 February 2023
PUBLISHED 20 February 2023

CITATION
Wang H, Jiang B, Jiao J and Li Y (2023), Overburden stress evolution characteristics and prediction of disasters with across-gully mining.
Front. Earth Sci. 11:1115323.
doi: 10.3389/feart.2023.1115323

Overburden stress evolution characteristics and prediction of disasters with across-gully mining

Hongwei Wang[1,2,3], Baolin Jiang[1]*, Jianqiang Jiao[1] and Yanjun Li[4]

[1]College of Energy Science and Engineering, Xi'an University of Science and Technology, Xi'an, China, [2]State Key Laboratory of Green and Low-carbon Development of Tar-rich Coal in Western China, Xi'an University of Science and Technology, Xi'an, China, [3]Key Laboratory of Western Mine Exploitation and Hazard Prevention Ministry of Education, Xi'an University of Science and Technology, Xi'an, China, [4]Xi'an Research Institute, China Coal Technology & Engineering Group Corp, Xi'an, China

The coal water co-mining of shallow coal seams in the loess gully area of Northern Shaanxi is affected by the coupling effect of overburden rock structure and topography. The development characteristics of mining fracture are complex and can induce mining and environmental disasters. To predict the disaster formation, taking the 113101 working face of the Kunyuan Coal Mine as the engineering background, numerical simulation, physical similarity simulation experiment, and theoretical analysis methods were used to analyze the mining gully of a shallow coal seam in a loess gully area. Based on the dynamic evolution characteristics of stress at different locations, the formation positions, dynamic development, and evolution processes of various fractures were studied; disaster-causing mechanisms were revealed and comprehensive methods were proposed. The results showed that in across-gully mining, the maximum horizontal compressive stress at the bottom of Gully No. 2 was approximately 20.00 MPa, the maximum horizontal tensile stress of the reverse slope section was approximately 1.50 MPa, the width of the F5 fracture of Gully No. 2 was 46.00 cm, and the elevation difference was up to 52.00 cm. The working face across-gully mining formed tensile fractures in most areas, collapsed fractures at the gully bottom, and extruded fractures in the reverse slope section. The fracture at the gully bottom could easily induce water–sand inrush and roof caving and supports crushing. The slope fracture could also induce a gully-induced landslide. According to the mechanisms and distribution areas of fracture disasters, the disaster areas were divided into water–sand inrush areas at the gully bottom, roof caving and supports crushing areas at the gully bottom and at the base of the slope section, and landslide areas at the upper part of the slope section and reverse slope section. Appropriate prevention and control measures were proposed, such as the upstream interception of surface water, slope reinforcement in the middle and upper part of the downhill section, artificial precracking of the roof in the middle and upper part of the downhill section, and grouting reinforcement at the gully bottom and slope toe of the downhill section. These measures were proven to effectively guarantee the safe and efficient mining efficiency of the working face.

KEYWORDS

loess gully area, shallow coal seam, coal water co-mining, characteristics and transfer of stress, fractures of overburden, prevention and control of disasters

1 Introduction

The Yushenfu (Yulin, Shenmu, and Fugu) mining area has two major characteristics: 1) the surface gullies are crisscrossed, the elevation difference is large, and hydrological conditions are complex, which differ from the evolution process of overburden breaking and transporting and cause all kinds of mining disasters to occur irregularly, which greatly affects the safe mining of underground coal resources; 2) the ecological environment is extremely fragile, characterized by drought, little rain, and low vegetation cover, and across-gully mining is prone to environmental disasters, such as gully breakage, vegetation death, and soil desertification, which seriously affects the fragile ecosystem balance of the loess gully areas. Therefore, it is important to study the law of overburden breaking and transport of coal water co-mining, analyze the dynamic evolution of fractures, predict the occurrence of disasters, and protect the ecological environment.

In 1992, China's geological scientists raised the issue of water protection mining. Over the past 20 years, scientists in the fields of geology, mining, ecology, and environment have explored and researched the issue of water conservation coal mining from multiple angles, initially establishing a water protection mining technology system, and significant progress has been made in engineering practice.

Coal water co-mining is the rational exploitation of two resources under the premise of water conservation, security, and environmental protection (Bai et al., 2009). After the concept and connotation of "coal-water" dual-resource mining were summarized, the technology and method of "coal-water" dual-resource mining were proposed (Gu et al., 2016; Wu et al., 2017). Mine water in the northwest of China's arid and semi-arid climate zone is characterized by high mineralization, which requires the use of desalination methods, such as distillation, ion exchange, membrane separation, and biological treatment, to reduce the mineralization, as well as to remove acids, suspended solids, trace elements, radioactivity, and toxic and hazardous substances (Sun et al., 2020; Gu et al., 2021). Lin et al. (2020) studied the spatial characteristics and regional differences of water use in coal mines of China and pointed out that coal production in Shaanxi uses more water and has higher coal-related wastewater emissions than in other areas. Zhang et al. (2021) found that longwall mining has an impact on groundwater levels, thereby affecting the growth of surface vegetation.

Researchers have carried out a series of studies on the formation and development of fissures in across-gully mining and achieved outstanding results. Wang et al. (2016) studied overburden transport and fracture development using empirical equations, physical similar simulations, and numerical simulations to determine the height of the overburden mining collapse zone and ensure the safe mining of shallow buried coal seams in gully terrain. Liu (2014) classified mining cracks in the gully area into tensile cracks, extrusion cracks, collapse cracks, and sliding cracks and analyzed their formation mechanisms. Li (2021) analyzed the linkage between the development and distribution characteristics of overburden fractures and overburden activities in shallow buried thick coal seam mining in the gully area. The number of mining fractures in the downhill section of mining overburden was less than that in the uphill section, while the width of fractures showed an opposite trend. Repeated mining leads to fracture activation development. Che et al. (2021) and Hou et al. (2021a); Hou et al. (2021b) used physically similar simulation experimental methods to analyze the development rules of the location and spacing of surface cracks in shallowly buried coal seams in the gully area and classified the surface cracks into three types: down-slope pushing cracks, reverse-slope tensioning cracks, and gully bottom uplift, based on the relationship between slope direction and mining direction, and concluded that overburden destruction and surface morphology jointly formed surface cracks. Zhang (2016) established a main roof cycle breaking trapezoidal load mechanics model for across-gully mining and analyzed the influence of gully geomorphology on fracture development. They found that the development of fractures in the gully slope and back groove slope bodies showed a trend of inversion toward the gully. The back groove slope body appeared with the gully slope body reverse tensile fractures, with the fractures developing gradually upward from the gully bottom to the top of the back groove. In contrast, the fractures in the back groove slope body developed downward and the slope body inverted toward the extraction areas. This inversion of the back groove slope body caused the formation of stable structures in the deep part of the overburden rock. Both Wang et al. (2022) and Wei et al. (2022) used PFC numerical simulation to analyze the dynamic development process of fractures, by which microfractures are first generated, extended and expanded, then agglomerated into clusters, and, finally, become fractures. This process can be divided into three stages of development: discontinuous jumping, continuous transverse extension, and lateral expansion. Wang et al. (2020) studied the overburden movement and stope stress evolution laws in the process of longwall mining through faults via Universal Distinct Element Code (UDEC) numerical simulation, theoretical analysis, and field measurement. These studies revealed the development characteristics and evolution process of overburden fractures in coal seam mining in gully areas.

The height of the overburden fractured zone determines whether water from the mine aquifer and the surface will have an impact on mining (Zhang et al., 2018). Liu (2014) studied the influencing factors and characteristics of mine water influx under different geological conditions and obtained different prediction methods for water influx simulation. Luo and Fan (2015) and Fang and Xia (2018) analyzed the possibility of occurrence of sudden water and sand collapse disasters at each stage of mining and formulated three-dimensional water damage control measures above and below the well in the gully area. Jiang et al. (2017) divided four types of areas by G_C (the ratio of bedrock to mining height), namely, water–sand inrush areas, water inrush areas, seepage areas, and water retention areas, and formulated reasonable water retention measures for each. Wei et al. (2022) analyzed the amount of surface gully water gushing into the mining area along the fracture under different conditions through UDEC and COMSOL numerical simulation experiments. Li et al. (2020) analyzed the mining gully channel flood filling mode of over-gully mining of shallow buried coal seam in loess hills, gave the formula for calculating the normal and maximum water gushing under the working face production flow-sink-seepage filling mode, and proposed corresponding water prevention and control measures. Chen (2020), Li (2013), and Chen (2015) analyzed the distribution law of "falling and fracture zones"

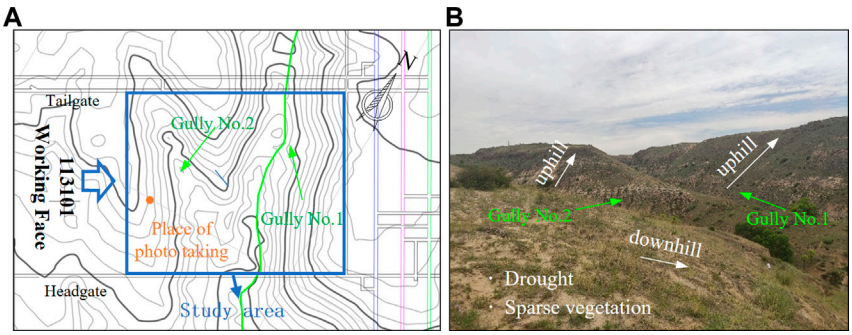

FIGURE 1
Spatial distribution of the study area and gullies, including **(A)** the relative position of the working face and gully and **(B)** photos of gully surface morphology.

TABLE 1 Mechanical parameters of rock strata.

Lithology	Thickness/m	Density/kg m^{-3}	Tensile strength/MPa	Cohesion/MPa	Bulk modulus/GPa	Shear modulus/GPa	Friction/°
Gritstone 1	30.00	2430	2.03	1.21	5.30	3.10	37.6
Coal 3^{-1}	1.81	1382	0.33	0.78	1.41	0.80	35.2
Mudstone	3.50	2170	0.49	0.63	1.70	0.60	30.5
Gritstone 2	7.50	2430	1.80	1.13	4.30	2.70	41.0
Medium-grained sandstone 1	6.50	2460	2.21	1.50	3.70	3.20	41.4
Siltstone 1	8.90	2400	2.20	1.55	4.50	3.10	40.8
Sandy mudstone	6.20	2510	1.72	1.40	4.70	2.20	37.3
Medium-grained sandstone 2	10.00	2450	2.16	1.60	4.81	3.80	41.1
Siltstone 2	28.80	2400	2.20	1.55	4.50	3.10	40.8
Aeolian sand	20.40	2080	0.07	0.04	0.85	0.31	31.0

on the roof of shallow buried coal seam across-gully mining, developed a prediction method of burst water volume and a zoning method of burst water hazard, revealed the mechanism of water–sand inrush under the action of multiple factors, and proposed technical measures of water–sand inrush prevention and control. Dong et al. (2021) analyzed water hazards caused by fractured zones in Northwest China. The aforementioned studies mainly revealed the mechanisms of water disasters induced by fracture development of shallow buried coal seam across-gully mining and formed water disaster prediction, zoning, and prevention measures. Disasters other than water disasters may be triggered by shallow buried coal seam mining in the gully area; therefore, it is necessary to study the different disasters that may occur in different locations in the gully area and judge the possible interconnection of each disaster to predict and manage water coal co-mining disasters under gullies.

This paper aims to predict possible induced disasters and carry out zoning and comprehensive management by studying the dynamic evolution characteristics of overburden stress, overburden fracture, and surface crack development in coal water co-mining under gullies using numerical simulations and physically similar simulation experiments, with the engineering context of the Kunyuan Coal Mine 113101 working face. This study provides reference for the prevention and control of coal water co-mining disasters under gullies and is based on the research background of coal and water co-mining.

2 Materials and methods

2.1 Study area and engineering background

The Kunyuan Coal Mine belongs to Daliuta Town, Yulin City, Shaanxi Province, China, and is located in the northern part of the Loess Plateau in Northern Shaanxi Province, at the southeastern edge of the Maowusu Desert. The geomorphological unit is a typical loess hilly area, and the

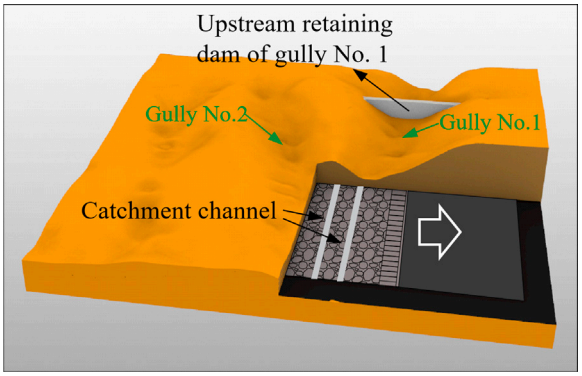

FIGURE 2
3D conceptual model of the 113101 working face, reflecting the concept of coal water co-mining underground and on the surface.

surface is basically covered by wind-bound sand. The gullies are deep in the bedrock, and the branch gullies are very well developed. There are two gullies crossing the surface of 113101 working face from northwest to southeast (Figure 1). Gully No. 1 is a wash gully, with average slope angles of 35.82° and 35.30° for the downhill and uphill sections, respectively (the downhill section is the side of the slope where the thickness of the overburden rock gradually decreases along the direction of advancement, and the opposite for the uphill section). There is a large weathering zone and burned rock on the east side of the slope and water flow in the gully all year, with an average flow rate of 197.30 m^3/h. Gully No. 2 is a cut gully, with average slope angles of 28.44° and 21.59° for the downhill and uphill sections, respectively. There is water flow only in the rainy season. Long-term water erosion has destroyed the structural integrity of the overburden rock, and two weathering erosion zones with vertical depths of 0.2–4.3 m have formed along the riverbed.

The 113101 working face is mainly mining a 3^{-1} coal seam with a buried depth of 29.36–91.80 m. The lowest depth of the coal seam in Gully No. 1 is 7.49 m, compared to 16.42 m in Gully No. 2. The average thickness of coal seam is 1.81 m, the structure is simple, and the bottom contains a stratum of gangue. The immediate roof is gray, gray–white mudstone, and sandy mudstone, with mud cementation and lamination development, containing a small amount of mica and plant fossils, and belongs to class III immediate roof; the main roof is gray and gray–white dense coarse-grained sandstone, with mud cementation and wavy lamination development, containing plant fossils, and belongs to class II main roof; and the floor is mainly gray and gray–white dense coarse-grained sandstone with mud cementation. The physical and mechanical parameters of the coal rock are shown in Table 1. The working face is 776 m in trend length and 280 m in inclination length. A longwall comprehensive mechanized coal mining method and natural collapse method are used to manage the roof, with a mining height of 1.80 m, five cycles of daily coal cutting, and a cut-off depth of 0.8 m. The purpose of coal water co-mining at working face 113101 is to recycle and utilize mine water, divert surface rivers, and restore the surface ecology of the mine area as much as possible after mining. As shown in Figure 2, the exploitation of water resources is divided into two parts: damming the surface to intercept the flow and pumping water in the collecting drain of goaf. The dam is

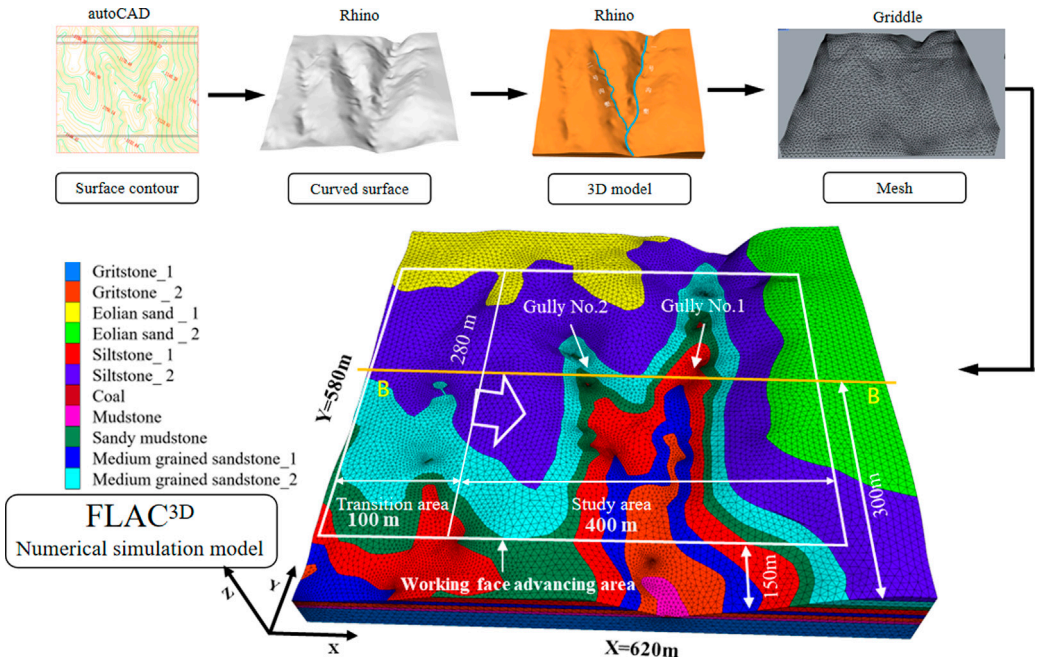

FIGURE 3
Establishment process from surface contour to 3D drawing, 3D mesh model, and FALC3D numerical simulation model.

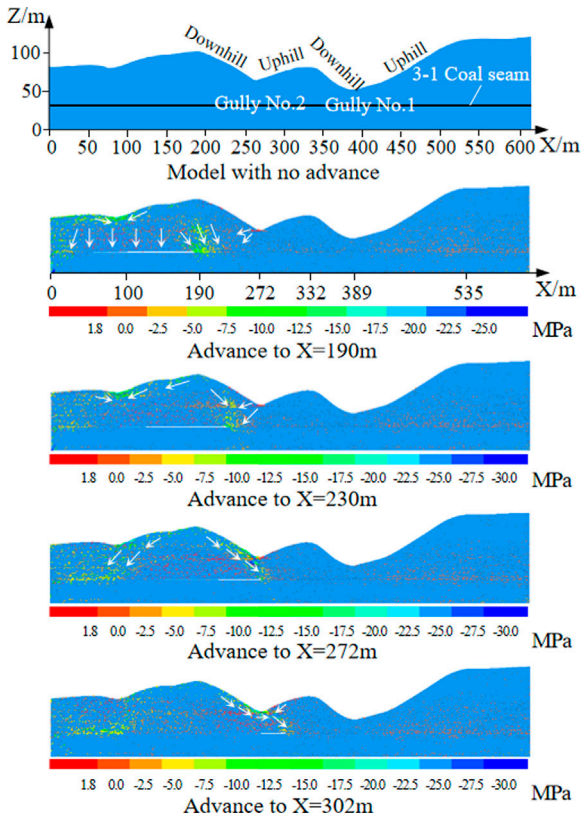

FIGURE 4
Distribution and transfer path of maximum principal stress in section B–B, with the working face advancing to X = 190 m, X = 230 m, X = 272 m, and X = 302 m.

located upstream of the first gully, 50 m from the tailgate of 113101 working face. The water collecting drain is advanced in the floor of the goaf in the middle of Gullies No. 1 and 2 and the water collecting drain is advanced in the floor at 30 cm in height and covered with a six-mesh screen.

2.2 Numerical simulation

Taking the Kunyuan Coal Mine 113101 working face as the engineering background, according to the engineering, geological, and production conditions as well as the physical and mechanical parameters of coal rocks (Table 1), a 3D model of the surface gully was established by Rhino software. Then, the grid was divided by Griddle and imported into FLAC3D software to generate a 3D numerical simulation model (Figure 3). The model size was L × W × H = 620 m × 580 m × 102 m, with 144,853 grid points and 795,173 cells. The Mohr–Coulomb principal structure model with large deformation stress mode was used. Taking the B–B section as reference, we analyzed the overburden stress evolution characteristics of shallow buried coal seam mining through the downhill section of Gully No. 2 (X = 190–270 m), uphill section of Gully No. 2 (X = 270–330 m), downhill section of Gully No. 1 (X = 330–390 m), and uphill section of Gully No. 1 (X = 390–535 m) to reveal the overburden transport law.

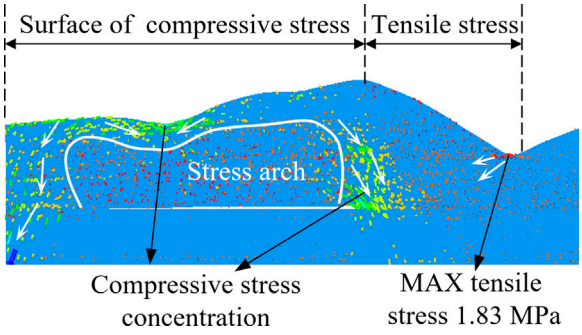

FIGURE 5
Shape of stress arch and the distribution characteristics of maximum principal stress when advancing to 190 m, and the maximum tensile stress of 1.83 MPa, located at the bottom of Gully No. 2.

3 Results

3.1 Path of stress transfer

The maximum principal stress distribution of the B–B section when the working face advances to Gully No. 2 (X = 190–332 m) is shown in Figure 4. The direction and size of the maximum principal stress deflection indicates that the overburden rock above the mining area formed a stress arch structure, with the rock strata below the stress arch in a stress release state and the rock strata above the "stress arch" in a compressive stress concentration state. This stress distribution state causes the surface behind the working face to be subjected to tensile stress, which is expressed as extrusion, and the surface above the working face to be subjected to tensile stress, which is expressed as tension. Specially, the bottom of Gully No. 2 was subjected to strong tensile stress effect for a long time and the effect was obvious, and the details are as follows.

The stress transfer law in Gully No. 1 was approximately the same as that in Gully No. 2. The details of the dynamic changes of the maximum principal stress during the advance of Gully No. 2 were as follows. As shown in Figure 5, the working face was advanced to X = 190 m. According to the route of maximum principal stress transmission, the stress arch was in the shape of a "saddle," similar to the shape of the surface, the overburden rocks above the stress arch were subject to compressive stress, and the overburden rocks below the stress arch were subject to tensile stress. From the surface stress situation, the back of the working face was subjected to compressive stress and the front of the working face was subjected to tensile stress, in which the concentration of tensile stress at the bottom of Gully No. 2 was the most obvious, with a maximum value of 1.83 MPa.

As shown in Figure 6, when the working face was advanced to 272 m, the stress arch shape returned to normal. Taking the gully bottom as the boundary, the surface behind the working face showed obvious compressive stress concentration and that in front of the working face showed tensile stress concentration. Currently, the most complicated changes were in the gully bottom and the

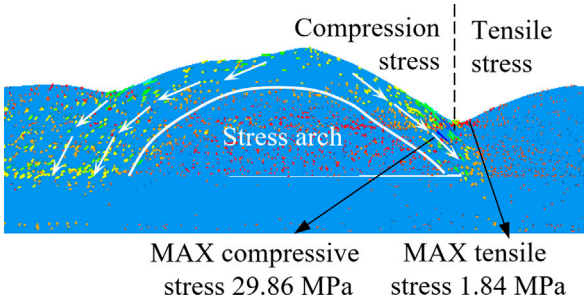

FIGURE 6
Shape of the stress arch and the distribution characteristics of maximum principal stress when advancing to 272 m; the maximum tensile stress is 1.84 MPa, and the maximum compressive stress is 29.86 MPa, both located at the bottom of Gully No. 2.

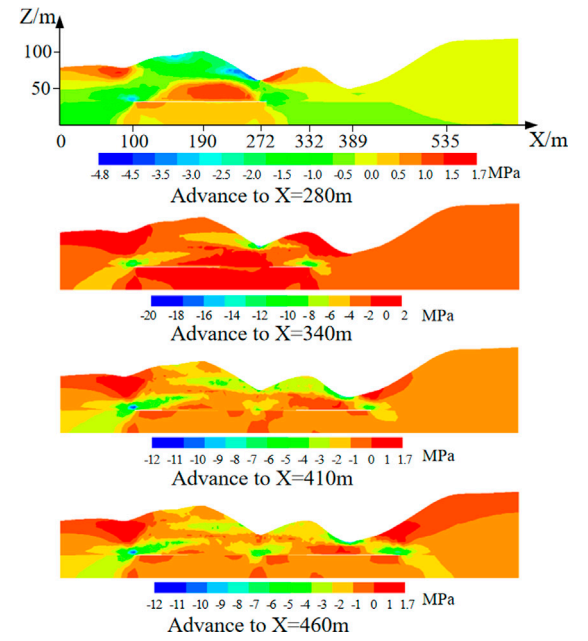

FIGURE 7
Evolution characteristics of XX stress of section B–B with the working face advancing to X = 280 m, X = 340 m, X = 410 m, and X = 460 m.

magnitude of stress changes was large, making it easy for the overburden rock to collapse with obvious elevation difference in the gully bottom.

In summary, the macroscopic stress transfer path was as follows: first, the stress behind the working face was transferred to both sides along the trend and the stress transferred to the working face was arched, resulting in the concentration of compressive stress behind the working face; then, the stress in front of the working face was transferred to the working face, and the tensile stress was concentrated in front of the working face; finally, the stress in the downhill and uphill sections above the goaf was transferred to the gully bottom.

3.2 Characteristics of stress distribution

When the working face was advanced to X = 280 m, the horizontal extrusion stress was concentrated in the lower part of the downhill section of Gully No. 2 and the gully bottom, the maximum horizontal extrusion stress was 4.68 MPa, the maximum horizontal tensile stress in the uphill section was 1.53 MPa. The downhill section of Gully No. 2 was above the goaf, and sliding fractures would be formed throughout the downhill section while extrusion fractures would only be formed at the base of it. The uphill section was above the coal and contained over-extension fractures as shown in Figure 7A. When the working face was advanced to X = 340 m, the horizontal extrusion stress at the bottom of Gully No. 2 was 8.00–12.00 MPa and the stress state changed from tensile stress to minor stress to compressive stress. The fractures healed or changed types to form other fractures, as shown in Figure 7B. When the working face was advanced to X = 410 m, a small range of horizontal compressive stress was concentrated in the lower part of downhill section of Gully No. 1, the maximum compressive stress was 6.00 MPa, the formed fractures were easily healed to varying degrees, a small range of horizontal compressive stress was concentrated in the lower part of the uphill section of Gully No. 1, the maximum horizontal tensile stress was 1.75 MPa, and tensile fractures were prone to form along the weak surface of rock joints, as shown in Figure 7C. When the working surface was advanced to X=460 m, horizontal extrusion stress concentration occurred at the bottom of Gully No. 1, and extrusion and collapse fractures formed at the base of the slope. The loose layer and weathering zone of the uphill slope body of Gully No. 1 were staggered with the bedrock under the action of tensile stress, which made it easier for sliding fractures to form, as shown in Figure 7D.

The horizontal stress of the surface first increased and then decreased during across-gully mining. The horizontal stress of the surface was 2.11–4.02 MPa in the downhill section and 5.92–17.35 MPa in the uphill section. The surface of the gully was in a horizontal compressive stress state far from the working face, as shown in Figure 8A. The vertical tensile stress of the surface first increased and then decreased. The vertical tensile stress at the surface of Gully No. 2 was 0.69–3.74 MPa, with the vertical stress at the surface being the largest across the gully. The vertical tensile stress at the surface of Gully No. 1 was 0.69–1.56 MPa and the uphill section was in a vertical compressive stress state behind the working face, as shown in Figure 8B. The vertical tensile stress reflected to the overburden collapse state and the tensile stress range in front of the working face included the overburden fracture development and overbreak areas. The tensile stress range in the gully area included the collapse fracture development area. The bottom of Gullies No. 2 and 1 was in a high-tensile stress state, which encouraged collapse fractures.

4 Discussion

The aforementioned research was based on FLAC^{3D} numerical simulation to study the across-gully mining of coal water co-mining mine. The stress state of each area at different stages of advancement was obtained from the path of stress transfer, and the stress state of each area was obtained from the characteristics of stress distribution, which

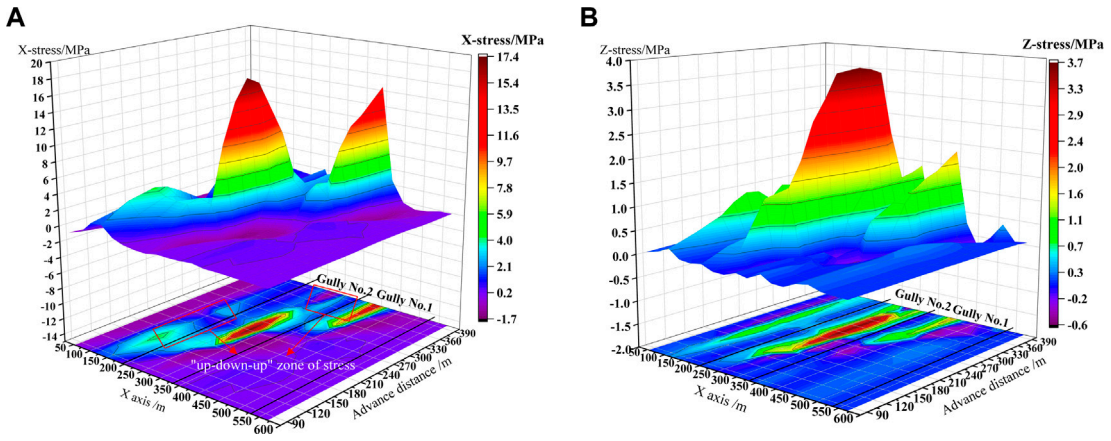

FIGURE 8
Stress distribution characteristics of certain surface measuring points on the B–B section when advancing to certain distances: **(A)** horizontal stress and **(B)** vertical stress.

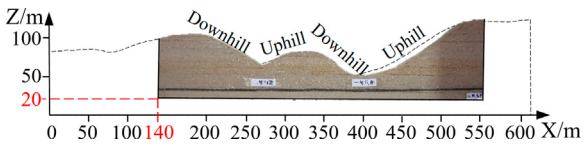

FIGURE 9
Location of the physical similarity simulation model and section B–B.

reflects the possible fractures and the movement trend of overburden. However, there are major limitations for using finite element methods to study rock breaking and fracture development. Its displacement field cannot directly analyze the dynamic development of fractures, so it is difficult to predict disasters. Currently, PFC numerical simulation is commonly used to analyze the stress field, displacement field, and force chain transmission law. However, this method requires the establishment of small particles, consumes a lot of memory and CPU computing power, and requires the selection of a constitutive model suitable for the rock strata to reasonably analyze and determine various parameters in theory. Much more research still needs to be carried out, and it is difficult to obtain scientific research results in a short time. Therefore, this study chose to conduct physical similarity simulation experiments to supplement the study and further investigate the overburden transport characteristics, fracture development, and evolution process, to predict possible disasters.

4.1 Evolution characteristics of overburden fractures

To verify the numerical simulation results and further determine the dynamic development process of fractures in across-gully mining, a 2D physically similar simulation model was established based on the B–B section (Figure 9), with a geometric similarity ratio of 1:200, capacity similarity ratio of 0.64, stress similarity ratio of 3.2×10^{-3}, and similar material ratios for each rock strata, as shown in Table 2. The model dimensions were L × W × H = 2000 × 200 × 506 mm. The coordinate system of the physically similar simulation model and the numerical simulation model were the same, and the coordinates of the lower left corner of the physically similar simulation model were X = 140 m and Z = 20 m) The left end of the model had no contact with the model frame and the model was advanced 20 cm to simulate the goaf in front of gully to avoid the error caused by the left boundary of the model.

When the working face advanced to X = 230 m, tensile fracture F2 developed to the top downhill section of Gully No. 2, the overburden breakage angle was 120°, and the topmost loess of the model was destroyed into seven parts of different sizes, with length ranging from 3.0 to 5.6 cm (Figure 10A). When the working face advanced to X = 250 m, the immediate roof collapse and main roof breakage caused the overburden rock to form a big intact rock. The center of gravity of this rock mass shifted above the mining areas, which led to the expansion of tensile fracture F4, the formation of tensile fracture F3, and the narrowing of fracture F2 (Figure 10B); fracture F4 was located at the base of the downhill section of Gully No. 2, which connected Gully No. 2 with the goaf and became a water–sand inrush channel. The formation of the big intact rock indicated that the overburden load decreased after the overburden thickness decreased, which led to the change of cycle collapse distance, and fractures were formed in the thin bedrock with low strength and weak surface as the working face advanced.

As shown in Figure 11, when advancing to X = 270 m, the working face was located below the bottom of Gully No. 2. The surface rift F4 broke downward, forming a break line of approximately 5 cm long, and stopped developing at 11.2 cm above the working face. In addition, a new break line developed from the bottom of Gully No. 2 downward, which exceeded the working face by 10.3 cm, called an overburden overbreak line. This line stopped developing at 6.1 cm above the working face and was the prototype of fracture F5. When the working face advanced to X = 280 m, the overburden overbreak line developed into collapse

TABLE 2 Similar material ratio for rock strata.

Lithology	Actual thickness of rock strata/m	Thickness of rock strata model/m	Mixing ratios of sand: gypsum: calcium carbonate
Gritstone 1	10.00	5.00	8:2:8
Coal 3^{-1}	1.81	0.91	26:1:2:16 (coal)
Mudstone	3.50	1.75	9:1:9
Gritstone 2	7.50	3.75	8:2:8
Medium-grained sandstone 1	6.50	3.25	8:4:6
Siltstone 1	8.90	4.45	8:3:7
Sandy mudstone	6.20	3.10	9:2:8
Medium-grained sandstone 2	10.00	5.00	8:4:6
Siltstone 2	28.80	14.40	8:3:7
Aeolian sand	20.40	10.20	10:1:9

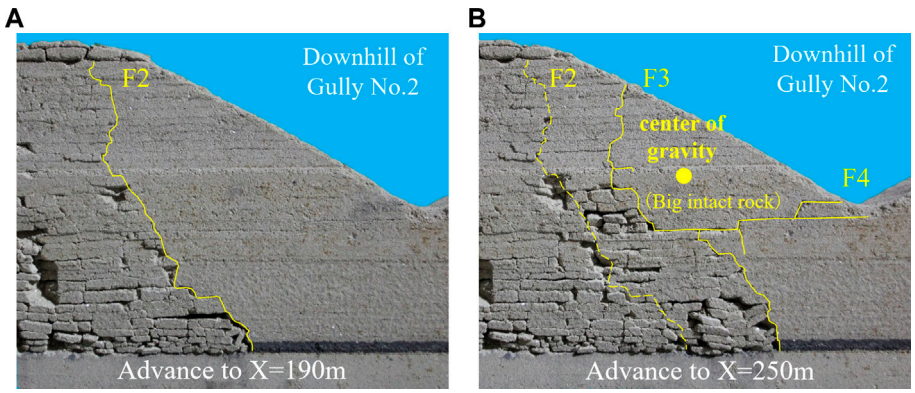

FIGURE 10
Characteristics of fracture development and overburden migration when advancing to **(A)** X = 190 m and **(B)** X = 250 m.

fracture F5, which penetrated the overburden to the working face from the surface. At this point, the overburden rock was cut off above or in front of the hydraulic supports, which caused the collapsed roof to press on and damage the supports. The width of fracture was approximately 1.8 mm, the elevation difference between both sides of fracture was approximately 2.6 mm, and a fracture with width of 2.3 mm and elevation difference of 2.6 mm was formed on the surface. In addition, the secondary development of fracture F3 occurred with the formation of fracture F5. When the working face advanced to X=290 m, tensile fracture F6 was formed and the width and elevation difference of fracture F5 were reduced to 0.6 and 1.1 mm, respectively. Fracture F6 was formed by tensile damage but showed the characteristics of collapse fracture at its surface. The width of surface fracture was 1.5 mm and elevation difference was 0.9 mm, which was presumed to be caused by the rotation of broken overburden to goaf. When the working face was advanced to X = 310 m, tensile fracture F7 was formed, and fractures F5 and F6 and the surface fractures were basically healed.

As shown in Figure 12, when the working face advanced to X = 330 m, it entered the downhill section of Gully No. 1 and tensile fracture F8 was formed, forming fractures on the surface. When the working face advanced to X = 350 m, the upper part of fracture F8 narrowed, the surface fractures healed, and the lower part showed secondary expansion; tensile fracture F9 was formed in front of the working face, which overshot the working face by 6.4 cm and was located at the base of the downhill section of Gully No. 1; another big intact rock was formed between fractures F8 and F9. The load of this rock was transferred to supports, which crushed the supports. When the working face advanced to X = 370 m, fractures F8 and F9 narrowed and collapse fracture F10 was formed at the base of the downhill section, which went straight from the surface to the working face and caused support crushing and water–sand inrush. In addition, the fracture F10 formed a surface crack with an elevation difference of 0.37 mm. The left side of this surface crack sank, and the right side was elevated, that is, the left side showed a collapse fracture and the right side showed an extrusion fracture. It is presumed that the overburden rock was caved

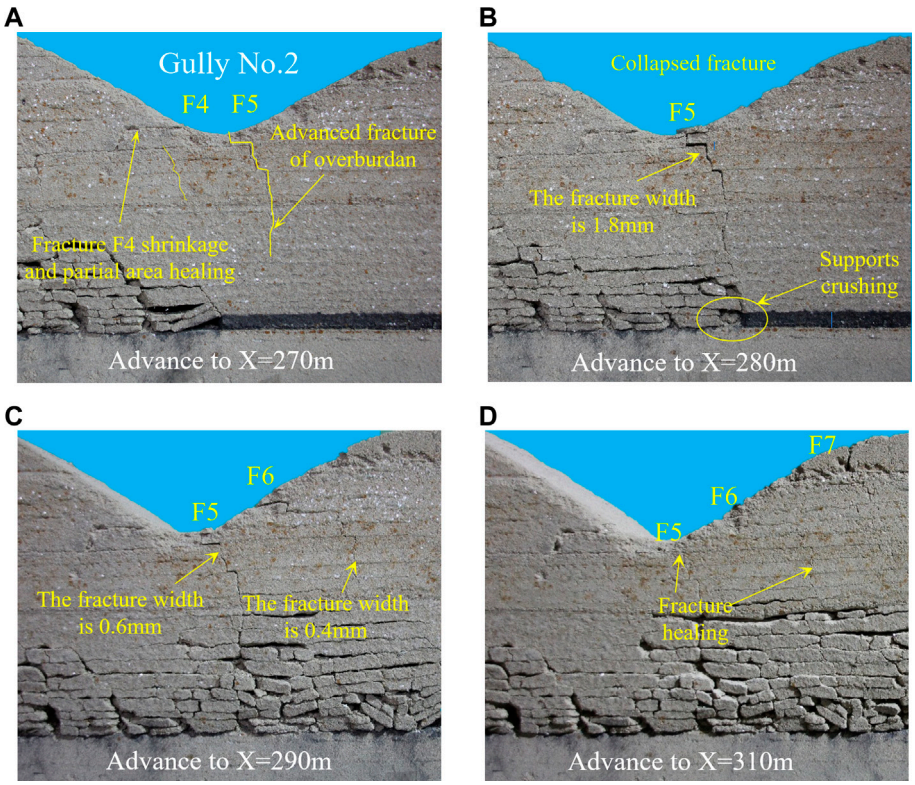

FIGURE 11
Characteristics of fracture development and overburden migration when advancing to **(A)** X = 270 m, **(B)** X = 280 m, **(C)** X = 290 m, and **(D)** X = 310 m.

and formed a collapse fracture, then the broken rock strata and the big intact rock in the back goaf deflected toward the working face, resulting in the left side of fracture F10 squeezing the right side and creating a collapse-extrusion surface crack on the surface near collapse fracture. When the working face was advanced to X = 390 m, tensile fracture F11 was formed, the overburden elevation difference between the two sides of fracture F10 was obviously reduced, and the surface fracture was healed to some extent; however, the extruded and lifted rock on the right side was still higher than the surrounding surface.

As shown in Figure 13, when the working face advanced to X = 410 m, tensile fracture F12 was formed and fracture F11 showed no obvious change. When the working face advanced to X = 430 m, tensile fracture F13 was formed, fracture F11 was narrowed, fracture F12 mostly healed, and both surface cracks disappeared. When the working face advanced to X = 450 m, tensile fracture F14 was formed, fracture F13 shrank, and the surface fracture healed. When the working face advanced to X = 470 m, a large collapse space was formed after the main roof collapsed, which led to further collapse and compaction of the collapsed rock strata on the left side of fracture F14. Fracture F14 was transformed into a collapse fracture and the elevation difference between the two sides of the fracture was 0.22 mm, forming a tensile-collapse crack on the surface.

The fractures in different areas had distinct characteristics, shown in Table 3. The fractures healed more easily in the gully bottom, while the junction between the base downhill section and gully bottom was most likely to collapse; the fracture formation of the slope body with obvious change of overburden thickness tended to be lagging behind and the fracture formation in the downhill section tended to form a big intact rock after the fracture formation was lagging behind. The fracture formation lagging behind in the uphill section tended to trigger the secondary development of the existing fractures and turned into collapse fractures. The distribution of each type fracture and the dynamic development of representative fractures are shown in Figure 14.

4.2 Types and formation mechanisms of disasters

Possible disasters that can occur during the mining of the 113101 working face are water–sand inrush, roof caving and supports crushing, and gully-induced landslide. The formation mechanisms of these disasters are as follows.

4.2.1 Water–sand inrush

The formation of water–sand inrush requires: 1) fractures connecting the surface and the working face (goaf); and 2) that water and sand can flow into the above fractures.

When the rock strata under the cover of water and sand in Gullies No. 1 and 2 produce tensile and collapse fractures that go straight through the goaf or working face,

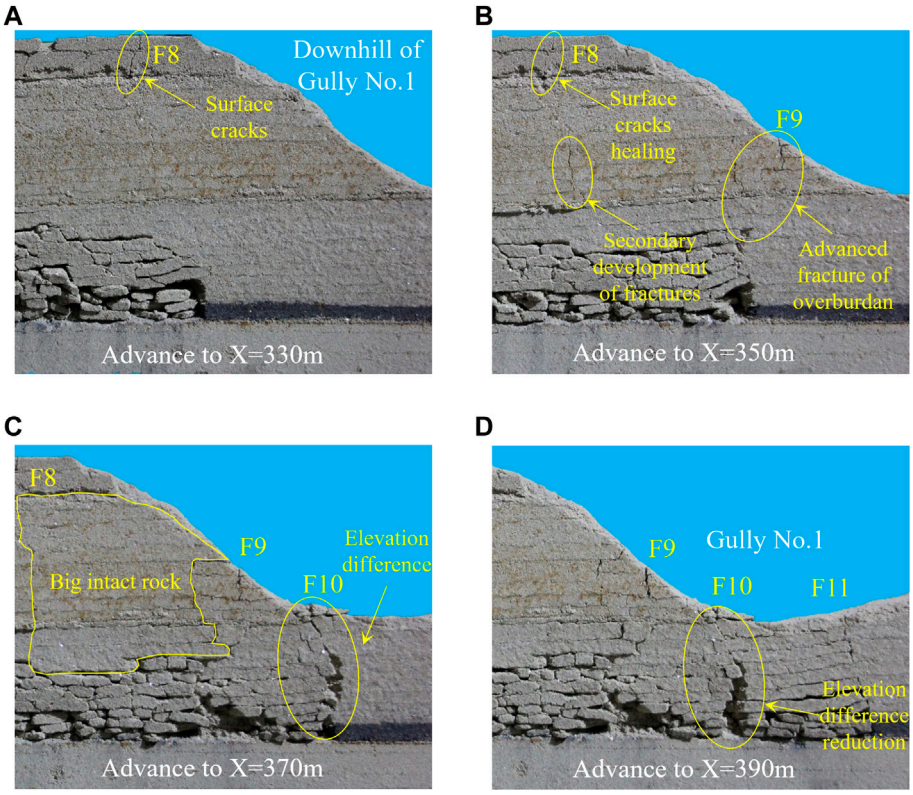

FIGURE 12
Characteristics of fracture development and overburden migration when advancing to **(A)** X = 330 m, **(B)** X = 350 m, **(C)** X = 370 m, and **(D)** X = 390 m.

TABLE 3 Dynamic developmental and evolutionary characteristics of representative fractures.

Number of fracture	Types of fracture	Dynamic developmental evolution
F2	Tensile fracture	Formed—reduced—stable
F3	Tensile fracture	Formed—stable—developed—stable
F4	Tensile fracture	Formed—expanded—reduced—healed
F5	Collapse fracture	Formed—developed—reduced—healed
F6	Tensile fracture	Formed—healed
F8	Tensile fracture	Formed—reduced—expanded—stable
F10	Collapse–extrusion fracture	Formed—changed types—reduced—stable
F11	Tensile fracture	Formed—stable—reduced—stable
F14	Tensile–collapse fracture	Formed—developed—changed types—reduced—stable

water and sand flow into the goaf or working face along these fractures, resulting in water–sand inrush disasters, as shown in Figure 15.

4.2.2 Roof caving and supports crushing

When the working face advances to the gully bottom, due to the incomplete structure of the overburden rock, it is eroded by running water while the hard rock strata, such as the key strata, are eroded. The rock strata are small in thickness and low in strength, and collapse fractures are easily produced above the working face, such as fractures F5 and F10. After the formation of such fractures, the load of the broken overburden above the working face acts on the hydraulic supports. The strong mine pressure causes the hydraulic supports to be crushed (shown in Figure 16), which can cause coal wall spalling, equipment damage, and casualties.

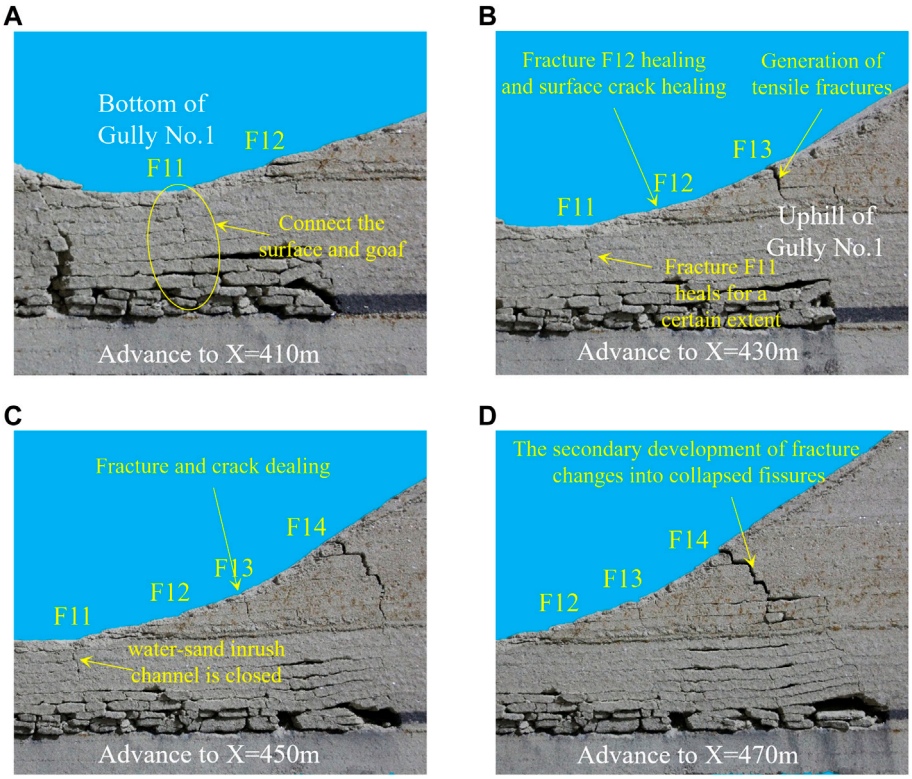

FIGURE 13
Characteristics of fracture development and overburden migration when advancing to **(A)** X = 410 m, **(B)** X = 430 m, **(C)** X = 450 m, and **(D)** X = 470 m.

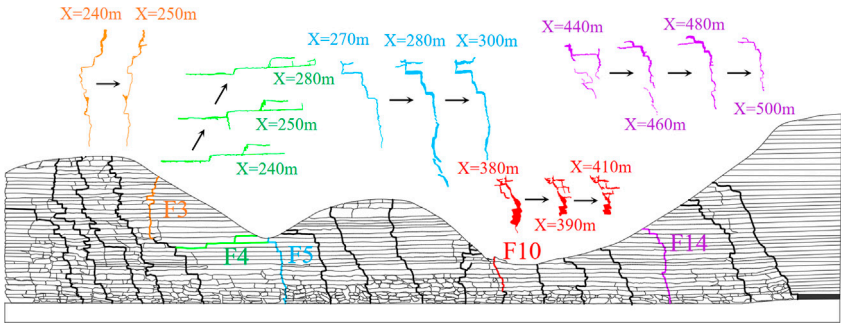

FIGURE 14
Distribution of all fractures and dynamic development of representative fractures (F3, F4, F5, F10, and F14)

4.2.3 Gully-induced landslide

There are loess and aeolian sands on the slope body and slope top of Gullies No. 1 and 2, and there is a weathering erosion zone with a height of 0.2–4.3 m at the slope toe, thus forming the characteristics of weak slope base and heavy slope body. When a mining fracture develops to the slope, the disturbed loose layer (loess and aeolian sand) is damaged and destabilized, forming a slope instability landslide. When the mining-induced fractures develop to the weathering erosion zone at the slope toe, the slope toe structure is destroyed, the supporting point of the slope disappears, and the loess and aeolian sand on the slope slide to the gully bottom under the action of gravity, forming a landslide of slope instability. When the working face is pushed through the gully bottom, if collapse fractures are generated at the gully bottom and toe of the slope, the slope foundation structure is missing, forming a landslide of base slope loss. In general, the probability of landslides in the downhill section is low and the impact on the working face is high. In contrast, the probability of landslides in the uphill section is high and the impact on the working face is low.

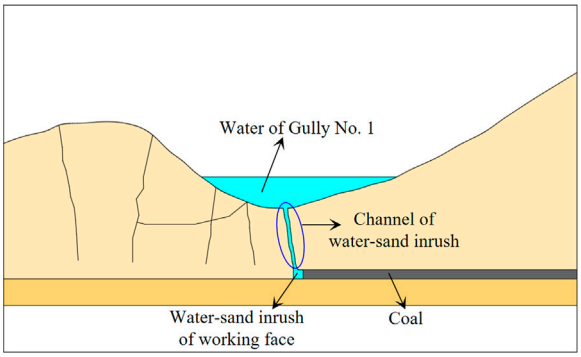

FIGURE 15
Formation mechanisms of water–sand inrush; channel that connects water and the working face (goaf).

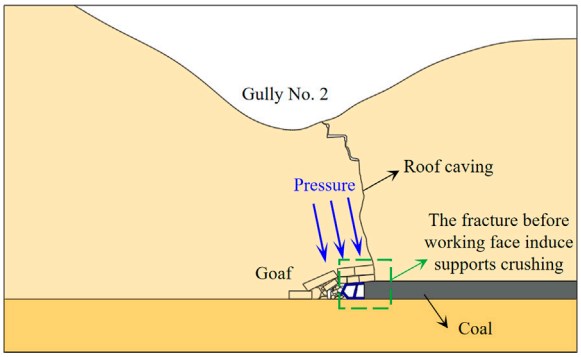

FIGURE 16
Formation mechanisms of roof caving and supports crushing; fractures are formed in front of or above the supports.

In simple terms, any crack under the water and sand at the gully bottom will lead to water and sand inrush. Collapse fractures near the gully bottom on the side of the slope will lead to roof caving and supports crushing. Tensile fractures and sliding fractures of the slope, and collapse fractures and tensile fractures at the base of the slope may lead to landslides.

4.3 Division of disaster areas

The disaster areas of the 113101 working face crossing gully was divided according to the types of disaster-causing fractures and disaster-causing mechanism as follows: water–sand inrush areas, water and sand covered areas which easily form water–sand inrush channels, roof caving and support-crushing areas like the gully bottom and the base of the slope where collapse fractures easily formed, landslide I areas where the displacement of the middle and upper part of the slope section evolves slowly and landslides easily occur along the weak surface after a large area of hanging roof, and landslide II areas where the inverse slope section is prone to slope toe instability landslides. These disaster areas are shown in Figure 17.

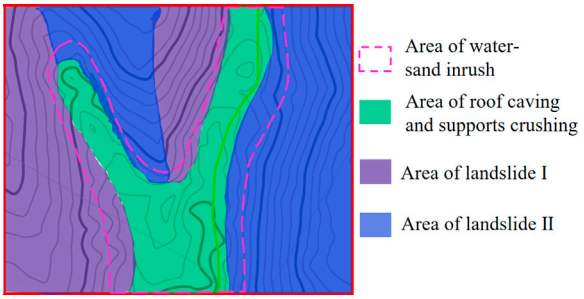

FIGURE 17
Zoning of water–sand inrush, roof caving and supports crushing, and landslide in the study area.

4.4 Prevention and control measures for disasters

The disasters caused by gully mining are interrelated. Therefore, they should be analyzed systematically and comprehensively for integrated disaster prevention and control, and corresponding disaster prevention and control measures should be formulated, as shown in Figure 18. The following measures can be taken for the effective prevention and control of disasters:

(1) Water–sand inrush prevention measures: for all types of fractures, the core of prevention is to remove water and sand and close the water–sand inrush channel.

A) Interception of surface water in advance: a dam should be built in the upper reaches of Gully No. 1 and high-power pumps and drainage pipes should be used to cross the working face 113101 to transport water to the lower reaches of Gully No. 1 to maintain the natural conditions of the surface water system and the ecological balance of the surface.

B) Laying a water-resisting layer: fine sand at the bottom of Gullies No. 1 and 2 should be removed and replaced with wet loess, covered with a layer of straw, degradable plastic film, more straw, and a layer of 20 cm thick loess. To prevent surface migration from tearing the degradable plastic film, the plastic film should contain folds.

C) Choosing the time to advance: across-gully mining should be conducted during the dry season or when there is no rainfall.

D) Water storage and sand fixation: on the slope, ecological grass blanket technology or planting low shrub vegetation should be implemented for water storage, sand fixation, soil and water conservation, and ecological restoration.

(2) Gully-induced landslide prevention measures: for sliding fractures, the core prevention measures are to remove possible landslide material and reinforce rock.

A) Reduction of slope height: engineering machinery and equipment are used to remove the loess and aeolian sand on the top of the slopes of Gullies No. 1 and 2, reducing the thickness of the loose layer, overburden load, possibility of landslide, and the working face dynamic load.

B) Slope reinforcement: the lower part of the rock along the slope can be reinforced using anchors, anchor cables, slope

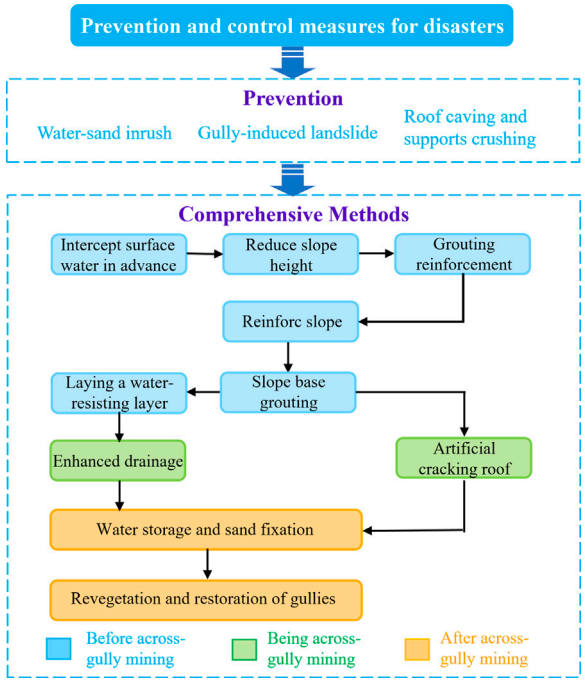

FIGURE 18
Comprehensive methods of disaster control, arranged in chronological order.

protection nets, cement, and other equipment to prevent slope instability landslides. The reinforcement range needs to be predicted and estimated. Such reinforcement measures are often used in the construction of highways and railways in mountainous areas. The technology is mature, highly effective, and low cost.

C) Slope base grouting: grouting reinforcement is used along the slope at the base of weak weathered rock to ensure the stability of the slope base to prevent slope foundation missing landslides.

(3) Aiming prevention and control measures of roof caving and supports crushing at big intact rocks and collapse fractures: the core of prevention and control is to strengthen the weak weathered rock strata at the gully bottom, control the collapse of the roof of the goaf, and maintain the normal mine pressure law.

A) Grouting reinforcement: the root cause of roof caving and supports crushing is that the roof rock strata are small in thickness and low in strength. Therefore, grouting reinforcement at the gully bottom on the ground and underground can reduce the possibility of roof breaking.

B) Artificial cracking of the roof: the length of the suspended roof can be shortened by presplitting the middle and upper rock strata of the downhill section, easily forming a large-scale complete rock mass to collapse the roof. This reduces the possibility of advanced fractures of the roof in front of the working face. Possible splitting methods include ground drill blasting, water pressure presplitting roof, and working face roof caving. The roof failure spacing is consistent with the periodic caving step and the special area can be modified.

(4) Other prevention and control measures:

In addition to the aforementioned targeted prevention and control measures, other methods can assist in the prevention and control of various disasters, such as strengthening drainage, advancing faster with small cutting depth, reducing mining height, and moving supports with pressure. In the production process, monitoring means and prevention awareness should be strengthened. The support of the working face and roadway should be strengthened moderately. The mining scheme can be further optimized and a comprehensive command, disaster prevention, and control system can be established.

During the across-gully mining of the 113101 working face in the Kunyuan Coal Mine, the aforementioned prevention and control measures were taken. No disasters occurred during the across-gully mining task, which ensured the safety of personnel and normal production and demonstrated the reliability of these measures.

5 Conclusion

(1) Numerical simulation revealed that the macroscopic stress transfer path was as follows: the stress moved from the goaf to the surroundings in an arch shape, from the front and back of the working face to the working face, and from the top of the slope to the gully bottom. The stress state at the gully bottom transitioned from tensile stress to minor stress to compressive stress. The reverse slope section often showed a compressive state. The base of the slope often showed compressive stress, while the downhill section often showed tensile stress.

(2) Physical similarity simulation revealed the common characteristics of the dynamic development and evolution of fractures and summarized their locations. Most fractures showed the dynamic evolution from formation and expansion to development and shrinkage to healing, while fractures at the gully bottom were easy to evolve into other fractures. Collapse fractures were mostly distributed in the gully bottom, extrusion fractures were distributed in the base of the downhill section, and sliding fractures were mostly distributed in the lower part of the downhill section and reverse slope section.

(3) According to the characteristics of fracture formation and evolution, the areas and types of disasters can be predicted, and the division of disaster areas can be determined. Water–sand inrush is caused by water and sand in the gully flowing into working faces through transfixion fractures caused by mining. Roof caving and supports crushing is caused by collapse fractures in the thin bedrock of the gully bottom which cause the roof to collapse as a whole and crush the supports of working face. Gully-induced landslides are caused by mining fractures which lead to slope failure and instability or collapse at the base of a slope, forming landslides of slope instability or of base slope loss. According to the characteristics of each disaster and possible disaster areas, the disaster areas are divided into water–sand inrush areas, roof caving and support-crushing areas, and gully-induced landslide areas.

(4) For the gully bottom, we implemented measures to prevent and control water–sand inrush, such as the interception of surface water in advance and the creation of a water barrier. For the gully bottom and base of the slope of the downhill section, we implemented measures to prevent and control roof caving and

supports crushing, such as grouting reinforcement and artificial roof precracking. For the middle and upper part of the downhill and uphill sections, we implemented measures to prevent and control gully-induced landslides, such as slope height reduction, slope reinforcement, and slope base grouting. These targeted prevention and control measures effectively ensured the safety of 113101 working face across-gully mining and achieved good social and economic benefits.

Data availability statement

The raw data supporting the conclusion of this article will be made available by the authors without undue reservation.

Author contributions

HW: formulation of overall idea of the paper, writing—original abstract, and analysis of simulation data. BJ: numerical simulation, physical similarity simulation, data curation, and writing—original draft. JJ: picture processing and format review. YL: providing original experimental data, investigation, and language review.

Funding

This work was supported by the National Natural Science Foundation of PRC under Grant Nos. 51634007 and 51974230 and the Major Science and Technology Innovation Projects in Shandong Province under Grant No. 2019JZZY020326. The Youth Innovation Team of Shaanxi Universities.

Acknowledgments

Support from the aforementioned agencies is gratefully acknowledged.

Conflict of interest

Author YL was employed by the China Coal Technology & Engineering Group Corp.

The remaining authors declare that the research was conducted in the absence of any commercial or financial relationships that could be construed as a potential conflict of interest.

Publisher's note

References

Bai, H., Mao, X., Yao, B., and Tang, J. (2009). Research on simultaneous exploitation of coal and groundwater in LU'AN coalfield. *Chin. J. Rock Mech. Eng.* 28, 395–402.

Che, X., Hou, E., Sun, X., Jiang, Y., Xie, X., Cong, T., et al. (2021). Research on overburden breaking characteristics and ground crack formation mechanism of shallow coal seam under the gully. *J. Xi'an Univ. Sci. Technol.* 41, 104–111+186. doi:10.13800/j.cnki.xakjdxxb.2021.0114

Chen, W. (2015). *Study on mechanism and control technology of mining water disasters under loess gully runoff in Northern Shaanxi*. [Dissertation]. Beijing, China: China University of Mining and Technology.

Chen, Y. (2020). *The law of ground collapse and the prediction of water bursting risk in ZhangJiaMao Coal Mine*. [Dissertation]. Xi'an, China: Xi'an University of Science and Technology. doi:10.27397/d.cnki.gxaku.2020.000695

Dong, S., Wang, H., Guo, X., and Zhou, Z. (2021). Characteristics of water hazards in China's coal mines: a review. *Mine Water Environ.*40, 325–333. doi:10.1007/S10230-021-00770-6

Fang, G., and Xia, Y. (2018). Prevention and control technology of water during mining extremely thick coal seam with thin rock roof under ditch in Chaigou coal mine. *J. Xi'an Univ. Sci. Technol.* 38, 758–766. doi:10.13800/j.cnki.xakjdxxb.2018.0509

Gu, D., Zhang, Y., and Cao, Z. (2016). Technical progress of water resource protection and utilization by coal mining in China. *J. China Coal Soc.* 44, 1–7. doi:10.13199/j.cnki.cst.2016.01.001

Gu, D., Li, T., Li, J., Guo, Q., Jiang, B., Bian, W., et al. (2021). Current status and prospects of coal mine water treatment technology in China. *Coal Sci. Technol.* 49, 11–18. doi:10.13199/j.cnki.cst.2021.01.002

Hou, E., Chen, Y., Che, X., Xie, X., and Gao, B. (2021a). Study on overburden failure characteristics and fracture evolution law of shallow buried coal seam through trench mining. *Coal Sci. Technol.* 49, 185–192. doi:10.13199/j.cnki.cst.2021.10.025

Hou, E., Feng, D., Xie, X., Cong, T., Li, M., Feng, C., et al. (2021b). Development characteristics and treatment methods of mining surface cracks in shallow-buried coal seam gully. *J. China Coal Soc.* 46, 1297–1308. doi:10.13225/j.cnki.jccs.2020.0143

Jiang, Z., Lei, S., Cao, H., Guo, L., Zhang, J., and Qiao, X. (2017). Coal mining under river recharged by desert. *J. China Coal Soc.* 42, 73–79. doi:10.13225/j.cnki.jccs.2016.5030

Li, T., Gao, Y., Guo, L., and Feng, H. (2020). Prediction of water inflow with mining across ditches in loess ridge area based on runoff-confluence seepage water filling mode. *J. Henan Polytech. Univ.* 39, 23–27. doi:10.16186/j.cnki.1673-9787.2020.6.4

Li, J. (2013). *Study on the mechanism and prevention and control technics of sand inrush and water blasting of shallow buried coal seam mining under thin bedrock*. [Dissertation]. Xi'an, China: Xi'an University of Science and Technology.

Li, X. (2021). *Study on evolution law and seepage characteristics of mining-induced fissure in overlying rock of shallow and thick coal seam in loess gully region*. [Dissertation]. Baotou, China: Inner Mongolia University of Science and Technology. doi:10.27724/d.cnki.gnmgk.2021.000394

Lin, G., Jiang, D., Fu, J., Dong, D., Sun, W., and Li, X. (2020). Spatial relationships of water resources with energy consumption at coal mining operations in China. *Mine Water Environ.* 39, 407–415. doi:10.1007/s10230-020-00663-0

Liu, H. (2014). *The development law and treatment technology of ground fissures due to underground mining in loess hilly area of Western China*. [Dissertation]. Beijing, China: China University of Mining and Technology.

Liu, Y. (2014). The water inflow prediction methods of working face under different mining conditions of shallow coal seam. *Saf. Coal Mines* 45, 158–161. doi:10.13347/j.cnki.mkaq.2014.02.049

Luo, L., and Fan, K. (2015). Water prevention and treatment system of shallow buried thin bedrock seam mining along valleys. *Saf. Coal Mines* 46, 203–206. doi:10.13347/j.cnki.mkaq.2015.12.057

Sun, Y., Chen, G., Xu, Z., Yuan, H., Zhang, Y., Zhou, L., et al. (2020). Research progress of water environment,treatment and utilization in coal mining areas of China. *J. China Coal Soc.* 45, 304–316. doi:10.13225/j.cnki.jccs.YG19.1654

Wang, F., Tu, S., Zhang, C., Zhang, Y., and Bai, Q. (2016). Evolution mechanism of water-flowing zones and control technology for longwall mining in shallow coal seams beneath gully topography. *Environ. Earth Sci.* 75, 1309. doi:10.1007/s12665-016-6121-4

Wang, F., Ma, Q., Zhang, C., and Feng, G. (2020). Overlying strata movement and stress evolution laws triggered by fault structures in backfilling longwall face with deep depth. *Geom. Nat. Hazards Risk* 11 (1), 949–966. doi:10.1080/19475705.2020.1763482

Wang, S., Wei, J., Song, S., Hou, E., and Sun, T. (2022). Study on overburden and surface damage characteristics of shallow-buried coal seam mining in loess gully area. *Coal Sci. Technol.* 50, 1–9. doi:10.13199/j.cnki.cst.2022-0389

Wei, B., Wang, H., and Shang, H. (2022). Study on overburden failure characteristics and surface water infiltration law of coal seam mining through gully. *Saf. Coal Mines* 53, 161–168. doi:10.13347/j.cnki.mkaq.2022.06.026

Wei, J., Wang, S., Song, S., and Sun, Q. (2022). Numerical simulation of evolution law of overburden fractures and surface cracks in shallow coal seam through ditch mining. *Coal Geol. Explor.* 10, 67–75. doi:10.12363/issn.1001-1986.22.03.0134

Wu, Q., Shen, J., and Wang, Y. (2017). Mining techniques and engineering application for "Coal-Water" dual-resources mine. *J. China Coal Soc.* 42, 8–16. doi:10.13225/j.cnki.jccs.2016.5032

Zhang, S., Fan, G., Zhang, D., and Li, Q. (2018). Physical simulation research on evolution laws of clay aquifuge stability during slice mining. *Environ. Earth Sci.* 77 (7), 278–310. doi:10.1007/s12665-018-7401-y

Zhang, S., Fan, G., Zhang, D., Li, S., Chen, M., Fan, Y., et al. (2021). Impacts of longwall mining speeds on permeability of weakly cemented strata and subsurface watertable: a case study. *Geom. Nat. Hazards Risk* 12 (1), 3063–3088. doi:10.1080/19475705.2021.1993354

Zhang, Y. (2016). *Study on mining overlying strata movement and fracture evolution law in shallow coal seam with gully developed landscape*. [Dissertation]. Beijing, China: China University of Mining and Technology.

Frontiers in Earth Science

Investigates the processes operating within the major spheres of our planet

Advances our understanding across the earth sciences, providing a theoretical background for better use of our planet's resources and equipping us to face major environmental challenges.

Discover the latest Research Topics

See more →

Frontiers

Avenue du Tribunal-Fédéral 34
1005 Lausanne, Switzerland
frontiersin.org

Contact us

+41 (0)21 510 17 00
frontiersin.org/about/contact